Fourier Optics Field Representations for the Design of Wide Field-of-View Imagers at Sub-millimetre Wavelengths

Dabironezare, Shahab

DOI
10.4233/uuid:23c845e1-9546-4e86-ae77-e0f14272517b

Publication date
2020

Document Version
Final published version

Citation (APA)
Dabironezare, S. (2020). *Fourier Optics Field Representations for the Design of Wide Field-of-View Imagers at Sub-millimetre Wavelengths*. [Dissertation (TU Delft), Delft University of Technology]. https://doi.org/10.4233/uuid:23c845e1-9546-4e86-ae77-e0f14272517b

Important note
To cite this publication, please use the final published version (if applicable).
Please check the document version above.

Fourier Optics Field Representations for the Design of Wide Field-of-View Imagers at Sub-millimetre Wavelengths

Fourier Optics Field Representations for the Design of Wide Field-of-View Imagers at Sub-millimetre Wavelengths

DISSERTATION

for the purpose of obtaining the degree of doctor
at Delft University of Technology
by the authority of the Rector Magnificus, Prof. dr. ir. T. H. J. J. van der Hagen,
chair of the board for Doctorates,
to be defended publicly on
Thursday 14 May 2020 at 12:30 o'clock

by

Shahab Oddin DABIRONEZARE

Master of Science in Electrical Engineering,
Delft University of Technology, the Netherlands,
born in Mashhad, Iran.

This dissertation has been approved by the promotors.

Composition of the doctoral committee:

Rector Magnificus	Chairman
Prof. dr. N. Llombart Juan,	Delft University of Technology, promotor
Prof. dr. A. Neto,	Delft University of Technology, promotor
Independent members:	
Prof. dr. ir. J. J. A. Baselmans,	Delft University of Technology
Prof. dr. G. Gerini,	Eindhoven University of Technology
Dr. S. Rao,	Northrop Grumman Aerospace Systems
Dr. M. Ettorre,	Institut d'Électronique et de Télécommunications de Rennes
Reserve member:	
Prof. dr. ir. L. C. N. de Vreede,	Delft University of Technology
Other members:	
Dr. G. Carluccio,	NXP Semiconductors, daily supervisor

European Research Council

Established by the European Commission

The work presented in this thesis has been performed at TU Delft and financed by the European Research Council starting grant (ERC-2014-StG LAA-THz-CC), No. 639749.

Keywords: Fourier Optics, Geometrical Optics, Quasi-Optical Systems, Wide Field of View Imagers, Lens Antennas, Reflector Antennas, Wide Band Imagers, Sub-millimetre Systems.

Cover design by: Shahab Oddin Dabironezare.

Printed by: Ipskamp Drukkers B.V., Enschede, Netherlands.

An electronic version of this dissertation is available at: http://repository.tudelft.nl/

ISBN 978-94-028-2047-8

To my parents, Vida and Mahmoud

Contents

Chapter 1

Introduction

1.1 Quasi-Optics

Quasi-Optics (QO) is the specific branch of electromagnetic science and engineering that investigates high frequency phenomena where diffraction due to the finite size of the scatterers cannot be neglected. This definition was reintroduced by Leopold Felsen in 1965 [1]. The term Quasi-Optics, is in fact much older, and has been used for the first time by F. Schroeter in 1929 [2], and then resurfaced in the academic publications about 30 years later [3]. For a period of time Quasi-Optics was also referred to as "Microwave Optics" in the literature [4, 5].

One can trace QO principles and its applications back to the Hertz experiments (1887) [6], Fig. 1.1, when he showed that the nature of electromagnetic waves and light are comparable, and measured the properties of electromagnetic waves as predicted by Maxwell's equations. He aimed for devices with sizes as small as possible for the experiment. To focus electromagnetic power in a directive beam, Hertz used a cylindrical parabolic reflector made of Zinc with an aperture of 2 m by 1 m and a focal distance of 12.5 cm. The experiment was performed at wavelength of 66 cm. Even though his reflector and beam size both were only 2 wavelengths in size, he managed to demonstrate the propagation laws of reflection and refraction for EM waves, previously only attributed to "Optics". Moreover, he studied the polarization of the EM waves in his experiment. Marconi, in his early research period (1894) [7], also employed reflector antenna, in the shape of parabolic cylinder, to obtain a directive beam of radiation at wavelength of 25 cm. He achieved a communication link over a distance of 6.5 km using this antenna. Similar early research were performed by Bose, Righi, Trouton and others [5]. However, eventually for a long period of time, the interest of researchers shifted towards longer wave lengths for communication purposes [5].

In the late 1950s, technological advancements allowed for development of near millimetre components and systems. Thanks to this technological push, QO principles were again employed to design systems (Quasi-Optical Systems) with high directive beams in this shorter wavelength regime [9]. Historically in EM science and engineering, whenever the community is struggling with developing high power sources, QO principles and careful design of QO components and their feeds resurface as a viable solution.

The term Quasi-Optics can also be referred to methods for modeling and characterizing propaga-

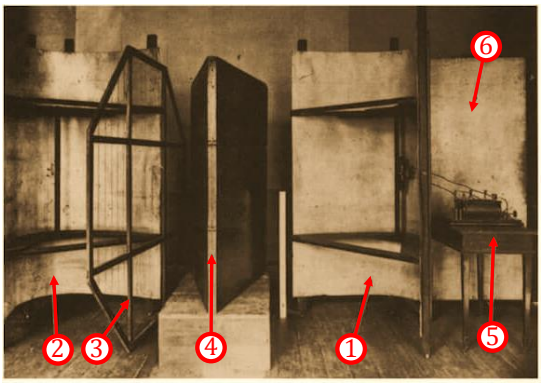

Figure 1.1: Hertz's experiment in 1887 on demonstrating the propagation laws in EM waves [8]. (1) Transmitter with a cylindrical parabolic reflector, (2) receiver with a similar cylindrical parabolic reflector, (3) octagonal wooden frame with parallel wires, for demonstration of polarization, (4) stack of three wooden boxes to hold dielectric materials for demonstration of refraction, (5) power supply, and (6) metal sheet reflector for the demonstration of reflection.

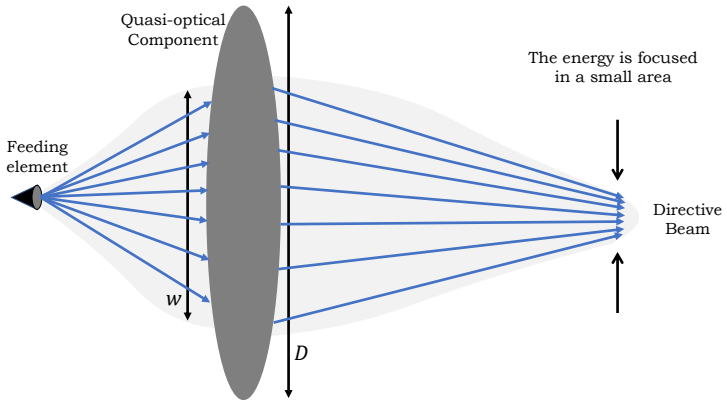

Figure 1.2: Schematic representation of a Quasi-Optical System.

tion and interaction of high frequency electromagnetic waves. In general, these methods are assumed to be accurate and computationally feasible when diameter of the components, D, are within the range $10 < D/\lambda < 1000$ (see Fig. 1.2). Since Quasi-Optics concerns with the propagation of EM radiation through optical components whose size is comparable to the wavelength where diffraction phenomenon is significant, these days, microwave, mm-wave and THz antennas, are their main frequency of interests. In comparison to classical Optics, at cm-, mm- and sub-mm wavelengths, EM propagation through QO components leads to more divergence and diffraction effects as well as coherence and definite polarization state [9].

1.2 Wide Field-of-View Quasi-Optical Systems at Sub-mm Wavelengths

In recent years, advanced QO based systems operating at (sub)-mm wavelengths are standard solutions for the state-of-the-art sensing and imaging applications. Most common application of these systems are for astronomical observations [10, 11, 12, 13, 14, 15, 16, 17, 18, 19], and standoff personnel screening [20, 21, 22, 23, 24, 25, 26]; while QO systems are also used for industrial remote sensing, atmosphere sensing and etc. Since operating in higher frequencies leads to higher data rates for communication systems, new areas of research based on QO systems in 5G and beyond 5G systems are emerging [27, 28, 29, 30, 31, 32, 33, 34, 35]. To meet the demanding performance requirements in these systems, highly directive radiative beams are essential. Higher directivity leads to better angular resolution, which is a key parameter in imaging scenarios; also in sensing and communication applications leads to a higher signal to noise ratio. To achieve these requirements, QO components, e.g. reflectors and dielectric lenses, are widely used in combination with antenna feeds. A few examples of such systems are reported in Fig. 1.3. As shown in Fig. 1.3(a), thanks to use of QO systems, the mm-wave and THz radiation can be focused into a certain direction. Here, based on the requirements in each application, gains in the orders of 20 to 120 dBis are achieved. The QO systems with the reported directivities, are shown in Fig. 1.3(b)-(l).

In the given examples, improving the Field of View (FoV) of the QO system is a key improvement for many applications. Future security imagers will require larger Field of Views (FoVs), comparable to the size of a human body (i.e. images with over 100000 pixels), and video rate speeds (> 10 Hz). The presence of many detectors in the focal plane of an optical system (e.g., charged coupled device (CCD) like configuration) enables the use of systems with none or very limited mechanical scanning. In space applications, large FoV is also favorable and leads to improvement in overall image acquisition speed [10, 11, 12, 13]. Future high frequency communication systems with wide scanning performance [35] are also required to improve the cell coverage.

Besides wider FoVs, improving the bandwidth of operation in the future QO systems is another major improvement for many applications. Recently, a THz 3D radar system with $3:1$ bandwidth ratio has been proposed [36] to achieve resolutions in the order of a millimetre. Passive radiometry systems also benefit from large available bandwidth to achieve high sensitivities [22]. Due to the lack of prior spectra knowledge from the source, the performance of astronomical spectrometers such as [37] enhances by looking at a larger portion of the spectrum simultaneously.

One of the promising detector array configurations for wide FoV applications is the Fly's eye lens arrays coupled to antennas or absorbers, Fig. 1.4(a) and (b). These systems are primarily integrated with on-chip lens antennas, and operate with similar principles to CCD cameras. For instance, cryogenic Kinetic Inductance Detectors (KIDs) based either on absorbers or planar antennas coupled lenses are employed for passive cameras [11, 12, 13]. Moreover, in recent years, to realize large FoV imaging systems, there has been a significant effort in developing large format Focal Plane Arrays (FPAs) of bare absorbers based detectors with medium sensitivities for commercial sub-millimetre imaging cameras, Fig. 1.4(c). Some current cameras make use of KIDs [10, 11, 21, 41] or uncooled micro-bolometers [42, 43]. Traditionally, since the heat capacity of most bolometers scales with the area, antenna coupling structures have been used to reduce the bolometer physical dimension [44], at the cost of a more complex FPA

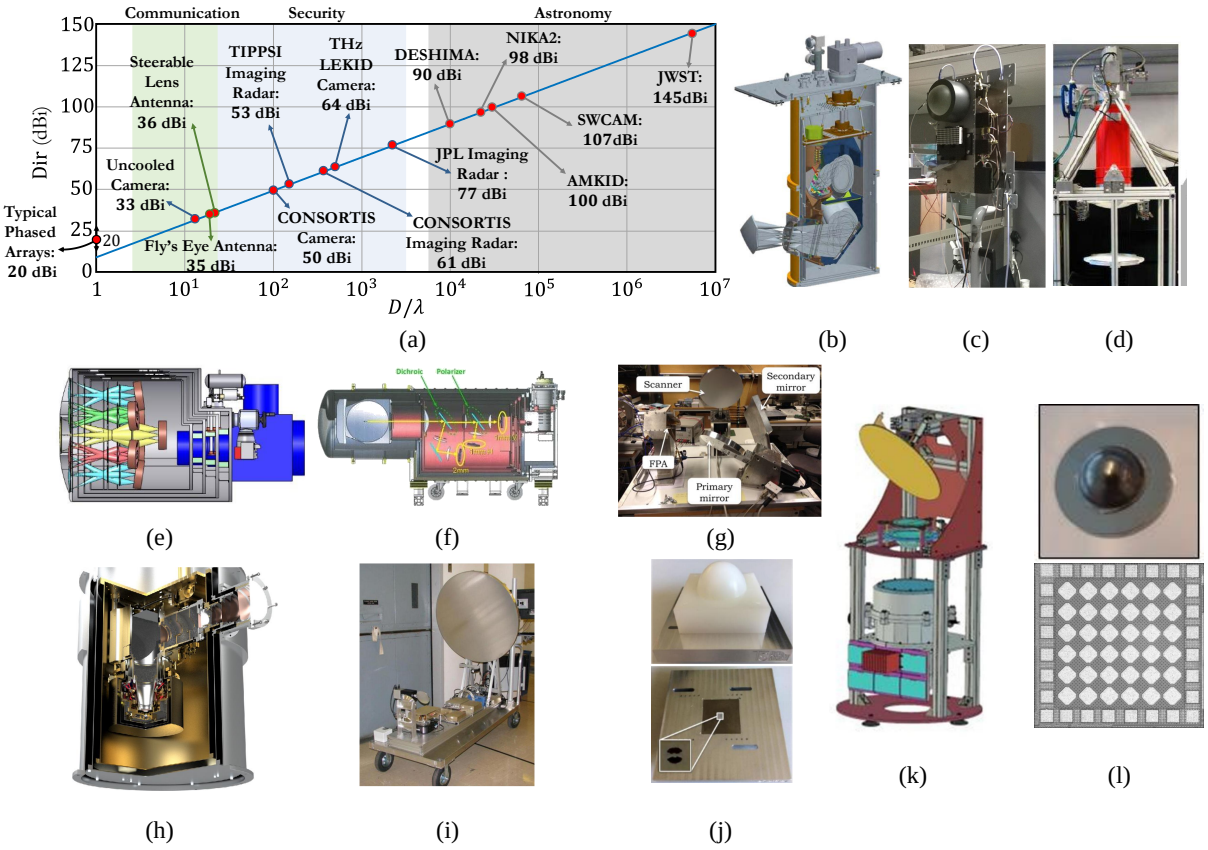

Figure 1.3: (a) Directivity of the state-of-the-art Quasi-Optical systems versus the size of their limiting aperture. (b) Cold stage QO system of AMKID [12]. (c) 2D steerable integrated lens antenna for 5g communication system [31]. (d) THz passive camera based on lumped element KIDS [21]. (e) Cold stage optics for Short Wavelength Camera (SWCAM) [11]. (f) Cold stage optics for NIKA 2 instrument [10]. (g) QO system of TIPPSI security Radar [26]. (h) Cold stage optics for DESHIMA spectrometer [38]. (i) QO system of THz security imaging Radar [20]. (j) A single element of fly's eye lens array for beyond 5g communication systems [35]. (k) QO system of CONSORTIS security imager which consists of a passive camera and an active radar [24, 39]. (l) Passive THz imaging array: lens component and the antenna array [40].

architecture (e.g., fly's eye lens arrays [45] or horn arrays [46]). Instead, in [47], the use of FPAs of bare absorbers was proposed for tightly sampled large format configurations, i.e. in combination with optical systems with limited mechanical scanning. Such configurations have been recently implemented in astronomical instruments [10, 42], and security imagers [21, 41].

The trade-offs which dominate the design of focal plane arrays based on antenna feeds are well-known, [48, 49], especially when the systems are required to operate over narrow frequency bands. Focal plane arrays of bare absorbers are, however, much less studied. The amount of power received, and the obtainable angular resolution are significantly different from the one of antenna feeds. The difference raises from the fact that absorbers, unlike single port antennas, respond incoherently to multiple aperture field distributions induced by the incident field [50].

In summary, development of wide band wide FoV QO systems operating at (sub)-millimetre wavelengths is an essential step forward for the future imaging systems aiming at security and space applica-

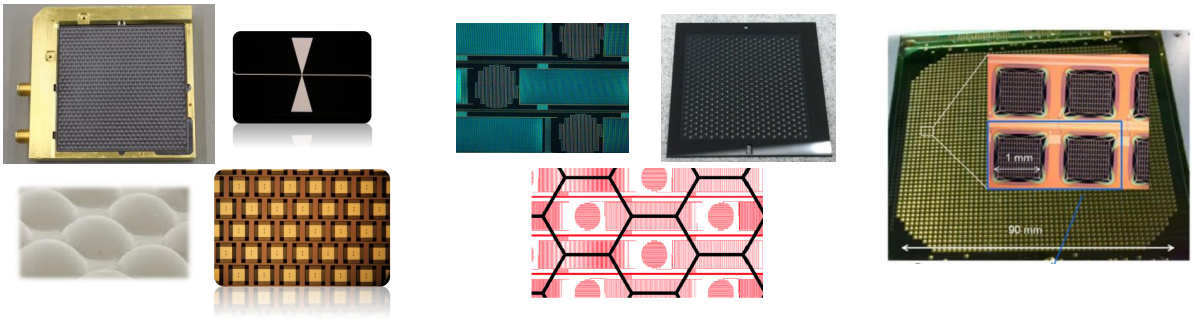

(a) (b) (c)

Figure 1.4: (a) Fly's eye configuration of KID coupled leaky wave antennas [12]. (b) Fly's eye configuration of lumped element KID absorbers [11]. (c) Focal plane array of bare absorbers based on Kinetic Inductance Bolometers [41].

tions, as well as communication systems. In these systems, large format absorber based FPAs are a cost efficient solution for passive cameras, while antenna based feeders are needed for applications where phase information should be preserved.

In these scenarios, a full-wave electromagnetic analysis, which includes the coupling between the Quasi-Optical (QO) system and the detector array, is numerically cumbersome and time-consuming. To develop these advanced wide field-of-view Quasi-Optical systems, and fulfill their demanding requirements, establishing a better theoretical frame-work for analysing and designing QO systems is essential.

1.3 Analysis of Quasi-Optical Systems in Reception

A well known technique to analyse QO systems is the ray tracing. This technique has being used to analyze Optics for centuries, as shown in Fig. 1.5(a). Ray tracing is packaged in commercial software such as OpticStudio [51], Fig. 1.5(b). This method is insightful and can be used to evaluate the propagation of rays through a QO system providing first order estimation of phase aberrations in the systems.

An analysis tool for QO systems that is elegant and simple is based on Gaussian Beam propagation [54], Fig. 1.5(c). This representation, assuming the fundamental Gaussian mode, is appropriate when the EM fields are well collimated with a clear direction of propagation and variation in transverse direction. Here, the Maxwell's equations are simplified to the Paraxial wave equation, where, it is assumed that the variation of the magnitude of the EM fields along the propagation direction is small over a distance comparable to the wavelength. This variation is also assumed small compared to the variation of the EM fields along the plane perpendicular to the propagation direction. This method is well suited for rapid analysis of on-axis propagation of EM waves through multiple QO components. Moreover, this model is also applicable for approximating the radiation patterns of simple (sub)-mm feeds such as corrugated or scalar horns [55]. As the result, the coupling of these feeds to the QO components can be addressed directly by a single Gaussian beam propagation through the system. Despite its merits, however, Gaussian beam propagation exhibits inaccuracies in analysing the current state-of-the-art of QO systems. In particular: I) the considered Paraxial wave approximations in this model limit

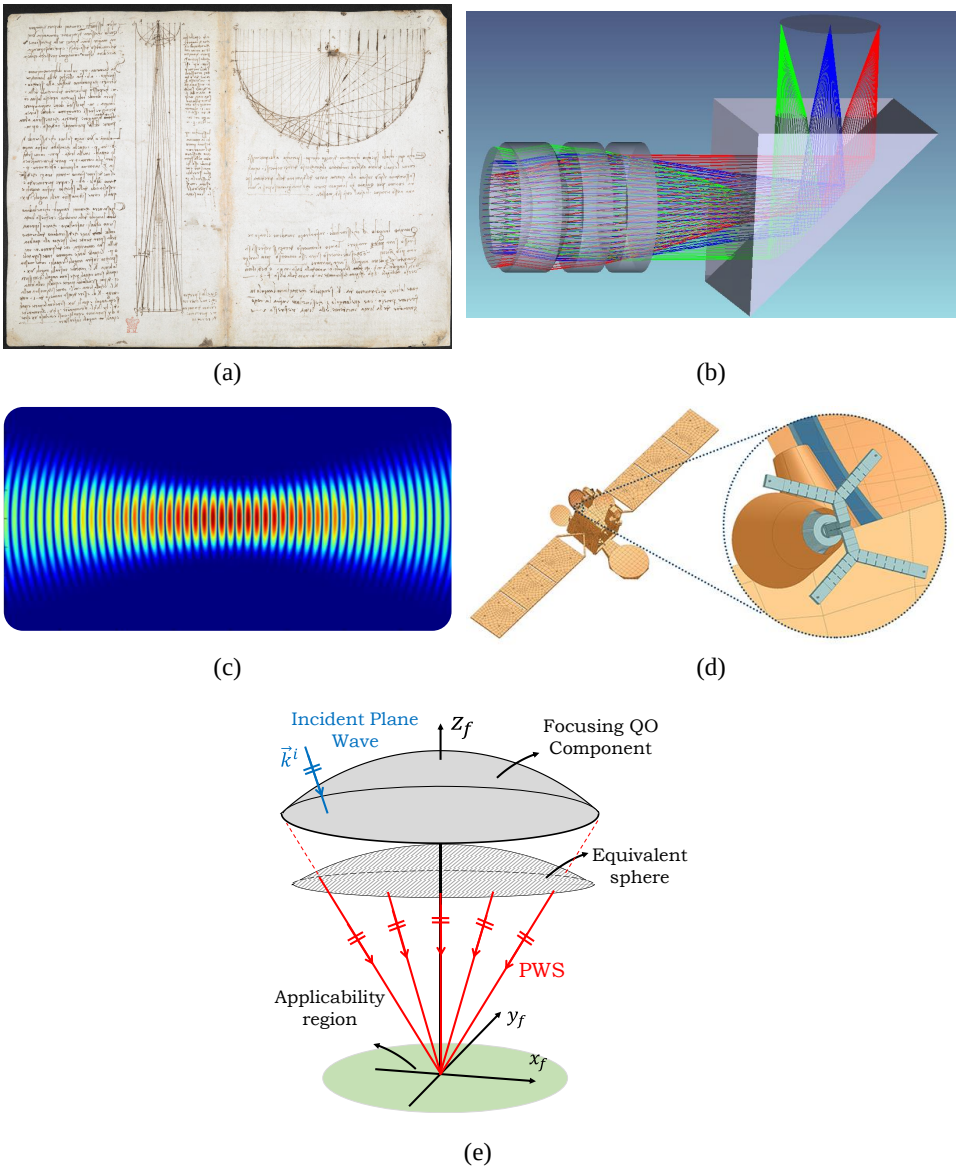

Figure 1.5: (a) Ray tracing picture of a spherical mirror and its caustic points, fifteenth century, Leonardo da Vinci's notebook [52]. (b) Ray tracing in OpticStudio environment [51]. (c) Gaussian beam propagation along the horizontal axes, where a focus point is identifiable in the middle. (d) TICRA tools environment [53]. (e) Plane Wave Spectrum representation of the field scattered by a QO component towards its focal plane.

its applicability to scenarios with small scanning angles. In the case of wide angle optics, one needs to analyse these structures using multi-mode Gaussian beams propagating through multiple QO components. The complexity of this solution grows rapidly with more advanced geometries, and ultimately the method loses its simplicity appeal. II) When the antenna feed is in the near field distance from QO components, the distribution of EM fields are more complex and cannot be accurately represented by Gaussian beam model. III) The model is not suitable for representing the radiation pattern of many relevant integrated antenna feeders [56]. As the result of these limitations, for analysing or designing QO

systems with wide field-of-views (wide angle optics) coupled to complex (wide band) feeders, modeling the radiation phenomena using Gaussian beam is not appropriate.

A more accurate tool to investigate Quasi-Optical systems is needed when the typology of the dominant scattering phenomenon is dictated by the actual size of the limiting apertures. In this situation, diffraction plays the role of the main phenomenon. Diffraction accurately describes the effects of the phase and amplitude distributions across radiating apertures [4]. A widely used high-frequency technique to analyse diffraction in QO systems is the Physical Optics (PO) which is packaged in commercial software such as TICRA tools [53], Fig. 1.5(d). PO technique is a well-established and accurate method to evaluate the fields radiated by electrically large scatterers. For instance, this method is suitable for optimizing the shape of reflectors coupled to standard feeders. However, in commercial software, the PO analysis of integrated lenses are not extensively explored when compared to the attention reflectors received.

Independently from the techniques adopted, QO components can be analysed either in transmission (Tx) or reception (Rx) modes. The reciprocity theorem states that the analyses in both modes are equivalent. In this work, we propose an analysis of emerging wide field of view imagers via the derivation of their plane wave spectrum (PWS) in reception, Fig. 1.5(e). This spectral representation of the field scattered by the QO system can be linked directly to other well known spectral methods for analysing high frequency EM problems. Namely, spectral Green's function for planar stratified mediums [57], Floquet-waves [58], and related analysis techniques for specific EM problems such as: surface wave and leaky wave radiations [59,60,61], connected arrays [62], artificial dielectrics [63], and etc. This approach also simplifies the procedure for co-design of QO components and their feeders, since both the lens (or mirror) shape and feeder radiation properties can be synthesized directly from this PWS. The optimal radiation pattern of an antenna feeder, and the optimal shape for QO components can be derived directly by applying a conjugate field match condition [64, 65, 35]. In case of absorbers, their optimal angular response can be derived by linking the PWS to an equivalent Floquet-modes circuit as in [66].

In [67], a numerical evaluation of the incident PWS in a reflector system was described. A much simpler approach using Fourier Optics (FO) [68] was proposed in [66]. Over a limited applicability domain, this later approach led to analytical expressions for the incident PWS for parabolic reflectors and elliptical lenses under broadside incident plane wave. In this work, we extend this analytical FO approach for more canonical QO components (adding hyperbolic lenses), slightly skewed incident angles; and combine the method with a numerical Geometrical Optics (GO) technique to analyse multi-component QO systems for wide field-of-view applications. The analysis in [66] was aimed to focal plane arrays of bare absorbers which are incoherent detectors. Therefore, the derived PWS neglected the quadratic dependence of the focal field phase. Here instead, to properly include the coupling between two QO components, especially for off-focuses cases and components located in the diffractive region of one another, this quadratic phase is efficiently introduced by applying a local phase linearization around the observation point in the focal plane.

In the case of QO systems with absorber based FPAs, in [47], a basic study for deriving the trade-offs between the performances of bare absorbers and antennas was presented within the scope of astronomical instruments. In this work, instead, an accurate analysis of FPAs based on bare absorbers is performed resorting to the described spectral analysis technique that links the spectrum of the optical system to the one of the distributed absorber. The latter allows considering generic optical systems, even with low

focal-to-diameter number, $f_{\#}$, (commonly referred also as F/D ratio [69]) and distributed absorbers. With respect to previous works, the terminology used here is also more common to the reflector antenna community [49].

1.4 Novel Contributions in this Thesis

The novel aspects of this thesis are summarized in two parts, new theoretical contributions, and novel designs achieved due to the developed theoretical work, as following:

Novel Theoretical Contributions

- A spectral technique for analysing Quasi-Optical systems, referred to as Fourier Optics (FO), is further developed with respect to the previous works. Namely, analytical expressions, in the case of broadside or slightly skewed incident plane wave angles, are obtained for analysing various canonical components. Moreover, Geometrical Optics (GO) based codes for representing the transmission of EM fields through dielectric material are studied. Together with available GO codes for analysing the interaction of the EM fields with a reflective component, computationally rapid codes based on GO-FO methods are developed for analysing QO systems with components coupled to one another geometrically or in diffraction region. The applicability of the original FO method is extended to wide angle QO scenarios, and for positions far away from the focus of the component. This extension is also achieved by combining the FO technique with the GO based codes.

- A spectral technique for analysing Quasi-Optical systems, referred to as Fourier Optics (FO), is further developed with respect to the previous works. Namely, analytical expressions, in the case of broadside or slightly skewed incident plane wave angles, are obtained for analysing various canonical components. Moreover, Geometrical Optics (GO) based codes for representing the transmission of EM fields through dielectric material are studied. Together with available GO codes for analysing the interaction of the EM fields with a reflective component, computationally rapid codes based on GO-FO methods are developed for analysing QO systems with components coupled to one another geometrically or in diffraction region. The applicability of the original FO method is extended to wide angle QO scenarios, and for positions far away from the focus of the component. This extension is also achieved by combining the FO technique with the GO based codes.

- The field scattered by a QO component at its focal plane is represented by a Plane Wave Spectrum (PWS) which includes both amplitude and phase of the incident field, referred to as the Coherent Fourier Optics (CFO). This development leads to analysing the diffractive coupling of multiple QO components using FO methodology, where one component is placed at the focal plane of another (placed at the diffraction limited region of the primary component).

- PWS representation of the focal fields scattered by QO components was combined with the spectral techniques for analysing strip absorbers in previous works. Specifically, equivalent Floquet-

modes circuits were used to model the periodic absorbing structure where the generators in these circuits are related to the direct (incident) PWS. Here the methodology is extended to generic absorber shapes and off-center positions in the FPA. This extended analysis tool is then employed to derive the trade-offs in absorber based imaging systems in terms of point source response, aperture efficiency, point spread function, focusing efficiency, and in-coherent distributed source response.

Novel Design Contributions

- Antenna analysis in reception technique is combined with the developed codes for analysing QO components. Together these methods are employed for analysing complete QO systems with antenna based feeders. Here, large format lens based focal plane arrays (Fly's eye configuration) with optimal scanning performance over very wide field-of-views are studied. The synthesized lens based FPA achieved scan losses much lower than the ones predicted by standard formulas related to the direct field coming from an equivalent reflector for horn based FPAs. In particular, a FPA with scan loss below 1 dB while scanning up to ±17.5° is presented with directivity of 52 dBi, complying with the needs for the future sub-millimetre imagers. Towards the edge of this FPA, surface of the integrated lenses are shaped based on the phase distribution of the derived incident PWS to improve the scanning performance. It is worth noting that these shapes are obtained directly as a solution given by the method, and not by employing iterative numerical optimization techniques. This direct approach for designing lens based FPAs is realized by developing the CFO methodology.

- The GO-FO method together with in reception analysis is also employed to design the wide band single pixel QO system of DESHIMA 2.0 spectrometer. The QO system in this design is based on hyper-hemispherical lenses coupled to reflector system. The lens is displaced from the focal point of the reflector system, and it is large in terms of the wavelength. Therefore, the performance of the architecture is less diffractive and has a more stable performance over the frequency with respect to lenses located at the focal plane of a reflector system. However, the geometry is in the near field distance from the reflector system, and traditional in transmission methods are time consuming and cumbersome for optimizing the performance of such geometry. The design achieved an stable performance over the bandwidth (240-720 GHz) with average aperture efficiency over frequency band of 65% including the feed losses. The preliminary beam pattern measurements of the system are matched well to the expected pattern from the design tool.

- FPA architectures based on multi-lens components for achieving wide band wide field-of-view performances have been proposed. These architectures consist of multiple lenses which are large in terms of the wavelengths and close to one another. Each multi-lens component scans a few wide band beams and together the system can achieve a wide scan performance. Similar constrains as the previous point are present in the analysis of these geometries in transmission mode. In fact, the proposed methodology in this thesis is orders of magnitude faster in analysing these structures with respect to multi-surface PO codes.

- These developed figures of merit for absorber based FPAs are employed to evaluate the performance of a dual band security imaging system (CONSORTIS) operating from 100 GHz to 600 GHz with a large format focal plane array of bare absorbers. The measured point spread function of this imager is matched very well to the results obtained from the theory.

1.5 Outline

This thesis is structured in four main parts. In Part I, which includes Chapters 2 and 3, the focus is on representing the field scattered by QO systems as a Plane Wave Spectrum (PWS). Part II of the thesis, Chapters 4, 5 and 6, focuses on antenna based Quasi-Optical systems with multiple QO components. In Part III, Chapters 7 and 8, QO systems with absorber based FPAs are modeled using EM terminologies. Part IV contains the conclusion remarks and future outlook for continuation of this work. A more detailed description of the chapters of this dissertation is given in the following:

- In Chapter 2, magnitude of PWS for 4 major canonical Quasi-Optical components (parabolic reflectors, elliptical, hyperbolic, and extended hemispherical lenses) is derived. In the case of a plane wave excitation, an analytical expression for this PWS is obtained using a Geometrical Optics (GO) code, for broadside and slightly skewed incident angles. A numerical GO code is also employed for cases of large skew incident angles. Moreover, in this chapter the Fourier Optics (FO) analysis is reviewed, and its applicability region is extended to cover large format FPAs.

- In Chapter 3, the FO methodology is further developed to represent both amplitude and phase of the incident PWS (referred to as Coherent Fourier Optics (CFO)). This goal is achieved by including a quadratic phase, present in the field focused by the QO component, into the inverse Fourier transform representation of the focal field of a QO component.

- Firstly in Chapter 4, the incident PWS derived using CFO method is used to represent the diffractive coupling in an example geometry: coupling between a FPA of elliptical lenses below a parabolic mirror. Secondly, in this chapter a lens based FPA with optimal geometry is described to maximize scanning performances in high frequency imaging systems. An example architecture, relevant to the state-of-the-art security imagers, which achieves scan loss below 1 dB while scanning up to $\pm 17.5°$ is also presented.

- In Chapter 5, a wide band single pixel QO system for DESHIMA 2.0 spectrometer is designed. This design is based on the developed methodology with a stable performance over a wide band, i.e. 65% average aperture efficiency of over a $3:1$ bandwidth ratio (240GHz-720GHz).

- In Chapter 6, a wide band wide field-of-view QO system is proposed for future multi-color imaging applications. This system has a FPA in which each element consists of multi-lens components coupled geometrically together. Moreover, each element is fed by an array of antennas. The computationally efficient tool for analysing this architecture is discussed in this chapter.

- In Chapter 7, absorber based FPAs for low cost QO systems are discussed. An EM based model for such structures is described using known terms in the community, such as: effective area, pattern in reception, aperture and focusing efficiency. The coupling of these geometries to point as well as distributed sources is explained here using these terminologies.
- Chapter 8, describes an absorber based FPA using Kinetic Inductance Bolometers for security applications. This passive imaging system operates approximately from 100GHz to 600GHz. The performance of this system is evaluated using the developed methodology and it is compared to the measurement point spread functions with excellent agreement.
- Chapter 9, concludes the dissertation with a review of the most significant results presented, and an overview on possible future developments.

Part I

Development of Coherent Fourier Optics Methodology

In this part, the spectral representation of scattered fields by a Quasi-Optical (QO) system is obtained using Fourier Optics (FO) approach. This representation is in the form of a plane wave spectrum (PWS). In Ch. 2, magnitude of this PWS for 4 major canonical QO components is derived. When these components are illuminated by a plane wave from broadside or slightly skewed angles, an analytical expression for this PWS is presented by combing the FO method with a Geometrical Optics (GO) code. In the case of wide angle optics, i.e. when QO components are illuminated by large skew incident angles, FO method is combined with a numerical GO code to obtain the PWS. Moreover, the applicability region of the FO method is extended to analyse these wide angle optics. In Ch. 3, to analyse coherent detectors far from the focus of a QO component, both magnitude and phase of the incident PWS is derived. This technique is referred to as the Coherent Fourier Optics (CFO).

Chapter 2

Plane Wave Spectrum of Quasi-Optical Components Using Fourier Optics

Future (sub)-millimetre imagers are being developed with large format focal plane arrays of detectors. This chapter presents a spectral technique for the analysis of such focal plane arrays in reception using Fourier Optics (FO). This analysis derives the Plane Wave Spectrum (PWS) of Quasi-Optical (QO) systems in reception for four widely used QO components. Namely: parabolic reflectors, elliptical, extended hemispherical, and hyperbolic lenses. An analytical expression for the PWS of 3 of these components is derived for broadside and moderately skewed incident angles. Moreover, exploiting a Geometrical Optics (GO) based approach, the method can be used to analyse FPAs with wide fields of view. The proposed technique is validated with full-wave simulations.

2.1 Introduction

As discussed in Chapter 1, in recent years, advanced Quasi-Optical (QO) based systems operating at (sub)-mm wavelengths are employed as the state-of-the-art solutions for sensing and imaging applications. These systems are employed for astronomical observations [10, 11, 12, 13], standoff personnel screening [20, 21, 22, 23, 26], and new generation of wireless communication [29, 30, 31, 32, 33, 34, 35].

These QO components can be analysed either in transmission (Tx) or reception (Rx) modes. The reciprocity theorem states that the analyses in both modes are equivalent. By employing a field matching technique, as detailed in Sec. 2.5, and [64], at a sphere centered at the focus of the QO component, the geometry of the antenna feeder can be optimized to match its radiated field to the incident Plane Wave Spectrum (PWS). This approach provides insight for directly designing QO systems with multiple components. This insight is not available when one cascades in Tx analysis to design such geometries. Moreover, in most cases of multi-mode antennas coupled to incoherent detectors, the current distribution at the antenna aperture is unknown. Therefore, it is more convenient to evaluate the coupling of these antennas to a QO system in Rx, as performed in [70]. In the case of absorber based systems, the incident PWS can be linked to spectral techniques such as equivalent Floquet-modes circuit model of absorbers to evaluate the power captured by the detectors, as discussed in Part III of this thesis.

A Physical Optics (PO) code, can be used to indirectly calculate the incident PWS of a QO component as the Fourier transform of the focal field as in [67]. However, the Fourier Optics (FO) method described here is a direct and much simpler approach (without the numerical Fourier transform integral) to obtain this PWS. The derivation of the standard FO representation of the scattered fields by a QO component is given in Appendix A. The proposed FO approach is a relevant and useful tool for synthesizing antennas or absorbers coupled to QO components.

In this chapter, the PWS of four canonical QO components, parabolic reflectors, elliptical, extended hemispherical, and hyperbolic lenses, are derived to provide design possibilities. These components are illustrated in Fig. 2.1.

The developed code can generate ray tracing plots for QO components, as shown in Fig. 2.1. These plots provide a first order understanding of the propagation scenario, including the incident, and scattered fields. The incident PWS of QO components are then obtained using a Geometrical Optics (GO) based code [71], detailed in Appendix B. In Sec. 2.5, this PWS is used to evaluate the performance of a few simple test cases of QO systems based on simple antenna feeders. The results obtained here are validated via full wave simulations and/or commerical PO based codes, with excellent agreements.

2.2 Plane Wave Spectrum Representation of the Focal Fields

Let us consider an example scenario where a QO component is illuminated by an incident plane wave as depicted in Fig. 2.2. This plane wave is expressed as $\vec{E}^i = E_0 \hat{p}^i e^{-j\vec{k}^i \cdot \vec{r}}$, where $\hat{p}^i$ represents the polarization of the incident plane wave, E_0 is its amplitude, $\vec{k}^i = k(\sin\theta^i \cos\phi^i \hat{x} + \sin\theta^i \sin\phi^i \hat{y} - \cos\theta^i \hat{z})$ is the wave-vector, k is the propagation constant of the medium where the plane wave is present, $\vec{r}$ is a vector indicating a position in the space, θ^i and ϕ^i represent the elevation and azimuth incident angles,

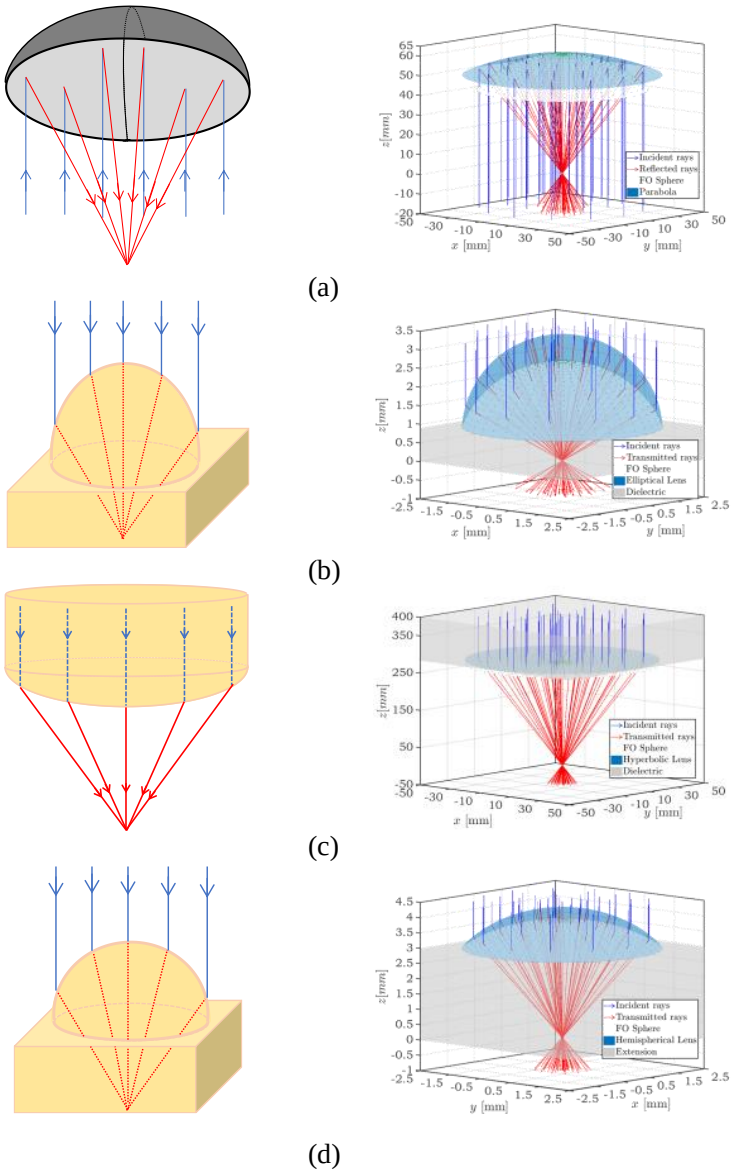

Figure 2.1: The four considered geometries with their corresponding ray tracing illustrations. Blue and red rays represent the incident plane waves, and scattered GO rays propagating to the focal plane of the QO component, where the antenna feeder is placed, respectively. Illustrations and the ray tracing representations obtained from the tool, are shown in left and right panels, respectively. (a) A parabolic reflector, (b) an elliptical lens, (c) a hyperbolic lens, and (d) an extended hemispherical lens.

respectively.

The field scattered by the QO component on its focal plane is represented as a PWS. To realize this step, an equivalent sphere centered at the focal point of the QO component, referred to as the FO sphere, is introduced (see Fig. 2.2). Where R_{FO} is the radius of this sphere; and θ^0 is the maximum rim angle of the QO component. The FO validity region in the focal plane, as shown later in this

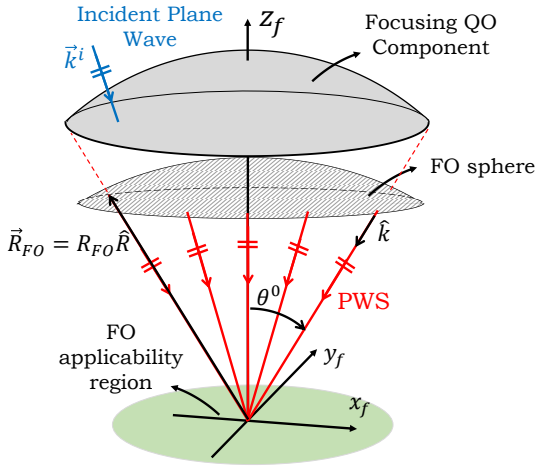

Figure 2.2: Schematic representation of a FO scenario for a QO component illuminated by a plane wave from $\vec{k}^i$ direction.

chapter, is directly related to the radius of the FO sphere; therefore, this parameter is chosen as large as possible. The field scattered by the QO component is evaluated over this equivalent surface using a GO approach. The field at the focal plane of the QO component can be calculated using the PO radiation integral via the introduction of equivalent surface currents which are proportional to the GO fields. By asymptotically evaluating the PO radiation integral for observation points close to the focus of the component, which leads to approximations on the amplitude, vector, and phase of the integrand, one can represent the focal field as an inverse Fourier transform (as discussed in Appendix A):

$$\vec{e}_f(\vec{\rho}_f, \vec{k}^i) = \frac{e^{-jk|\vec{\rho}_f|^2/(2R_{FO})}}{4\pi^2} \iint_{-\infty}^{+\infty} \vec{E}^{FO}(k_x, k_y, \vec{k}^i) e^{j\vec{k}_\rho \cdot \vec{\rho}_f}\, dk_x dk_y \tag{2.1a}$$

$$\vec{h}_f(\vec{\rho}_f, \vec{k}^i) = \frac{e^{-jk|\vec{\rho}_f|^2/(2R_{FO})}}{4\pi^2} \iint_{-\infty}^{+\infty} \vec{H}^{FO}(k_x, k_y, \vec{k}^i) e^{j\vec{k}_\rho \cdot \vec{\rho}_f}\, dk_x dk_y \tag{2.1b}$$

where $\vec{\rho}_f$ is a position on the focal plane of the QO component, $\vec{k}_\rho$ is the spectral vector defined as $\vec{k}_\rho = k_x\hat{x} + k_y\hat{y} = k\sin\theta(\cos\phi\hat{x} + \sin\phi\hat{y})$, and k is the wave number in the medium of the focal plane of the QO component.

In this chapter, for representing the focal fields close to the center of the FO sphere, the quadratic phase term, $e^{-jk|\vec{\rho}_f|^2/(2R_{FO})}$, in front of the Fourier transform is neglected. This phase term is included into the spectrum in Ch. 3. The dependency of the parameters in (2.1) to the direction of the incident plane wave is shown explicitly by the term $\vec{k}^i$. The focal fields, $\vec{e}_f$ and $\vec{h}_f$, are expressed as a summation of plane waves with amplitudes of $\vec{E}^{FO}(k_x, k_y, \vec{k}^i)$ and $\vec{H}^{FO}(k_x, k_y, \vec{k}^i)$, respectively. In other words, $\vec{E}^{FO}$ and $\vec{H}^{FO}$ are the PWS representations of $\vec{e}_f$ and $\vec{h}_f$, respectively. The approximations taken to derive (2.1) are applicable for a region around the center of the FO sphere. This region, shown in Fig. 2.2, is a function of the geometrical parameters of the considered scenario, as described in Appendix A, (A.22):

Table 2.1: Maximum realizable radius of the FO sphere

QO component	R_{FO}
Parabolic Reflector	Focal length: f
Elliptical Lens	$0.5D/\sin\theta^0$
Hyperbolic Lens	Focal length: f
Extended Hemispherical Lens	$0.5D/\sin\theta^0$

$$D_{FO} = f_{\#} min\{0.4D, \sqrt{2f_{\#}D\lambda}\} \tag{2.2}$$

where D_{FO} is the diameter of a circle in the focal plane which represents the FO applicability region; λ is the wavelength in the medium; D and $f_{\#}$ are the diameter and f-number of a QO component, respectively. The latter is uniformly defined for all the components as the ratio between the maximum realizable radius of a FO sphere and diameter of the component, i.e. $f_{\#} = R_{FO}/D$. This radius is reported for each QO component in Table 2.1.

The PWS in (2.1) can be expressed as a function of the tangent electric field scattered by the QO component and evaluated over the FO sphere (see Appendix A, Eqs. (A.25) to (A.27)):

$$\vec{E}^{FO}(k_x, k_y, \vec{k}_i) = \frac{j2\pi R_{FO} e^{-jkR_{FO}}}{\sqrt{k^2 - (k_x^2 + k_y^2)}} \hat{R} \times [\vec{E}^{GO}(k_x, k_y, \vec{k}_i) \times \hat{R}] \tag{2.3a}$$

$$\vec{H}^{FO}(k_x, k_y, \vec{k}_i) = -\frac{1}{\zeta} \hat{R} \times \vec{E}^{FO}(k_x, k_y, \vec{k}_i) \tag{2.3b}$$

where ζ is the characteristic impedance of the medium of the FO sphere, $\hat{R} = \hat{k}_\rho + \sqrt{1 - k_\rho^2/k^2}\hat{z}$, and $\hat{R} \times [\vec{E}^{GO} \times \hat{R}]$ is the tangent component of the GO field scattered by the QO component and evaluated over the FO sphere. As it can be seen in (2.3), the PWS is proportional to the GO field evaluated over the FO sphere; therefore, the focus of the following section is on calculating these GO fields for different QO components.

2.3 Geometrical Optics Representation of the Fields Scattered on the Fourier Optics Sphere

As mentioned in Sec. 2.2, the field scattered by the QO surface, $\vec{E}^{GO}$, and propagated to the FO sphere can be evaluated resorting to a GO based analysis. The GO method is commonly used in high-frequency scattering scenarios, i.e. when the scatterers are large in terms of wavelength, to determine wave propagation for both incident and scattered fields, including amplitude, phase, and polarization information. This method is applicable for generic incident fields and scattering surfaces far from the

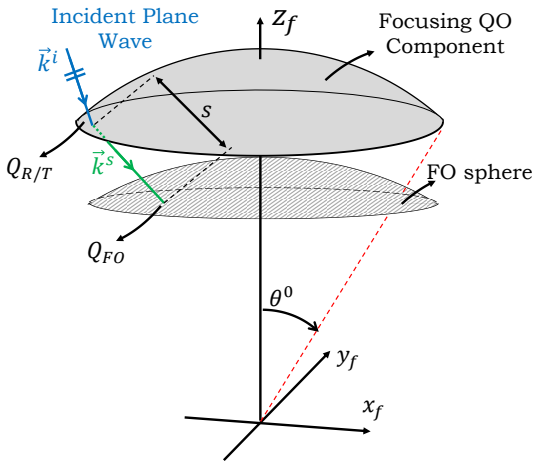

Figure 2.3: Schematic representation of a GO propagation scenario: a plane wave is scattered by a QO component and propagated to the FO sphere.

focus (or in general caustics) point. In this method, EM waves can be approximated as tubes of rays propagating in a homogenous medium from one point to another. The scattered ray fields follow the laws of reflection and refraction at a two-media interface. In the following a numerical GO code for calculating $\vec{E}^{GO}$ is described. An analytical expression is also provided for cases when the QO component is illuminated by plane waves with slightly skewed incident angles.

2.3.1 Numerical Geometrical Optics Representation

Let us assume an incident plane wave, $\vec{E}^i = (E_0^{TE}\hat{p}^{i,TE} + E_0^{TM}\hat{p}^{i,TM})e^{-j\vec{k}^i\cdot\vec{r}}$, is illuminating the QO surface, Fig. 2.3, where $\hat{p}^{i,TE/TM} = p_x^{i,TE/TM}\hat{x} + p_y^{i,TE/TM}\hat{y} + p_z^{i,TE/TM}\hat{z}$ represent the TE and TM polarized unit vectors of the incident field, respectively; E_0^{TE} and E_0^{TM} represent the amplitude of the TE and TM polarized fields, respectively. The GO scattered (reflected or transmitted) field on the QO surface, $\vec{E}^s$, can be calculated as:

$$\vec{E}^s(Q_R) = \vec{E}^i \cdot \bar{R}(Q_R) \tag{2.4a}$$

$$\vec{E}^s(Q_T) = \vec{E}^i \cdot \bar{T}(Q_T) \tag{2.4b}$$

where $Q_{R/T}$ represents a reflecting surface (Q_R) such as the parabolic reflector or a transmitting one (Q_T) such as a lens; $\bar{R} = \Gamma^{TE}p^{i,TE}p^{r,TE} + \Gamma^{TM}p^{i,TM}p^{r,TM}$ and $\bar{T} = \tau^{TE}p^{i,TE}p^{t,TE} + \tau^{TM}p^{i,TM}p^{t,TM}$ are the reflection and transmission dyads, respectively. Here Γ^{TE} and Γ^{TM} are the TE and TM reflection coefficients on the QO surface; τ^{TE} and τ^{TM} are the transmission ones; $p^{r,TE/TM}$ and $p^{t,TE/TM}$ represent the polarization unit vectors of the reflected and transmitted rays, respectively.

In this work, a ray tracing code is developed which launches incident rays toward the QO component. These rays are scattered by the component and propagated toward the surface of the FO sphere. The position where each ray intercepts with the FO sphere, Q_{FO}, is obtained using this code, see Fig.

2.3. In scenarios with a very skewed incident plane wave angle, scattered rays can be intercepted by the FO sphere outside the geometrical maximum rim angle of the QO components (θ^0 in Fig. 2.3). As the result, FO spheres are not necessarily limited within this angular region. The reflected or transmitted fields evaluated over this FO sphere can be expressed as:

$$\vec{E}^{GO} = \vec{E}^{s}(Q_{R/T})S_{spread}(Q_{FO})e^{-jks(Q_{FO})} \tag{2.5}$$

where s is the propagation distance from the QO surface to the FO sphere (see Fig. 2.3), e^{-jks} is the phase propagation for each ray. The amplitude of GO field spreads as the ray propagates. This spreading is represented by S_{spread} in (2.5). This parameter can be evaluated by enforcing the law of conservation of energy among the incident, reflected, and transmitted rays. In other words, when an incident EM field interacts with a QO surface, the power carried by the incident ray tube is equal to the summation of the power reflected by and transmitted into the surface. By approximating the radiation scenario by a ray propagation one, far from the focus (or caustic) point, one can asymptotically evaluate the PO radiation integral to derive a GO representation of the EM fields. The spreading factor is then computed using this method as described in [72, 73] and in Appendix B:

$$S_{spread}(Q_{FO}) = \sqrt{\frac{\rho_1^{r/t}(Q_{FO})\rho_2^{r/t}(Q_{FO})}{[\rho_1^{r/t}(Q_{FO}) + s(Q_{FO})][\rho_2^{r/t}(Q_{FO}) + s(Q_{FO})]}} \tag{2.6}$$

where $\rho_1^{r/t}$ and $\rho_2^{r/t}$ are the principal radii of curvature of the reflected or transmitted wave fronts, respectively. These radii are express in (B.18)-(B.21), and (B.24)-(B.25), for transmitted and reflected radii of curvature, respectively. The details of these derivations are provided in Appendix B.

The GO field calculated in (2.5) is a function of the position where the scattered rays are intercepted by the FO sphere, Q_{FO}. However, as indicated in (2.3), the GO field should be represented as a function of the spectral parameters, i.e. k_x and k_y. This change of variables is achieved by employing a standard interpolation code in MATLAB.

2.3.2 Analytical Geometrical Optics Representation for Broadside Incident Plane Waves

For the three listed QO components, when illuminated by a plane wave from broadside direction, we also derived the corresponding analytical representation of the amplitude spreading factors, as shown in Table 2.2. In this table, for the elliptical lens, a is the semi-major axis, $2c$ is the distance between the foci, $e = c/a$ is its eccentricity, and R_{FO} is the rim distance from the lower focus of the lens to its edge. For a hyperbolic lens, e represents its eccentricity. The geometrical parameters of each QO component are shown in Fig. 2.4.

Moreover, the phase term, e^{-jks}, in (2.5) can also be represented analytically for specific cases. In the case of broadside illumination of a parabolic reflector, due to its geometrical shape, the reflected GO field has a constant phase over its FO sphere. Similarly, for elliptical lenses and hyperbolic lenses, their eccentricities are chosen in such a way to ensure constant phase fronts for transmitted fields over

Table 2.2: Analytical spreading factors for listed QO components illuminated by a plane wave from broadside direction

QO component	Broadside Spreading Factor: $S_{spread}(\theta, \theta^i = 0)$
Parabolic Reflector	$2/(1+\cos\theta)$
Elliptical Lens	$a(1-e^2)/(R_{FO}(1-e\cos\theta))$
Hyperbolic Lens	$(1-e)/(1-e\cos\theta)$

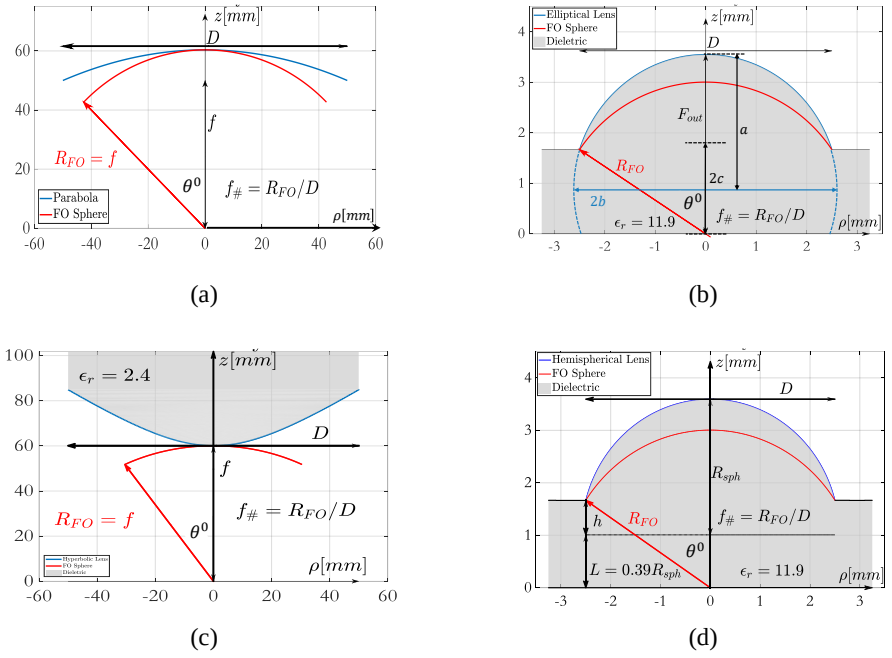

Figure 2.4: Geometrical parameters of the considered QO components. (a) Parabolic reflector, (b) elliptical, (c) hyperbolic, and (d) extended hemispherical lenses.

their corresponding FO spheres when illuminated by a plane wave from the broadside direction. These eccentricities are $e = 1/\sqrt{\varepsilon_r}$ and $e = \sqrt{\varepsilon_r}$, for elliptical and hyperbolic lenses, respectively, where ε_r is the relative permittivity of the lens material. Therefore, for broadside incidence of the considered canonical QO components, one can neglect the constant phase term of the reflected or transmitted GO fields over their FO sphere.

2.3.3 Analytical Geometrical Optics Representation for Slightly Skewed Incident Plane Waves

When an external plane wave is incident from a direction slightly off broadside, $(\Delta\theta^i, \Delta\phi^i)$, a simplifying approximation, employed typically in FO to evaluate the PWS in a computational efficient way, is that the polarization of the incident field $\vec{E}^i$, in the phase reference plane of the focusing system (Fig. 2.5), is the same as for the broadside plane wave case, while the progressive phase shift is explicitly accounted for. This means that the following expression of the incident plane wave applies along the phase reference plane:

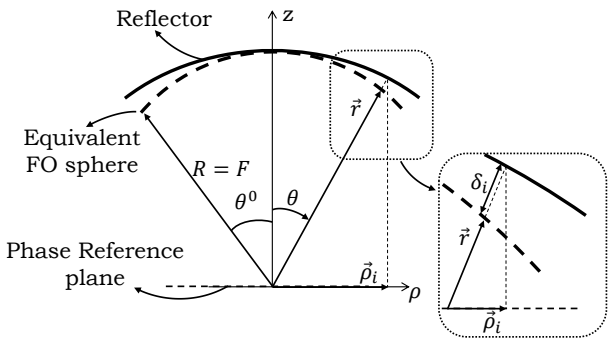

Figure 2.5: Illustration of the geometry of a parabolic reflector to evaluate the phase term of the PWS for slightly off-broadside incidence with respect to a phase reference plane.

$$\vec{E}^i(\vec{\Delta k}_\rho^{\,i}) \simeq E_0 e^{-j\vec{\Delta k}_{\rho i}\cdot\vec{\rho}_i(\vec{r})}\hat{p}^i \tag{2.7}$$

where $\hat{p}^i$ represents the polarization of the incident plane wave, $\vec{\Delta k}_\rho^{\,i} = \Delta k_x^i\hat{x} + \Delta k_y^i\hat{y} = k_0 \sin\Delta\theta^i \cdot(\cos\Delta\phi^i\hat{x} + \sin\Delta\phi^i\hat{y})$ is the transversal projection of the incident wave vector, $\vec{\Delta k}^{\,i}$; and $\vec{\rho}_i$ represents the observation point in the phase reference plane (see Fig.2.5).

As discussed, the field distribution on the equivalent sphere can be obtained by propagating the incident field via GO up to the equivalent sphere. Applying the approximation in (2.7), the GO field will be the same as broadside, except for a phase term

$$\vec{E}^{GO}(\vec{k}_\rho, \vec{\Delta k}_\rho^{\,i}) \simeq \vec{E}^{GO}(\vec{k}_\rho, \vec{\Delta k}_\rho^{\,i} = 0)e^{-j\vec{\Delta k}_\rho^{\,i}\cdot\vec{\rho}_i(\vec{r})} \tag{2.8}$$

The approximation in (2.8) corresponds, for the worst polarization case, to neglect a field contribution proportional to $\tan\Delta\theta^i$. Retaining a 20% error on the field as tolerable, i.e., $\tan\Delta\theta^i < 0.2$, corresponds to an angular limitation $\Delta\theta^i < 11°$. The choice of 20% error in the GO field amplitude is consistent with the one taken in [66] for deriving the limits of the FO method. This error choice assures that the field computed with the expressions given here matches the PO one with less than a 0.5dB difference over the whole FO region of validity defined in [66].

As shown in Fig. 2.5(inset), $\vec{\rho}_i = \rho_i\hat{k}_\rho$ can be parametrized with respect to an observation point on the FO equivalent sphere, $\vec{r} = R_{FO}\hat{r}$, as

$$\vec{\rho}_i = (R + \delta_i(\theta)) \sin\theta\hat{k}_\rho \tag{2.9}$$

where $\delta_i(\theta)$ quantifies the phase delay from the surface of the QO component to its equivalent sphere [see Fig. 2.5(inset)] and we made use of the fact that $\hat{k}_\rho = \vec{k}_\rho/(k_0\sin\theta) = \hat{\rho}$. The normalized phase delay, $\delta_n = \delta_i/R_{FO}$, is reported in Table 2.3 for each QO component.

Table 2.3: Normalized distance between listed QO components from their corresponding FO spheres.

QO component	Normalized distance $\delta_n(\theta)$
Parabolic Reflector	$(1-\cos\theta)/(1+\cos\theta)$
Elliptical Lens	$e(\cos\theta-\cos\theta^0)/(1-e\cos\theta)$
Hyperbolic Lens	$e(\cos\theta-1)/(1-e\cos\theta)$

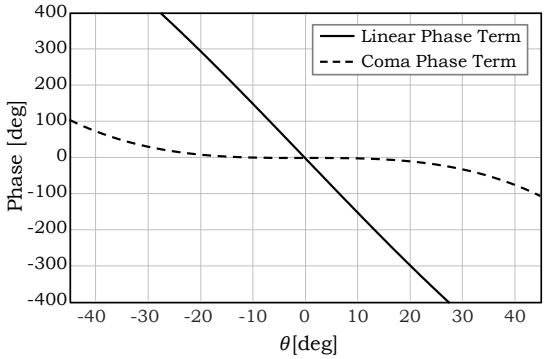

Figure 2.6: Phase terms of the slightly off broadside PWS in the case of a parabolic reflector with $f_\# = 0.6$ and $D = 100\lambda$ illuminated by a plane wave with $\Delta\theta^i/(\lambda/D) = 4$, $\Delta\phi^i = 0°$.

By substituting (2.9) into (2.8), we can observe two phase terms. The first phase term ($R_{FO}\sin\theta\vec{\Delta k}_\rho^{\,i}\cdot\hat{k}_\rho$) corresponds to a linear phase shift (beam steering) while the second one ($\delta_i\sin\theta\vec{\Delta k}_\rho^{\,i}\cdot\hat{k}_\rho$) is a coma phase error (associated with asymmetric high side lobes [74]) coming from the curvature of the QO component. Assuming an equivalent sphere with the radius equal to the maximum possible radius (R_{FO} in Table 2.1), the beam steering observed at the focal plane (here defined as the flash point), $\vec{\Delta\rho}_i$, can be evaluated directly from the linear phase term as

$$\vec{\Delta\rho}_i = \frac{R_{FO}\vec{\Delta k}_\rho^{\,i}}{k_0} \tag{2.10}$$

The flash point in (2.10) quantifies the location of the peak of the field in the focal plane of the QO component when the linear phase term is dominant (assuming beam deviation factor [75] is 1). In Fig. 2.6, an example of the variation of the two phase terms is shown versus the spectral angle θ, when the plane wave incident on a parabolic reflector impinges with a skewed angle with respect to broadside.

By using the approximation in (2.8), the phase term in the GO field can be expressed as a function of the spectral vector, $\vec{k}_\rho$, as follows:

$$e^{-j\vec{\Delta k}_\rho^{\,i}\cdot\hat{\rho}(R+\delta_i(\theta))\sin\theta} = e^{-j\vec{\Delta\rho}_i\cdot\vec{k}_\rho(1+\delta_n(\theta))} \tag{2.11}$$

In [76], it is shown that the dominant phase aberration in dual reflector systems is the coma one. This coma phase term is explicitly given in [77] for a paraboloid illuminated by an antenna feeder. Typically, the coma phase term is given for the small angle approximation as cubic dependence of θ [78].

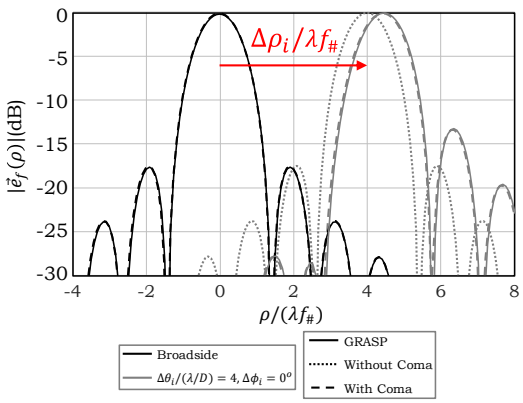

Figure 2.7: Direct fields focalized by a reflector with $f_\# = 0.6$ and $D = 100\lambda$. The reflector is illuminated by two plane waves: at broadside and with $\Delta\theta^i/(\lambda/D) = 4$,$\Delta\phi^i = 0°$. Dashed and dotted lines represent the fields with and without including the coma phase term in the PWS, respectively. The solid lines are relevant to the fields calculated with GRASP.

In conclusion, the GO representation of the scattered fields evaluated over the FO sphere, for slightly off-broadside plane wave incidences, can be expressed analytically as:

$$\vec{E}^{GO}(\theta, \Delta\theta^i) \simeq S_{spread}(\theta, \Delta\theta^i = 0)\vec{E}^s(\theta, \Delta\theta^i = 0)e^{-j\vec{k}_\rho\cdot\vec{\Delta}\rho_i(\Delta\theta^i)[1+\delta_n(\theta)]} \tag{2.12}$$

Similar to the case in (2.5), the GO fields calculated in (2.12) are also interpolated to be represented as a function of spectral parameters.

The coma phase term $\vec{\Delta}\rho_i \cdot \vec{k}_\rho \delta_n(\theta)$ in (2.12) can be neglected depending on the $f_\#$ and the numbers of scanned beams (i.e., $N = \Delta\theta^i/(\lambda/D)$). By imposing such coma phase term over the FO sphere to be smaller than $\pi/8$, we can evaluate the maximum number of scanned beams where the focalized field is almost a linear translation of the broadside one. In the case of a parabolic reflector,

$$N_{max}^{coma} = 0.25[f_\# + \sqrt{f_\#^2 - 0.25}]^2. \tag{2.13}$$

In Fig. 2.7, the field focalized in the focal plane by a parabolic reflector with $f_\# = 0.6$ is shown for two plane wave incidences: broadside and $\Delta\theta^i = 4\lambda/D$ (corresponding to scanning 4 beams). The field is evaluated with and without the coma phase term in the PWS, and compared with the field solution obtained by GRASP [53] when the PO solver option is used. It can be noted that the coma phase term changes the amplitude level of the first sidelobe, and the location of the maximum field [not anymore given by (2.10)]. It is evident that, for this low $f_\#$, the coma phase term cannot be neglected even for a single scanned beam, i.e., $N_{max}^{coma} \leq 1$, as derived in (2.13).

In this work, for incident angles $\Delta\theta^i \leq 11°$, the analytical solution in (2.12), using the analytical spreading factors in Table 2.2, is implemented. For larger incident angles, the numerical solution in (2.5), using the numerical spreading factor (2.6), is employed. Since an analytical expression is not available for the extended-hemispherical lenses, in their case, only the numerical GO representation is implemented.

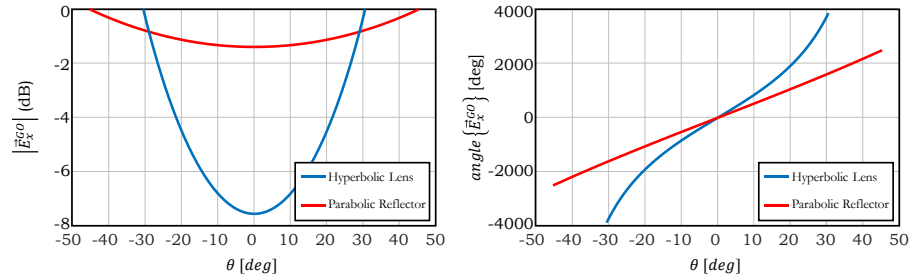

(a) (b)

Figure 2.8: x-component of the GO fields of a parabolic reflector, and a hyperbolic lens. These fields are evaluated at $\phi = 0°$ plane, the operative frequency is 300 GHz. The diameter and f-number of both components are $D = 100$mm and $f_{\#} = 0.6$, respectively. The incident plane wave is TM polarized with the skew angle of $(\theta^i = 8°, \phi^i = 0°)$. For the hyperbolic lens, the permittivity of the dielectric is $\varepsilon_r = 2.4$. (a) Amplitude, and (b) phase terms.

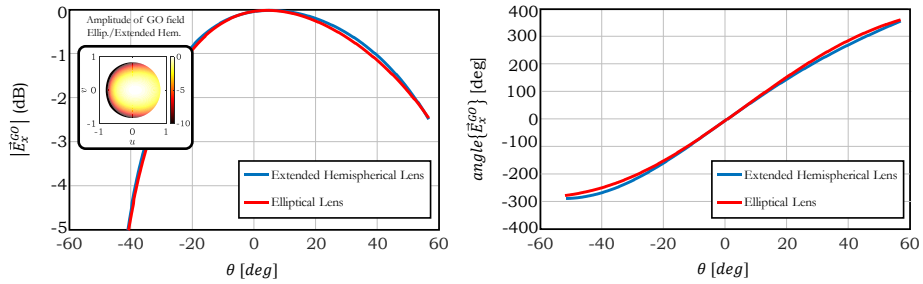

(a) (b)

Figure 2.9: x-component of the GO fields of an elliptical lens and an extended hemispherical lens. These fields are evaluated at $\phi = 0°$ plane, the operative frequency is 300 GHz, and the diameter and f-number of both components are $D = 5$ mm, and $f_{\#,l} = 0.6$, respectively. The incident plane wave is TM polarized with the skew angle of $(\theta^i = 21°, \phi^i = 0°)$. The permittivity of the dielectric is $\varepsilon_r = 11.9$. (a) Amplitude. (b) Phase. The shadow region is visible in amplitude 2D figure at the left side of the lens surfaces.

2.3.4 Numerical Examples of Fourier Optics Representation of the Focal Fields

In the following, firstly the GO fields for different QO components are shown and compared. We divided the QO components into two sets: components large in terms of wavelengths, Fig. 2.8, parabolic reflector and hyperbolic lens ($\varepsilon_r = 2.4$), respectively; and components small in terms of the wavelengths, Fig. 2.9, elliptical and hemispherical lenses ($\varepsilon_r = 11.9$), respectively. The operative frequency is 300 GHz, the plane wave is TM polarized, and for all components the f-number is 0.6. For the reflector and the hyperbolic lens, the diameter is chosen as 100 mm, and the incident skew angle is $\theta^i = 8°$. As it can be seen, for the hyperbolic lens, both the amplitude and phase terms of the GO field vary more significantly with respect to the ones of the parabolic reflector. In the case of the elliptical and hemispherical lenses, the diameter is 5 mm, and the skew angle is $\theta^i = 21°$. The radius of hemisphere and the extension length for the hemispherical lens are $R_{sph} = 2.6$ mm, and $L = 0.34R_{sph}$, respectively. In the case of integrated lenses, since the incident plane wave angle is very skewed, part of the lens surface is obscured from the incident plane wave. This shadow region is evident in the inset of Fig. 2.9(a).

In the remaining part of this sub-section, the GO fields calculated by the tool are indirectly validated

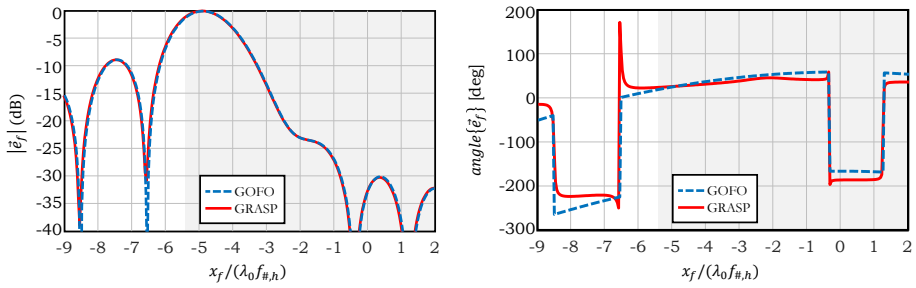

Figure 2.10: x-component of the electric field on the focal plane of a hyperbolic lens made of plastic ($\varepsilon_r = 2.4$) with $D_h = 100$ mm and $f_{\#,h} = 0.6$, illuminated by a unitary TM polarized plane wave with the skew angle of $\theta^i = 1.3°$, $\phi^i = 0°$. This field is evaluated at $y_f = 0$ plane, calculated using the analytical GO-FO approach, (2.3), and is compared against the one obtained using the PO based code of GRASP: (a) Amplitude. (b) Phase. The grey region represents the FO validity region (2.2).

by resorting to full-wave simulations similar to [66]. In particular, we calculated the focal fields of QO components using (2.1). For the case of a hyperbolic lens, these fields are compared against the ones evaluated using the PO based code of GRASP simulation software [53], and for an elliptical lens using CST MS [79].

First let us consider a hyperbolic lens made of plastic ($\varepsilon_r = 2.4$) with a diameter of $D_h = 100$ mm and a f-number of $f_{\#,h} = 0.6$. This lens is illuminated by a TM polarized plane wave operating at 300 GHz with an incident skew angle of $\theta^i = 1.3°$, $\phi^i = 0°$. In Fig. 2.10, the amplitude and phase of the x-component of the focal electric field calculated by using the GO-FO analysis, as in (2.1), are compared against PO results, respectively. As it can be seen, the agreement between the two methods, both in the amplitude and phase, is very good within the FO validity region (2.2).

As another example, we consider an elliptical lens made of silicon ($\varepsilon_r = 11.9$) with a diameter of $D_l = 5$ mm and a f-number of $f_{\#,l} = 0.6$. To improve the transmission at the silicon-air interface, the lens surface is covered by a quarter-wavelength Anti-Reflection (AR) coating made of Parylene with relative permittivity of $\varepsilon_m = 2.6$. The lens is illuminated by a TM-polarized plane wave operating at 300 GHz with two incident skew angles. As it can be seen in Fig. 2.11(a) and (b), for the case of plane wave illumination with incident angle of $\theta^i = 8°$ and $\phi^i = 0°$, the amplitude and phase terms of the focal field evaluated by analytical GO-FO method are in very good agreement with results reported by CST MS within the FO validity region (2.2).

In the case of a plane wave illumination with incident angle of $\theta^i = 21°$ and $\phi^i = 0°$, the analytical GO approximation is not valid anymore ($\theta^i > 11°$); therefore, the numerical GO approach in (2.5) is employed. Here, the results from the GO-FO approach are also in good agreement with the CST MS within the FO applicability region, Fig. 2.11(c) and (d). However, since a considerable portion of the power at the focal plane is focused outside this applicability region, another approach is also employed here to indirectly validate the GO code. Namely, a GO-PO approach, where the scattered field is still calculated over the FO sphere using the numerical GO approach, and then a PO radiation integral is used to calculate the field at the focal plane of the elliptical lens. As it can be seen, the amplitude and phase of the focal fields calculated using the GO-PO approach are also in good agreement with the results reported by CST MS outside the FO applicability region.

The GO fields of the remaining QO components are also validated in a similar manner. In the

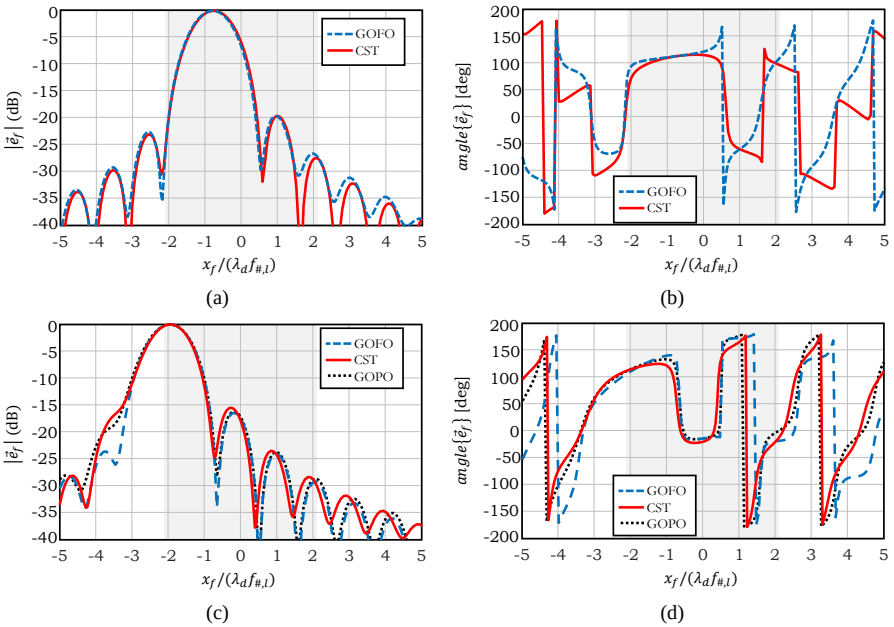

Figure 2.11: x-component of the electric field on the focal plane of an elliptical lens made of silicon ($\varepsilon_r = 11.9$) with $D_l = 5$mm and $f_{\#,l} = 0.6$, illuminated by a unitary TM polarized plane wave with skew angles. This field is evaluated at $y_f = 0$ plane, calculated using the analytical or numerical GO-FO approaches, and compared against the one obtained from CST. In the case of $\theta^i = 8°$ and $\phi^i = 0°$, (a) amplitude and (b) phase. In the case of $\theta^i = 21°$ and $\phi^i = 0°$, (c) amplitude and (d) phase. The grey region represents the FO validity region (2.2).

following section, the validity region of the described GO-FO method to derive the PWS of a QO component is expended to cover very large FPAs.

2.4 Deriving the Plane Wave Spectrum of Wide Angle Optics

The method reported in Sec. 2.3 can represent the PWS of a QO component within the FO applicability region (2.2). However, this region limits the maximum size of a FPA under analysis. Moreover, the FPA of future imaging systems could be several times larger than the applicability region of the classic FO approach. To enlarge this region, one can divide a large FPA into sub-regions where at the center of each sub-region a FO sphere (off-centered) is placed, as shown in Fig. 2.12. The GO field is then evaluated over the new sphere. The maximum subtended angle of the sphere (θ^m in Fig. 2.12) is then defined by the GO ray propagation. Once the center of the reference system has been changed to $\vec{O}^m$, and the off-centered GO fields on the new FO sphere calculated, identical steps to the ones described in Appendix A and Sec. 2.3 can be taken to derive the PWS of a QO component.

As discussed in Sec. 2.2, the validity region of the FO representation is directly proportional to the radius $R_{FO,m}$ chosen for the FO sphere. Moreover, the field tangent to an off-focus FO sphere can be approximated by using the GO ray propagation when the surface of the sphere is far from the caustic points of the geometry (here the focus of a QO component). Specifically, the GO representation is accurate when the radius of the off-focus FO sphere is at least larger than the depth of focus, $\Delta z_{HPBW} =$

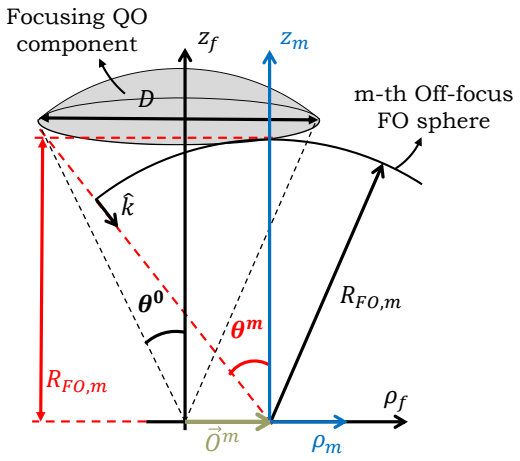

Figure 2.12: A schematic representation of the m-th off-focus FO sphere placed in the focal plane of a focusing QO component.

$1.77F/N_F$, where $N_F = D/(4\lambda f_{\#})$ is the Fresnel number. Therefore, to maximize this radius, it is convenient to define $R_{FO,m}$ as the z-position where the off-focus sphere is touching the surface of the QO component (Fig. 2.12). For this case, the maximum rim angle for the m-th off-focus sphere can be expressed as follows:

$$\theta^m = \arctan\left\{\frac{|\vec{O}^m|+D/2}{R_{FO,m}}\right\}, \tag{2.14}$$

where $|\vec{O}^m|$ indicates the distance of the center of off-focus FO sphere, in the focal plane, from the QO component origin.

As example cases, we considered a parabolic reflector with $D_r = 500\lambda_0$ and $f_{\#,r} = 4$, and one with $f_{\#,r} = 0.6$, illuminated by a plane wave impinging with an angle far from the broadside. The normalized focal field for these two cases is shown in Fig. 2.13, and compared, with an excellent agreement, with a standard PO based approach.

As described in Sec. 2.2, the FO representation of the focal fields can be derived by performing approximations in the PO radiation integral. Specifically, approximations on magnitude, vector, and phase terms in the integrand. The applicability region for the FO method can then be derived by imposing a maximum acceptable value for the error committed in these approximations, ε for the magnitude and vector cases, and ε_Φ for the phase. By following the same steps as in [66], for the m-th off-focus FO, one can define the following validity regions:

$$D_{FO,m} = 2min\left\{\varepsilon R_{FO,m}, \frac{1}{\sin\theta^m}\sqrt{\frac{\varepsilon_\Phi \lambda R_{FO,m}}{\pi}}\right\} \tag{2.15}$$

Fig. 2.14 shows the validity region of the off-focus FO for QO components with different f-numbers assuming $\varepsilon = 0.2$ and $\varepsilon_\Phi = \pi/8$. As it can be seen, the broadside FO validity region is larger for larger

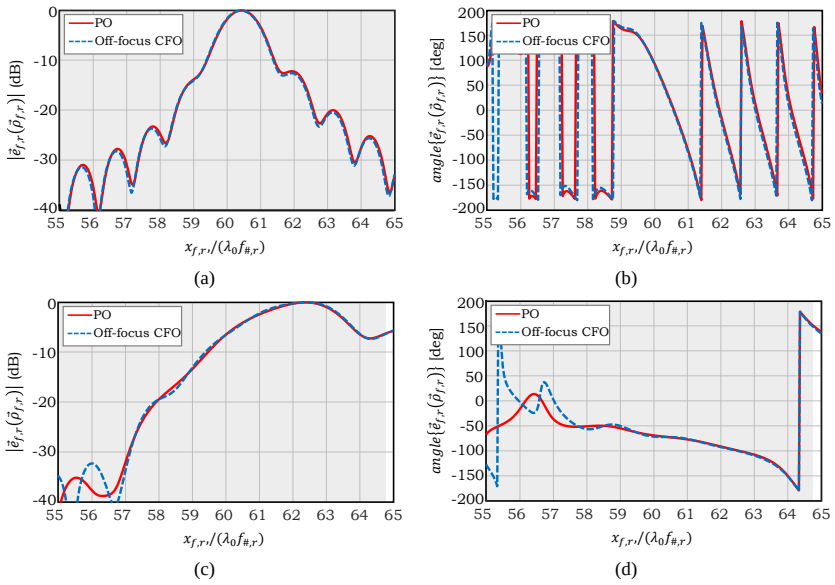

Figure 2.13: Magnitude and phase of the x-component of the electric field at the focal plane of a parabolic reflector with $D_r = 500\lambda_0$ and (a)-(b) $f_{\#,r} = 4$, and (c)-(d) $f_{\#,r} = 0.6$. The plane wave impinging angle is $\theta^i = 60\lambda_0/D_r$, and the off-focus FO sphere is placed at $\vec{O}^m = 50\lambda_0 f_{\#,r}\hat{x}$. Grey region indicates the applicability region of the FO approximation as stated in (2.15).

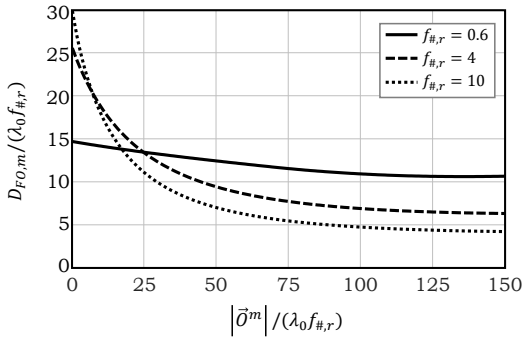

Figure 2.14: Validity region of the FO method, when analysing a parabolic reflector with diameter $D_r = 141.4\lambda_0$, versus the position of the FO sphere center in the focal plane.

f-numbers; however, this region decreases more rapidly as the sphere is away from the focus. This is because $1/\sin\theta^m$ grows rapidly when the reflector f-number is large.

2.5 Representing the Coupling of Quasi-Optical Systems to Antenna Feeders in Reception

The developed codes are also capable of analysing the coupling of antenna feeds to Quasi-Optical (QO) components in reception (Rx). Let us assume a reception scenario where an incident plane wave, prop-

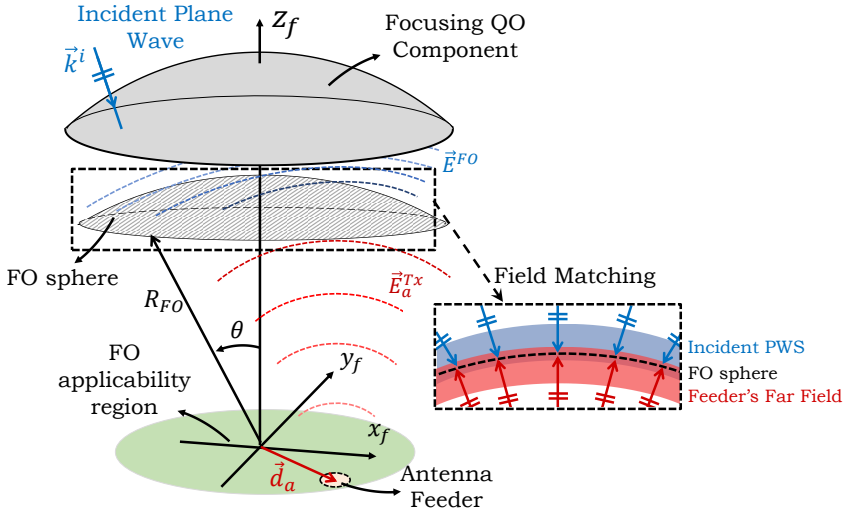

Figure 2.15: Antenna in Rx scenario. An antenna is placed at a certain position in the focal plane of a focusing component.

agating from $\vec{k}^i$ direction, illuminates a QO component, Fig. 2.15, θ^i and ϕ^i are the incident elevation and azimuth angles, respectively. This field is then scattered by the QO surface and captured by a feeding antenna which is placed at the focal plane of the QO surface. To evaluate the power received by the antenna and delivered to its load (assuming impedance match condition), we resort to antenna in reception formalism as discussed in [64] and [35]. The equivalent Thévenin open circuit voltage V_{oc} of the antenna can be evaluated as follows:

$$V_{oc}(\vec{k}^i)I_0 = \frac{R_{FO}}{\pi k_{FO}\zeta_{FO}} \int_0^{2\pi} \int_0^{+\infty} \vec{E}_a^{Tx}(\vec{k}_\rho) \cdot \vec{E}^{FO}(\vec{k}_\rho, \vec{k}^i) k_\rho dk_\rho d_\phi \tag{2.16}$$

where ζ_{FO} is the wave impedance of the medium in which the FO sphere is located; $\vec{k}_\rho$ is the spectral vector given by $\vec{k}_\rho = k_x\hat{x} + k_y\hat{y} = k_{FO}\sin\theta(\cos\phi\hat{x} + \sin\phi\hat{y})$, k_{FO} is the wave number of the FO sphere medium; θ and ϕ represent the elevation and azimuth angles representing this sphere, respectively; $\vec{E}_a^{Tx}$ is the far field of the feeder radiated in transmission (Tx), when fed by a current of I_0; $\vec{E}^{FO}$ is the PWS of the QO system. Both of these fields are evaluated at the FO equivalent sphere as shown in Fig. 2.15.

This Thévenin open circuit voltage can also be represented using the GO field, as:

$$V_{oc}(\vec{k}^i)I_0 = \frac{2}{\zeta_{FO}} \int_0^{2\pi} \int_0^{\theta^0} \vec{E}_a^{Tx}(\theta, \phi) \cdot \vec{E}^{GO}(\theta, \phi)(R_{FO})^2 \sin\theta d\theta d\phi \tag{2.17}$$

where θ and ϕ represent the elevation and azimuth angular positions on the FO sphere, respectively; θ^0 is the maximum rim angle of the QO component; R_{FO} is the radius of the FO sphere.

The power delivered to the load of the receiving antenna can be calculated as

$$P_L = \frac{|V_{oc}I_0|^2}{16P_{rad}} \tag{2.18}$$

where P_{rad} is the total power radiated by the antenna when fed with the current I_0:

$$P_{rad} = \frac{1}{2\zeta}\int_0^{2\pi}\int_0^{\pi}|\vec{E}_a^{Tx}|^2 R_{FO}^2 \sin\theta d\theta d\phi \tag{2.19}$$

As it can be seen from (2.16), the power delivered to the load is maximized when the feeder's far field is equal to the conjugate of the PWS of the QO system, $\vec{E}^{FO}$. This condition is referred to as the field match condition.

Once the power delivered to the load of the antenna is calculated, efficiency terms, directivity, and gain in reception can be computed as a function of the incident plane wave direction. The aperture efficiency in reception is evaluated as the ratio between the delivered power to the antenna load, P_L, and the incident power captured by the QO component, P_{inc}, as:

$$\eta_{ap}^{Rx}(\vec{k}^i) = \frac{P_L(\vec{k}^i)}{P_{inc}} \tag{2.20}$$

where, $P_{inc} = 0.5|E_0|^2\mathcal{A}_{QO}/\zeta$, and $\mathcal{A}_{QO}$ is the physical area of QO component.

In the case of a lens antennas below a primary QO component (e.g. a parabolic reflector), the described aperture efficiency can be divided into two contributions. The one related to the lens antenna performance, i.e. the feeder efficiency: the impedance matching, η_Ω; the front to back ratio of the antenna, η_{F2B}, which indicates how much of the total power radiated by the antenna is launched into the lens medium; the spill-over efficiency of the antenna far field over the lens surface, $\eta_{so,a}$; and the reflection efficiency at the dielectric-air interface, η_Γ. In other words, the feeder efficiency can be expressed as:

$$\eta_{feed} = \eta_\Omega \eta_{F2B} \eta_{so,a} \eta_\Gamma \tag{2.21}$$

Secondly, the contribution related to a proper illumination of the primary QO component, i.e. the illumination efficiency: the amplitude, polarization, and phase matching between the spectral field ($\vec{E}^{GO}$ or $\vec{E}^{FO}$) and the antenna far field, η_{amp}, η_{cx}, and η_Φ, respectively; and the spill-over efficiency of the field generated by the main QO component over the lens surface, $\eta_{so,l}$. In other words, the illumination efficiency can be expressed as:

$$\eta_{ill} = \eta_{amp}\eta_{cx}\eta_\Phi\eta_{so,l} \tag{2.22}$$

Together these two contributions represent the overall aperture efficiency of the system, i.e. $\eta_{ap}^{Rx} = \eta_{feed}\eta_{ill}$.

Moreover, the gain of the system is represented in reception as

$$G^{Rx}(\vec{k}^i) = D^{max}\eta_{ap}^{Rx}(\vec{k}^i) \tag{2.23}$$

where $D^{max} = (4\pi/\lambda^2)\mathcal{A}_{QO}$ is the maximum achievable directivity for a given size of the QO component coupled to a single mode antenna feeder.

By using reciprocity, the electric field $\vec{E}_{QO}$ that the antenna coupled QO system would radiate to $(R_{FF}, \theta^{FF}, \phi^{FF})$ position, at a far distance from the QO component, is evaluated as:

$$\vec{E}_{QO}(R_{FF}, \theta^{FF}, \phi^{FF}) = \frac{k_{FO}\zeta_{FO}I_0}{E_0}[V_{oc}^{TE}(\theta^{FF}, \phi^{FF})\hat{\theta} + V_{oc}^{TM}(\theta^{FF}, \phi^{FF})\hat{\phi}]\frac{e^{-jk_{FF}R_{FF}}}{4\pi R_{FF}} \tag{2.24}$$

where E_0 is the amplitude of the incident plane wave; $V_{oc}^{TE/TM}$ are the induced TE and TM polarized Thévenin open circuit voltages, respectively. These voltages are evaluated using (2.16); where $\vec{E}^{FO,TE/TM}$ corresponds to the incident PWS when TE/TM polarized incident plane waves illuminated the QO component from the direction $\theta^i = \theta^{FF}$ and $\phi^i = \phi^{FF}$.

In order to construct the pattern in reception, one needs to illuminate the QO component by a set of incident fields with different skew angles: $\theta^{FF} = [0, \theta^{Rx}]$, $\phi^{FF} = [0, 2\pi]$, where θ^{Rx} represents the maximum elevation angle in the observation grid.

2.5.1 Numerical Examples of Antenna Coupled Quasi-Optical Components

In this subsection, the performance of antenna feeders coupled to QO systems are evaluated in reception (Rx), and compared against the ones obtained in a conventional in transmission mode (Tx). Let us first consider the case of an integrated lens antenna illuminated by incident plane waves. Here we consider a y-polarized Gaussian feeder as a example of a receiving antenna. The far field pattern of this feeder (when placed at the lower focus of an elliptical lens) can be expressed as:

$$\vec{E}_a^{FF}(u, v) = E_{a0}e^{-\left\{\left[\frac{u}{u_0}\right]^2+\left[\frac{v}{v_0}\right]^2\right\}}[\sin\phi_l\hat{\theta}_l + \cos\phi_l\hat{\phi}_l] \tag{2.25}$$

where u_0 and v_0 are Gaussian feeder parameters which determine the shape of the beam; $u = \cos\theta_l\cos\phi_l$ and $v = \cos\theta_l\sin\phi_l$; $E_{a0} = 1$ V/m is a normalization factor; θ_l and ϕ_l are the elevation and azimuth angles from the lower focus of the lens which parametrize its surface. It is worth noting that this far field, $\vec{E}_a^{FF}$, is not necessary equal to the field radiated by the antenna evaluated at the FO sphere, $\vec{E}_a^{Tx}$, as shown in Fig. 2.15. The later can be calculated by propagating the former to the FO sphere surface.

This feeder is integrated with an elliptical silicon ($\varepsilon_r = 11.9$) lens as shown in Fig. 2.16. The Gaussian feeder parameters are designed in such a way that the far field of the feeder is symmetric and has −11dB field taper at the edge of the lens surface. The lens has a diameter of $D_l = 5$ mm, and a maximum rim angle of $\theta_l^0 = 56°$ (corresponding to $f_{\#,l} = 0.6$), illuminated by unitary-amplitude plane waves in co-polarization with respect to the polarization of the antenna. To improve the transmission at the silicon-air interface, the lens surface is covered by a quarter-wavelength Anti-reflection (AR) coating made of Parylene with relative permittivity of $\varepsilon_m = 2.6$. The frequency of operation is 300GHz. In this example scenario, the feeder is shifted by $\vec{d}_a = 0$, $0.174\hat{x}$ mm, and $0.348\hat{x}$ mm from the lower focus of the lens. These shifts correspond to scanning the radiation pattern by 0 (broadside), 1 and 2

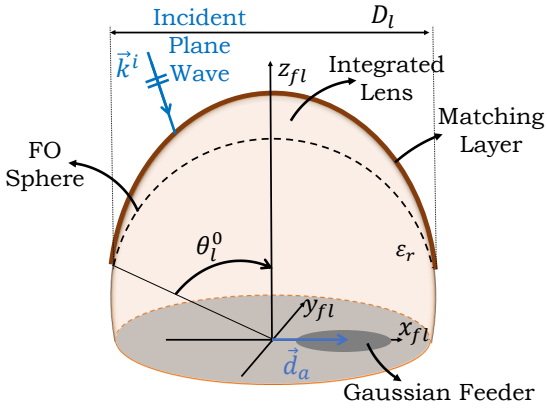

Figure 2.16: Gaussian pattern feeder coupled to an elliptical silicon lens.

Table 2.4: The performance of a test elliptical lens antenna compared in Tx and Rx.

Analysis in Tx/Rx	Aperture Eff.	Directivity	Gain
Broadside	80.7%/79.9%	23.8/23.7dBi	23.0/22.9dBi
Scanning 1 beam	73.4%/78.4%	23.6/23.7dBi	22.6/22.7dBi
Scanning 2 beams	56.9%/60.5%	23.0/23.4dBi	21.5/21.7dBi

beams (3dB overlapping beams) with respect to broadside direction, respectively, i.e. the main beam is pointing to $\theta^{FF} = 0°, 10.5°$ and $21°$, respectively, and $\phi^{FF} = 180°$.

For the described configuration, the analysis performed in Rx is compared to the one in Tx. The radiation patterns are compared in Fig. 2.17. The analysis in Tx is performed by using an in-house PO code which is validated by CST MS full-wave simulation [79]. As it can be seen in the figure, the patterns in reception in all three cases are in good agreement with the one obtained in Tx. In Tx analysis, the field radiated by the antenna is propagated out of the lens (from silicon to air). This field is evaluated outside the lens surface and shown for the case of scanning 2 beams in inset of Fig. 2.17(c). As it can be seen, the large scanning angle in this case leads to total reflection from a considerable portion of the lens surface. In such an extreme case, when the angle of rays inside the lens approaches the critical angle, a transition field is present at the lens interface, which creates corrections to GO fields and relevant PO currents [80]. The aperture efficiency, directivity and gain evaluated in Rx are also compared against the ones obtained in Tx for all three cases with very good agreement, as shown in Table 2.4.

As another example, let us consider a scenario with integrated lens antenna elements coupled to the rest of the QO chain. For simplification, here this QO chain is modeled by a single on-axis parabolic reflector, as depicted in Fig. 2.18. The diameter of the reflector is D_r=125 mm, and its f-number is $f_{\#,r} = 2.6$ (maximum rime angle of $\theta_r^0 = 11°$). Here, the same y-polarized lens antenna as in the previous sub-section is employed as the receiving antenna. However, in this case, the antenna feeder is kept at the lower focus of the elliptical lens, i.e. $|\vec{d}_a| = 0$. On the other hand, the lens antenna is shifted from the center of the parabola's focal plane by a distance $\vec{d}_l = 13\hat{x}$ mm or $65\hat{x}$ mm for the two considered scanning cases. These shifts correspond to scanning the radiation pattern of the complete QO system by 5 beams or 25 beams (3dB overlapping beams) with respect to broadside direction, i.e. the main

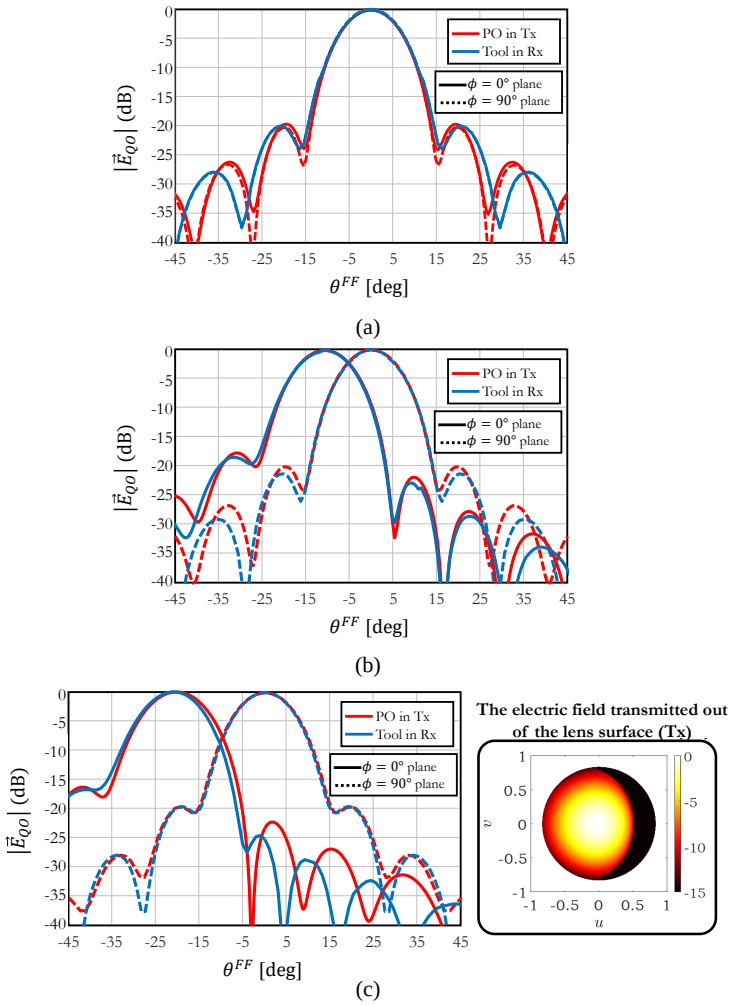

Figure 2.17: Amplitude of the radiation co-pol. pattern of the lens antenna: (a) scanning broadside direction, (b) scanning 1 beam, i.e. pointing the main beam to $\theta^{FF} = 10.5°$ and $\phi^{FF} = 180°$, (c) scanning 2 beams, i.e. pointing the main beam to $\theta^{FF} = 21°$ and $\phi^{FF} = 180°$. Inset in (c) shows the electric field transmitted out of the integrated lens and evaluated on its surface in Tx.

beam is pointing to $\theta^{FF} = 2.3°$ or $\theta^{FF} = 11.45°$, respectively and $\phi^{FF} = 0°$.

As shown in Fig. 2.19(a)–(d), the radiation patterns obtained in Rx are comparable to the ones in Tx. In this example, when calculating the pattern in Rx, the far field radiated by the lens antenna, $\vec{E}_a^{Tx}$, is the field transmitted outside the lens, using a PO in Tx code, and evaluated at the FO sphere of the reflector. This far field is shown in Fig. 2.17(a). A better FO method to analyse cascade QO components is described in Ch. 3. The pattern in Tx is obtained by importing the far-field pattern of the lens antenna (results obtained from PO in Tx) into GRASP [53] as a tabulated feeder source which illuminates the reflector. In Table 2.5, the aperture efficiency, directivity, and gain of the lens antenna-coupled reflector, evaluated in Rx, are shown and compared against the ones obtained in Tx with excellent agreement between the two methods.

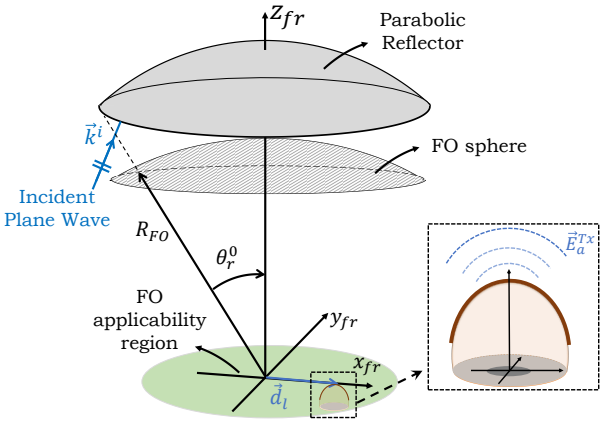

Figure 2.18: Geometry of a lens antenna coupled to a parabolic reflector. The reflector has a diameter D_m = 125 mm, and f-number $f_{\#,r}$ = 2.6 (θ_r^0 = 11°). It is illuminated by unitary plane waves. The test lens antenna is shifted by $\vec{d}_l$ from the parabola's focus.

Table 2.5: The performance of a test elliptical lens antenna below a parabolic reflector compared in Tx and Rx.

Analysis in Tx/Rx	Aperture Eff.	Directivity	Gain
Scanning 5 beams	52.4%/53.0%	51.3/51.3dBi	49.1/49.1dBi
Scanning 25 beams	13.2%/12.3%	49.1/48.9dBi	43.1/42.8dBi

2.6 Conclusion

Imaging systems at millimetre and sub-millimetre wavelengths are entering a new era with the development of large format arrays of detectors. Typically, such FPAs are coupled to a Quasi-Optical (QO) components. In this chapter, a GO-FO based technique for deriving the PWS of QO components in reception is presented. In particular, this PWS is derived analytically for three QO component, parabolic reflector, elliptical lens, hyperbolic lens, illuminated by broadside or slightly skewed plane wave incident angles. Moreover, a numerical GO method is also described for the cases when the component is illuminated by plane waves with large incident angles. By introducing the off-focus FO approach, the proposed PWS representation can be used to analyse, and design systems composed of tens of thousands of pixels, while the original FO would provide accurate spectra for only a few tens of elements. Finally, field matching technique is reviewed and a few simple test cases of antenna coupled QO components are analysed with excellent agreement with the full wave simulations.

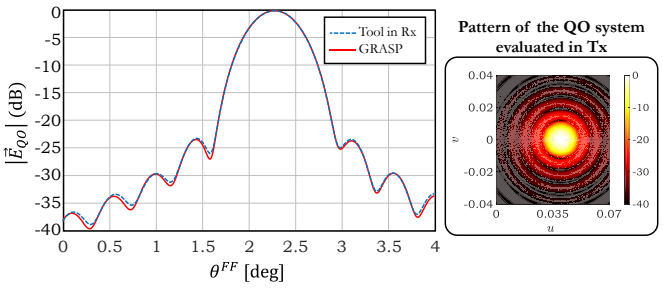

(a)

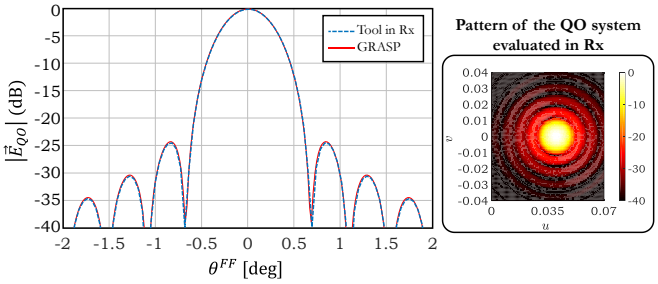

(b)

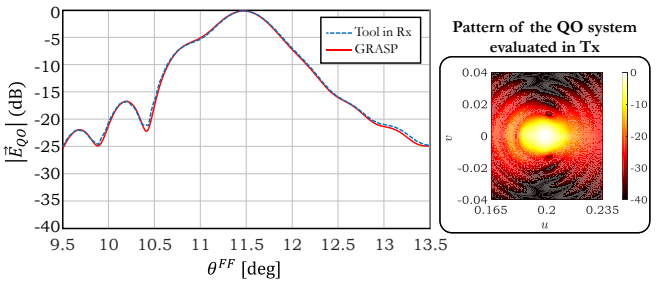

(c)

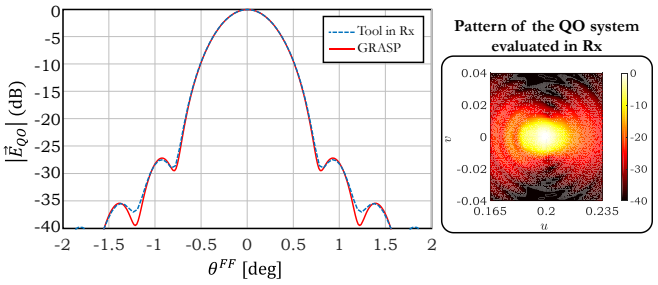

(d)

Figure 2.19: Amplitude of the co-polarization of the radiation pattern of the lens antenna-coupled parabolic reflector. Scanning 5 beams, i.e. pointing to $\theta^{FF} = 2.3°$: at (a) $\phi^{FF} = 0°$ cut, and (b) $\phi^{FF} = 90°$ cut. Scanning 25 beams, i.e. pointing to $\theta^{FF} = 11.45°$ at (c) $\phi^{FF} = 0°$ cut, and (d) $\phi^{FF} = 90°$ cut. The 2-D co-polarized amplitude patterns evaluated in Rx, and Tx by GRASP are shown in the insets.

Chapter 3

Coherent Fourier Optics

Future sub-millimetre imagers are being developed with large format focal plane arrays of lenses to increase the field of view and the imaging speed. A full-wave electromagnetic analysis of such arrays is numerically cumbersome and time-consuming. This chapter presents a spectral technique based on Fourier Optics for analysing lens based FPAs in reception. The proposed technique provides a numerically efficient methodology to derive the Plane Wave Spectrum (PWS), in magnitude and phase, of a secondary Quasi Optical component. This PWS can be used to calculate the power received by an antenna placed at the focal region of a lens.

3.1 Introduction

As discussed in Ch. 1, one of the promising detector array configurations in wide Field-of-View (FoV) Quasi-Optical (QO) systems is the Fly's eye lens arrays coupled to antennas or absorbers. These systems operating with similar principles to CCD cameras can achieve images with high resolution. At the moment, such detectors based on absorbers coupled lenses are employed in cameras where the absorbers are cryogenic lumped element Kinetic Inductance Detectors (KIDs) [11]. Moreover, Microwave KID lens-antenna system have shown technological readiness for use in a space based observatory [12]. Next generation of imaging cameras, such as [22], and communication systems, such as [35], will also employ these integrated lens antenna feeders.

The future goal for sub-mm imagers is to develop systems with focal plane arrays (FPAs) with over 10000 detectors to improve the overall image acquisition speed. In these scenarios, a full-wave electromagnetic analysis which also includes the coupling between the QO system and the detector array is not applicable, since it is numerically cumbersome and time-consuming. A typical approach for analysing such coupling resorts to the use of the Physical Optics (PO) based technique for antennas [81], and simplified Geometrical Optics (GO) based considerations for absorbers [47]. Antenna based systems are typically designed by using standard Gaussian pattern feeders, whereas in case of the absorbers the coupling to the QO system is evaluated only by considering the geometrical parameters of the structure.

In lens coupled absorbers, the plane wave spectrum (PWS) of the QO system can be linked to an equivalent Floquet-modes circuit to evaluate its coupling to the QO system, as described in Ch. 7. Moreover, for the lens coupled antenna cases, the PWS can be used to obtain the power captured by the antenna, by using the antenna in reception formalism described in [64] and Sec. 2.5. This approach simplifies the antenna feeder optimization since the power delivered to the antenna terminals is maximized when there is a field matching between the field pattern radiated by the feeder and the incident PWS. In [67] an asymptotic procedure for the numerical evaluation of the PWS of the focal field of a reflector system is described. A much simpler approach using Fourier Optics (FO) is discussed in Ch. 2 leading to analytical expressions for the PWS of focusing elliptical lens, hyperbolic lens, and parabolic reflector geometries.

The analysis in Ch. 2 is applicable only for a single-element (lens or reflector) Quasi-Optical system coupled to array of bare absorbers or antennas close to the focal point of the focusing component. In particular, by neglecting a phase term, which presents a quadratic dependence of the distance between the focal point and a generic point on the focal plane, the field in the focal plane is expressed as a Fourier transform of the field calculated on the equivalent FO sphere centered at the focal point of the system. This approximation is appropriate because absorber-based detectors are incoherent detectors (i.e. they are not sensible to the phase of the illuminating field), and in the geometries under analysis, the detector is placed below a single QO component. To analyse the coupling between two QO components, especially for off-focuses cases, this quadratic phase term cannot be simplified anymore.

In this chapter, firstly in Sec. 3.2, a FO approach is proposed which, in its described range of validity, allows us to effectively analyse the coupling of the QO system, the lens based FPA, and the detectors (either absorbers or antennas), including the phase information. The developed technique can rapidly and accurately represent the coupling between the full FPA and the QO system. Secondly, in Sec. 3.3, FO applicability region is extended to vertical axis with respect to the focal plane. This extension is es-

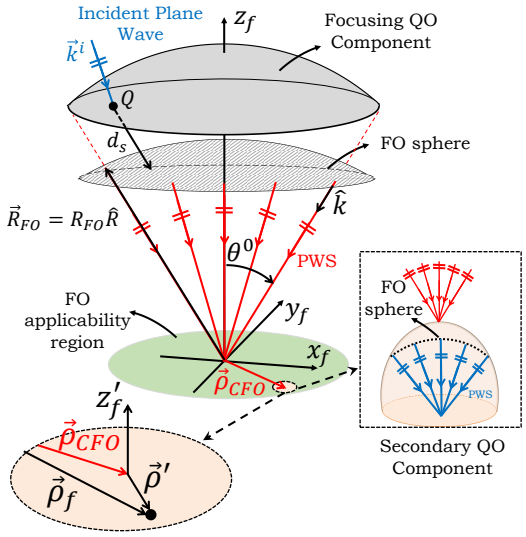

Figure 3.1: Coherent FO scenario: a focusing QO component is illuminated by an incident plane wave. Its focal field is represented as a PWS with respect to the origin of the reference system (x_f, y_f, z_f). The PWS is used to represent the field impinging on a secondary QO component (shown in the inset) located at $\vec{\rho}_{CFO}$. The local reference system at the neighborhood of $\vec{\rho}_{CFO}$ is also shown.

sential to determine positions in the focal plane of a primary QO component (e.g. parabolic reflector), where the secondary QO components (e.g. fly's eye lens array) can be analysed using FO approximations.

3.2 Derivation of the Coherent Fourier Optics

In this section, a plane wave spectrum (PWS) representation in both the magnitude and phase of the focal field is derived for a QO component illuminated by a plane wave. This PWS is valid at the immediate surrounding of the focal point (i.e. within the FO applicability region given in (2.2)). In Sec. 2.4 the validity region is extended to the case of wide angle optics.

Let us consider a generic focusing QO component illuminated by a plane wave $\vec{E}^i = E_0\hat{p}^i e^{-j\vec{k}^i\cdot\vec{r}}$, with wave-vector $\vec{k}^i$. As shown in Fig. 3.1, an equivalent FO sphere centered at the focus of the component can be used to represent the *direct field*, $\vec{e}_f(\vec{\rho}_f)$, on the focal plane ($z_f = 0$) in terms of a PWS (Chapter 2, Eq. (2.1)).

As discussed in Ch. 2, the PWS representation of the focal fields (neglecting the quadratic phase term), is related to the scattered GO fields on the surface of the FO sphere (see Eq. (2.3a)). This GO field can be calculated analytically as in Sec. 2.3.2, (2.12), when a parabolic reflector, hyperbolic, and elliptical lens is illuminated by a slightly skewed incident plane wave ($\theta^i \leq 11°$). For larger illumination angles and for a generic QO component, a numerical GO based approach can be employed as in Sec. 2.3.1, (2.5). The expression of the GO parameters for the transmission and reflection cases are provided in Appendix B.

The integral in (2.1a) resembles an inverse Fourier transform which relates the spectral field $\vec{E}^{FO}(\vec{k}_\rho)$

to the spatial one, $\vec{e}_f(\vec{\rho}_f)$. Due to the presence of the quadratic phase term, $e^{-jk|\rho_f|^2/(2R_{FO})}$, in (2.1a), $\vec{E}^{FO}(\vec{k}_\rho)$ is not actually the spectral representation of the amplitude and phase of the focal field, $\vec{e}_f(\vec{\rho}_f)$. In [66], the term $\vec{E}^{FO}$ was used only to calculate the magnitude of the focal field, since the effort was the analysis of incoherent detectors. Conversely, including the quadratic phase term is now essential for accurately representing the coupling between multiple QO components, depicted in the scenario shown in Fig. 3.1, or for evaluating the performance of a QO system with a coherent detection scheme.

As an example for demonstrating the importance of including the quadratic phase term into the Fourier transform representation, let us consider a parabolic reflector with a diameter of $D_r = 141.4\lambda_0$, and a f-number $f_{\#,r} = 2$. The reflector is assumed illuminated by a TM_{z_f} polarized plane wave with $|E_0|= 1$ V/m and incident angle $\theta^i = 2.43°$ which corresponds to scanning the reflector by 6 beams. The corresponding variation of the quadratic phase term is shown in Fig. 3.2(a). The position of the geometrical flashpoint, $\vec{\rho}_{i,r}$ is also shown. We define the geometrical flash point as the position of the peak of the focalized field over a focal plane assuming that no higher order aberrations are present, i.e. the beam deviation factor (BDF) [75] is 1. Figure3.2(b) shows the magnitude of the LHS of (2.3a) along $k_{x,r} = k \sin\theta_r$ when $k_{y,r} = 0$. By considering the quadratic phase term constant and equal to the one taken at the flashpoint (i.e. $e^{-jk|\vec{\rho}_{i,r}|^2/(2R_{FO})}$) the spectrum is flat over the reflector spectral domain (solid black line). Figs. 3.2(c) and (d), show the focal field $\vec{e}_{f,r}$ magnitude and phase values, respectively, along the x-axis in a region close to the flash point. Comparing the result obtained by assuming the quadratic phase term constant (solid black line) with the one obtained by using a standard PO based code (dotted blue line), that can be considered as a reference solution, it is evident that the magnitude of the focal field is accurately represented, but the phase not.

To properly represent the phase, we can rewrite (2.1a) as the product of two spatial functions:

$$\vec{e}_{f,r}(\vec{\rho}_f) = \frac{1}{4\pi^2}\phi(\vec{\rho}_f)FT^{-1}\{\vec{E}^{FO}(-\vec{k}_\rho)\} \tag{3.1}$$

where $\phi(\vec{\rho}_f) = e^{-jk|\vec{\rho}_f|^2/(2R_{FO})}$ is the quadratic phase term, and $FT^{-1}\{\vec{E}^{FO}(-\vec{k}_\rho)\}$ represents the inverse Fourier transform of $\vec{E}^{FO}(-\vec{k}_\rho)$. The spatial field in (3.1) can then be expressed as an inverse Fourier transform of the function $\vec{E}^{CFO}(-\vec{k}_\rho)$ that is here referred to as the coherent FO (CFO) spectrum, as follows:

$$\vec{e}_{f,r}(\vec{\rho}_f) = \frac{1}{4\pi^2}\int_0^{2\pi}\int_0^{+\infty}\vec{E}^{CFO}(-\vec{k}_\rho)e^{j\vec{k}_\rho\cdot\vec{\rho}_f}k_\rho dk_\rho d\alpha. \tag{3.2}$$

Specifically, the CFO spectrum is given by:

$$\vec{E}^{CFO}(-\vec{k}_\rho) = \Phi(\vec{k}_\rho) * \vec{E}^{FO}(-\vec{k}_\rho), \tag{3.3}$$

where $*$ is the convolution operator, and $\Phi(\vec{k}_\rho)$ is the Fourier transform of the quadratic phase term, which can be expressed analytically as follows:

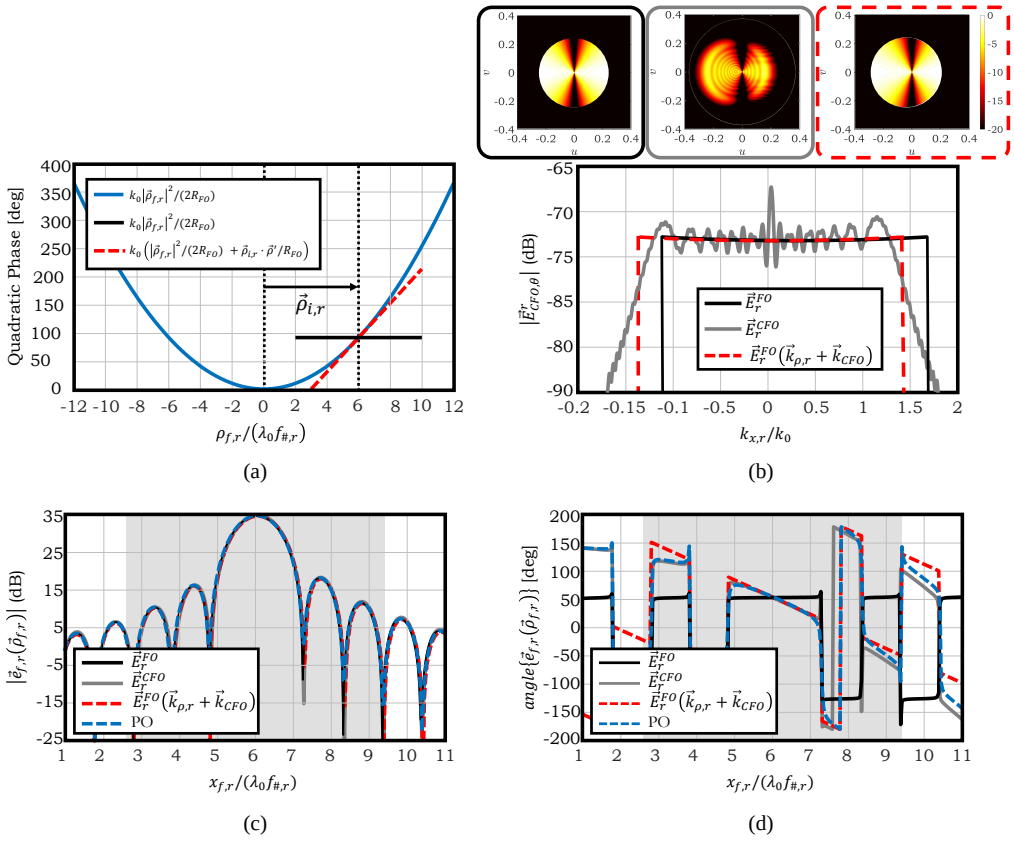

Figure 3.2: For a parabolic reflector with $D_r = 141.4\lambda_0$ and $f_{\#,r} = 2$ illuminated by a plane wave with an incident angle of $\theta^i = 6\lambda_0/D_r = 2.43°$ (a) The quadratic phase term, (b) The FO spectrum. The insets illustrate the 2-D spectrum of the θ-component of the field, where left, middle, and right panels represent the $\vec{E}^{FO}$, convoluted spectrum, and the shifted one, respectively. (c) The magnitude, and (d) the phase of the electrical focal field. The grey region indicates the applicability region of linearization approximation as stated in (3.9).

$$\Phi(\vec{k}_\rho) = \frac{1}{4\pi^2}\frac{2\pi R_{FO}}{k} e^{-j\pi/2} e^{jR_{FO}|\vec{k}_\rho|^2/(2k)}. \tag{3.4}$$

With reference to the previous example, the grey curve of Fig. 3.2(b) shows the variation of the coherent FO spectrum magnitude. It can be noted that now the spectrum is highly oscillating and shifted with respect to the one of the FO approximation. Fig. 3.2(c) and (d) show that it is possible to accurately calculate both magnitude and phase of the spatial field in the focal plane by using (3.4). However, due to the oscillations present in the convoluted spectrum (see Fig. 3.2(b)), the numerical convergence of the integral in (3.2) is demanding. Furthermore, (3.3) is a convolution that is both time consuming and numerically cumbersome.

One can simplify the calculation of the coherent FO spectrum by using an approximation of the quadratic phase term which accurately represents the field only at the surrounding of a specific position in the focal plane, referred to as the CFO position, $\vec{\rho}_{CFO}$. This approximation is achieved by introduc-

ing a new reference system in the focal plane centered at this position, where $\vec{\rho}' = \vec{\rho}_f - \vec{\rho}_{CFO}$ (Fig. 3.1), and retaining the first two terms of the Maclaurin series of the quadratic phase argument, as follows:

$$k\frac{|\vec{\rho}_f|^2}{2R_{FO}} \simeq k\frac{|\vec{\rho}_{CFO}|^2}{2R_{FO}} + k\frac{\vec{\rho}_{CFO}\cdot\vec{\rho}'}{R_{FO}} \tag{3.5}$$

The result of this linearization is shown in Fig. 2.12(a) (dash red line), where $\vec{\rho}_{CFO} = \vec{\rho}_i$ is chosen (at the flash point position). The Fourier transform of the quadratic phase term, $\Phi(\vec{k}_\rho)$, can be approximated as

$$\Phi(\vec{k}_\rho) \simeq e^{\frac{-jk|\vec{\rho}_{CFO}|^2}{2R_{FO}}}\delta(-\vec{k}_\rho - \vec{k}_{CFO}) \tag{3.6}$$

where $\vec{k}_{CFO} = \frac{k}{R_{FO}}\vec{\rho}_{CFO}$. Therefore, the convolution operation in (3.3) simply results in a shift of the FO spectrum along $\vec{k}_{CFO}$. Then, the focal field can be evaluated in the new reference system via

$$\vec{\rho}_f(\vec{\rho}') = \frac{1}{4\pi^2}\int_0^{2\pi}\int_0^{+\infty}\vec{E}^{CFO}(-\vec{k}_\rho)e^{j\vec{k}_\rho\cdot\vec{\rho}'}k_\rho dk_\rho d\alpha, \tag{3.7}$$

where the coherent FO spectrum is approximated as follows:

$$\vec{E}^{CFO}(\vec{k}_\rho) \simeq e^{\frac{-jk|\vec{\rho}_{CFO}|^2}{2R_{FO}}}\vec{E}^{FO}(\vec{k}_{CFO} - \vec{k}_\rho)e^{j[\vec{k}_{CFO}-\vec{k}_\rho]\cdot\vec{\rho}_{CFO}} \tag{3.8}$$

When examining Fig. 3.2(b), we can notice that the approximated coherent FO spectrum (dash red line) has a spectral domain similar to the one calculated by using (3.3), but without oscillations. In Figs. 3.2(c) and (d), both magnitude and phase of the spatial field are reported (dash red line), respectively. The agreement of the results with the PO solution (dash blue line) is evident. This agreement holds in the whole grey region shown in the same figure, that corresponds to the applicability region of the approximation (3.5). This region is defined as a circular region, centered on $\vec{\rho}_{CFO}$, with diameter D_{CFO}^{max} where a maximum phase error of $\pi/8$ is allowed in the quadratic phase term:

$$D_{CFO}^{max} = \sqrt{\frac{Df_\#\lambda_0}{2}} \tag{3.9}$$

where D and $f_\#$ are the diameter and the f-number of the corresponding QO component, respectively. It is worth noting that the applicability region is not a function of the chosen CFO position, $\vec{\rho}_{CFO}$. Fig. 3.3 shows the diameter of this applicability region for a few f-numbers of a parabolic reflector versus its diameter $D = D_r$. It can be noted that as the reflector f-number increases, the number of beams that

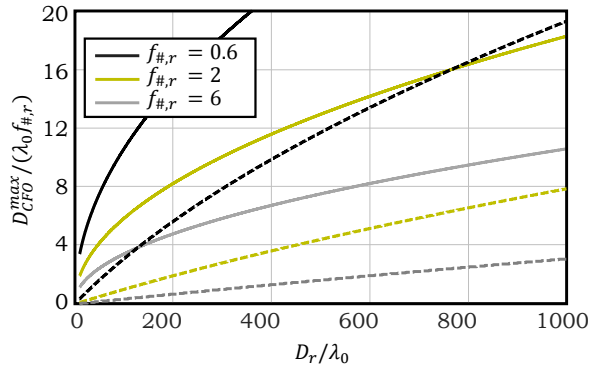

Figure 3.3: Maximum diameter of the applicability region normalized to $\lambda_0 f_{\#,r}$ for different parabolic reflector f-numbers versus its linear dimension. The solid and dashed curves correspond to the phase linearization, and a constant phase at $\vec{\rho}_i$ approximations, respectively. The latter limit is shown for a parabolic reflector scanning to 6 beams.

could be analysed with the approximation (3.5) decreases. For comparison, the dashed curves in the figure also show the applicability region of the spectrum in (2.1a) when a quadratic constant phase evaluated at $\vec{\rho}_f = \vec{\rho}_{i,r}$ is considered. In the latter case, applicability region depends on the chosen $\vec{\rho}_f$, and the approximation can only be used for a region close to the origin, and small $f_\#$.

By developing the PWS representation in (3.9) for the focal field of the primary QO component, one can now easily couple it to a secondary component, as shown in Fig. 3.1. The focal field of this secondary QO component can also be represented using (2.1) and (2.3). In this case, if the secondary component surface is within the 3D applicability region of FO, the GO field on the FO sphere of the secondary QO component, $\vec{E}_{sec}^{GO}(\vec{k}_{\rho,sec})$, is calculated by propagating each incoming plane wave from the primary QO component (i.e. the PWS in (3.8) to the FO sphere of the secondary component. As a result, $\vec{E}_{sec}^{GO}(\vec{k}_{\rho,sec})$, is the summation of the contribution of all these plane waves.

3.3 Expanding the Fourier Optics Representation to Vertical Positions

In this section, the standard FO applicability region, derived in Appendix A, is expanded in z-axis (perpendicular to the focal plane), Fig. 3.4. This 3D applicability region, determines a region where the coupling between QO components can be approximated by the diffraction phenomena; and at which locations the secondary QO components can be analysed using FO. In this case, the representation of the electric field scattered by a QO component toward its focus point, using PO technique, is similar to (A.3).

Similar to what is discussed in Appendix A, by approximating the integrand of (A.3) one can derive the FO representation of the field. However, in this case, this representation is not limited to observation points on the focal plane. In the case of amplitude and vector approximations the results are the same as before. On the other hand, the steps and expressions for the phase approximation alters as shown in the following.

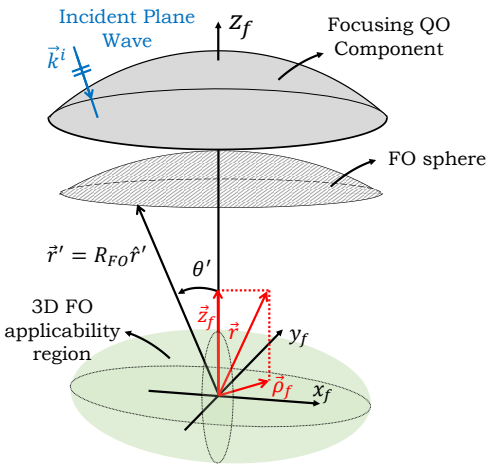

Figure 3.4: The Fourier Optics scenario for a focusing component illuminated by an incident plane wave from $\vec{k}^i = k_0 \sin\theta^i$ direction. Here the green sphere represents the applicability of the FO methodology around the focal plane of the component.

One can again expand the term $|\vec{r} - \vec{r}'|$ using the Maclaurin series as:

$$|\vec{r} - \vec{r}'| = R_{FO}\sqrt{1 - \frac{2}{R_{FO}}[\vec{r}\cdot\hat{r}'] + \frac{\vec{r}^2}{R_{FO}^2}} \simeq R_{FO} - \vec{r}\cdot\hat{r}' + \frac{r^2}{2R_{FO}}[1 - [\hat{r}\cdot\hat{r}']^2] + \frac{r^3}{2R_{FO}^2}[\hat{r}\cdot\hat{r}'] \quad (3.10)$$

The terms $-\frac{r^2}{2R_{FO}}[\hat{r}\cdot\hat{r}']^2$ and $\frac{r^3}{2R_{FO}^2}[\hat{r}\cdot\hat{r}']$ are again neglected in the FO representation of the field. By allowing a phase error of ε_Φ, the error committed in the phase approximation of the FO integral can be expressed as:

$$|\frac{k}{2R_{FO}}(\rho_f \sin\theta' + z_f\cos\theta')^2 - \frac{k}{2R_{FO}^2}r^2(\rho_f\sin\theta' + z_f\cos\theta')| \leq \varepsilon_\Phi \quad (3.11)$$

where $\vec{r} = \rho_f\hat{\rho} + z_f\hat{z}$.

By using these approximations, the FO representation of the scattered field close to the focal plane of a QO component can be expressed as:

$$\vec{e}(\vec{r}) = \frac{jR_{FO}e^{-jkR_{FO}}e^{\frac{-jkr^2}{2R_{FO}}}}{4\pi}\iint_{-\infty}^{+\infty}\vec{E}^{GO}(k_x, k_y)e^{jk_x x}e^{jk_y y}e^{jk_z z}\frac{1}{\sqrt{k^2 - k_\rho^2}}dk_x dk_y \quad (3.12)$$

where $\vec{k} = k_x\hat{x} + k_y\hat{y} + k_z\hat{z}$ is the wave vector, and $\vec{E}^{GO}$ is limited within the angular region of the QO component.

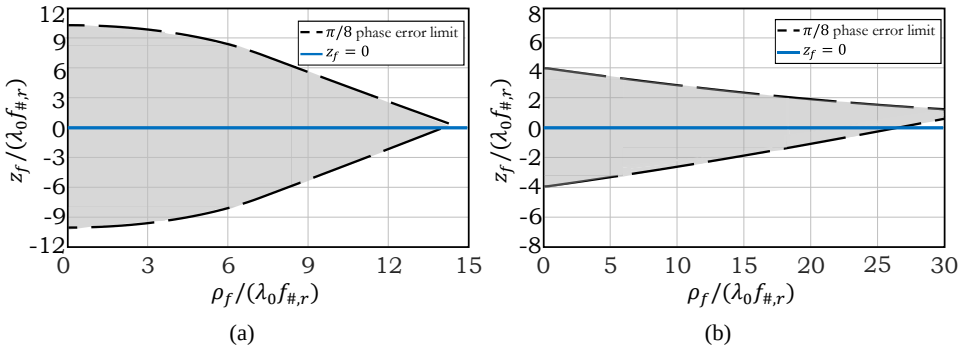

Figure 3.5: The applicability region of FO method located within the black dashed curve ($\pi/8$ error level). For a parabolic reflector with diameter $D_r = 500\lambda_0$, (a) $f_{\#,r} = 0.6$ and (b) $f_{\#,r} = 4$.

In the following, for a few example cases, this FO representation of the field is compared to a standard PO code, and the corresponding applicability regions are also shown. Let us consider a parabolic reflector with diameter $D_r = 500\lambda_0$, where λ_0 is the free-space wavelength at 300 GHz, with f-number 4 or 0.6. The 3D FO applicability region for these two geometries are shown in Fig.3.5, assuming $\varepsilon_\Phi = \pi/8$. In these figures, in the region withing the dashed black curves, electric field can be represented as a FO integral. As it can be seen, for the scenario with small f-number, the applicability region is wider in both $z-$ directions with respect to scenarios with larger f-number.

In Figs. 3.6 and 3.7, the electric field is calculated using FO and compared to standard PO codes at different z quotes around the focal plane of the reflectors for different incident angles. As it can be seen, these fields are well represented withing the described FO applicability region.

3.4 Conclusion

Imaging systems at millimetre and sub-millimetre wavelengths are entering a new era with the development of large format arrays of detectors. A fly's eye lens array coupled to absorbers or antennas is a common FPA architecture for such imagers. Typically, such FPAs are coupled to a Quasi-Optical (QO) system involving reflectors. For such large QO systems, a full-wave electromagnetic analysis of the entire system is not applicable since it is numerically cumbersome and time-consuming.

In this chapter, firstly the original FO procedure has been extended to derive the spectrum of the incident field on a reference system centered on antennas located at a large distance from the focus. The procedure, named here "coherent" FO, has been used to express the spectrum of the incident field in realistic cases which include large arrays of lenses within reflectors focal planes. In particular, the methodology can be linked to spectral techniques commonly used for arrays, such as Floquet-modes theory, for analysing absorbing mesh grids, and antenna in reception formalism to analyse the performance of antenna feeders in reception. By also employing the off-focus FO approach, the proposed coherent FO representation can be used to analyse and design wide field-of-view QO systems based on Fly's eye lens array configuration. Secondly, the applicability region of standard Fourier Optics (FO) method is extended to the vertical direction with respect to the focal plane of a focusing QO component.

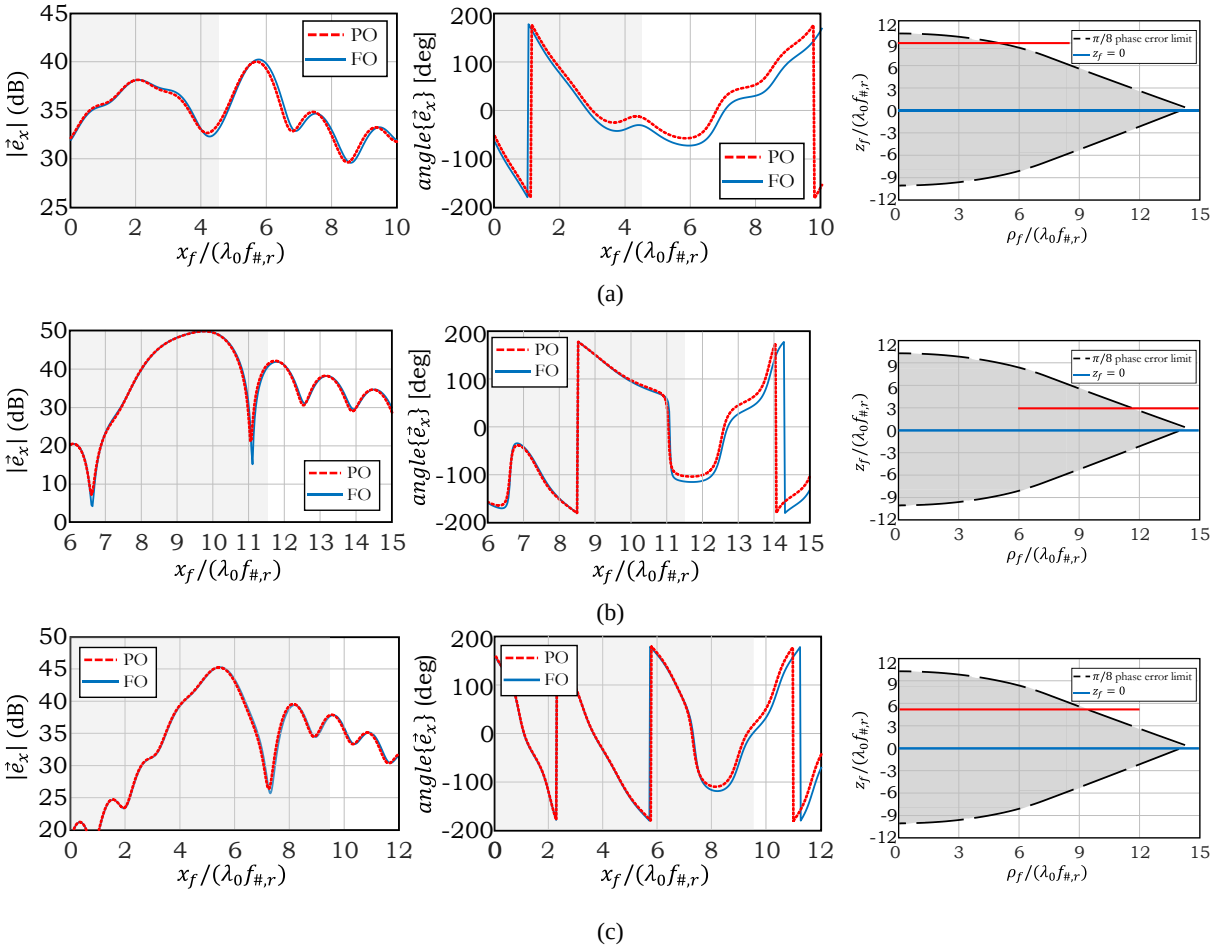

Figure 3.6: The amplitude (left panel) and phase (right panel) of the electric field calculated close to the focal plane of the parabolic reflector with $f_{\#,r} = 0.6$ and $D_r = 500\lambda_0$. (a) at $z_f = 9\lambda_0 f_{\#,r}$ when scanning 5 beams (i.e. $\theta^i = 5\lambda_0/D_r$). (b) at $z_f = 3\lambda_0 f_{\#,r}$ when scanning 9 beams (i.e. $\theta^i = 9\lambda_0/D_r$). (c) at $z_f = 5\lambda_0 f_{\#,r}$ when scanning 6 beams (i.e. $\theta^i = 6\lambda_0/D_r$). The grey region indicates the discussed 3D FO applicability region. The red line in the inset of each case indicates the observation positions in which the fields are evaluated, with respect to the applicability region diagrams.

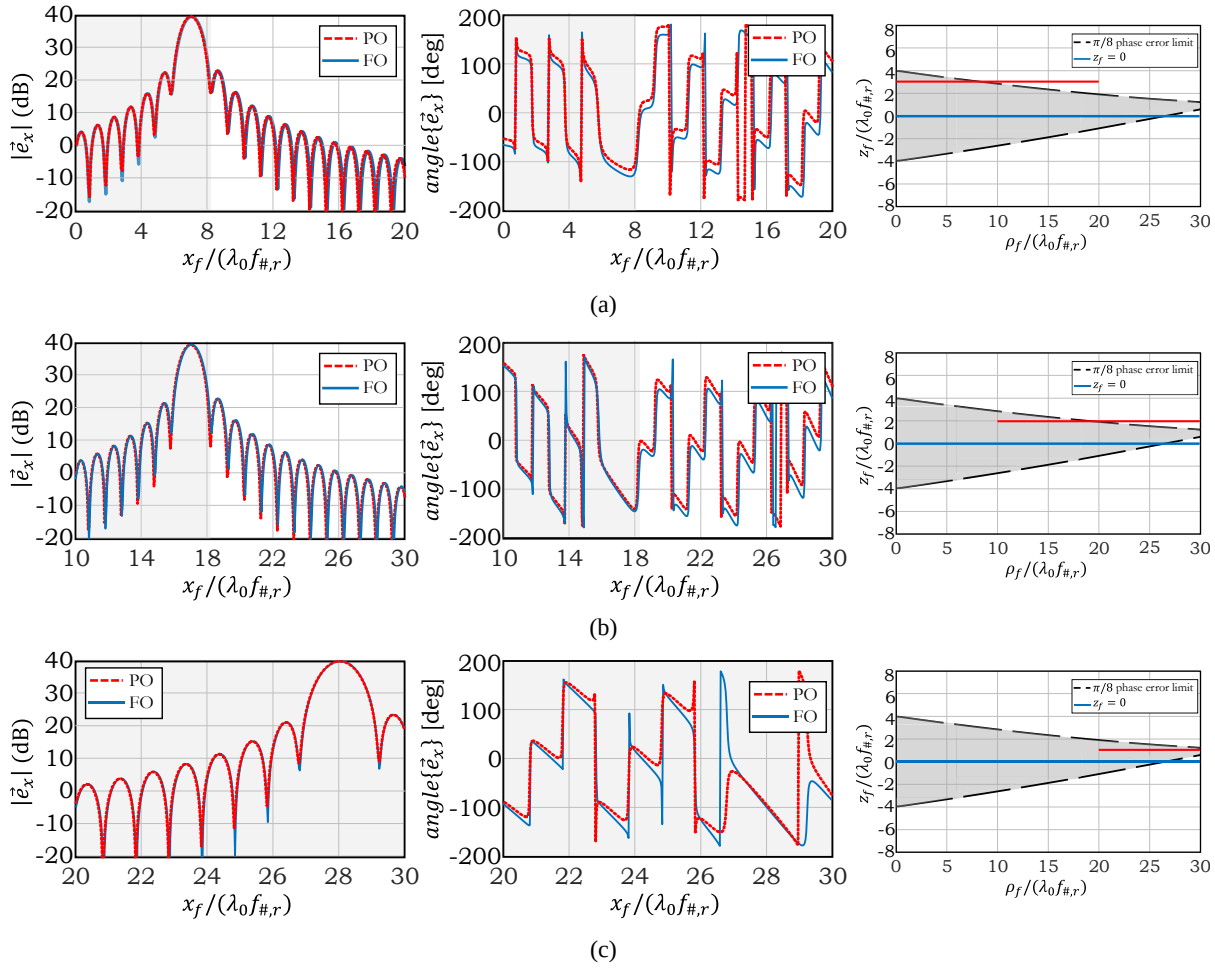

Figure 3.7: The amplitude (left panel) and phase (right panel) of the electric field calculated close to the focal plane of the parabolic reflector with $f_{\#,r} = 4$ and $D_r = 500\lambda_0$. (a) at $z_f = 3\lambda_0 f_{\#,r}$ when scanning 7 beams (i.e. $\theta^i = 7\lambda_0/D_r$). (b) at $z_f = 2\lambda_0 f_{\#,r}$ when scanning 17 beams (i.e. $\theta^i = 17\lambda_0/D_r$). (c) at $z_f = 1\lambda_0 f_{\#,r}$ when scanning 28 beams (i.e. $\theta^i = 28\lambda_0/D_r$). The grey region indicates the discussed 3D FO applicability region. The red line in the inset of each case indicates the observation positions in which the fields are evaluated, with respect to the applicability region diagrams.

Part II

Advanced Multi-Component Quasi-Optical Systems Based on Antenna Feeders

In this part of the thesis, methods for analysing the coupling between multiple Quasi-Optical components are discussed. In general, two QO components can be coupled geometrically or in the diffraction region. The former refers to scenarios where QO components are placed far away from focus points of one another; whereas the later describes scenarios where a QO component (secondary) is located close to caustic points (focus point) of a focusing (primary) QO component.

In the Geometrical Optics (GO) method, the EM radiation integral is approximated asymptotically for observation points far from the focus point. As the result, GO is accurate for representing geometrical coupling between QO components, and inaccurate for representing the diffractive couplings. In latter cases, Fourier Optics (FO) can be employed, since in this method the EM radiation integral is asymptotically approximated assuming observation points close to the focus point (center of a FO sphere). Here, Coherent Fourier Optics (CFO) method is used to represent the field scattered by the focusing (primary) component to its focal plane as a Plane Wave Spectrum (PWS), see Ch. 3. The coupling to secondary components can be evaluated as the summation of their responses to each one of these plane waves. In Sec. 3.3, the FO applicability region was expanded in z-axis (perpendicular to the focal plane). This 3D applicability region, determines the region where the coupling between QO components can be approximated by diffraction phenomena, and analysed using FO based techniques.

In Ch. 4, a case of diffractive coupling between two set of QO components is described. Specifically, the CFO method is applied to analyse the coupling between a large format lens based FPA (secondary components) and a parabolic reflector (primary component). In Ch. 5, a wide band QO system is described where the coupling between its integrated lens and the primary component is a mixture of geometrical and diffractive coupling depending on the frequency of operation. In particular, the coupling is geometrical at the higher frequency band portion, and diffractive at the lower frequency band portion. Moreover, in Ch. 4, GO and FO methods are combined to represent the coupling between multiple QO components, where multiple geometrical couplings are present.

Chapter 4

Wide Scanning Lens Based Focal Plane Arrays

Future sub-millimetre imagers are being developed using large format focal plane arrays (FPAs) of lenses to increase the field of view and the imaging speed. A full-wave electromagnetic analysis of such arrays is numerically cumbersome and time-consuming. In this chapter the coherent Fourier Optics methodology, introduced in Part I, is employed for analysing advanced lens based FPAs in reception. Here, the method is applied to a monolithically integrated focal plane array based on integrated lenses with optimal scanning performance without employing any optimization algorithm. The synthesized FPA achieved scan losses much lower than the ones predicted by standard formulas related to the direct field coming from the reflector. In particular, a FPA with scan loss below $1\,dB$ *while scanning up to* $\pm 17.5°$ *is presented with directivity of* $52 dBi$*. The technique is validated via a Physical Optics code with an excellent agreement.*

4.1 Introduction

As discussed in Ch. 1, Fly's eye configurations, i.e. lens based focal plane arrays (FPAs), are viable solutions for wide Field-of-View (FoV) imaging systems operating at millimetre and sub-millimetre wavelengths [10,82,35]. In this chapter, CFO technique is applied to the synthesis of such a wide FoV imager complying with the needs for future sub-millimetre imagers for security applications [24, 20, 22, 26]. For these applications antenna gains of about 50 to 60dBi are needed [24] with more than 100×100 beams.

In the literature, various solutions have been proposed in the past to improve the scanning performance of Quasi-Optical systems either using Gaussian horn feeders combined with shaped reflector or lens antennas [83, 39, 84, 85] (with most of the cases over sizing the radiating aperture) and/or determining an optimum focal surface [77, 86], where the array elements are placed [26]; or by using array clusters of feeders to achieve a conjugate field match condition with the focal plane field [87,88,89]. This work considers a relatively simple FPA architecture based on a lens array. All the lens feeders are placed over a flat surface, enabling monolithic integration at high frequencies. The surface shape of the lenses is linked directly to the phase of the incident PWS, while the radiation of the lens feeders is matched to the amplitude of the PWS via a Gaussian model approximation. For simplicity, the main reflector aperture is modelled as a symmetric non-oversized parabola. The obtained performances, validated via a conventional PO analysis, show significantly lower scan loss than it would be obtained by placing Gaussian horns in the optimal focal surface of such reflector as in [26]. The proposed technique could be easily extended to more practical reflector implementation (e.g. a Dragonian dual reflector [90]) by linking the PWS derivation to a GO field propagation in the reflector system and adjusting accordingly the lens surfaces, as well as in combination with oversized shaped surfaces.

4.2 Analysing Fly's Eye Lens Arrays

In this section, the proposed CFO methodology is applied to the analysis of elliptical lens based focal plane arrays coupled to a parabolic reflector. The geometry of the problem is sketched in Fig. 4.1.

By extending the applicability region of the FO method, see Sec. 2.4, a large format lens based FPA such as the one in Fig. 4.1 is divided into several regions. At the center of each region an off-focus FO sphere is centered. At the position of the apex of each lens element, a local phase linearization is performed, see (3.5), where $\vec{\rho}_{CFO} = \vec{\rho}_{ant}$. By doing so, the PWS of the scattered field by the reflector, $\vec{E}_r^{CFO}(\vec{k}_{\rho,r})$, is derived at the surrounding of the lens element. Each plane wave of this spectrum is propagated using a GO approach to a FO sphere defined inside the lens element as shown in the inset of Fig. 4.1, as:

$$\vec{E}^{GO}_{l,PW}(\vec{k}_{\rho,l}, \vec{k}_{\rho,r}) = \bar{\tau} \cdot \vec{E}_r^{CFO}(\vec{k}_{\rho,r}) e^{j\vec{k}_\rho \cdot \vec{Q}_l} \sqrt{\frac{\rho_1^t \rho_2^t}{\left[\rho_1^t + d_{s,l}\right]\left[\rho_2^t + d_{s,l}\right]}} e^{-jk_d d_{s,l}} \tag{4.1}$$

where $\vec{Q}_l$ is the corresponding point on the lens surface (see inset of Fig. 4.1) and $d_{s,l}$ is the length of the corresponding transmitted GO ray between the lens and FO surfaces.

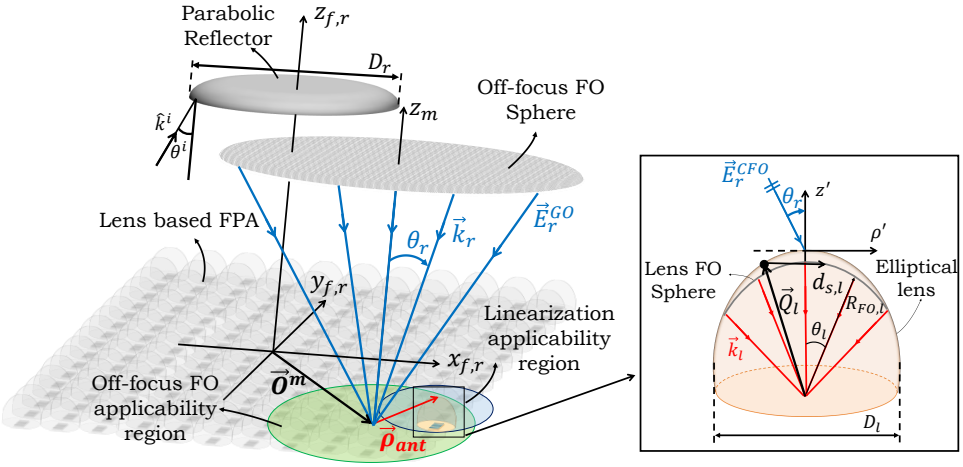

Figure 4.1: Illustration of an off-focus coherent FO scenario with a lens based FPA coupled to a parabolic reflector. The linearization (3.9), and off-focus FO (2.15) applicability regions are indicated by blue and green regions, respectively. Inset shows the dielectric lens under consideration.

To derive the PWS of the lens fed by the reflector, the GO fields in (4.1) are coherently summed:

$$\vec{E}_l^{GO}(\vec{k}_{\rho,l}) = \int_{\Omega_{FO}} \vec{E}_{l,PW}^{GO}(\vec{k}_{\rho,l}, \vec{k}_{\rho,r}) k_{\rho,r} dk_{\rho,r} d\alpha_r \tag{4.2}$$

where Ω_{FO} is the domain of integration which covers the entire angular region subtended by the reflector FO sphere of the reflector.

When the plane waves impinging on the lens are characterized by small incident angles, i.e. $\theta \leq 11°$, the GO field can be approximated (with a 20% maximum error in the field magnitude estimation) as follows (Sec. 2.3.3):

$$\vec{E}_{l,PW}^{GO}(\vec{k}_{\rho,l}, \vec{k}_{\rho,r}) \simeq \vec{E}_{l,PW}^{GO}(\vec{k}_{\rho,l}, \vec{k}_{\rho,r} = 0) e^{-j\vec{k}_{\rho,l}\cdot\vec{\Delta\rho}_{i,l}[1+\delta_{n,l}]} \tag{4.3}$$

where the term $e^{-j\vec{k}_{\rho,l}\cdot\vec{\Delta\rho}_{i,l}[1+\delta_{n,l}]}$ indicates the linear and the coma phase shifts; $\vec{\Delta\rho}_{i,l} = R_{FO,l}\vec{k}_{\rho,r}/k_d$ represents the flashpoint position, when assuming Beam Deviation Factor [75] is equal to 1; $\delta_{n,l}(\theta_l) = e[\cos\theta_l - \cos\theta_l^0]/[1 - e\cos\theta_l]$ where e is the eccentricity of the elliptical lens, and θ_l^0 is its maximum rim angle. The condition $\theta^i \leq 11°$, and the FO limit given in (2.15) define the validity region of (4.3).

To check the validity of the above methodology, let us consider the same reflector geometry described in the previous section but including a focal plane array of elliptical lenses. In Fig. 4.2, the sub-figures to the left panel represent the field at the focal plane of the reflector, i.e. the direct field on the top of the lens based FPA. The corresponding direct field cross-section in the $\rho_{f,r}$-$z_{f,r}$ plane, including the position of the lens, is shown in each inset. In the middle and right panels, the magnitude and the phase of the field at the focal plane of a lens are shown, respectively. The CFO is obtained for all cases assuming that the phase linearization point is that of the lens location, i.e. $\vec{\rho}_{CFO} = \vec{\rho}_{ant}$. The

amplitude of the plane wave impinging on the reflector is $|E_0|$= 1 V/m, and it is TM_{z_f} polarized for all cases. Figs. 4.2(a)-(c) consider a parabolic reflector with $D_r = 141.4\lambda_0$ and $f_{\#,r} = 2$, and a lens with diameter $D_l = 2\lambda_0 f_{\#,r}$, while for Fig. 4.2(d) $f_{\#,r} = 0.6$ and $D_l = 4\lambda_0 f_{\#,r}$. The f-number of the elliptical lens is defined as $f_{\#,l} = R_{FO,l}/D_l$ (see inset of Fig. 4.1), and in all the four cases $f_{\#,l} = 0.6$ (i.e., the lens is truncated). For Figs. 4.2(a) and (b), the lens under analysis is positioned in the focal plane of a reflector at $\vec{\rho}_{ant} = 8\lambda_0 f_{\#,r}$, but the plane wave angles of incidence are $\theta^i = 8\lambda_0/D_r$ and $\theta^i = 10\lambda_0/D_r$, respectively. The results are compared to those obtained using a multi-surface PO code (solid black line) that makes use of the formulation described in [91]. The excellent agreement inside the validity region of the FO is evident between the methods. The broadside FO applicability region for the discussed parabolic reflector is approximately 11 beams ($|\vec{\rho}_{f,r}| \leq 11\lambda_0 f_{\#,r}$). Moreover, to demonstrate the necessity of a coherent FO representation for the reflector's focal field, in Fig. 4.2(a) the lens focal field is also calculated assuming a constant quadratic phase term in the spectrum of the reflector focal field. From this figure it is evident that one commits a large error in analysing the coupling of the lens to the reflector by not accurately describing the quadratic phase term.

Figs. 4.2(c) and (d) consider a scenario which involves off-centered FO spheres in the x-direction (using the methodology described in Sec. 2.4). The lens under analysis is assumed positioned in the focal plane of the reflector at $\vec{\rho}_{ant} = 40\lambda_0 f_{\#,r}\hat{x}$ and the reflector is illuminated by a plane wave with an incident angle of $\theta^i = 40\lambda_0/D_r$. In this scenario, one can define an off-centered FO sphere positioned at $\vec{O}^m = 44\lambda_0 f_{\#,r}\hat{x}$ to evaluate the reflector CFO spectrum. In the left panel of Fig. 4.2(c) the magnitude of the incident field on the lens is compared with that obtained with a standard PO evaluation. Instead, the field on the lens focal plane compared with the multi-surface PO evaluation is shown in the other two panels.

Finally, Fig. 4.2(d) shows a case where the incident angle and the lens location are the same as in Fig. 4.2(c), but the f-number of the reflector is $f_{\#,r} = 0.6$ and the diameter of the lens is $D_l = 4\lambda_0 f_{\#,r}$. In this case, the propagation to the lens FO sphere requires the use of the numerical GO given in (4.1). The agreement with the multi-surface PO evaluation is also very good.

4.3 Estimating the Flash Point Position in a Wide Optics Scenario

As discussed in Sec. 2.3.3, in a scenario when a QO component scans a large number of beams, comma phase term, present in the PWS, can not be neglected. As a result, the actual flash point position is different from the one predicted geometrically (when assuming beam deviation factor is 1). In this section, a technique for approximating the flash point position, using CFO, in wide Optics QO systems is presented. The described technique is employed in the next section for designing the Fly's eye lens array. By using this technique, we determined the optimal position of off-centred lens elements in the FPA as the flash point position of the beams scanned by the reflector.

Within the applicability region of the Coherent Fourier Optics (CFO) method, (3.9), the field generated by a QO component at its focal plane is represented by an inverse Fourier transform (3.7). By examining the integrand of this Fourier transform, it is apparent that when the component are illuminated by an incident plane wave impinging from the broadside, a position (focus) exists on the focal

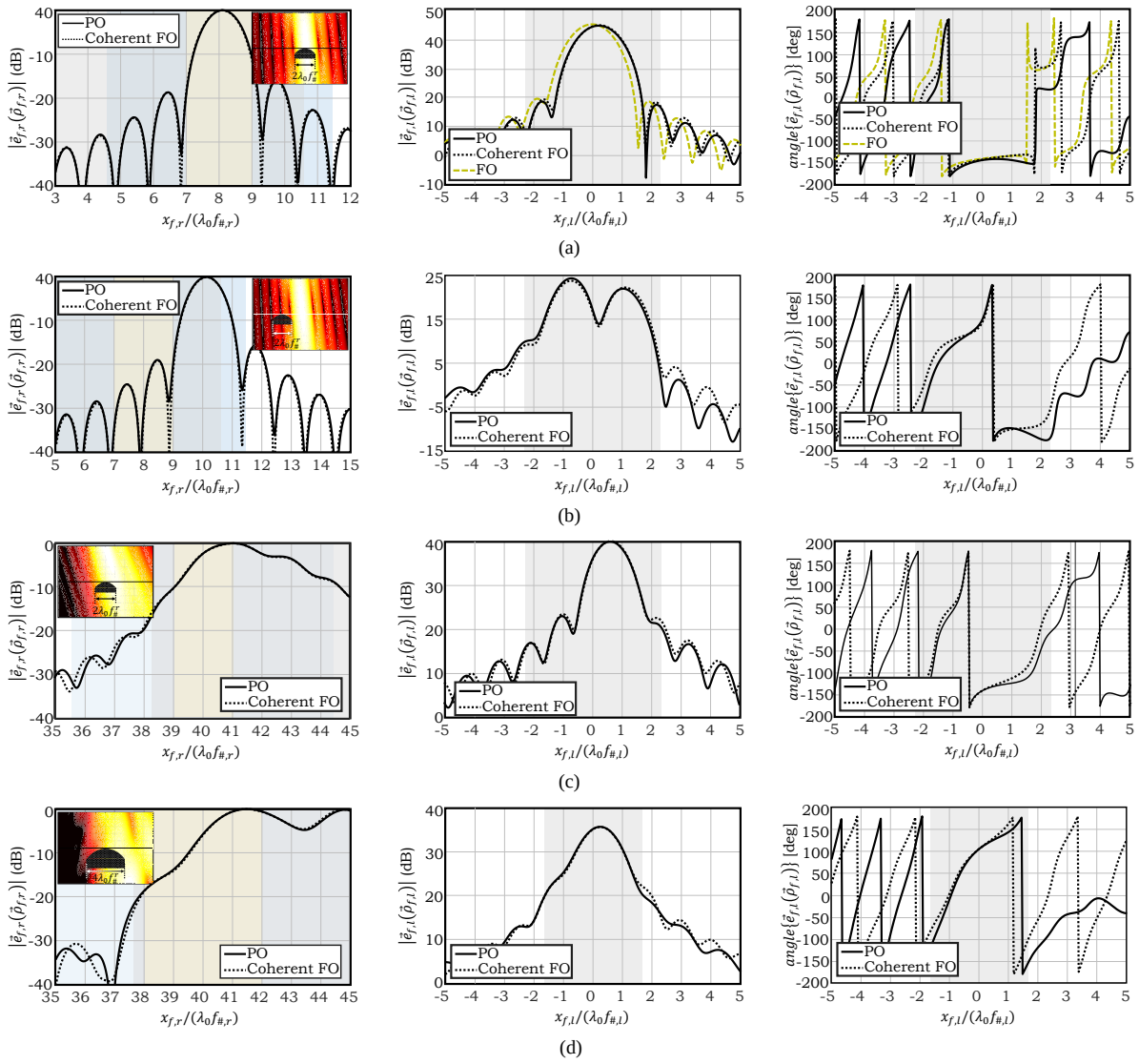

Figure 4.2: x-component of the electric field along the x-axis. The magnitude of the electric field evaluated on the focal plane of the parabolic reflector is reported at the left panel. In its inset, the 2D reflector focal field and the lens position are shown. On the middle and the right panel, the magnitude and phase of the electric field are evaluated on the focal plane of an elliptical lens. The figures (a)-(d) refer to the cases in which: (a) the reflector is scanning 8 beams and the lens is located at $\vec{\rho}_{ant} = 8\lambda_0 f_{\#,r}\hat{x}$ and the lens diameter is $D_l = 2\lambda_0 f_{\#,r}$; (b) the reflector is scanning 10 beams and the lens is located at $\vec{\rho}_{ant} = 8\lambda_0 f_{\#,r}\hat{x}$ and the lens diameter is $D_l = 2\lambda_0 f_{\#,r}$; (c) the reflector is scanning 40 beams and the lens is located at $\vec{\rho}_{ant} = 40\lambda_0 f_{\#,r}\hat{x}$ and the lens diameter is $D_l = 2\lambda_0 f_{\#,r}$ resorting to the off-focus FO approach (described in Sec. 2.4); (d) the incident angle and the lens location are the same as (c) but the reflector f-number is $f_{\#,r} = 0.6$ and the lens diameter is $D_l = 4\lambda_0 f_{\#,r}$. In all the cases, the lens f-number is $f_{\#,l} = 0.6$. The coherent FO approach refers to using (3.7) and (3.8), and the FO approach refers to the case where the PWS of the reflector is calculated assuming a constant quadratic phase. Grey, blue and orange regions indicate the applicability region of FO approximations (as given in (2.15) for the off-focus FO, and in (2.2) for the broadside FO), the applicability region of the coherent FO (linearization approximation) (as given in (3.9)), and the position of the lens in the focal plane of the reflector, respectively.

plane $\vec{\rho}_f$, in which all the components of PWS of the direct field, $\vec{E}^{CFO}$, are summed coherently. In other words, at this specific position on $\vec{\rho}_f$ we have

$$e^{j\Psi(\vec{k}_\rho)} e^{j\vec{k}_\rho \cdot \vec{\rho}_f} = 1 \quad \forall \vec{k}_\rho \leq k_{\rho 0} \tag{4.4}$$

where $k_{\rho 0} = k_0 \sin\theta^0$ and θ^0 is the maximum rim angle of the QO component, and $\Psi(\vec{k}_\rho)$ is the phase term of the dominant component of $\vec{E}^{CFO}$, i.e. $\Psi(\vec{k}_\rho) = \angle(E_{co}^{CFO})$.

The condition in (4.4) is not satisfied for every $\vec{k}_\rho$ when the component is scanning off-broadside plane waves. Therefore, one cannot find a unique position on the focal plane where the phase of the Fourier transform integrand is zero. However, when the component is not scanning extreme off-broadside angles, we can clearly identify a single bright spot on the focal plane. In this case, we can estimate a position where the phase of the integrand is almost zero over the whole $\vec{k}_\rho$ set by introducing the error function

$$\varepsilon(\vec{k}_\rho) = \Psi(\vec{k}_\rho) + \vec{k}_\rho \cdot \vec{\rho}_f \tag{4.5}$$

The flash point position, $\vec{\rho}_i$, is then estimated as the position where the sum of this error function over the whole whole $\vec{k}_\rho$ set, i.e.

$$\varepsilon_t = \int_0^{2\pi} \int_0^{+\infty} \varepsilon(\vec{k}_\rho) k_\rho dk_\rho d\alpha, \tag{4.6}$$

is minimum.

This method can be used to estimate the optimal position of lens antennas below a reflector system or the optimal position of the feeder on the focal plane of an integrated lens. By doing so, these elements receive the maximum power coming from the desired plane wave direction.

4.4 Wide Field of View with Non-homogenous Lens Antenna Arrays

It is well known that the scanning capabilities of reflector antennas are limited for large off-broadside angles. Focal plane arrays of homogenous (i.e. identical) horns or lenses have scanning properties proportional to the size of the beam illuminating the focal plane. In [26], formulas to derive the field of view (defined with a 3dB scan loss criterion) were given for opto-mechanical imaging systems. At low frequencies, the use of feed clusters has been proposed to enlarge the field of view [87, 88, 89]. Here, we investigate, instead, the possibility to enlarge the field of view by properly designing lens based feeders (lens dimension, lens surface, and lens feeder). The concept is applied to a focal plane array where the elements will be non-homogenous. The feeders of the lens array are placed over a flat surface to facilitate a monolithic integration at high frequencies.

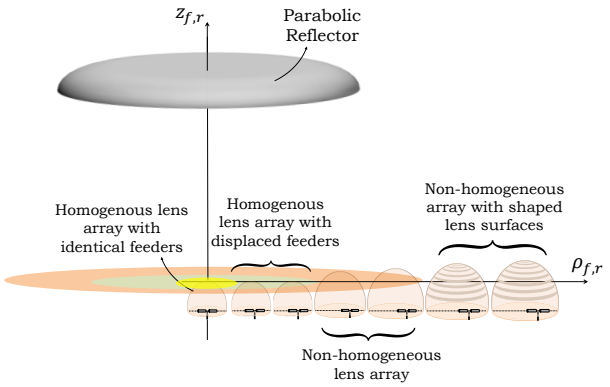

Figure 4.3: A large format flat FPA based on lens antennas with a hybrid architecture. The yellow, green, and orange regions represent the identical (4.9), displaced (4.10), and enlarged elements (4.11) regions, respectively.

For lens elements close to the focus of the reflector, the quadratic phase in (3.1) and the comma phase in the associated reflector CFO are not significant, and a homogenous lens array can be used with negligible scan penalty.

For mm- and sub-wavelength systems, the use of large f-numbers ($f_\# \geq 1$) is common due to their intrinsic larger scanning property [77]. In these cases, the quadratic phase term is the dominant source of error for off-focus lenses and the CFO has a dominating linear phase term. To achieve a conjugate field matching condition, as described in Sec. 2.5, the lens feeders should be laterally displaced along the lens focal plane with respect to the lens focus. For elements even farther away from the center, the CFO spectrum contains higher order phase terms. This is due to the fact that the optimum focal plane is curved instead of a flat surface. These phase terms lead to a widening of the beams impinging on the lens array. To improve the coupling to these distorted fields, one can first enlarge the lens diameters (amplitude matching) and introduce a non-rotationally symmetric lens feeder. Secondly, the phase of the distorted CFO spectrum can be matched by reshaping the surface of the lenses. Fig. 4.3 schematically describes a possible composition of an optimum focal plane array where different regions, filled with different types of lenses, have been identified.

As an application case, we consider a scenario compatible with wide-angle QO systems used in the state-of-the-art compact imaging systems such as those described in [26] and [24]. As baseline for the design of the FPA, we consider a silicon elliptical lens ($\varepsilon_{si} = 11.9$) of variable diameter and coated with a standard quarter wavelength matching layer with relative permittivity of $\varepsilon_m = \sqrt{\varepsilon_{si}} = 3.45$. The parameters of the considered reflector coupled lens antenna are listed in Table 4.1. The far field of the lens feeders is modeled via a Gaussian beam as follows:

$$\vec{E}_a^{FF} = E_{a0} e^{-\left([\frac{u}{u_0}]^2+(\frac{v}{v_0})^2\right)} [\sin\phi_l \hat{\theta}_l + \cos\phi_l \hat{\phi}_l] \tag{4.7}$$

where $u = \sin\theta_l \cos\phi_l$, and $v = \sin\theta_l \sin\phi_l$; u_0 and v_0 are chosen in such a way that the antenna far field matches the CFO at −11dB level; $E_{a0} = 1$ V/m is a normalization factor. The Gaussian patterned antenna feeders are placed at the lower focus of each elliptical lens.

The performance of such an array is evaluated in terms of scan loss, which is defined as follows:

Table 4.1: The Geometrical Parameters for the Scan Loss Example

D_r	$f_{\#,r}$	freq.	$f_{\#,l}$
$141.4\lambda_0$	2	340 GHz	1

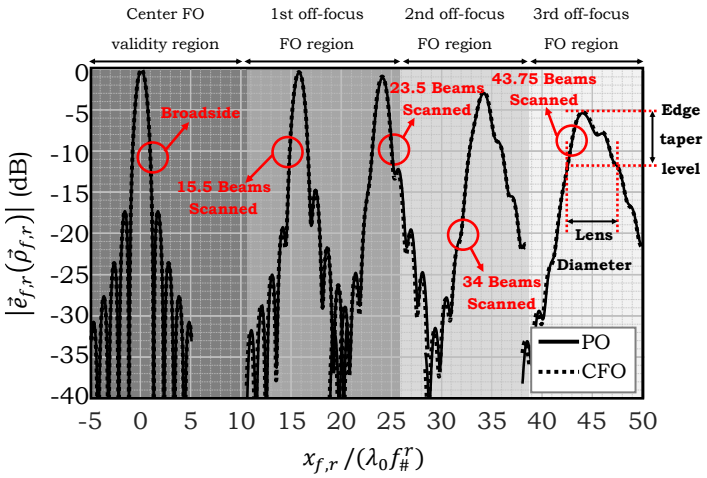

Figure 4.4: Normalized electric field in the focal plane of the parabolic reflector when scanning 0 (broadside), 15.5, 23.5, 34, and 43.75 beams. The shaded regions represent the FO applicability regions. The edge taper level of power entering a lens element is also shown as an example.

$$SL_{dB}(N_b^s) = -10\log_{10}\left[\frac{P_L(N_b^s)}{\max\{P_L(N_b^s)\}}\right], \tag{4.8}$$

where $N_b^s = \theta^i/(D_r/\lambda_0)$ represents the number of beams scanned by the reflector, and θ^i is the angle of the incident plane wave illuminating the reflector; P_L is the power delivered to antenna terminals as described in Sec. 2.5 and (2.18); $\max\{P_L(N_b^s)\}$ is the maximum power that can be received by the detector when the reflector is pointing at broadside direction.

A TM_{z_f} polarized plane wave with magnitude $|E_0|= 1\ V/m$ is impinging on the parabolic reflector from $\phi^i = 0°$. Fig. 4.4 shows the field on the reflector focal plane when 0 (i.e. broadside direction), 15.5, 23.5, 34, and 43.75 beams are scanned. The maximum of the focal field for each considered scanning position is located inside one of the validity region of the central, 1st, 2nd and 3rd off-focus FO sphere located at $\vec{O}^m = 18.2\lambda_0 f_{\#,r}\hat{x}$, $32.3\lambda_0 f_{\#,r}\hat{x}$, and $44.4\lambda_0 f_{\#,r}\hat{x}$, respectively. When the reflector is scanning 15.5 beams, the focal field exhibits asymmetric side lobes, due to the comma phase terms as described in Sec. 2.3.3, while scanning 23.5, 34 and 43.75 beams the first two side lobes and the main lobe of the focal field are merged, due to higher order phase distortions.

In Fig. 4.5, the scan loss of this incident focal field is shown (solid grey line). The circle mark represents the number of beams scanned, $N_b^s = \theta^i/(D_r/\lambda_0)$, through the parabolic reflector before reaching a scan loss of 3dB. The value is obtained by using Eq. (3) of [26]. It is worth noting that the incident scan loss curve (solid grey line) calculated here matches the standard formulas, and it is in line with the approximations available in the literature.

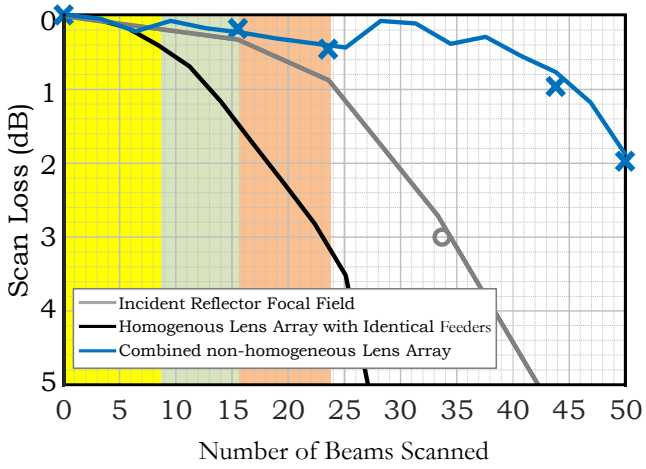

Figure 4.5: Scan loss of the QO system versus the number of beams scanned, for the geometry reported in Table 4.1. The yellow, green, and orange regions represent the identical (4.9), displaced (4.10), and enlarged elements (4.11) regions, respectively. The value identified by the grey circle symbol shows the number of beams scanned with less than 3dB scan loss and is calculated by using [26]. The cross marks indicate the scan loss obtained by using the PO solver of GRASP [53].

In the following subsections, the four FPA regions identified for optimizing the scanning performance of the reflector system are described. In the left column of Fig. 4.6, the magnitude and phase of the CFO spectrum of the parabolic reflector is shown for several of the cases in Fig. 4.4.

4.4.1 Region 1: Homogenous Lens Array with Identical Feeders

In this region, the diameter of these lenses is chosen as $D_l = 2\lambda_0 f_{\#,r}$ which corresponds to the width of the main beam of the reflector focal field when looking at the broadside direction. In Fig. 4.6(a), the CFO spectrum of the lens is compared to the corresponding one calculated from the antenna far field, when the lens element is placed at the reflector focus. It can be noted an excellent matching between the two fields (middle and left panels). As a result, the aperture efficiency for the central array element is about 80%.

Fig. 4.5 shows the scan loss when an array of homogeneous lenses with identical centered feeders are considered (solid black lines). It is worth noting that for this lens array the scan loss reaches 3dB only scanning 23 beams. The rapid increase of the loss is due to the phase mismatch between the CFO spectrum and the antenna far field. This phase mismatch is mainly due to the quadratic phase of the reflector focal field. One can calculate the quadratic phase difference over a lens surface as $|\Phi^q_A - \Phi^q_B| = \left|\frac{k_0|\rho_A|^2}{2R_{FO,r}} - \frac{k_0|\rho_B|^2}{2R_{FO,r}}\right|$, where ρ_A and ρ_B represent the edge positions of the lens element on the reflector focal plane; $R_{FO,r}$ is the radius of the reflector FO sphere. Imposing a maximum of $\pi/2$ phase difference leads to a scan loss of 0.5dB. Taking this scan loss value as the limit, the maximum number of beams scanned by homogenous lens array (i.e. with identical uniformly spaced feeder elements) defines the limit for this region as follows:

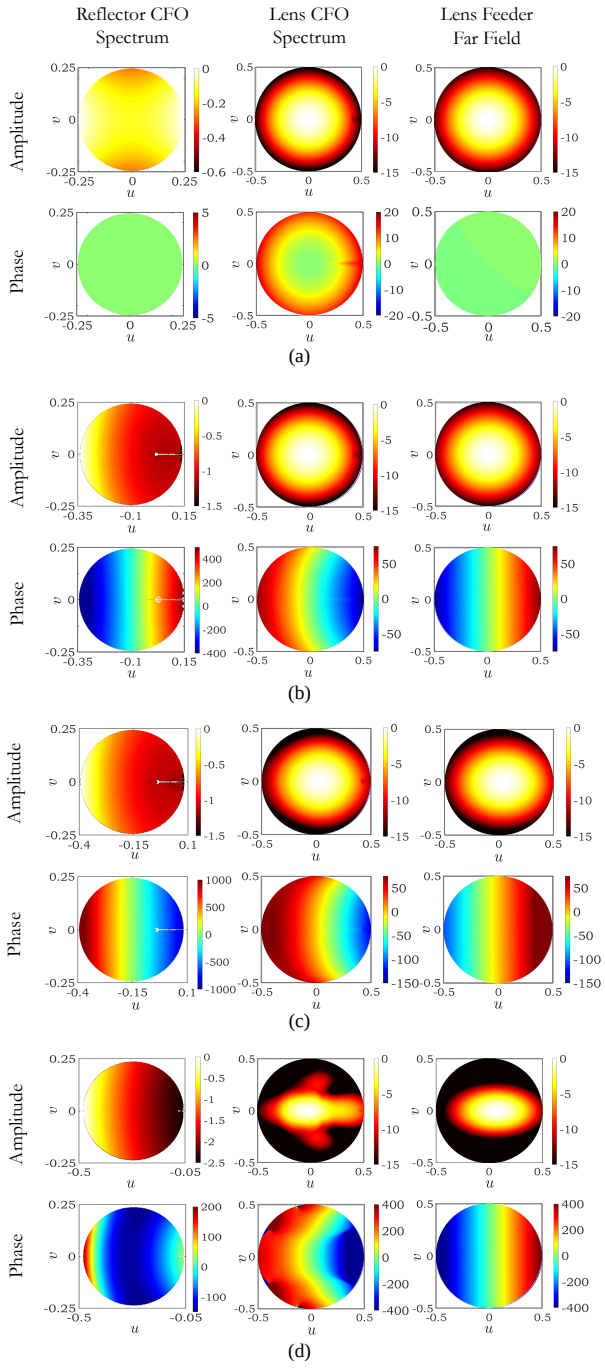

Figure 4.6: Magnitude and phase of the CFO spectrum at the reflector FO sphere (left panel), and the lens FO sphere (middle panel). The far field of the lens feeder is also shown in the right panel. (a) The central element of the homogenous lens array with identical feeders; (b) an element of the homogenous lens array with displaced feeders, 15.5 beams away from the center; (c) an element of the non-homogeneous lens array with displaced feeders, 23.5 beams away from the center; (d) an element of the non-homogeneous lens array with displaced feeders, 43 beams away from the center.

$$N^1_{max} = \frac{\rho_{max}}{\lambda_0 f_{\#,r}} = \frac{D_r}{8\lambda_0 f_{\#,r}} \tag{4.9}$$

In Fig. 4.5, this region is marked with a yellow color. As expected, at the edge of this region, the identical element array exhibits about 0.5dB of scan loss. Within the region identified by (4.9), the architecture of the proposed optimum lens based FPA is also synthesized using identical elements. The scan loss of this array is also shown in Fig. 4.5 (blue line).

4.4.2 Region 2: Homogenous Lens Array with Displaced Feeders

For elements farther away than N^1_{max}, see (4.9), the CFO spectrum exhibits a linear phase as can be seen in Fig. 4.6(b). One can conjugate match this phase term by displacing the lens feeders laterally in their respective lens focal planes. In this second region, the diameter of the lenses is kept constant over the array ($D_l = 2\lambda_0 f_{\#,r}$) since higher order phase terms are still not relevant. The optimum position for each feeder is determined by using the method described in Sec. 4.3. Specifically, the method estimates the position of the maximum of the focal field, i.e. the flashpoint position. As shown in Fig. 4.6(b), for an element 15.5 beams away from the center of the reflector focal plane both the magnitude and phase of the incident field and the antenna far field are well matched reaching an aperture efficiency of 76%. Fig. 4.7(a) summarizes the optimum feeder position found using the procedure detailed in Sec. 4.3 for all regions.

The limit of this region is associated to the higher order phase distortions in the reflector CFO, specifically the comma error. By using the formula derived in Sec. 2.3.3 (2.13), for the estimation of the comma phase in a parabolic reflector, one can calculate a maximum number of beams scanned by the displaced feeders reaching at most 0.5dB of scan loss, as follows:

$$N^2_{max} = \left[f_{\#,r} + \sqrt{f^2_{\#,r} - 0.25} \right]^2 \tag{4.10}$$

In Fig. 4.5, this region is marked with a green color. Within this region, the architecture of the proposed optimum lens based FPA is synthesized using the homogenous lens array with displaced feeders. The scan loss of this array is shown in Fig. 4.5 (blue line). As expected, at the edge of the region identified by (4.10), this array exhibits about 0.5 dB of scan loss. The performance of the homogenous lens array with displaced feeders is significantly improved with respect to the one with identical elements (black line).

4.4.3 Region 3: Non-Homogeneous Lens Array

For elements farther away than N^2_{max}, see (4.10), the diameter of the lens elements should increase to compensate the widening of the reflector field due to the higher order phase distortions. As shown in Fig. 4.4, this focal field is asymmetric in this region. We define a larger rim (e.g. diameter) for the lenses in this region by finding the contour of the reflector focal field at a certain level with respect to its maximum, referred here as lens edge taper level. As an example, Fig. 4.4 shows that the last lens element

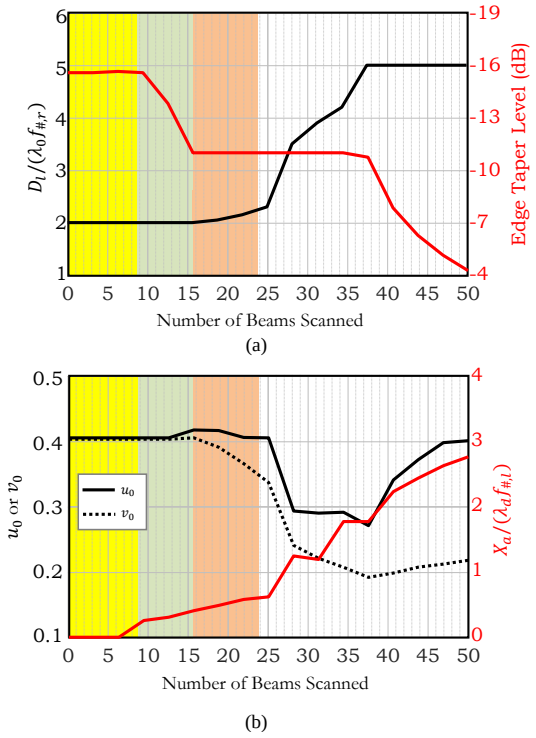

Figure 4.7: The geometrical parameters of the synthesized non-homogeneous lens array. (a) Gaussian feeder parameters (black curves), and feeder displacement in the lens focal plane (red curve). (b) Diameter of the lens elements (black curve), and edge taper level for each lens for the worst case 1D cut over its surface. The yellow, green, and orange regions represent the identical (4.9), displaced (4.10), and enlarged elements (4.11) regions, respectively.

is defined with an edge field taper level of $\simeq -7$ dB. An automatic procedure is established to define the lens rim for every element by initially using a -11 dB edge field taper. However, as discussed in Sec. 3.3, the FO validity region is also limited in the vertical direction. Therefore, the considered lens heights and consequently their diameters are limited. In the described example scenario, this maximum lens diameter is $\simeq 5\lambda_0 f_{\#,r}$. The automatic implemented produce limits the diameters to this number, and consequently, the obtained edge taper levels are reduced at the edge of the array. Figure 4.7(b) reports the obtained lens diameters and field edge levels for the considered scenario. The reported edge taper level is for the worst case of the 1D cut over the lens surface, e.g. for scanning in x-direction along $x_{f,r}$ when $y_{f,r} = 0$. As a consequence, the Gaussian beam waists in (4.7) will be different now in the two main planes.

As is shown in Fig. 4.6(c), for the lens element located 23.5 beams away from the center the field match is very good, both in magnitude and phase. Figs. 4.7(b) and (c) summarize the optimum lens diameters and Gaussian feeder parameters for all regions. By using the formula derived in [26], one can calculate the maximum number of beams scanned in this region with a scan loss below 0.5dB, as follows:

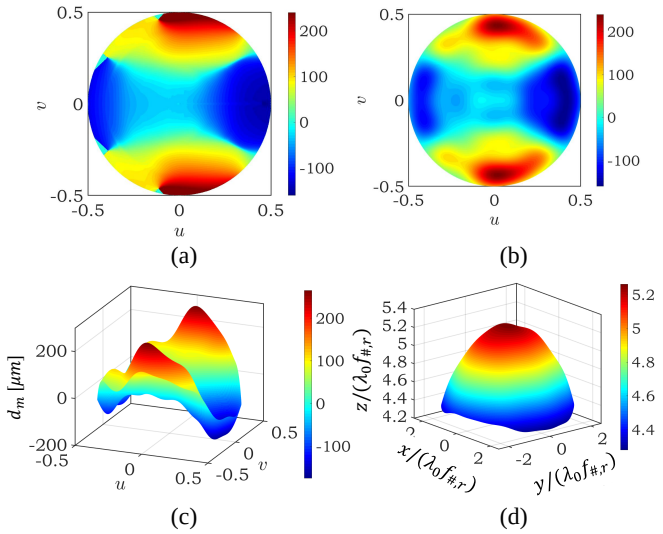

Figure 4.8: Shaping the surface of the lens element scanning 43.75 beams. (a) The phase needed to be compensated, i.e. the hologram phase. (b) The Zernike expansion of the hologram phase using 30 by 30 order polynomials. (c) The required modification on the lens surface. (d) The elliptical + modification shape of the lens.

$$N_{max}^3 = 3.15\sqrt{\frac{D_r}{\lambda_0}}\frac{\sqrt[3]{f_{\#,r}}}{2} \tag{4.11}$$

In Fig. 4.5, this region is marked with an orange color. Within this region, the proposed optimum lens based array is synthesized using the design steps described in this subsection. As expected, at the edge of this region, the array exhibits about 0.5dB of scan loss.

4.4.4 Region 4: Non-Homogeneous Array with Shaped Lens Surface

For elements farther away than N_{max}^3, see (4.11), the CFO spectrum cannot be matched with a translated non-symmetric Gaussian lens feeder. Fig. 4.6(d) shows a significant difference in phase distribution between the two, leading to about 5dB scan loss for this case. To improve this scan loss, one can reshape the surface of the lens to remove the higher order phase terms on the lens CFO. Specifically, the difference between the phase of the elliptical lens CFO spectrum and the translated non-symmetric Gaussian lens feeder, referred to as the hologram phase, is approximated by a Zernike expansion [92], [93], also described in Appendix C. The surface of the elliptical lens is then modified using the following expression:

$$d_m(\rho, \phi) = \frac{Z_h(\rho, \phi)}{k_{dz} - k_0} \tag{4.12}$$

where d_m is the modification of the height of the lens; ρ and ϕ represent positions on the lens surface;

Z_h is the Zernike approximation of the hologram phase (see Appendix C); and $k_{dz} = k_d \cos\theta_l$ is the z-component of the wave-vector in the lens material.

In the region outside the one identified by (4.11), the proposed optimum lens based array is synthesized according to the design steps described in this subsection using enlarged lens elements with modified elliptical surfaces. The scanning performance of this array is shown in Fig. 4.5 (blue line).

As an example case, the surface of a lens element located at $\vec{\rho}_{f,r} = 43\lambda_0 f_{\#,r}\hat{x}$ is considered. The hologram phase, its approximation by a $Z_{M=30}^{N=30}$ Zernike expansion, the needed height modification, and the shape of this lens are shown in Figs. 4.8(a) to (d), respectively. The discontinuities in the phase hologram are due to the numerical artifact caused by the 2-D phase unwrapping algorithm [94], but they are not considered in the generated lens surface. The required modification of the lens surface is within the specifications given by commercial silicon micro-machining companies such as [95]. By reshaping the surface of this lens element, its scan loss is improved from 5 to 1 dB.

4.4.5 Validation of the Methodology

In this subsection, the coupling of the described Quasi-Optical system calculated using the proposed methodology is compared to the one obtained by performing a PO analysis that exploits the reciprocity of the problem and studies it in transmission. In particular, the field radiated outside the lens antenna is obtained by using an in-house developed PO formulation similar to the one described in [70]. Depending on the array element under study, the lens surface is either elliptical or modified elliptical as shown in Fig. 4.8. According to the size of the lens element and its distance from the parabolic reflector, the field is calculated in the lens radiative near field or in the far field region. This field is then provided to the PO solver of GRASP [53] as a tabulated source illuminating the parabolic reflector, to obtain the field radiated by the entire Quasi-Optical system. In the proposed CFO method, the first-order PO diffraction effects are taken into account; while in GRASP simulation, the diffraction contribution from the edges (using PTD method) are also included.

Table 4.2 compares the aperture efficiency, evaluated with both methods for the four considered examples in Fig. 4.6. The same excellent agreement can be observed in Fig. 4.9, where the radiation patterns of the complete Quasi-Optical system are shown. Moreover, the scan loss obtained by the PO analysis in transmission is shown with cross marks in Fig. 4.5. Again, the results are very well matched to the ones obtained by the proposed CFO method. It is worth noting, that the CFO derivation provides the lens and feeder geometries with a single calculation that lasts about 4 minutes. In comparison, the PO analysis in transmission takes about 30 minutes in the same computer. Therefore, this second analysis procedure would lead to very long elapsed times to find the optimal lens geometry using iterative simulations. All the simulations were performed by using a single core Intel i7–4790 processor with a clock frequency of 3.6 GHz, Cache and RAM memory of 10MB and 16GB, respectively.

4.4.6 Conclusion

Imaging systems at millimetre and sub-millimetre wavelengths are entering a new era with the development of large format arrays of detectors. A fly's eye lens array coupled to absorbers or antennas is a common FPA architecture for such imagers. Typically, such FPAs are coupled to a Quasi-Optical (QO) system involving reflectors. For such large QO systems, a full-wave electromagnetic analysis of the entire

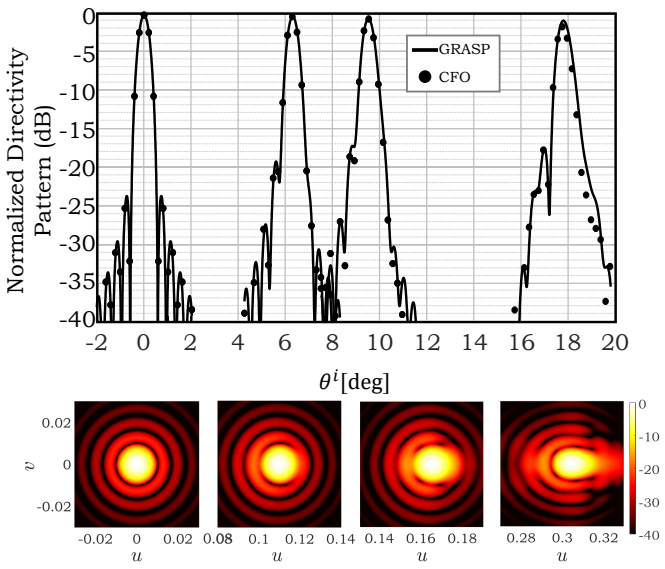

Figure 4.9: Radiation pattern of the lens antenna elements coupled to the parabolic reflector ($\phi^i = 0°$). These elements are scanning broadside ($\theta^i = 0°$), 15.5 beams ($\theta^i = 6.3°$), 23.5 beams ($\theta^i = 9.5°$), and 43.75 beams ($\theta^i = 17.76°$). The solid lines, and dot marks represent the pattern obtained in transmission by using PO, and reception by using the proposed method, respectively. The former and the inset, illustrating the pattern in the u-v plane, are calculated by using GRASP.

Table 4.2: The Aperture Efficiency of the Array Elements

	Sec. 4.4.1 Broadside	Sec. 4.4.2 15.5 beams	Sec. 4.4.3 23.5 beams	Sec. 4.4.4 43 beams
Proposed CFO method	80.0%	75.8%	72.8%	67%
GRASP	78.8%	75.4%	70.7%	64.2%

system is not applicable since it is numerically cumbersome and time-consuming. This chapter focuses on a scenario involving a lens based Focal Plane Array (FPA) with diffractive coupling to a primary focusing component. The technique described in Chapter 3, Coherent Fourier Optics (CFO), can be used to assess the scanning performance of such large format lens based FPAs. In particular, by using the developed analysis tool, it was shown that a scan loss lower than the one of the direct field (given by standard formulas in the literature) can be achieved for a wide-angle optics coupled to a lens based FPA. The proposed array is synthesized according to the described design rules, namely field matching between the CFO spectrum and the far field of the lens feeder. It is worth noting that in this design process no numerical optimization algorithms were employed and the methodology provides the exact optimal solution in terms of scan loss. Here, scan loss of less than 1dB has been achieved while scanning up to ±17.5° for an example relevant to the state-of-the-art wide-angle imaging systems with reflector f-number of 2 and directivities of 52dBi. The proposed technique has been validated via a standard Physical Optics based analysis in transmission with excellent agreement.

Chapter 5

A Quasi-Optical System with 3 to 1 Bandwidth Ratio for the ASTE Telescope

DESHIMA 2.0 *is a spectrometer for astronomical applications targeting known point sources at sub-mm wavelengths from* 240 *GHz to* 720 *GHz. The system will be installed in the ASTE telescope at Atacama Desert, Chile. In this chapter, a Quasi-Optical system based on a hyper-hemispherical leaky lens antenna and a series of Dragonian reflectors is presented as coupling chain for the EM radiation captured by the telescope into the detector. The design procedure is based on a field matching technique in reception. Specifically, the ASTE telescope is modeled by a single equivalent on-axis parabolic reflector which is illuminated by an incident plane wave. This plane wave is scattered by the reflector, propagates into the integrated lens and couples to the antenna terminals. By employing this methodology, the performance of the design is rapidly optimized over the whole* 3 : 1 *bandwidth ratio. The achieved average illumination efficiency over the band is approximately* 70%. *The directivity patterns in the sky are also estimated. The side lobe, and cross-polarization levels, over the whole frequency band, are below* −16*dB, and* −18*dB, respectively.*

5.1 Introduction

Far infrared astronomy considers radiation roughly from 50 GHz to 10 THz, which is emitted by cold, distant and often optically dark objects in the universe. Important examples of such objects are dust, gas and far away galaxies. Often these galaxies are also dust-rich environments, therefore, they are almost completely invisible in optical wavelengths. An important tool for observation of these objects is ultra-wide band spectroscopy. Until recently, this tool was technologically inaccessible. In recent years, efforts toward designing broadband on-chip spectrometers have been pursued. DESHIMA 1.0 [38] is a terahertz spectrometer based on a single superconducting chip with a bandwidth ratio of 1.14 : 1 (13%). This instrument achieved its first-light campaign on the ASTE telescope in 2017 [37]. Moreover, a similar instrument with a bandwidth ratio of 1.7 : 1 (38%) has been demonstrated in [96]. In these systems, an on-chip filter bank from superconducting material divides the radiation into narrow spectral bands. Behind each filter is an individual Microwave Kinetic Inductance Detector (MKID), that detects the radiation only in its designated spectral band [97].

DESHIMA 2.0, a follow up on DESHIMA 1.0, is an on-chip spectrometer based on direct-detection using MKIDs at sub-mm wavelengths. The system is being developed as a collaboration between the Delft University of Technology and the Netherlands Institute for Space Research (SRON). DESHIMA 2.0 aims at analysing astronomical sources from 240 GHz to 720 GHz with a bandwidth ratio of 3 : 1 (100%). The system will host 550 MKIDs and will be installed at the Atacama Sub-millimeter Telescope Experiment (ASTE) in Chile. The first implementation of DESHIMA 2.0 will have a reduced bandwidth ratio of 2 : 1, analysing sources from 220-440 GHz and will be installed in the ASTE telescope in Chile at the end of 2020. A later upgrade will use the full 240-720 GHz bandwidth.

In order to comply with the requirements of the instrument, a wide band antenna with 3 : 1 bandwidth ratio is required. At millimetre wavelengths, designs with stable wide band performance have been demonstrated using coupling elements such as: quadruple-ridged flared horns [98], and eleven antenna [99]. These elements achieve good coupling performance to the optical system, i.e. average illumination efficiencies above 65% over a large bandwidth ratios of 4 : 1 (excluding the impedance matching efficiency). However, both elements cannot be integrated into a chip design. Machining and assembly of a flared horn operating at sub-mm wavelengths is also yet to be achieved. Moreover, matching the eleven antenna's impedance to its load at sub-mm wavelengths is proven difficult. A relatively narrow band solution, with respect to the application under consideration, is the corrugated horn antennas operating at sub-mm wavelength, such as the ones described in [100]. These elements achieve stable performance (average illumination efficiency of 80% excluding the dielectric and reflection losses over the intermediate lens component) over bandwidth ratio of 1.8 : 1. In more relevant works, solutions such as the connected array of leaky slots [101], or the focused connected array [102], are proposed. In these cases, in order to realize the feeding network, microstrip technology at sub-mm wavelengths is required. This technology is currently under development. New techniques such as [103] are introduced to assess the loss in the dielectric for these microstrip feeding networks at sub-millimetre wavelengths. Despite these complications, such designs show promising performances. In particular, the connected array of leaky slots achieved an average illumination efficiency of 70% over a bandwidth ratio of 3 : 1 (excluding the lens reflection efficiency, impedance matching, and losses in the feeding network). On the other hand, the focused connected array achieved an average illumination

efficiency of 60% over the same relative bandwidth (excluding the losses in the feeding network).

In this chapter, a single lens antenna element coupled Quasi-Optical system has been proposed to receive the incoming electromagnetic radiations at the corresponding 3 : 1 frequency bandwidth ratio. Specifically, a wide band design which consists of a hyper-hemispherical leaky lens antenna coupled Quasi-Optical system is presented, Fig. 5.1(a). The integrated hyper-hemispherical lens is a particular variation of the extended hemispherical lens [104]. Its geometry consists of a hemispherical surface with radius R_s and an extension length $L_e = R_s/\sqrt{\varepsilon_r}$. Here ε_r is permittivity of the lens material. This lens has a virtual focus behind its apex at $F_v = R_s(1 + \sqrt{\varepsilon_r})$. The lens feeder is placed at its focal plane as shown in Fig. 5.1(b).

The lens feeder is a tapered leaky slot, similar to the one described in [70] where a leaky radiation phenomena is achieved by introducing an air gap distance of h_g between the slot and the lens base [105]. The geometry of this tapered slot is shown in Fig. 5.1(c). The leaky slot antenna element is a good candidate for feeding dielectric lenses in a wide-band application [105, 106]. This antenna shows an effective illumination of the top part of the lens over multi-octave bandwidth as well as a good impedance matching performance. As described in [70], tapering the slot with an angle γ leads to better cross-polarization rejection by the antenna, as well as reducing the level of the leaky wave peak with respect to the radiation in broadside direction. By reducing the air gap distance, h_g, one can improve the front to back ratio of the antenna as well as its cross-polarization level. In this work, the base-line design for the leaky slot antenna is similar to the one described in [70]. However, to further decrease the cross-polarization level, the slot tapering angle is increased from $\gamma = 15°$ to $35°$.

The proposed design is specifically tailored for the DESHIMA 2.0 spectrometer. The performance of this design in terms of the aperture efficiency and directivity patterns is reported in this chapter. The leaky lens antenna is fabricated and the preliminary measurement of the system is also presented. In this measurement, the beam pattern of the system at the lower frequencies of the band is determined. This beam pattern is obtained directly from the response of the super conductive Kinetic Inductance Detectors coupled to the antenna.

In comparison to a connected array of leaky feeders without a lens component [102], a single leaky lens design does not require long sub-micron feeding lines which leads to much simpler fabrication process. However, a broad band AR coating, which creates assembly and integration complexities, is required for the leaky lens.

In order to design the proposed geometry, firstly the ASTE QO system is modeled by a single on-axis parabolic reflector to speed up the optimization process. Secondly, the developed Geometrical Optics (GO) codes, discussed in Sec. 2.3 and more in details in Appendix B, are employed to analyse the equivalent QO system, Fig. 5.1(a). Specifically, 1) the reflector is illuminated by a plane wave, the field scattered by the reflector are propagated to the lens surface. 2) These fields are then transmitted into the lens surface up to a equivalent sphere centered at the lens focus (see Fig. 5.1(b)). These two steps are executed using GO codes, and the analysis method is referred to in this chapter as the GO method. Since the lens surface is in the diffractive region of the reflector at lower portion of the bandwidth of operation, as estimated using the discussion on 3D FO applicability region in Sec. 3.3, a Physical Optics (PO) code is also employed to obtain the fields scattered by the reflector on the lens surface (step 1), while step 2 is performed using the same GO code as before. In this chapter, this method is referred to as the PO-GO method. The far field of the feeder inside the lens is simulated assuming a semi-infinite dielectric slab using CST MWS [79]. The performance of the optimized design is compared to the

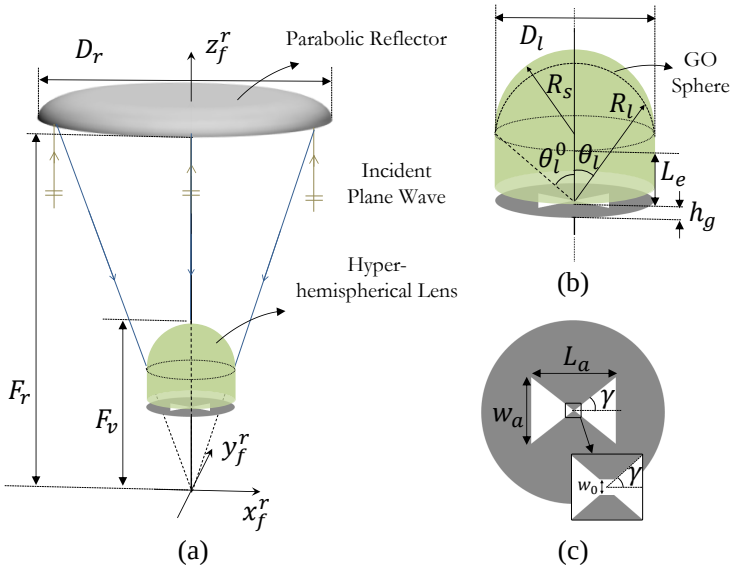

Figure 5.1: (a) Schematic representation of the imaging scenario in reception. A parabolic reflector illuminated by a plane wave arriving from broadside direction. A hyper-hemispherical leaky lens is placed above the focal point of the reflector. (b) Detailed illustration of the hyper-hemispherical lens, and (c) the tapered leaky slot.

results obtained from GRASP [53] using equivalent QO system or the full ASTE system with excellent agreement.

The chapter is structured as follows. The actual DESHIMA 2.0 QO system and an equivalent optics model of the system are described in Sec. 5.2. Section 5.3 describes the steps taken in the design process of the system. The field matching technique, discussed in details in Sec. 2.5, is used in this section. Moreover, the optimization process is described in this section. In Sec. 5.4, the performance of the equivalent model and the DESHIMA 2.0 Quasi-Optical system are evaluated and validated. In Sec. 5.5, the preliminary beam pattern measurements of this QO system is presented. Section 5.6 contains some concluding remarks.

5.2 ASTE Quasi-Optical System

In this section, the full ASTE Quasi-Optical system and the equivalent optics used for optimization are presented. As shown in Fig. 5.2, the main components of the system consist of the hyper-hemispherical leaky lens, two off-axis parabolic reflectors placed inside a cryostat (cold optics), and a Dragonian Quasi-Optical system [90] and [107], where the paraboloid primary mirror is exchanged by an ellipsoidal primary (warm optics). The cold optics mirrors are cryogenically cooled to 4 K (−269° C), while the warm optics are at the room temperature. These components are placed inside the cabin of ASTE telescope and are coupled to its Cassegrain system. The primary and secondary mirrors of this Cassegrain system are a parabolic dish with a diameter of 10 m, and a hyperbolic mirror with a diameter of 62 cm, respectively.

One can describe geometrically the radiation scenario in this structure as follows. By placing a

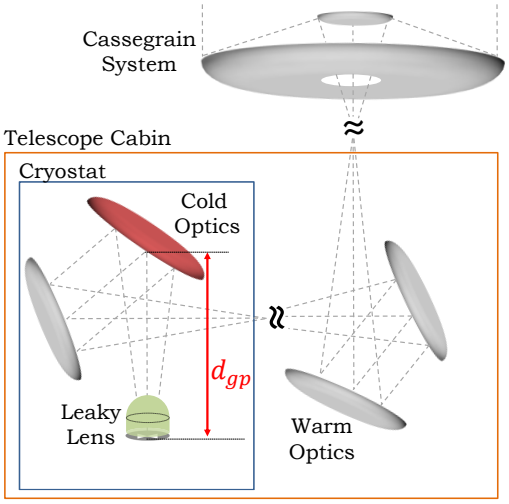

Figure 5.2: The schematic representation of the DESHIMA 2.0 optical system at ASTE telescope, including: the leaky lens antenna, two off-axis parabolic reflectors inside the cryostat; a Dragonian system with an ellipsoid primary and a hyperboloid secondary mirror inside the ASTE cabin; and the Cassegrain system of the telescope.

point source at the focus of the hyper-hemispherical lens, diverging rays are generated outside the lens which propagate from a virtual focus at a distance F_v from the lens apex. By placing this lens at a F_v distance above a parabola's focal point, the reflector is effectively illuminated by a point source placed at its focus. Due to the large size of the lens and its displacement from the focus of the reflector, the radiation phenomena in the hyper-hemispherical lens coupled reflector is geometrically limited. As the result, this concept, leads to a more stable performance over frequency in comparison to the typical diffraction limited lens antennas which are located at the focus of the reflector as in [70].

In the described geometry, part of the optical system is inherited from DESHIMA 1.0, specially the cryostat geometry. As the result, the diameter of the two cold optics parabolic reflectors could not be altered. However, their f-numbers could be modified. Moreover, the warm optics is also kept as the one of DESHIMA 1.0 for simplicity. Finally, the distance between the antenna ground plane and the first cold optics mirror, d_{gp} in Fig. 5.2, is also fixed. These limitations are marked with red color in this figure.

Performing an optimization procedure over the whole ASTE Quasi-Optical system is time consuming. In order to speed up this procedure, this system is modeled using a single parabolic reflector, Fig. 5.1(a). The parameters of this equivalent optics, namely its diameter and f-number, should be chosen in such a way to approximate the ASTE optical system. The first cold optics mirror is over dimensioned with respect to the first (and limiting) aperture stop inside the cryostat. Since the diameter of this mirror can not be modified, the diameter of the equivalent optics is chosen equal to the diameter of this mirror without over-dimensioning. Moreover, the f-number of the equivalent optics is kept as an optimization parameter for the new design.

5.3 Design Methodology

In the following sub-sections, the design and optimization procedure, of the described structure is discussed.

5.3.1 Reception Analysis: Field Matching Technique

To analyse the scenario of Fig. 5.1(a) in reception, we assume that a plane wave illuminates the parabolic reflector from broadside direction. By resorting to a GO code, similar to the one described in Appendix B, the EM field at the lens surface, $\vec{E}_l^i$ and $\vec{H}_l^i$, scattered by the reflector, can be calculated. The direction of propagation of the EM radiation into the lens surface is determined by Snell's law. In this chapter, this method is referred to as the GO method. As a validation procedure, these fields are also calculated using a PO code. In this case, the Poynting vector associated to these fields, i.e. $\vec{S}_l^i = 0.5\vec{E}_l^i \times (\vec{H}_l^i)^*$, determines the direction of propagation into the lens surface. In this chapter, this method is referred to as the PO-GO method.

By using another GO code, the incident fields at the lens surface are propagated into the lens up to the surface of a sphere centered at the antenna's position. This sphere is indicated in Fig. 5.1(b), and referred to as the GO sphere (similar to FO spheres in previous chapters). The field at the surface of this sphere, $\vec{E}_l^{GO}(\theta_l, \phi_l)$, is referred to as the GO field. By knowing this field and resorting to antenna in reception formulations [64], [65], and detailed in Sec. 2.5, the coupling mechanism between the Quasi-Optical system and an antenna can be analysed. In particular, the power delivered to the load of the antenna, P_{load}, in the focal plane can be calculated using (2.18). Here θ_l^0 is the maximum rim angle of the lens, θ_l and ϕ_l are the angular parameters representing the GO sphere, and R_l is its radius; $\vec{E}_a^{FF}$ is the far field radiated by an antenna evaluated at the same GO sphere; $P_{rad} = 1/(2\zeta_d)\int_0^{2\pi}\int_0^{\pi}|\vec{E}_a^{FF}(\theta_l, \phi_l)|^2(R_l)^2 \sin\theta_l d\theta_l d\phi_l$ is the total power radiated by the antenna in the far field when it is operating in transmission; and ζ_d is the wave impedance in the dielectric.

After computing the power delivered to the load, one can estimate the aperture efficiency of the imaging system in reception as in (2.20). As discussed in Sec. 2.5, in order to maximize the aperture efficiency of the system, the far field radiated by the antenna, $\vec{E}_a^{FF}$, should be matched to the incoming GO field, $\vec{E}_l^{GO}$. The described aperture efficiency is divided into two contributions. The one related to the lens antenna performance, i.e. the feeder efficiency (see (2.21)), and the contribution related to a proper illumination of the reflector, i.e. the illumination efficiency (see (2.22)).

In this work, the described field matching technique is employed to design a leaky lens antenna coupled reflector. The goal of the design is to maximize the averaged aperture efficiency of the system over its frequency bandwidth.

5.3.2 Incident Geometrical Optics Field

As discussed in Sec. 5.3.1, to maximize the aperture efficiency of the structure, the incoming GO field should be matched to the far field of the antenna. In this sub-section this GO field is discussed.

Let us consider an example scenario based on the equivalent optics, described in Sec. 5.2, with the following geometrical parameters. The operative bandwidth is defined as 240 GHz to 720 GHz. The

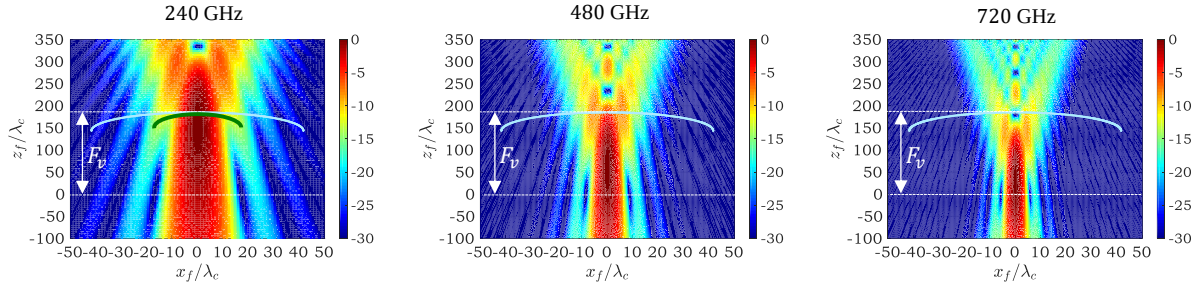

Figure 5.3: Field at the surrounding of the focal point of a reflector with $f_{\#,r} = 7$. The focal point is indicated by ($x_f = 0$, $z_f = 0$) position. At frequency of (a) 240 GHz, (b) 480 GHz, (c) and 720 GHz. The surfaces of a hyper-hemispherical lens with diameter of $D_l = 83\lambda_c$ and $32\lambda_c$ are shown with light blue and green curves, respectively. The distance of the lens apex from the reflector focus, in both lens cases is $F_v = 180\lambda_c$.

f-number of the reflector is chosen equal to 7. Its diameter is $D_r = 82.3\lambda_c$, where λ_c is the wavelength at the center of the frequency band, 480 GHz, in free space. As mentioned before, this reflector is illuminated by a plane wave from broadside direction. At 3 frequency points over the 3 : 1 bandwidth ratio, the fields scattered by the reflector surrounding its focal point are shown in Fig. 5.3. As it can be seen, over the 3 : 1 bandwidth ratio, the dimension of the spot size varies significantly. When a hyper-hemispherical lens is located above the focal point of the reflector, the field generated by the reflector and intercepted by the lens surface is a combination of geometrical and diffraction contributions.

5.3.3 Optimization Procedure

To match the GO field at the GO sphere inside the lens to the far field of the leaky slot, a hyper-hemispherical lens with virtual focus distance, F_v, close to the depth of focus of the reflector at the center of the band is considered. By optimizing the lens diameter, one can further improve this field matching.

As an example, let us assume the following geometry. The described equivalent parabolic reflector is illuminated by a plane wave with unitary amplitude from broadside. A hyper-hemispherical lens is displaced from the focus of the reflector by a distance of $F_v = 180\lambda_c$. Assuming a full hemisphere lens, $f_{\#,l} \simeq 0.5$, and by using the geometrical definition of a hyper-hemispherical lens, the diameter of the lens is related to the displacement as $D_l = (2F_v)/((1 + \sqrt{\varepsilon_r}))$. Therefore, in this example, the diameter of the lens would be $83\lambda_c$.

In Fig. 5.4(a), at the central frequency, the co-polarized GO field evaluated at the GO sphere of the lens, $E^{GO}_{l,co}$, solid and dotted blue curves, is compared against the co-polarized far field of the leaky antenna, $E^{FF}_{a,co}$, solid and dotted black curves. As it can be seen, the two fields are not well matched. As result, the aperture efficiency of this structure would be low. To improve the field matching, one could reduce the diameter of the lens from its geometrical definition. As an example, the GO field for a lens with a diameter $D_l = 32\lambda_c$ is also shown in Fig. 5.4(a), solid and dotted green curves. This figure illustrates a significant improvement in the amplitude field matching between GO incident field and antenna far field by changing the lens diameter. However, by reducing the lens diameter, the spill-over

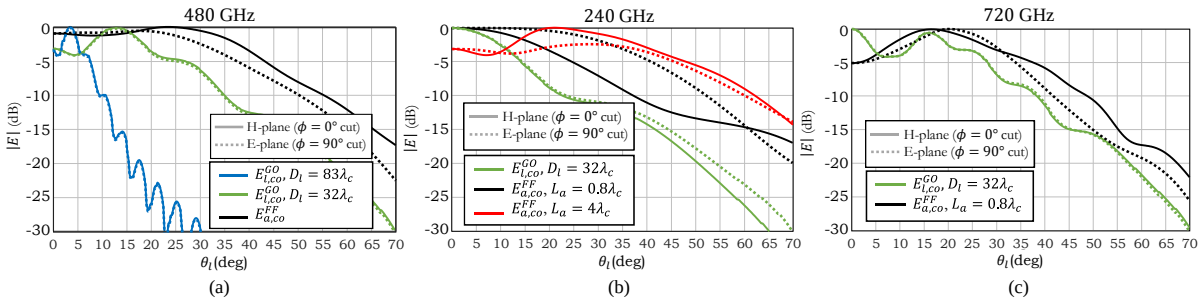

Figure 5.4: Magnitude of the co-polarized incident GO field radiated inside a hyper-hemispherical lens evaluated at its GO sphere, $E^{GO}_{l,co}$, compared against the magnitude of the co-polarized far field of leaky antenna, $E^{FF}_{a,co}$. (a) At center frequency (480 GHz) where the amplitude field match is improved by reducing the lens diameter. (b) At beginning of frequency band (240 GHz), where the amplitude field match is improved by reducing the length of the leaky slot. (c) At the end of the 3 : 1 frequency bandwidth ratio (720 GHz).

efficiency of the incident field on the lens surface is reduced. As the result, one can identify a trade-off between the amount incident field power spilled over the lens surface and the amplitude field matching by altering the diameter of the hyper-hemispherical lens.

In Fig. 5.4(b), at the beginning of the frequency band, the GO field for a lens with $D_l = 32\lambda_c$, solid and dotted green curves, is compared to the antenna far field with slot length of $L_a = 4\lambda_c$, solid and dotted red curve. As it can be seen, and predicted from Fig. 5.3(a), at low frequencies, the GO field is already focused toward the broadside direction. Therefore, the GO and leaky far field at low frequencies are not well-matched. In order to improve this matching, the slot length is decreased to $L_a = 0.8\lambda_c$. By doing so, only at low frequencies the antenna behaves as a resonant slot. The far field radiated by such antenna is maximum at the broadside direction as shown in Fig. 5.4(b), solid and dotted black curves. This step leads to better amplitude field match at the beginning of the frequency band.

By using the lens with smaller diameter, and leaky slot with shorter length, in Fig. 5.4(c), at the end of the frequency band, the GO field, solid and dotted green curves, is compared to the antenna far field, solid and dotted black curves. As it can be seen, the two fields are already well matched at this portion of the bandwidth.

In summary, the performance of a hyper-hemispherical leaky lens antenna coupled parabolic reflector can be optimized using the following lens parameters: the displacement from focus of the reflector, F_v, diameter, D_l, and extension length, L_e. By modifying the first two, the amplitude field match is achieved. By changing the extension length, one can phase match the antenna far field to the one of the incoming GO field. By choosing the optimized value for these three parameters, one can maximize the average aperture efficiency over the full bandwidth. However, as discussed in Sec. 5.1, in DESHIMA 2.0 optical system, the distance between the antenna ground plane and the first cold mirror, d_{gp}, is fixed. Therefore, instead of changing the virtual focus distance, F_v, the f-number of the first cold mirror is altered.

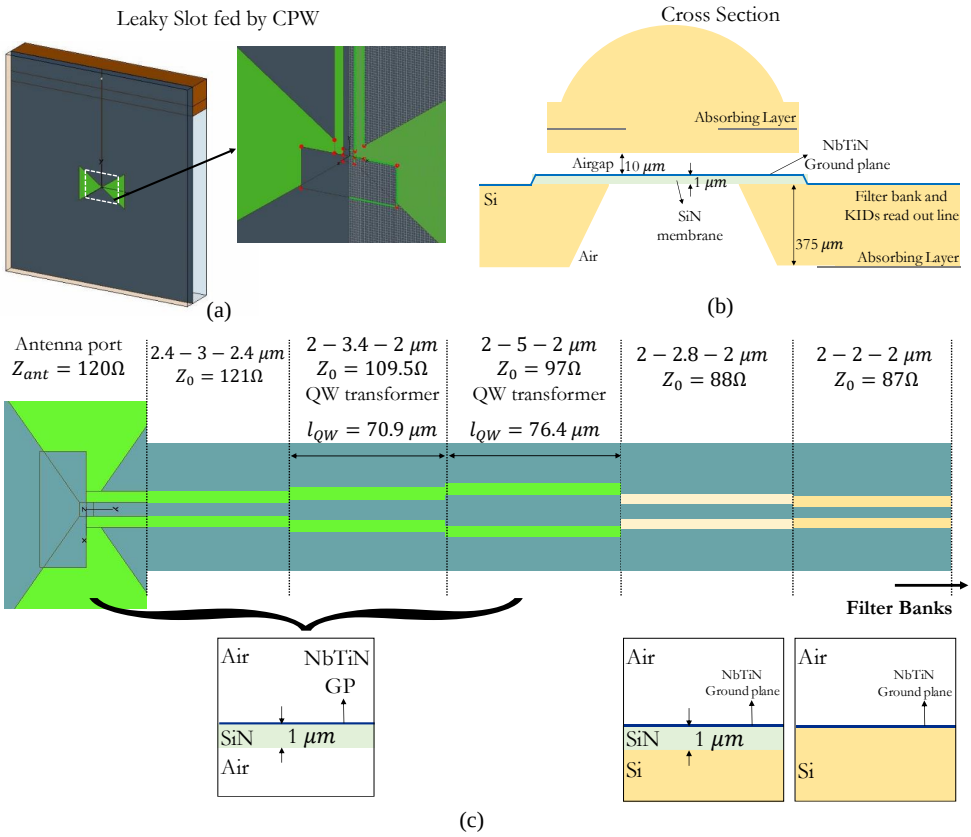

Figure 5.5: (a) Geometry of the leaky slot antenna fed by a CPW line. (b) Cross section of the leaky lens antenna with detailed description of the stratification presented in the chip. (c) A detailed illustration of the CPW feeding line which connects the antenna to the filter banks. Two Quarter Wavelength (QW) transformers are used to match the impedance of the two sides over a wide bandwidth of operation. The insets in (c) indicate the stratification for each CPW line.

5.4 Performance of the Optimized Structure

In this section, the performance of the optimized wide-band Quasi-Optical system is reported. The optimized parameters are the following: lens diameter of $D_l = 38\lambda_c$, reflector f-number of $f_{\#,r} = 7$, corresponding to $F_v = 185\lambda_c$, and lens extension length of $L_e = 5.22\lambda_c$ which is slightly shorter than the geometrical definition for the extension length of a hyper-hemispherical lens, $L_e = R_s/\sqrt{\varepsilon_r}$, to compensate for the phase center position of the feeder with respect to the lens focal point.

Based on the discussion related to Fig. 5.4, the geometrical parameters of the tapered leaky slot are slightly altered from the previous design in [70]. These parameters are the following: slot length, $L_a = 0.8\lambda_c$; tapering angle, $\gamma = 35°$; the air gap distance between the lens and the slot ground plane, $h_g = 0.016\lambda_c$; the initial width and the end width of the slot are $w_0 = 0.005\lambda_c$, and $w_a = 0.56\lambda_c$, respectively. The leaky slot is fed by a Co-Planar Waveguide (CPW) line as shown in Fig. 5.5(a). The cross section of the lens antenna is shown in Fig. 5.5(b). The detailed geometry of the CPW line connecting the antenna to the filter banks is shown in 5.5(c). The characteristic impedance of each CPW line is indicated by Z_0 in the figure. Moreover, the $w1$-$w2$-$w1$ formatted dimensions given in μm indicate the width of the slots

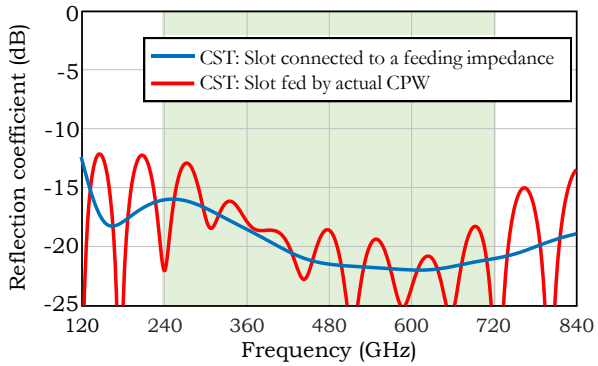

Figure 5.6: Reflection coefficient at the antenna terminals. The blue and red curves indicate this reflection coefficient at the antenna terminals connected to a single value equivalent feeding impedance (120Ω), and to the realized feeding network shown in Fig. 5.5(c), respectively.

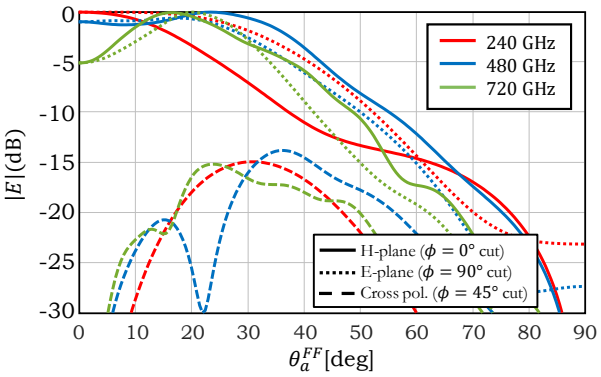

Figure 5.7: Far field patterns of the optimized leaky slot feeder inside the silicon hyper-hemispherical lens, evaluated at 3 frequency points in the 3 : 1 frequency bandwidth ratio.

($w1$) and the strip line ($w2$) for each CPW line. The ground plane of this structure is made of NbTiN with surface inductance of 1pH, and the 1μm thick SiN membrane has a permittivity of $\varepsilon = 7$. In Fig. 5.6, the reflection coefficient of this feeder is shown with excellent impedance matching over the desired bandwidth (green shaded region). The far field of this feeder inside the lens over 3 : 1 bandwidth ratio is also shown in Fig. 5.7.

In Fig. 5.8(a), the aperture efficiency of the optimized design below a single reflector, which is analyzed in reception, is shown. As it can be seen in the figure, the match between the results obtained via the proposed GO or PO-GO method is good. As expected, as the geometry becomes larger in terms of the wavelength (at the higher portion of the frequency band), the GO method matches better to the PO-GO method. In Fig. 5.8(b), the aperture efficiency of the optimized design obtained in reception is compared against the described PO based analysis performed in transmission when considering a single parabolic reflector or the DESHIMA 2.0 Quasi-Optical system. In this figure, the results for the equivalent optics model and the full optical chain modeled in GRASP [53] are compared to the PO-GO method with very good agreement. The discrepancies between the results from the equivalent model and the full optics model are due to the fact that the whole QO chain was modeled by only one

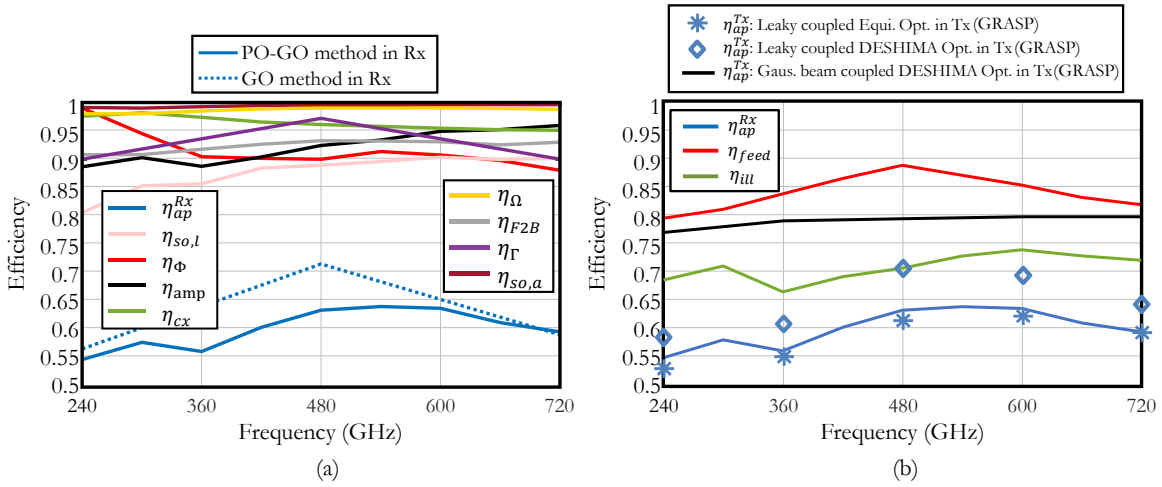

Figure 5.8: (a) Aperture efficiency and other sub-efficiency terms for equivalent optics using GO and PO-GO methods in reception. (b) Aperture, feeder, and illumination efficiencies of the equivalent optics evaluated in reception. The cross and diamond marks indicate the aperture efficiency of the equivalent optics and QO system of ASTE, respectively, which both are analysed in transmission mode using GRASP. The efficiency terms reported here are described in Sec. 2.5, (2.20)-(2.22).

parabolic reflector to speed up the optimization. The averaged illumination efficiency of the design is above 70% over the whole 3 : 1 bandwidth ratio. To improve the reflection efficiency at the dielectric-air interface, a broad band matching layer consist of dual layer anti-reflective coating, similar to the one described in [108], is considered on top of the lens. Including the feed losses, an averaged aperture efficiency of 65% is achieved.

For comparison, a Gaussian beam with a comparable tapering angle to the one of the leaky antenna is also simulated as the feeder of the ASTE Quasi-Optical system. As shown in Fig. 5.8(b), the illumination efficiency of the leaky antenna is comparable to the aperture efficiency obtained by assuming a Gaussian beam illumination with −11 dB taper on the sub-reflector rim of the optics (in that case the feeder is assumed to be loss-less).

Moreover, in Fig. 5.9, the patterns of the designed QO system after the ASTE primary (beam in the sky) are shown for three frequency points over the full frequency band. The side lobe, and the cross-polarization levels of these patterns are below −16dB, and −18dB, respectively. These patterns are simulated in transmission using a PO based code in GRASP.

5.5 Preliminary Measured Beam Patterns

The hyper-hemispherical lens was fabricated and mounted on antenna chip using Perminex glue [109]. A Parylene layer was initially used as the anti-reflection (AR) coating on top of the lens surface. However, in the cool down cycles, this layer cracked in various positions and also broke parts of the silicon lens. Therefore, a lens without any AR coating was fabricated, Fig. 5.10(a), to perform preliminary beam pattern measurements of the QO system. At the moment, a new lens with an AR coating material based on foam layers [110], Fig. 5.10(b), is being prepared for the second measurement campaign.

The performance of the leaky lens antenna coupled to the KID detectors is evaluated in SRON

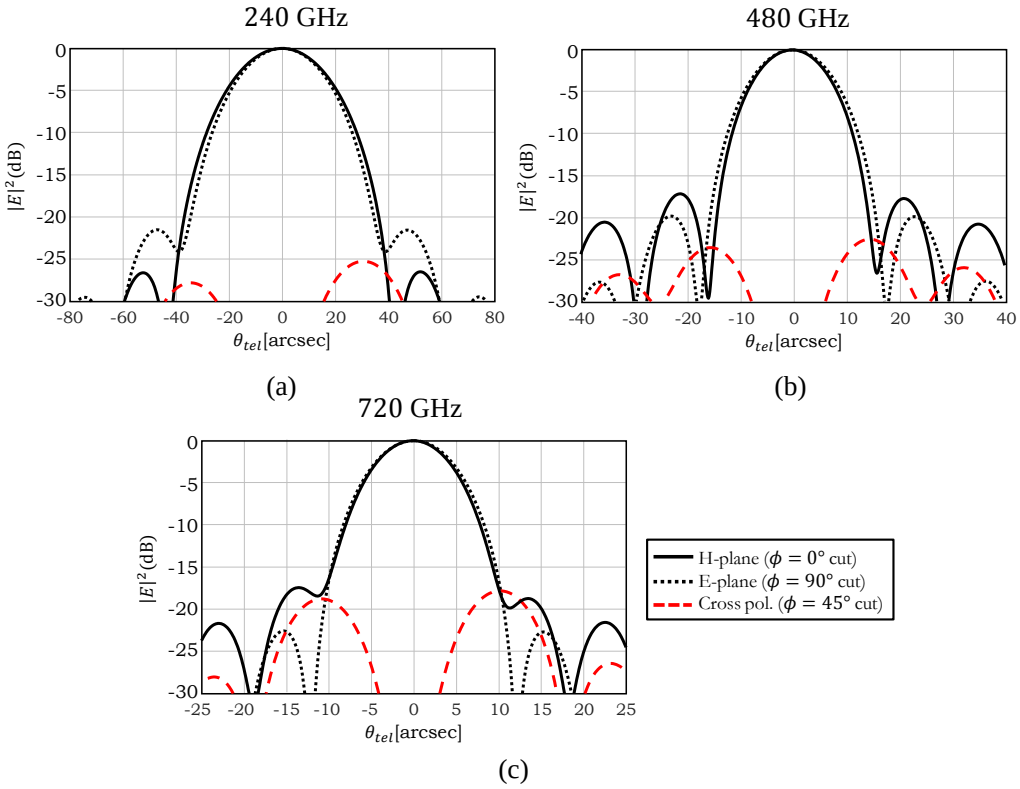

Figure 5.9: Directivity pattern of the leaky lens antenna coupled DESHIMA optics after the telescope main dish, at (a) 240 GHz, (b) 480 GHz, and (c) 720 GHz.

directly using the three-stage measurement setup shown in Fig. 5.10(c). The setup measured complex beam pattern at 234GHz, using two harmonic mixers [112]. The scanned source has an open ended wr04 waveguide. This source is placed at 23.5 cm from the cryostat. In the cryostat, the integrated lens antenna is located below the two cold mirrors, see the illustration of the cryostat box in Fig. 5.2 and more detailed view in Fig. 5.10(d). A polarizer is also mounted inside the cold box to limit the stray ray propagation into the cold stages. As shown in Fig. 5.10(c), a beam splitter is placed between the source and cryostat window. Half of the power radiated by the source enters into the cryostat and read-out directly by the KIDs. Another half is received by the second measurement antenna for phase locking. A free-standing hyperbolic lens is placed in front of the second antenna to improve its coupling to the source.

A standing wave associated to the scanner was removed by averaging the results from two measurements with quarter wavelength displacement in the direction perpendicular to the measurement plane. However, a second strong standing wave due to absence of an AR coating exists within the lens which was unaffected by the quarter wavelength displacement. This standing wave was avoided by slightly changing the operation frequency. Moreover, a beam tilt of about 2° was observed with respect to the cryostat axis. However, none of the aperture stops, present in the cold box, intercepted the tilted beam. Since the cryostat box is hung from the ceiling of the measurement lab, it is concluded that this beam tilt is due to slight rotation of the cryostat axis with respect to the floor of the lab.

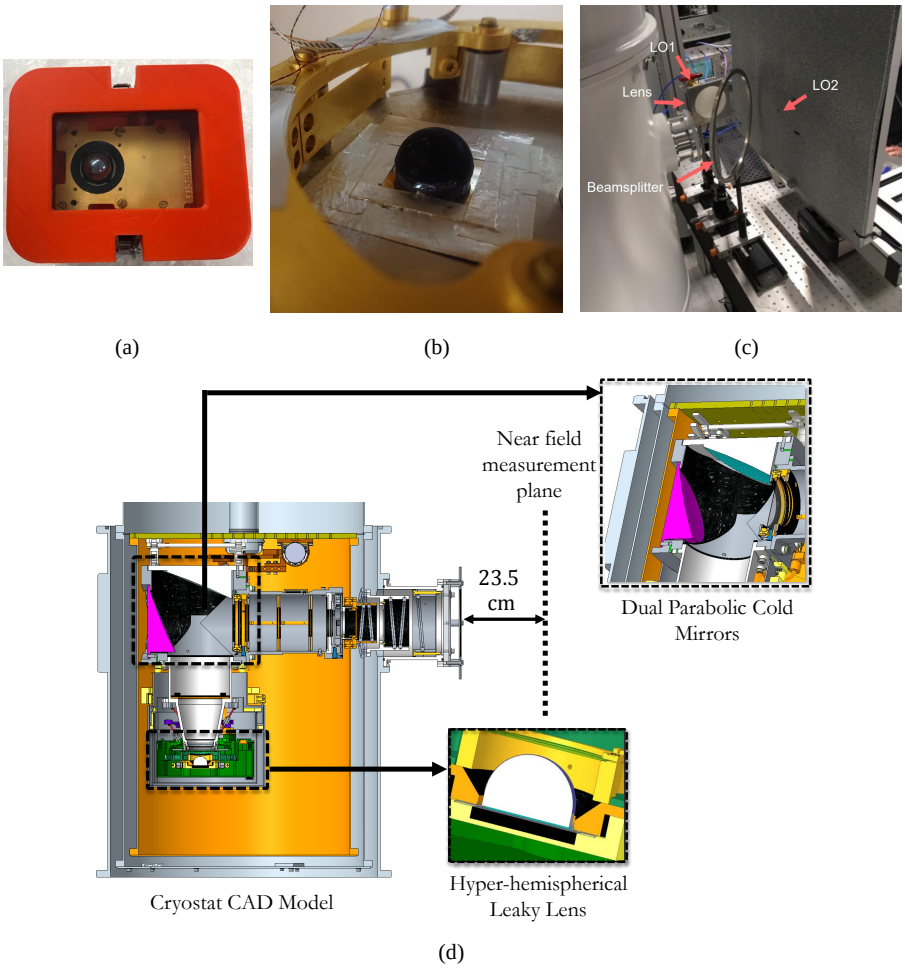

Figure 5.10: (a) Fabricated integrated leaky lens antenna without AR coating. (b) New lens element with AR coating based on foam layers. (c) Measurement setup. (d) Detailed CAD model of the cryostat [111].

The measured complex beam pattern is propagated to a far field sphere, which is centered at the focus of the cold optics. This far field is given to GRASP, as a tabulated source. By using the model of the ASTE telescope and the optics in its cabin (warm optics), this far field is propagated to the telescope primary. In Fig. 5.11, the designed pattern in the sky is compared to the one measured in near field and propagated using GRASP. The beam tilt in the measured data is compensated in the model. As it can be seen, despite the described issues in this measurement, the measured beam pattern is in good agreement with the designed one. In the inset of Fig. 5.11, this beam is also given in u-v coordinates.

5.6 Conclusion

In this chapter, a wideband Quasi-Optical system for the ASTE telescope based on a hyper-hemispherical leaky lens antenna is presented. The lens antenna is optimized to maximize its coupling to a parabolic reflector. The design procedure is based on a field matching technique in reception. The Quasi-Optical

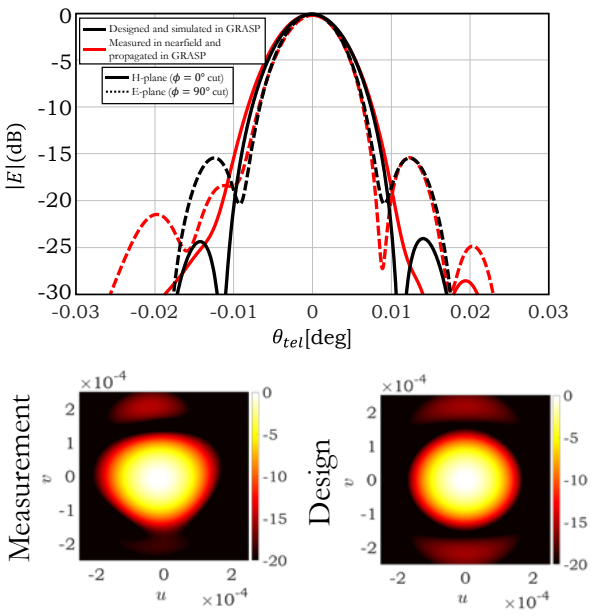

Figure 5.11: Measured (in near field and propagated using GRASP) beam pattern in the sky at 234 GHz compared against the designed one. The inset shows the same patterns in in 2D.

system has an average illumination efficiency over 70% in the whole 3 : 1 bandwidth ratio. Including the feeder losses, an averaged aperture efficiency of 65% is obtained. The pattern in the sky of the system is also simulated in GRASP. The side lobe, and the cross-polarization level of this pattern, over the bandwidth, is below −16dB, and −18dB, respectively. The beam pattern of the system at 234 GHz is presented here with good agreement to the simulated results. DESHIMA 2.0 system will be fully tested in the coming months (the new AR coating is stable in cooling cycle tests).

Chapter 6

Wide Band Wide Scanning Architectures Using Multi Lens Chains

Sub-millimetre imaging systems with wide frequency bandwidth of operation as well as large steering capabilities are required for future security and space imaging applications. In this chapter, a Quasi-Optical (QO) system with multiple refractive components is proposed to achieve these requirements. The system consists of hyper-hemispherical lenses antenna feeders at its focal plane. Double-sided hyperbolic free-standing lenses are then used to link to the rest of QO chain. A fast and accurate method based on Fourier Optics combined with Geometrical Optics is proposed to analyse these types of multi transmitting QO surfaces. The tool is validated against time consuming multi-surface Physical Optics with excellent agreement and orders of magnitude faster execution time. As a result, the proposed method can be used to design and optimize the performance of such QO systems. To demonstrate the capability of the analysis method in designing these architectures, an example case is also presented, and its performance is evaluated. In this scenario, for the central element of the proposed lens based focal plane array, a scan loss of about $1dB$ *is achieved over a* $3:1$ *bandwidth ratio and scanning up to* ± 7 *beams at the center of the operative band.*

6.1 Introduction

As discussed in Ch. 1, in (sub)-millimetre imaging and sensing systems, large Field-of-Views (FoVs) and wide bandwidth are two key improvements in many applications, e.g. in radar systems [36], and passive radiometry systems [22]. Also for astronomical applications, a single pixel wide band spectrometer as designed for DESHIMA 2.0 (see Ch. 5) can be upgraded to a multi-pixel array to create an imaging spectrometer or integral field unit for far infrared astronomy. Such systems exist for optical astronomy [113, 114, 115, 116] but were, until now, difficult to construct for the far-infrared applications. In this chapter a QO architecture that could potentially achieve wide band and wide scanning capabilities is proposed and studied.

The proposed architecture is shown in Fig. 6.1. It consists of a focal plane array whose element is a multiple lens chain. Each of the chains creates a virtual focus at a different location in the focal plane of the main parabolic reflector. This serves for two purposes: enlarging the bandwidth for efficient aperture illumination, and enabling the scanning of the beams in the sky by each of the focal plane array elements. Let us consider the case when the reflector is illuminated by a feeder displaced from its focal plane, such as the ones shown in Fig. 6.1, composed of a hyper-hemispherical lens and a double hyperbolic lens. In this case a nearly geometrically limited and frequency independent field is radiated by the structure. This behavior leads to broadband illumination of the reflector. A similar concept, with a single lens instead, was discussed in Ch. 5. This near field virtual spot can be scanned by putting multiple feeders at the focal plane of the hyper-hemispherical lens or by moving the lens laterally. These scanning capabilities of the proposed QO system are suitable to be integrated with a leaky connected antenna array similar to [22], or with a single leaky antenna coupled to a piezo motor similar to [117]. The former feeder type leads to the generation of multiple simultaneous beams after the reflector associated to each of the chains, while the latter type leads to a steerable beam for each of the chains. As a result, the final system will parallelize multiple chains of these scanning/steerable beams.

It is well known that employing multiple lens surfaces can improve the scanning performance of a QO system [39, 118, 119]. To introduce wide scan capabilities, we also follow a similar reasoning for each of the chains shown in Fig. 6.1, i.e. hyper-hemispherical lens coupled to a double sided hyperbolic free-standing lens. Moreover, in order to efficiently scan beams in such a chain, a field lens, at the focus of the second hyperbolic surface is required. This field lens steers the scanned beams toward the center of the next QO component while not disturbing the broadside beam.

Analysing these multi-lens electrically large geometries using full-wave electromagnetic analysis is not computationally feasible. Moreover, due to the presence of multiple transmitting surfaces close to one another in terms of wavelength, high frequency techniques such as Physical Optics (PO) are also very time-consuming. This chapter presents an analysis technique based on Fourier Optics (FO) combined with Geometrical Optics (GO) to represent the coupling between the antenna based FPA to the rest of the QO system. The proposed technique is a numerically efficient methodology which achieves an accurate representation of the EM fields, while it is orders of magnitude faster with respect to the traditional multi-surface PO analysis. As a result, this proposed methodology enables us to rapidly and accurately design and optimize complex QO systems including multi-lens architectures.

To demonstrate the capability of the analysis tool, an example of a wide band integrated lens with an antenna based FPA is considered here. Similar concept is a suitable candidate for future high frequency

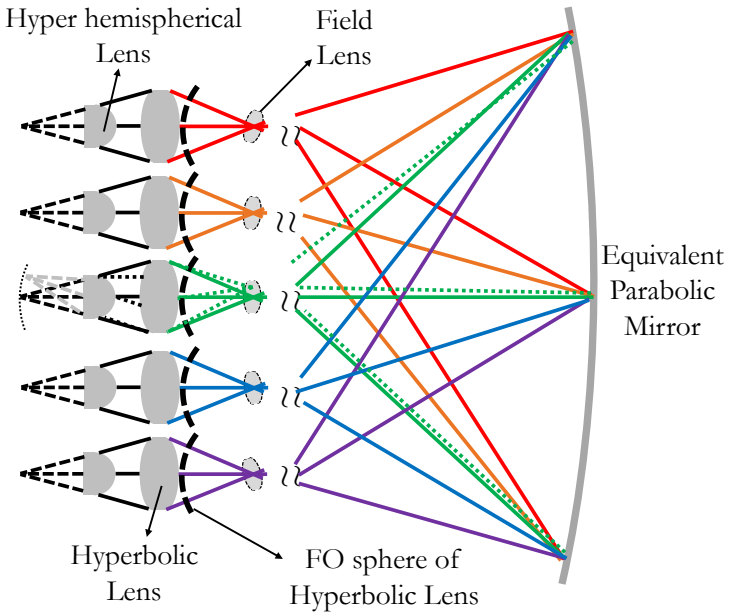

Figure 6.1: Proposed FPA of lenses under an equivalent parabolic reflector. An element in this FPA consists of a hyper-hemispherical lens, a double sided hyperbolic free-standing lens, and a field lens in front. The solid coloured rays correspond to the central beam coming out of each element of the multi-lens FPA, while dotted rays correspond to a scanned beam by the central element of the multi-lens FPA.

imaging and sensing systems such as the Tera-Hertz pulse radar proposed in [36] or as an upgrade to existing wide band single pixel spectrometer in Ch. 5. An example case of the proposed QO system, which corresponds to a single lens chain element in Fig. 6.1, is presented and analysed in Sec. 6.3. In this example scenario, a low (1 dB) scan loss performance over a wide (3 : 1) bandwidth ratio with wide scanning capabilities (±7, 3dB overlapping beams at the center of the band), is demonstrated.

6.2 Analysis of Integrated Lens Antennas Coupled to Free Standing Lenses

As described in Sec. 6.1, multi-lens QO architectures are required to realistically couple a large hyper-hemispherical lens antenna to the rest of the QO system. In this chapter, in order to focus on the analysis of the QO system, simple array of antenna feeders with Gaussian far field patterns are considered. These feeders are decoupled, and a single feeder corresponds to a single beam.

In Fig. 6.2, a more detailed illustration of an example element of three-lens based FPA is shown. The focus of the first hyperbolic surface (closer to the antenna) is shared with the virtual focus of the lens antenna. The focus of the second surface (farther from the antenna) is shared with the next QO component (here shown by an equivalent parabolic reflector). The field lens is also placed at this position. In such architecture, a magnification is introduced between the hyperbolic lens and the next reflector component. In the following subsections, firstly an analysis method based on field matching,

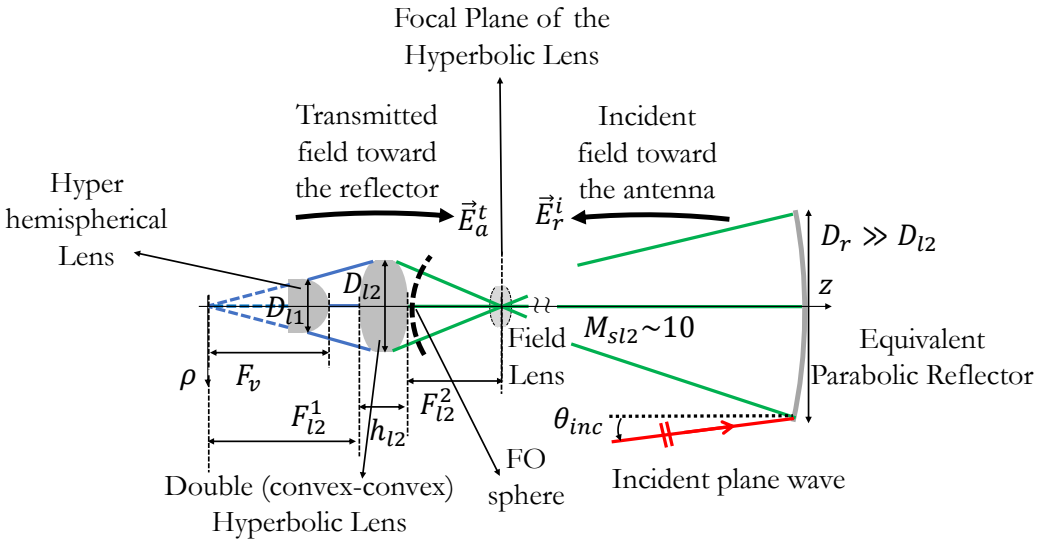

Figure 6.2: An element in the proposed lens based FPA. This element is placed below an equivalent parabolic reflector. The field matching interface, at the FO sphere of the 2nd hyperbolic lens, are also shown.

to evaluate the coupling of the antenna to the rest of the QO system, is described. To perform this analysis, the field transmitted from the antenna side toward the equivalent parabolic reflector and the incident field coming from the reflector to the lens FPA are required (see Fig. 6.2). Secondly, a numerically efficient method for calculating these required fields is presented. Finally, the performance of this method is compared against a traditional multi-surface PO code.

6.2.1 Fourier Optics - Geometrical Optics Based Analysis

The antenna in reception technique, as described in details in Sec. 2.5, is employed to calculate the aperture efficiency of the proposed QO system to an equivalent parabolic reflector. The field matching integral, see (2.17), between the transmitted, $\vec{E}_a^t(\theta, \phi)$, (coming from the antenna side) and incident fields, $\vec{E}_r^i(\theta, \phi)$, (coming from the parabola), is performed at the FO sphere of the 2nd hyperbolic lens. Here θ, ϕ represent the angular parameters defining the sphere where the field matching is performed; the radius of the FO sphere is equal to the focal length of the second hyperbolic surface F_{l2}^2; and θ_{l2}^0 is its maximum subtended angle. By knowing the amount of power delivered to the load, one can estimate the aperture efficiency of the entire QO system using (2.20). As discussed in Sec. 2.5, the power delivered to the load of the feeder is maximized when the incident and transmitted fields are equal and conjugate of one another. This condition is referred to as the field match condition.

In order to analyse the coupling of the antenna to the whole system, two fields must be evaluated at the FO sphere of the second surface of the hyperbolic lens. In the following, the steps to calculate these fields are described. In the proposed architecture, the hyper-hemispherical lens antenna is coupled to a convex hyperbolic surface. The following steps are followed to analyse this portion of the QO system:

1. The far field of an antenna feeder located at a certain position in the focal plane of the integrated

lens is propagated to its surface. Moreover, the transmitted fields ($\vec{E}^o_{la}$ and $\vec{H}^o_{la}$) outside the surface of the lens antenna are calculated. Here a wide band Anti Reflection (AR) coating is considered between integrated lens and air interface (e.g. multi-layer coating).

2. By using an in-house analytical ray tracing code, the ray paths from the surface of the integrated lens to the first hyperbolic surface are calculated. In this step, $\vec{E}^o_{la}$ and $\vec{H}^o_{la}$ are approximated as spherical waves originated from the focal plane of the first hyperbolic surface. Afterward, a numerical GO based code, described in Appendix B, is employed to calculate the field outside the surface of the free-standing lens ($\vec{E}^o_{b1}$ and $\vec{H}^o_{b1}$). Similar to step 1, the transmitted fields inside the hyperbolic lens surface are obtained ($\vec{E}^i_{b1}$ and $\vec{H}^i_{b1}$).

   To continue the analysis from 1st hyperbolic surface to the second, these next steps are followed:

3. By employing similar numerical GO propagation and analytical ray tracing codes, the field inside the first hyperbolic surface is propagated to a flat interface just below the second convex surface ($\vec{E}^i_f$ and $\vec{H}^i_f$). As expected, and calculated by the GO code, the wave front inside the free-standing lens is approximately planar.

4. An analytical GO propagation expression, given in Ch. 2 in (2.12), is used to calculate the radiated field outside the 2nd hyperbolic lens ($\vec{E}^{o,FO}$ and $\vec{H}^{o,FO}$) at a sphere centered at its focus (FO sphere), see Fig. 6.2.

   As for the incident field coming from the equivalent parabolic reflector:

5. A similar GO code is employed to propagate the incident plane wave from the reflector surface to the FO sphere shown in Fig. 6.2.

   In order to validate the described methodology, a final step is added to represent the field at the focal plane of the second hyperbolic surface. This focal field is later compared against a PO based code.

6. By using a FO radiation integral (2.1), the field at the focal plane of the 2nd hyperbolic surface is obtained as an inverse Fourier transform of the field evaluated at the FO sphere, see (2.1).

Similar to the geometry in Fig. 6.2, another lens chain candidate, Fig. 6.3, is also considered. This geometry consists of an integrated hyper-hemispherical lens antenna coupled to a convex-concave hyperbolic double lens. The analysis of this geometry is similar to the one listed above. The difference here is the following: similar to step 3, the field at the 1st hyperbolic surface is now propagated to the 2nd surface ($\vec{E}^i_{b2}$ and $\vec{H}^i_{b2}$), and then transmitted outside the lens ($\vec{E}^o_{b2}$and $\vec{H}^o_{b2}$). By employing a similar numerical GO code, the fields propagating from the 2nd hyperbolic surface toward a far field sphere centered at its virtual focus are obtained, see Fig. 6.3. These fields are obtained for validation purposes.

6.2.2 Validation Using Physical Optics

In order to validate the discussed methodology, a multi-surface PO code, similar to [91], is employed. This code calculates the focal field of the 2nd convex surface in geometry of Fig. 6.2, and the field

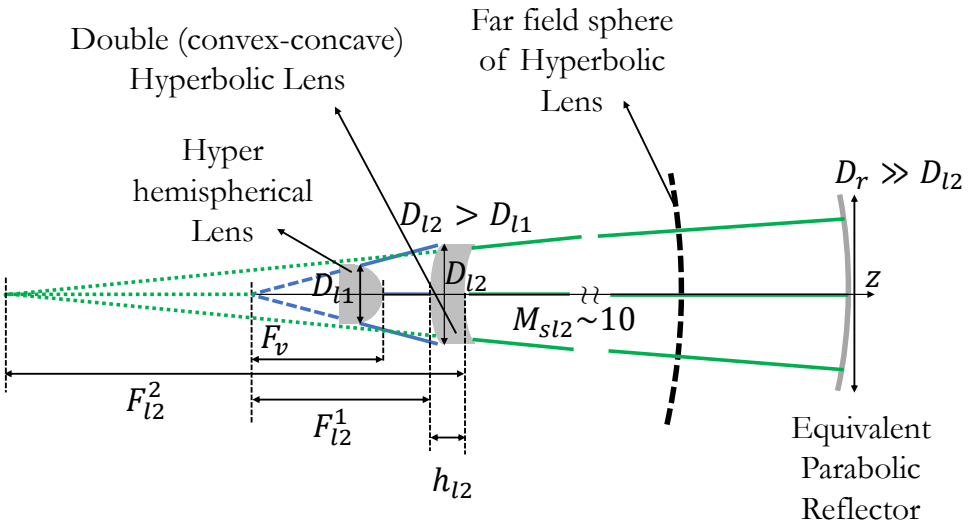

Figure 6.3: A lens chain element with a convex-concave double hyperbolic lens. This element is placed below an equivalent parabolic reflector.

Table 6.1: Geometrical parameters in the considered scenarios

Feeder −11dB taper angle	f_c	D_{l1}	$R_{l1,s}$	F_v	D_{l2}
45°	480 GHz	$48\lambda_c$	$25\lambda_c$	$106.8\lambda_c$	$82\lambda_c$
Perm. l1	Perm. l2	h_{l2}	F_{l2}^1	F_{l2}^2	D_r
$\varepsilon_r^{l1} = 11.9$	$\varepsilon_r^{l2} = 2.4$	$29.6\lambda_c$	$144\lambda_c$	$200\lambda_c$	$800\lambda_c$

at the far field sphere in geometry of Fig. 6.3. As mentioned before, the distance between the three transmitting surface is relatively short in terms of the wavelength. The direction of the propagation of the fields into the transmitting surfaces is determined using Poynting vector; therefore, both electric and magnetic fields must be calculated at each interface. Due to these two reasons, the PO based analysis for these geometries is time consuming.

Here, an example case is considered. The geometrical parameters are summarized in Table 6.1. In this table $l1$ and $l2$ refer to the hyper-hemispherical lens and double hyperbolic lens, respectively; $R_{l1,s}$ is the radius of the hemisphere in the hyper-hemispherical lens (similar to R_s parameter in Fig. 5.1). The parameter needed for defining the Gaussian patterned antenna feeders is also reported in this table. Here, antenna elements are y-polarized. Three scanning scenarios are considered here: broadside (with a feeder at the center of the hyper-hemispherical lens), scanning 4, and 7 beams (feeder at the middle and the edge of FPA). The ray tracing pictures, obtained by the analysis tool, are shown in Figs. 6.4 and 6.5.

The amplitude and phase of the focal fields of geometry in Fig. 6.2 are shown in Fig. 6.6. As it can be seen, the proposed GO-FO based tool is in excellent agreement with the multi-surface PO code up to about scanning 7 beams. The shown discrepancy at the last scanning case is due to the approximation

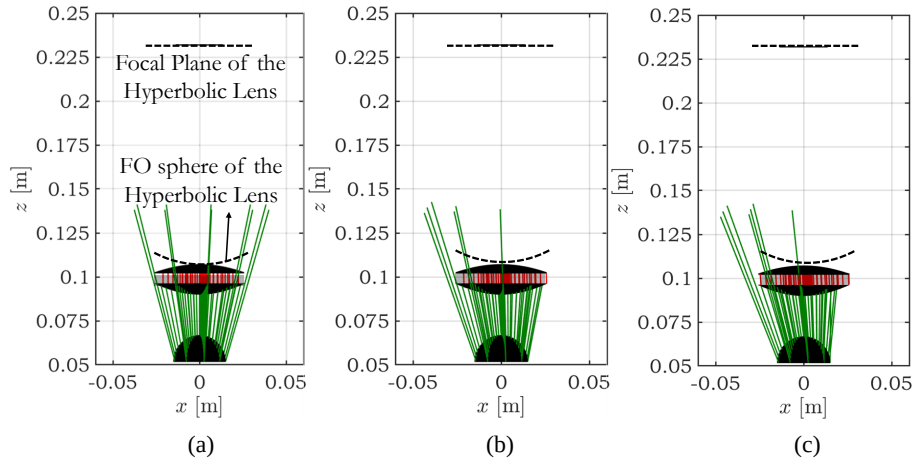

Figure 6.4: Ray tracing picture of the architecture in Fig. 6.2, obtained from the analysis tool: (a) broadside, (b) scanning 4 beams, and (c) 7 beams.

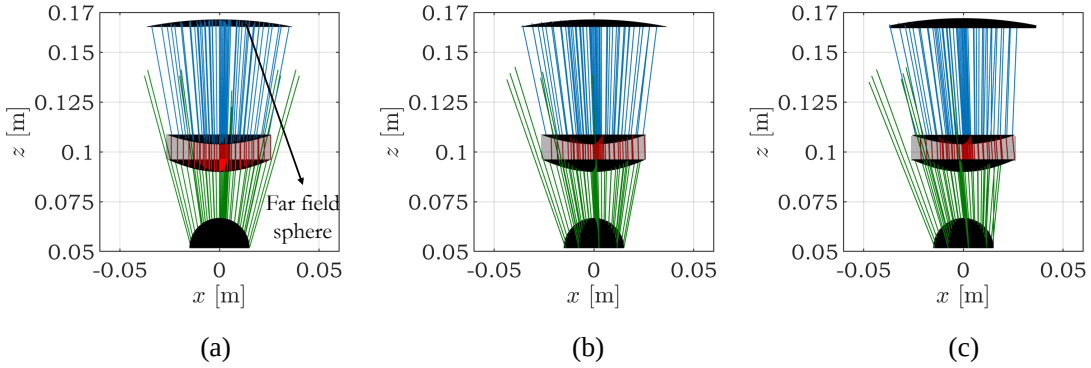

Figure 6.5: Ray tracing picture of the architecture in Fig. 6.3, obtained from the analysis tool: (a) broadside, (b) scanning 4 beams, and (c) 7 beams.

considered in 2nd step of the method. Namely, the approximation on the position of the phase center of the spherical wave illuminating the 1st hyperbolic surface from the integrated lens surface. As next step in the development of this proposed methodology, more rigorous considerations should be taken into account to determine this phase center more precisely.

As shown in Fig. 6.7 for the structure of Fig. 6.3, the fields evaluated over the far field sphere using the GO code is compared against the multi-surface PO code with also excellent agreement and similar limitations as the previous case. The oscillations in the fields evaluated by the PO code are due to the diffraction effects. Moreover, in Fig. 6.7(b) and (c), the linear phase shift in one plane due to scanning are visible.

It is also worth noting that the elapsed time in evaluating the fields for the proposed methodology is about 4 minutes while the multi-surface PO method, required about 6 hours to achieve a numerically stable result. Both of these codes have been executed on a typical workstation PC with a 64 GB of RAM and a CPU with 3.10 GHz clock cycle.

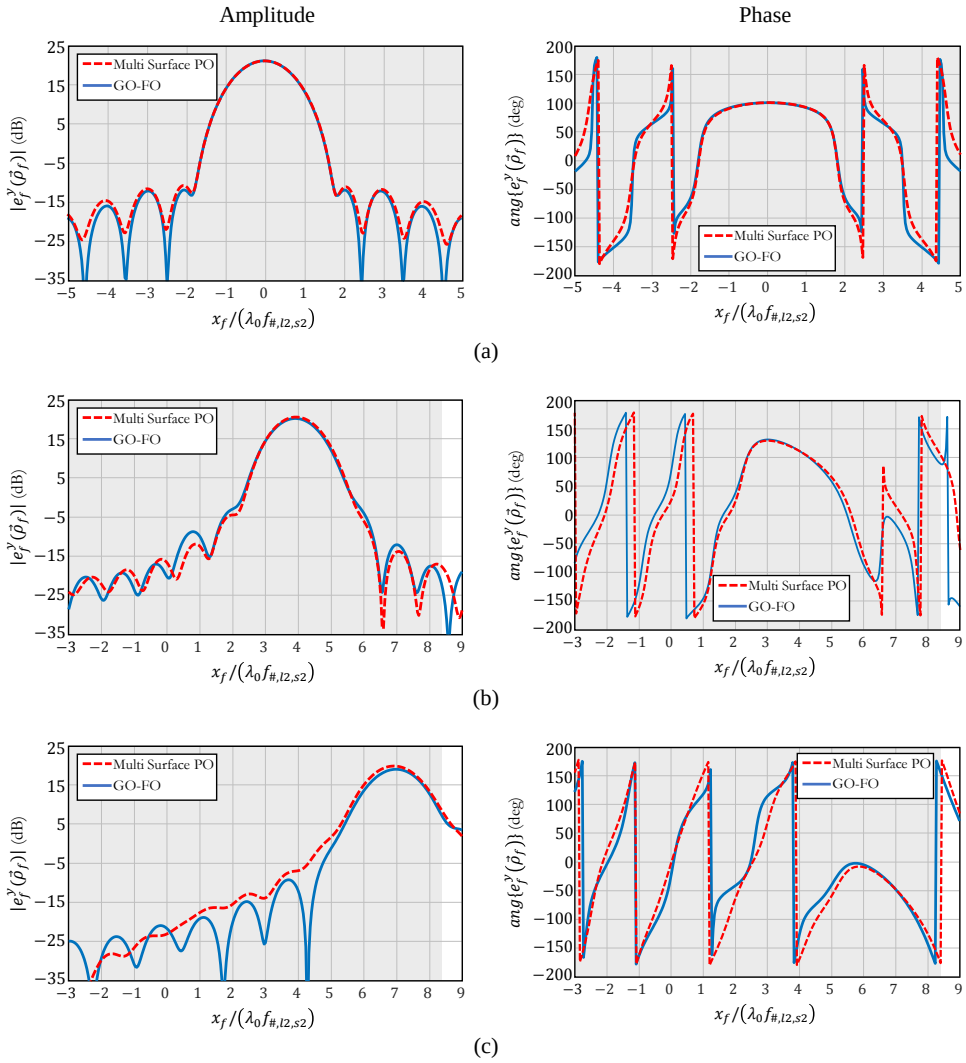

Figure 6.6: Amplitude and phase of the focal field of the 2nd hyperbolic surface (convex-convex in Fig. 6.2), obtained by the proposed tool and compared against multi-surface PO code: (a) broadside, (b) scanning 4 beams, and (c) scanning 7 beams. The grey region indicates the FO applicability region as stated in (2.15). The term $f_{\#,l2,s2}$ represents the f-number of the second surface of the hyperbolic lens, i.e. $f_{\#,l2,s2} = F_{l2}^2/D_{l2}$.

6.3 Example Case of the Proposed Wide Band Wide Scanning Quasi-Optical System

In this section a proof of concept design is discussed for a wide band wide scanning QO system. In this example we focus on the central element, 6.2, of the lens based FPA shown in Fig. 6.1. Here, a reflector chain is approximated by an equivalent parabola which shares its focus with the one of the second hyperbolic surface, Fig. 6.2. The equivalent parabola is illuminated by plane waves with different incident angles, θ_{inc}, corresponding to broadside, 4 beams (3dB overlapping beams at the center of the

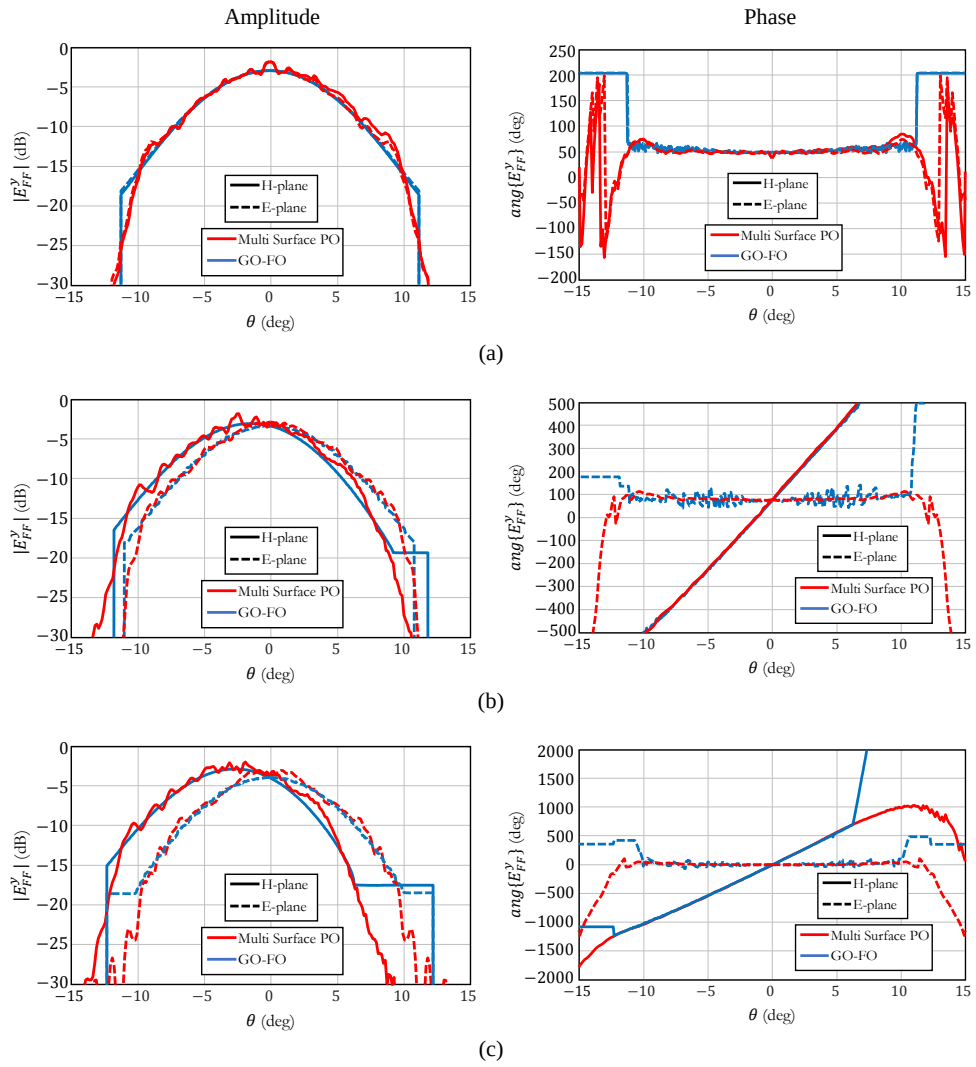

Figure 6.7: Amplitude and phase of the field transmitted out of the 2nd hyperbolic surface (convex-concave in Fig. 6.3) evaluated over a sphere center at its virtual focus. These fields are obtained using the proposed tool and compared against multi-surface PO code: (a) broadside, (b) scanning 4 beams, and (c) 7 beams.

band) and 7 beams scanning. The geometrical parameters of the scenario are summarized in Table 6.1. The antenna elements are again y-, and the incident plane waves are TM_z polarized. The diameter of the equivalent parabolic reflector is $800\lambda_c$, where λ_c is the wavelength at the center of the frequency band. As a result, a factor of about 10 magnification is present in the QO system between the hyperbolic lens and the main mirror.

In Fig. 6.8, the performance of a single lens chain of Fig. 6.1, is shown in terms of the aperture efficiency of the antenna feeder coupled to the rest of QO system at the center, and edge of a feeder FPA, for beginning, center and end of the $3:1$ frequency bandwidth ratio. This aperture efficiency includes the illumination efficiency (how efficiently the system is coupled to the rest of the reflector chain) and the losses in the integrated silicon lens-air interface (with a wide band AR coating) and the

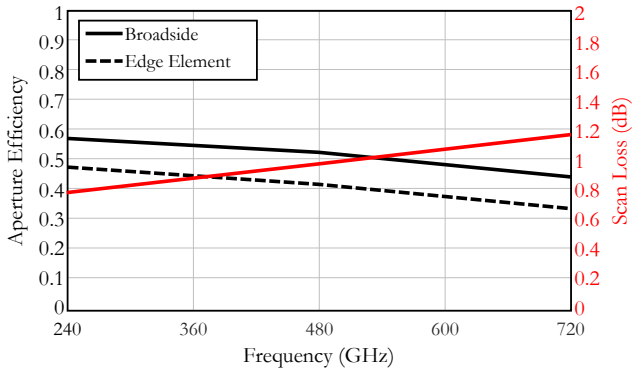

Figure 6.8: Performance of the scenario shown in Fig. 6.2. The solid and dashed black curves represent the aperture efficiency of the whole system for broadside and edge element, respectively. The red solid curve represents the scan loss of the system for the edge element as a function of the frequency.

two plastic-air interfaces for the hyperbolic lens (without an AR coating), and the spill-over of the far field of the antenna elements over the integrated lens surface. The scan loss of the system is also reported in Fig. 6.8 by red solid curve. As it can be seen, the proposed concept achieves about a 1 dB scan loss for scanning ±7 beams at the center of the frequency band, which corresponds to ±3.5 and ±10.5 beams at the beginning, and the end of the frequency band, respectively. The scan loss in this QO system is mainly associated to spill-over loss between the two lenses (visible even in ray tracing picture in Fig. 6.4 as missed rays) and the phase miss-match between the incident and transmitted fields. Therefore, over sized hyperbolic lenses and shaped lens profiles are possible solution to optimize the overall wide scanning performance. In this example scenario, the number of beams scanned by the central element of the multi-lens FPA, Fig. 6.1, at the central frequency is $15 \times 15 = 225$. Assuming a 5 by 5 multi-lens FPA, we can expect about 5600 broad band beams with low scan loss. However, at the moment this estimate is based only on the presented preliminary study, and without anticipating difficulties in the implementation of the actual QO system.

6.4 Conclusion

In this chapter, a QO architecture to achieve wide band wide scanning performance in a (sub)-millimetre imaging and sensing system is proposed. In order to design the elements of this lens based FPA architecture, with multiple transmitting surfaces close to one another, a fast and accurate analysis tool was developed. In this work, the tool is discussed and validated against a time-consuming multi-surface PO code with excellent agreement. Moreover, as a proof of concept of the proposed QO system, an example scenario is described and its performance over a $3:1$ bandwidth ratio is evaluated. For the central element of the proposed QO system, the design achieved $\sim$ 1dB of scan loss over the whole band while scanning up to ±7 beams at the center of the frequency band. Therefore, based on the presented preliminary study, without anticipating difficulties in the implementation of the actual Quasi-Optical system, potentially, about 5600 broad band beams with low scan loss can be generated using a 5 by 5 multi-lens focal plane array.

Part III

Quasi-Optical Systems with Absorber Based Focal Plane Arrays

Large format absorber based Focal Plane Arrays (FPAs) are commercially attractive solutions for passive security cameras operating at sub-millimetre wavelengths. These detectors are also a common solution in astronomical imaging systems to reduce the complexity of the feeder design. In these scenarios, by removing the antenna feeder, the incoming radiation is directly coupled to the detectors. In Ch. 7, an EM based model for absorber based FPAs is described using known terms in the community, such as: effective area, pattern in reception, aperture and focusing efficiency. The coupling of these geometries to point as well as distributed sources is explained using these terminologies. Chapter 8, describes an absorber based FPA using Kinetic Inductance Bolometers for security applications. This passive imaging system operates approximately from 100GHz to 600GHz. The performance of this system is evaluated using the developed methodology and it is compared to measured point spread functions with excellent agreement.

Chapter 7

Reception Power Pattern of Distributed Absorbers in Focal Plane Arrays

Passive imaging cameras at millimetre and sub-millimetre wavelengths are currently entering a new era with the development of large format arrays of direct detectors. Several of these arrays are being developed with bare absorbing meshes without any antenna coupling (lens or horn) structures. The design of such arrays is typically done resorting to geometrical considerations or basic broadside plane wave incidence analysis. The spectral techniques presented in Part I are employed here for the spectral analysis of focal plane arrays of absorbers in reception. This chapter provides an accurate and efficient way to estimate the point-source angular response and the throughput from a distributed incoherent source of an absorbing mesh in the focal plane of a Quasi-Optical component (e.g., a parabolic reflector or lens). The proposed technique is validated with full-wave simulations. After presenting the analysis, in this chapter the performance of arrays of bare absorber in the focal plane of a Quasi-Optical component is compared to those of corresponding antenna based arrays. It is found that absorbers lead to a comparable tradeoff, in terms of spill-over and focusing efficiency, only for very tight samplings. For larger samplings, the focusing efficiency of absorbers is significantly lower than the one for antenna feeders.

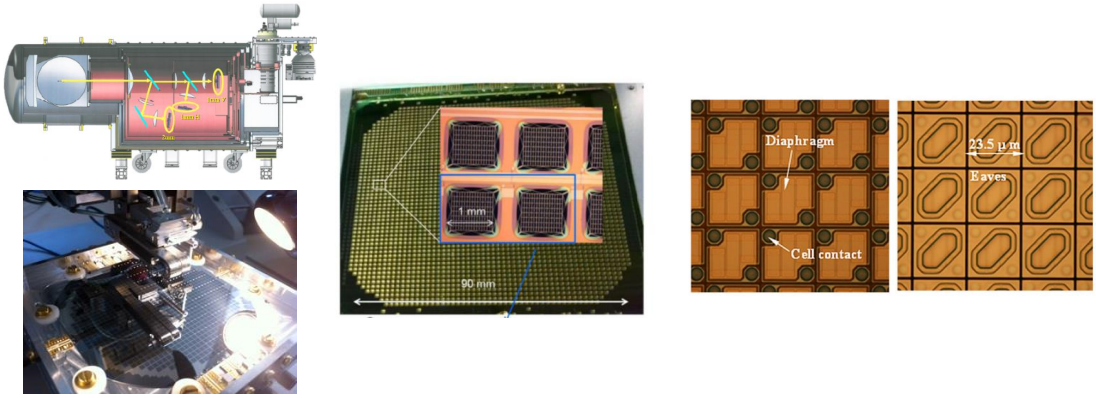

(a) (b) (c)

Figure 7.1: (a) The NIKA 2 instrument and its absorber based FPA [10]. (b) A FPA of Kinetic Inductance Bolometers for security applications [41]. (c) a FPA of microbolometers for THz cameras [42].

7.1 Introduction

Sub-millimetre imagers for stand-off security applications are widely used to detect hazardous objects concealed under clothing [20, 120, 121, 122]. As discussed in Ch. 1, future security imagers will require larger Field of Views (FoVs), comparable to the size of a human body (i.e. images with over 100000 pixels), and video rate speeds (> 10 Hz). The presence of many detectors in the focal plane of an optical system (e.g., charged coupled device (CCD) like configuration) enables the use of systems with none or very limited mechanical scanning. As a consequence, the requirement on the detector's sensitivity is relaxed, in such configuration, thanks to the possibility of using an integration time comparable to the frame rate. In the last years, there has been a significant effort in developing large format Focal Plane Arrays (FPAs) of bare absorbers based detectors with medium sensitivities for commercial sub-millimetre imaging cameras. Some current cameras make use of cryogenic Kinetic Inductance Detectors (KIDs) [10, 11, 12, 21, 41] or uncooled micro-bolometers [42, 43].

Traditionally, since the heat capacity of most bolometers scales with the area, antenna coupling structures have been used to reduce the bolometer physical dimension [44], at the cost of a more complex FPA architecture (e.g., fly's eye lens arrays [45] or horn arrays [46]). Instead, in [47], the use of FPAs of bare absorbers was proposed for tightly sampled large format configurations, i.e. in combination with optical systems with limited mechanical scanning. Such configurations have been recently implemented in astronomical instruments [10, 42], and security imagers [21, 41]. There have been astronomical instruments developed with hybrid configurations such as multi-mode horns coupled to distributed absorbers [123, 124]. A few of such absorber based FPAs are shown in Fig. 7.1.

The trade-offs which dominate the design of focal plane arrays based on antenna feeders are well-known, [48, 49], especially when the systems are required to operate over narrow frequency bands. Focal plane arrays of bare absorbers are, however, much less studied. The amount of power received, and the obtainable angular resolution are significantly different from the one of antenna feeders. The difference raises from the fact that absorbers, unlike single port antennas, respond incoherently to multiple aperture field distributions induced by the incident field [50]. As a consequence, the effective area

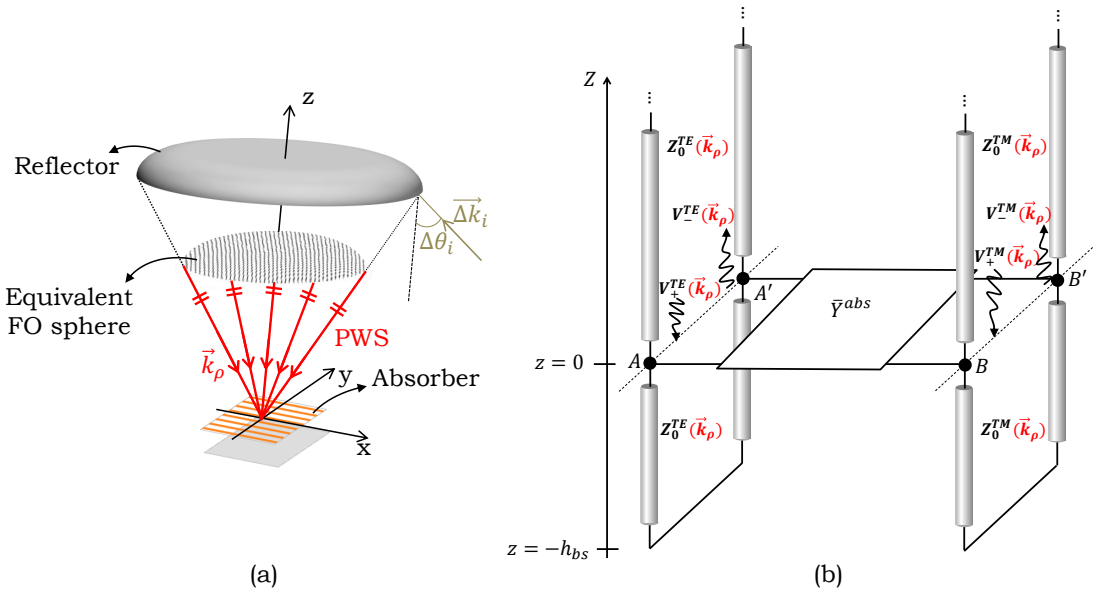

Figure 7.2: (a) PWS representation of the focal field of a parabolic reflector with an absorber based focal plane array. (b) Equivalent transmission line model of a periodic absorber with period smaller than half wavelength under a certain incident plane wave direction, $\vec{k}_\rho$.

in absorbers cannot be related to the directivity as in the case of antennas. Section 7.2 discusses the effective area of an ideal absorber in comparison with that of antennas, highlighting that its value cannot be related to transmitting parameters such as directivity.

In [47], a basic study for deriving the trade-offs between the performances of bare absorbers and antennas was presented within the scope of astronomical instruments. In this contribution, instead, an accurate analysis of FPAs based on bare absorbers is performed resorting to a spectral analysis technique that links the spectrum of the optical system to the one of the distributed absorber. The latter allows considering generic optical systems, even with low focal-to-diameter number, $f_\#$, (commonly referred also as F/D ratio [69]) and distributed absorbers. With respect to previous works, the terminology used here is more common to the reflector antenna community [49].

There have been several works [123, 124] that model distributed absorbers under multi-mode horns by combining mode matching techniques with a partially coherent summation of modes. Here, instead, we treated absorbers distributed directly in the focal plane. A schematic representation of the studied geometry is shown in Fig. 7.2(a). A canonical geometry of a symmetric parabolic reflector under plane wave illumination is chosen. Such geometry represents well the behavior of more complex multi-reflector systems for detectors closed to the focal point [69]. Moreover, the use of such geometry is commonly used to derive basic imaging system performance, and to compare different array elements [125, 126].

The tool used for the analysis of this canonical problem is described in Part I of this thesis. It is based on a Fourier Optics (FO), [68], spectral field representation. The power received by a periodic absorber is evaluated by using a Floquet-modes based equivalent circuit model similar to the one introduced in [66], whose generators are obtained by expanding the direct fields in terms of plane waves coming

from the Quasi-Optical system, Fig. 7.2. Section 7.3 describes the technique for coupling absorbers to the optical systems, and describes the Floquet-modes based model. In particular, the methodology in [127] is extended to skew incidence, and to any type of periodic absorber. The analysis of reflector systems in reception has also been used for characterizing antenna feeders [64,127]. Using this approach, we accurately derive both the point source angular response of a bare absorber under a reflector, and the power received from an angularly distributed incoherent source.

In Section 7.4, the analysis of the power received from a point source as a function of the incident angle onto the optical system allows the introduction of aperture and focusing efficiencies of an absorber under an optical system. The aperture efficiency quantifies how much power is received from a broadside plane wave. The focusing efficiency quantifies how much the achieved angular response of the optical system is diffraction limited. It is worth noting that both of these efficiencies are calculated in reception.

For point sources, it turns out that the use of absorbers leads to a power received comparable to that obtained by antenna feeders, but at the cost of much lower focusing efficiency. The maximum of the product between the spill-over and focusing efficiency is 37% for absorbers with a dimension of $w = 1.2\lambda f_{\#}$, whereas in case of Gaussian antennas the maximum is 82% [54] for an antenna aperture dimension of about $2\lambda f_{\#}$. Therefore, an array of absorbers guarantees an effective use of the reflector area, comparable to that of antenna arrays, only in a highly populated FPAs with spacing $d \leq 0.75\lambda f_{\#}$.

In Section 7.5, we derive the throughput, $A\Omega$, from an incoherent distributed source associated with an absorber located in the focal plane of an optical system. This term is typically adopted in optical research communities, and $A\Omega/\lambda^2$ is commonly referred to as the number of effective spatial modes, [50]. Here, the throughput is expressed in terms of antenna efficiencies. Whereas for single-mode antennas the throughput is bounded to $A\Omega \leq \lambda^2$, for absorbers it has an upper limit related to the reflector physical area (i.e. $A\Omega \leq \pi \mathcal{A}_{ref}$) leading to a larger received power (or better sensitivity) with respect to antenna based FPAs, but at the cost of a reduced angular resolution.

In the literature, the term $A\Omega/\lambda^2$ is approximated resorting to basic radiometry calculations via geometrical approximations [128] or Airy pattern considerations [47]. Here, instead, a more rigorous methodology that makes use of an accurate evaluation of the angular response of the optical system is proposed. It includes coherence effects coming from the optics, such as phase errors due to the curvature of the optics, specially for low F/D ratios, or non-ideal absorber geometries, or changes in the frequency response because of resonant geometries, [21, 129].

The proposed method is validated in Section 7.6 by full wave simulations. Section 7.7 contains some concluding remarks.

7.2 Effective Area of Bare Absorbers without the Presence of Optical Components

The power received by antennas or absorbers due to an incident plane wave, P_r, can be evaluated via an effective area

$$\mathcal{A}_{eff}(\theta, \phi) = \frac{P_r(\theta, \phi)}{S_i} \tag{7.1}$$

where $S_i = |E_0|^2/(2\zeta_0)$ is the incident power density, with ζ_0 being the free space wave impedance (377 Ω).

Antennas are typically characterized also by directivity transmitting patterns, and the corresponding effective area can be related to the directivity by $A_{eff}^{ant} = D_{ir}\lambda^2/4\pi$. Instead, the directivity is not a useful parameter to derive the effective area for electrically large distributed absorbers, since their radiation patterns cannot be related to a coherent aperture distribution. For this reason, it is more convenient to use the effective area as reference parameter for comparing the properties between antennas and absorbers. An ideal electrically large planar absorber, see Fig. 7.4(inset), can be achieved using a thin continuous sheet made of a material with conductivity σ and thickness h on top of quarter wavelength back-short, $h_{bs} = \lambda/4$, [43, 130]. The surface resistance of this sheet, since its thickness is smaller than the skin depth, can then be chosen to be $R_s = \zeta_0 = 1/(h\sigma)$ ($\Omega/\square$) [131].

To evaluate the power absorbed by such ideal absorber, one can use the equivalent circuit shown in Fig. 7.2(b), where the TE/TM equivalent lines are decoupled. For a generic plane wave incidence, $\vec{e}^i = E_0\hat{p}_i e^{-j\vec{k}^i\cdot\vec{r}}$, assuming that the back-short has no losses, and considering an electrically large absorber of area A, the power absorbed is the active power density flowing across any $z > 0$ transmission line cross section multiplied by the physical area of the absorber. After some algebraic manipulations, the absorbed power can be expressed as a function of the back-short distance h_{bs} for each plane wave angle of incidence (θ_i, ϕ_i) and polarization $\hat{p}_i$, as follows:

$$P_{abs}^{PW}(\theta_i, \phi_i) = S_i \mathcal{A} \cos\theta_i [(\hat{p}_i \cdot \hat{k}_{\rho i})^2 \chi_{TM} + (\hat{p}_i \cdot \hat{\phi}_i)^2 \chi_{TE}] \tag{7.2}$$

where $\hat{k}_{\rho i} = \sin\theta_i(\cos\phi_i\hat{x}+\sin\phi_i\hat{y})$ and $\hat{\phi}_i = -\sin\phi_i\hat{x}+\cos\phi_i\hat{y}$. The efficiencies $\chi_{TM} = (4\cos\theta_i)/((1+\cos\theta_i)^2 + \cot^2(k_0\cos\theta_i h_{bs}))$ and $\chi_{TE} = (4\cos\theta_i)/((1+\cos\theta_i)^2 + \cos^2(\theta_i)\cot^2(k_0\cos\theta_i h_{bs}))$ take into account for the impact of the back short.

Fig. 7.3 shows the normalized received power of the ideal planar absorber versus the plane wave angle of incidence for a standard back-short distance, i.e., $\lambda/4$. Both a $\hat{\theta}$- and $\hat{\phi}$-polarized incident plane waves are considered. The curves differ from the standard *Lambert's cosine law*, commonly used in optics, due to the presence of the back-short. The larger the back-short (e.g., as the ones used in [41]) the larger is the angular variation.

Equation (7.2) shows that for broadside plane wave incidence and $h_{bs} = \lambda/4$, the power received by the ideal absorber is the incident power density times the absorber area. Hence, for this case, the effective area is identical to the physical one. Instead for single mode[1] antennas the effective area can be related to the directivity by the relation $A_{eff}^{ant} = D_{ir}\lambda^2/(4\pi)$, where the directivity depends on the angular distribution of the antenna radiation pattern. Therefore, an antenna with an angular receiving power pattern of $\cos\theta$, similar to the one shown in Fig. 7.3, has an effective area of $A_{eff}^{ant} = \lambda^2/\pi$ irrespectively of its dimensions. In the case of electrically large absorbers, the effective area, instead, increases linearly with the physical area, while having the same angular receiving pattern.

Fig. 7.4 shows the effective area of the ideal absorber (with an infinite and a finite back short of the same size than the absorber). This effective area is reported as a function of the absorber's phys-

[1]Single mode antenna referred to antennas with a feeding port that excites a specific equivalent current distribution.

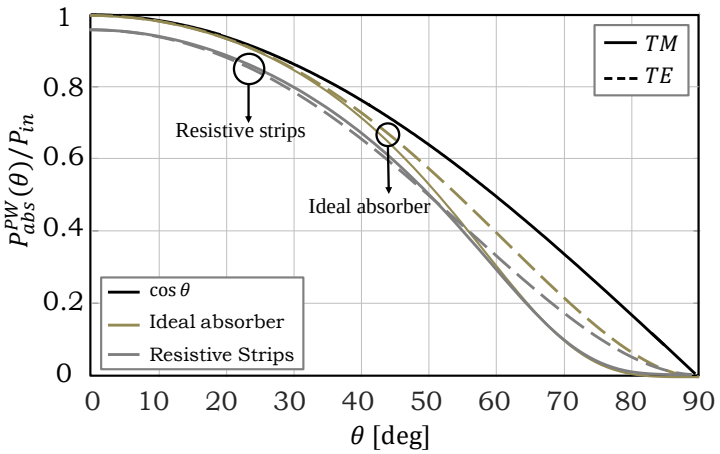

Figure 7.3: Power absorbed by an ideal planar absorber and a strip absorber for a $\hat{\theta}$-(TM) and $\hat{\phi}$-polarized (TE) plane wave incidence at different incidence angles. Both designs use back shorts at $\lambda/4$ distance. The curves are normalized to $P_{in} = S_i A$.

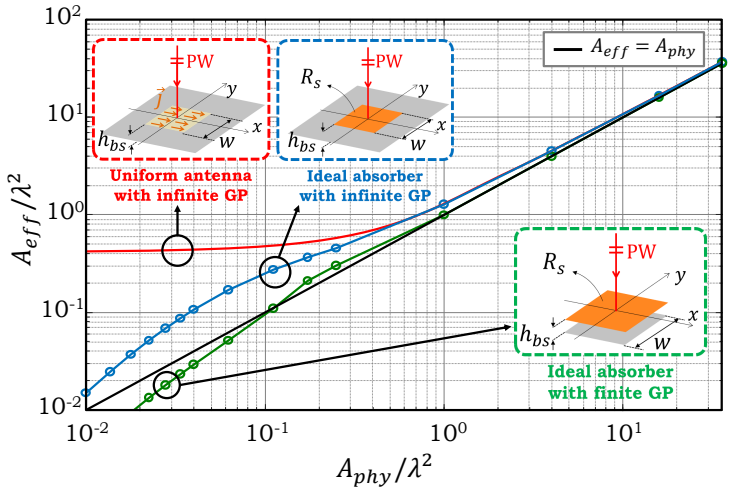

Figure 7.4: Effective area of the ideal absorber (with an infinite and a finite back-short of the same size than the absorber) versus the physical area compared to the effective area of an impedance matched antenna with uniform square electric distribution above an infinite ground plane. The distance to the back-short is $\lambda/4$ for all cases.

ical area calculated using full-wave simulations done with CST MS [79] under broadside plane wave illumination. The simulated geometry is shown in Fig. 7.4(inset).

It is apparent that the effective area of absorbers matched to the wave impedance ζ_0 remains equal to the physical area, even when the dimension of the overall absorber is small in terms of the wavelength. For the sake of comparison, the effective area of a matched antenna radiating above an infinite ground

plane characterized by an equivalent electric current distribution $\vec{j} = rect(x, w/2)rect(y, w/2)\hat{x}$, is also shown in Fig. 7.4. For small dimensions, in terms of the wavelength, the antenna effective area can be much larger than its physical area. However, their designs are much more complex since they require the design of an impedance matching network which is frequency and dimension dependent.

7.3 Spectral Field Representation for Absorber Feeders

In [66] an analytical method, based on a FO approach, for calculating the power absorbed by a resistive linear strip mesh in the focal plane of an optical system, was presented. The FO method can be used to derive in a simple way a spectral wave expansion of the direct field focused on the focal plane. In [66], the spectral plane wave expansion derived by using FO was linked to a periodic spectral field representation in the surrounding of the absorbers (via a Floquet-modes expansion [132]). In this section, the extension of the analysis to generic planar periodic absorbing geometries, and slightly off-broadside incidence, is discussed. In Section 7.4, this extension will be used for the accurate estimation of both the aperture efficiencies, and the point-source responses of an imaging system based on bare absorber's FPAs.

Let us consider the geometry depicted in Fig. 7.2: an absorber based FPA below a on-axis parabolic reflector. In this sub-section, the direct field (without the presence of the absorber) at the reflector focal plane position, as well as the total field (in the presence of the absorber) are derived. As described in Sec. 2.2, the field scattered by a QO component at its focal plane can be represented as a Plane Wave Spectrum (PWS) by using the described FO based technique (see (2.1)). This PWS represents the direct field at the focal plane of the QO component. Moreover, the coupling mechanism between an impinging plane wave and a periodic structure, such as the considered absorbers, can be represented via an equivalent Floquet-modes circuit model [66]. By using this model, in the following, the response of the absorber to the PWS of the direct field is described as another PWS representing the total field at the focal plane of the QO component.

The field in the surrounding of a periodic absorber coupled to an optical system can be expressed as a coherent summation of the absorber response to each plane wave coming from the optical system. The spectral response of the absorber to a plane wave can be modeled by using the fundamental Floquet-modes field representation, neglecting any finiteness effect, and assuming a periodicity less than half wavelength, i.e., $d_{x/y} < \lambda/2$.

In general, any periodic planar structure can be modeled by using the equivalent network shown in Fig. 7.2(b), where the TE and TM transmission lines represent the propagation of the respective fundamental Floquet-modes having characteristic impedances $Z_0^{TE}(k_\rho) = \zeta_0 k_0/k_z$ and $Z_0^{TM}(k_\rho) = \zeta_0 k_z/k_0$ respectively, where $k_z = \sqrt{k_0^2 - k_\rho^2}$. The matrix

$$\bar{Y}_{abs}(\vec{k}_\rho) = \begin{bmatrix} Y_{abs}^{TETE}(\vec{k}_\rho) & Y_{abs}^{TETM}(\vec{k}_\rho) \\ Y_{abs}^{TMTE}(\vec{k}_\rho) & Y_{abs}^{TMTM}(\vec{k}_\rho) \end{bmatrix}$$

represents the absorbers response to the TE and TM plane wave excitations. The components of this matrix can be derived analytically for a few structures as in [133, 134], or evaluated numerically using periodic boundary conditions via a commercial electromagnetic tool such as CST MS, as in [132, 135].

For a periodic structure placed at the focal plane of an optical system, the voltage sources in the Floquet equivalent network are related to the PWS of the direct field coming from the optical system as described in [66]. They can be evaluated as

$$V_+^{TM}(\vec{k}_\rho) = \sqrt{d_x d_y} E_\theta^d(\vec{k}_\rho) \frac{k_z}{k_0} \tag{7.3a}$$

$$V_+^{TE}(\vec{k}_\rho) = \sqrt{d_x d_y} E_\phi^d(\vec{k}_\rho) \tag{7.3b}$$

where d_x and d_y are the periods of the array along x and y, respectively; $E_\theta^d(\vec{k}_\rho)$ and $E_\phi^d(\vec{k}_\rho)$ are the θ- and ϕ-spectral components of the PWS of the direct field as in (2.1a) and (2.3a).

By using the scattering parameters representation of the structure, one can evaluate the current flowing, $I^{TE/TM}(\vec{k}_\rho, z)$, and voltage drop, $V^{TE/TM}(\vec{k}_\rho, z)$, at the transmission line quote above the absorber as follows:

$$V^{TE/TM}(\vec{k}_\rho, 0^+) = V_+^{TE/TM} + V_-^{TE/TM} \tag{7.4a}$$

$$I^{TE/TM}(\vec{k}_\rho, 0^+) = \frac{1}{Z_0^{TE/TM}} (V_+^{TE/TM} - V_-^{TE/TM}) \tag{7.4b}$$

where $\begin{bmatrix} V_-^{TE} \\ V_-^{TM} \end{bmatrix} = \bar{S}(\vec{k}_\rho) \begin{bmatrix} V_+^{TE} \\ V_+^{TM} \end{bmatrix}$ are the reflected voltages at AA'/BB' terminal, Fig. 7.2(b), since

$$\bar{S}(\vec{k}_\rho) = \begin{bmatrix} S^{TETE}(\vec{k}_\rho) & S^{TETM}(\vec{k}_\rho) \\ S^{TMTE}(\vec{k}_\rho) & S^{TMTM}(\vec{k}_\rho) \end{bmatrix}$$

represents the scattering matrix of the transmission line at $z = 0^+$ quote.

The averaged magnetic and electric spectral fields over the absorber unit cell can be derived as follows:

$$E_{k_\rho}^t(\vec{k}_\rho, z) = \frac{1}{\sqrt{d_x d_y}} V^{TM}(\vec{k}_\rho, z) \tag{7.5a}$$

$$E_\phi^t(\vec{k}_\rho, z) = \frac{1}{\sqrt{d_x d_y}} V^{TE}(\vec{k}_\rho, z) \tag{7.5b}$$

$$H_{k_\rho}^t(\vec{k}_\rho, z) = -\frac{1}{\sqrt{d_x d_y}} I^{TE}(\vec{k}_\rho, z) \tag{7.5c}$$

$$H_\phi^t(\vec{k}_\rho, z) = \frac{1}{\sqrt{d_x d_y}} I^{TM}(\vec{k}_\rho, z) \tag{7.5d}$$

Combining expressions in (7.5), one can express the average electric and magnetic spectral fields (PWS of the total field) in Cartesian coordinates as

$$\begin{bmatrix} E_x^t(\vec{k}_\rho, z) \\ H_x^t(\vec{k}_\rho, z) \end{bmatrix} = \begin{bmatrix} E_{k_\rho}^t(\vec{k}_\rho, z) \\ H_{k_\rho}^t(\vec{k}_\rho, z) \end{bmatrix} (\hat{k}_\rho \cdot \hat{x}) + \begin{bmatrix} E_\phi^t(\vec{k}_\rho, z) \\ H_\phi^t(\vec{k}_\rho, z) \end{bmatrix} (\hat{\phi} \cdot \hat{x}) \tag{7.6a}$$

$$\begin{bmatrix} E_y^t(\vec{k}_\rho, z) \\ H_y^t(\vec{k}_\rho, z) \end{bmatrix} = \begin{bmatrix} E_{k_\rho}^t(\vec{k}_\rho, z) \\ H_{k_\rho}^t(\vec{k}_\rho, z) \end{bmatrix} (\hat{k}_\rho \cdot \hat{y}) + \begin{bmatrix} E_\phi^t(\vec{k}_\rho, z) \\ H_\phi^t(\vec{k}_\rho, z) \end{bmatrix} (\hat{\phi} \cdot \hat{y}). \tag{7.6b}$$

These spectral electric field, averaged over each absorber period (d_x, d_y), are related to the voltage solution, $V^{TE/TM}(\vec{k}_\rho, z)$, whereas the magnetic field to the current solution, $I^{TE/TM}(\vec{k}_\rho, z)$.

This methodology can be applied to any periodic structure embedded into a generic dielectric stratification (transverse to the z-direction). By solving the equivalent circuit, one can evaluate the PWS of the total average fields, $[\vec{E}^t\ ,\ \vec{H}^t]$, at any z-quote, that includes both the absorber and optical system spectral responses. The spatial fields representing the response of the absorber to the optical system is then evaluated as the inverse Fourier transform of this PWS

$$\vec{e}^t(\vec{\rho}, z, \vec{k}_\rho^i) = \frac{1}{4\pi^2} \iint_{-\infty}^{+\infty} \vec{E}^t(\vec{\rho}, z, \vec{k}_\rho^i) e^{j\vec{k}_\rho \cdot \vec{\rho}} k_\rho dk_\rho d\alpha. \tag{7.7}$$

In the case of slightly off-broadside incidences, indicated by representing the direction of incident plane wave by $\vec{\Delta k}_\rho^{\,i}$ instead of $\vec{k}_\rho^i$, can be approximated as the inverse Fourier transform of the spectral total field evaluated at broadside times the linear and coma phase terms (similar to the representation in (2.12))

$$\vec{e}^t(\vec{\rho}, z, \vec{\Delta k}_\rho^{\,i}) \simeq \frac{1}{4\pi^2} \iint_{-\infty}^{+\infty} \vec{E}^t(\vec{\rho}, z, \vec{\Delta k}_\rho^{\,i} = 0) e^{-j\vec{k}_\rho \cdot \vec{\Delta\rho}_i (1+\vartheta_n)} e^{j\vec{k}_\rho \cdot \vec{\rho}} k_\rho dk_\rho d\alpha. \tag{7.8}$$

Only for the scanning angles imposed by (2.13), one can neglect the coma phase term $\vec{k}_\rho \cdot \vec{\Delta\rho}_i \vartheta_n$ and the spatial fields can be computed as a linear translation to the flash point $\vec{\Delta\rho}_i$ of the broadside spatial total field

$$\vec{e}^t(\vec{\rho}, z, \vec{\Delta k}_\rho^{\,i}) \simeq \vec{e}^t(\vec{\rho} - \vec{\Delta\rho}_i, z, \vec{\Delta k}_\rho^{\,i} = 0). \tag{7.9}$$

7.4 Point-Source Response of Absorber Feeders

In this section, we derive the response of resistive periodic absorber under a focusing system when the latter is illuminated by a single plane wave of amplitude E_0, impinging from a direction $\vec{\Delta k}_i$ (Fig. 7.5). Using (7.8), i.e., a coherent summation of the spectral total fields, averaged over each unit cell of the

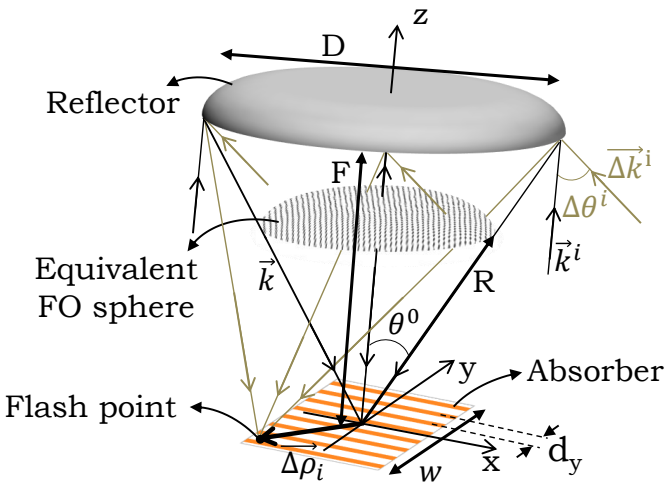

Figure 7.5: The considered Fourier Optics scenario for broadside or oblique plane wave incidence onto a parabolic reflector with a square strip mesh absorber in its focal plane.

periodic absorber, we can estimate the total spatial electric and magnetic field, $\vec{e}^{t}(\vec{\rho})$ and $\vec{h}^{t}(\vec{\rho})$, at the focal plane. These fields are in effect evaluated as an inverse Fourier transform of the PWS of the optical system times the spectral plane wave response of the absorber. The shape of the total fields depends on the response of the absorber to plane waves with incidence angles impinging from broadside up to the reflector subtended angle, θ^0. Once the fields are known, the power absorbed by a finite periodic mesh can be evaluated, assuming local periodicity, as the integral, over the absorber area w, of the z-component of the Poynting's vector associated with the spatial total fields, as follows:

$$P_{abs}(f, \vec{\Delta k}_{\rho}^{\,i}) = \frac{1}{2} Re\left\{ \int_{-w/2}^{w/2}\int [\vec{e}^{t}(\vec{\rho}, \vec{\Delta k}_{\rho}^{\,i}) \times \vec{h}^{t*}(\vec{\rho}, \vec{\Delta k}_{\rho}^{\,i})] \cdot \hat{z} dS \right\}. \tag{7.10}$$

7.4.1 Aperture Efficiency

The aperture efficiency, η_{ap}, of an absorber under a reflector relates the effective area, $\mathcal{A}_{eff}$, to the physical area, $\mathcal{A}_{ref}$, of the reflector (or of the considered Quasi-Optical system). This efficiency can be calculated as the ratio between the power absorbed (7.10) for broadside incidence, and the power incident to the reflector, $P_{in} = S_i \mathcal{A}_{ref}$

$$\eta_{ap}(f) = \frac{P_{abs}(f, \vec{\Delta k}_{\rho i} = 0)}{P_{in}} = \frac{\mathcal{A}_{eff}}{\mathcal{A}_{ref}} \tag{7.11}$$

As an example, we evaluate this efficiency for the case of the ideal planar absorber described in Section 7.2 but under an optical system. For focusing systems with subtended angles smaller than 20°, i.e., $f_{\#} > 1.4$, the angular response of the ideal absorber can be considered nearly constant (see Fig. 7.3). In

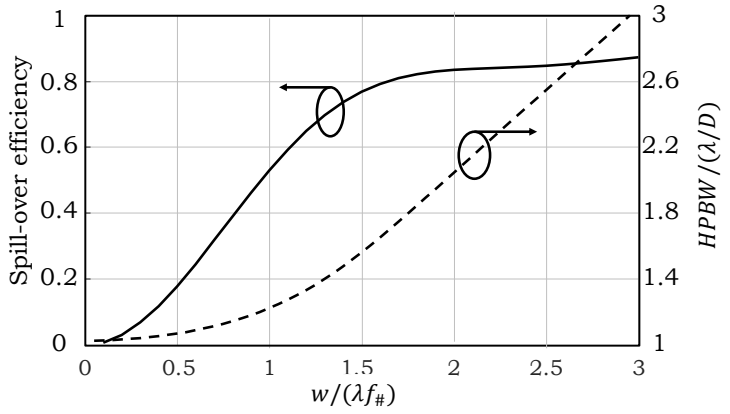

Figure 7.6: Spill-over efficiency (solid) and HPBW (dashed) for an ideal absorber under an optical system characterized by $f_\# = 2$ and diameter $D = 100\lambda$ versus the physical size of the absorber normalized to $\lambda f_\#$.

this case the absorber spatial fields in (7.8) will resemble the direct fields arriving from the optical system. Thus, the aperture efficiency will be, for an ideal reflector, the well-known spill-over efficiency[2], η_{so}, of the corresponding Airy pattern, except for the cases of electrically small impedance-matched absorbers which are not considered here.

In Fig. 7.6 the spill-over efficiency, evaluated for normal plane wave incidence on the reflector, versus the size of the ideal absorber, normalized to $\lambda f_\#$, is shown for $f_\# = 2$. When the absorbers would have a nonflat angular response over the reflector subtended angle, the total spatial fields, $\vec{e}^t(\vec{\rho}, z = 0, \vec{\Delta k}^i_\rho)$, will be spatially wider than the direct fields, and therefore, the aperture efficiency would be lower than the spill-over efficiency of the direct fields. This will be also the case when the absorber is not well matched or has a resonant frequency response. Therefore, the use of multilayer absorbers with stable angular response [136, 137, 138] will improve the coupling with the optical system, especially for low $f_\#$ optics.

Fig. 7.6 also reports the half-power beamwidth (HPBW) normalized to the minimum theoretical HPBW given by a diffraction limited aperture ($HPBW_{min} = \lambda/D$) in the right axis versus the absorber size. It is worth noting that this curve is similar to the one presented in Fig. 4 of [47], since it is presented for a large $f_\#$ and an ideal absorber. The HPBW of the point spread function is a figure of merit for the quality of the generated image. The penalty in terms of system angular beamwidth is further quantified in Section 7.4.2.

[2] $\eta_{so} = \dfrac{\iint_A (|e^d_x(\vec{\rho})|^2 + |e^d_y(\vec{\rho})|^2) dS}{\iint_\infty (|e^d_x(\vec{\rho})|^2 + |e^d_y(\vec{\rho})|^2) dS}$

7.4.2 Point-Source Angular Response

The angular response of an absorber coupled to an optical system, typically referred as the point spread function in optics, can be evaluated by calculating how much the absorbed power (7.10) changes versus the impinging plane wave wave-vector $\vec{\Delta k}_\rho^{\,i}$. A normalized point spread function will be defined here as follows:

$$F(f, \Delta\theta^i, \Delta\phi^i) = \frac{P_{abs}(f, \vec{\Delta k}_\rho^{\,i})}{P_{abs}(f, 0)}. \tag{7.12}$$

Thus, the power absorbed can be expressed as:

$$P_{abs}(f, \Delta\theta^i, \Delta\phi^i) = S_i \mathcal{A}_{ref} \eta_{ap}(f) F(f, \Delta\theta^i, \Delta\phi^i) \tag{7.13}$$

To evaluate the angular response in a computationally efficient way, we can use the approximated spatial fields derived in (7.9). In the case of focusing systems with large $f_\#$, one can neglect the coma term for most of the FO validity region. This approximation allows us to evaluate the power absorbed, (7.10), as a convolution of the spatial Poynting's vector for broadside incidence, ($\vec{\Delta k}_\rho^{\,i} = 0$), and the absorber domain (square in this case)

$$P_{abs}(f, \vec{\Delta k}_\rho^{\,i}) \simeq \frac{1}{2} Re \iint_{-w/2}^{w/2} [\vec{e}^{\,t}(\vec{\rho} - \vec{\Delta\rho}_i, 0) \times \vec{h}^{t*}(\vec{\rho} - \vec{\Delta\rho}_i, 0)] \cdot \hat{z} dS. \tag{7.14}$$

The validity region of (7.14) is where one can neglect the comma phase term, and given in (2.13).

Fig. 7.7(a) shows the angular response of the ideal absorber compared to that of a uniform aperture antenna [Fig. 7.4(inset)] coupled to a parabolic reflector with $f_\# = 2$ for different absorber sizes. It can be noted that, in both cases for physical dimensions small in terms of $\lambda f_\#$, the angular response resembles the well-known Airy distribution. Instead the imager angular response gets much wider when the physical dimension of the absorber increases than in the case of antennas. This implies that as the absorber size increases, the HPBW increases faster than for a uniform aperture antenna.

This peculiar behavior of the absorbers can be understood if one imagines an absorber large in terms of the wavelength divided in portions having dimension in the order of half wavelength, similar to the multi-mode antenna proposed in [50]. Since the power received by each portion sums up almost incoherently, the result is an overall less angular discriminating optical system. For example, Fig. 7.7(b) shows that for a skewed plane wave incidence, the flash point of the direct field is at the edge of the detecting area. An ideal absorber will receive power proportional to the flux of the Poynting's vector of the direct field, across the entire absorber area, but with maximum contribution from the portion of area at the flash point. On the contrary, an antenna, designed to receive coherently the direct field from broadside, will not receive properly this off-set direct field.

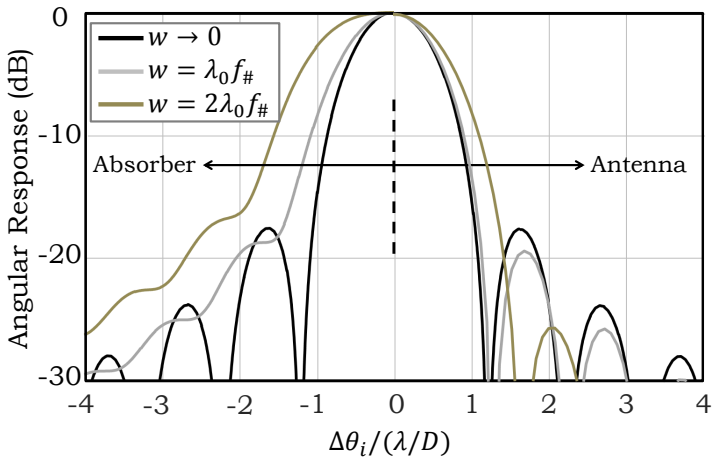

(a)

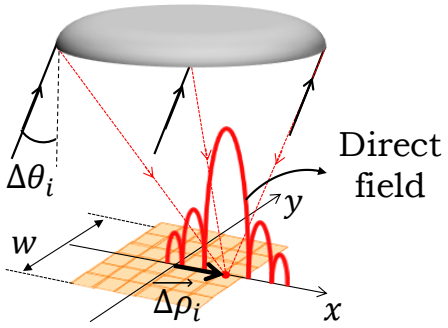

(b)

Figure 7.7: (a) Angular response to a plane wave impinging from $\Delta\theta_i$ of both an ideal absorber, and a uniform aperture antenna coupled to a parabolic reflector with $f_\# = 2$. Different curves correspond to several absorber and antenna sizes. (b) Sketch showing the detecting device (antenna/absorber) and direct field for a case of a squinted plane wave incidence.

7.4.3 Focusing Efficiency

In Figs. 7.6 and 7.7, we have shown that the angular resolution of the imager in Fig. 7.5 gets worse with enlarging the dimension of the absorber. To quantify this angular resolution penalty, we now introduce a *focusing efficiency* that relates the solid angle of the Airy pattern Ω_{Airy} to that of the actual imager angular response, Ω_0, as follows:

$$\eta_f = \frac{\Omega_{Airy}}{\Omega_0} \tag{7.15}$$

The imager solid angle is defined as follows:

$$\Omega_0 = \int_0^{2\pi} \int_0^{\pi/2} F(f, \theta, \phi) \sin\theta d\theta d\phi \tag{7.16}$$

and one can demonstrate that

$$\Omega_{\mathcal{A}iry} = \frac{\lambda^2}{\mathcal{A}_{ref}} \tag{7.17}$$

The focusing efficiency quantifies how much the angular response enlarges with respect to the diffraction limited case. In the case of antenna feeders, this efficiency corresponds to the ratio between the achieved directivity in the optical system and the directivity of a uniform circular aperture [3] . In Fig. 7.8 this efficiency is shown as a function of the absorber size normalized to $\lambda f_\#$ together with the spill-over efficiency for an ideal absorber under a reflector of $f_\# = 2$. It is apparent that for absorbers, the focusing efficiency is much lower than what would be theoretically possible for an antenna with a current distribution that is field matched to the direct field.

The spill-over and focusing efficiencies are commonly used in the antenna reflector community. For comparison, we include in Fig. 7.8 these efficiencies for a reflector fed by a uniform aperture antenna of side length w [Fig. 7.4(inset)]. The spill-over efficiencies (for the antenna calculated as defined in [139]) are nearly the same for both types of feeders, but the focusing efficiency is significantly different. Indeed, except for very small sizes, the antenna type feeders are more directive with respect to a commensurate absorber.

To quantify the tradeoff between the two different efficiencies in Fig. 7.8, we also plot the product of these two efficiencies. The maximum value of this product, in case of absorber feeders, is only 37% and it is achieved for $w = 1.2\lambda f_\#$, whereas antenna feeders achieved 71% for $w = 1.55\lambda f_\#$, thanks to a higher focusing efficiency, which can reach 82% for Gaussian horns [54]. Note, in the case of antennas the product between the spill-over efficiency and the focusing one corresponds to the aperture efficiency [139], except for any other losses in the antenna feeder itself. Instead, in the case of absorbers this product is simply a figure of merit that reminds the designer that larger absorbers lead to an inefficient use of the reflector aperture from an angular resolving point of view.

Tightly spaced FPAs of bare absorbers can sometimes be considered the preferred option due to a lower fabrication cost. As it can be seen from Fig. 7.8, bare absorber FPAs with $w \leq 0.75\lambda f_\#$, and focusing efficiencies higher than 80%, have a product of the two key efficiencies comparable to the one of antenna feeders. However, the background noise coming from the box surrounding the absorber should be properly controlled or calibrated, since the absorber has a wide angular response leading to higher sensitivity to undesired sources [47].

The conclusions drawn here can be applied to detectors located close to the focus, where a multi-cascade reflector system can be well modeled with a simplified on-axis parabolic reflector [69]. The achieved spill-over and focusing efficiencies of detectors located far from the focus highly depend on the actual optical system configuration.

[3] In the literature, the focusing efficiency for antennas can be referred to utilization efficiency [139], aperture efficiency [140] or taper efficiency [141].

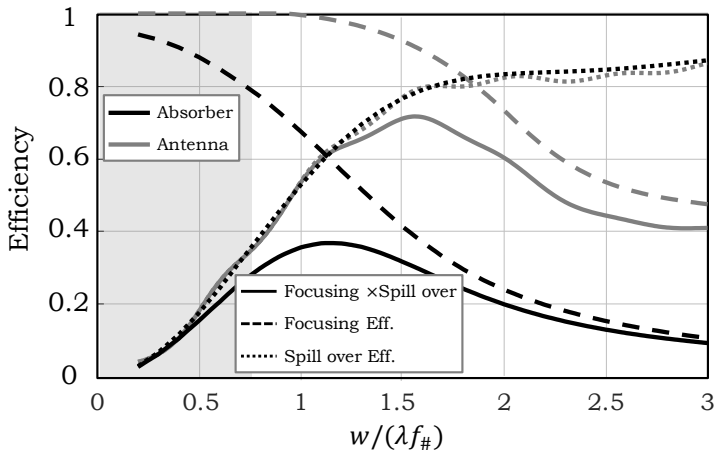

Figure 7.8: Focusing and spill-over efficiencies for both ideal antenna and absorbers, with a square dimension of side length w, under a reflector with $f_{\#} = 2$. The gray area indicates the region where the product of the two efficiencies, for the absorber and antenna feeders, are comparable.

7.5 Distributed-Sourse Response of Absorber Feeders

The optimization of a densely populated FPA requires finding a suitable trade-off between the sensitivity of each element and the imager resolution. In [47], the optimal FPA architecture that makes use of bare absorbers was studied in the case of background limited noise. Instead, most of the uncooled or medium cooled detectors are limited by the detector noise. In case of bolometric detectors [44], this noise is dependent on the bolometer physical dimensions w. Therefore, the optimal FPA architecture for these detectors will depend significantly on the aperture and focusing efficiencies, which should accurately be quantified.

The sensitivity of a passive imager can be related to the ability of the system in detecting variations in the temperature of a distributed incoherent source [22, 47]. Thus, it is related to the power received from a distributed source P_{abs}^{DS} , with an average temperature T_s, and angular dimension much larger than the beam of the reflector (imager point spread function).

The received power P_{abs}^{DS} over a certain bandwidth BW $= f_2 - f_1$, from incoherent sources operating in Rayleigh Jean's limit with an average temperature, T_s distributed over the full solid angle can be expressed as follows [142]:

$$P_{abs}^{DS} = \int_{f_1}^{f_2} \frac{k_B T_s}{\lambda^2} A_{eff}(f) \int_0^{2\pi} \int_0^{\pi/2} F(f, \theta, \phi) \sin\theta d\theta d\phi df \tag{7.18}$$

where $A_{eff}(f) = \eta_{ap}(f) A_{ref}$ is the effective area of the imager, k_B is the Boltzmann's constant, and $F(f, \theta, \phi)$ is the imager normalized angular response. Equation (7.18), with the efficiency definitions introduced in Section 7.4, becomes extremely useful for the design of absorbers. Using the definition in (7.15), (7.18) can be rewritten as follows:

$$P_{abs}^{DS} = k_B T_s \int_{f_1}^{f_2} \frac{\eta_{ap}(f)}{\eta_f(f)} df \tag{7.19}$$

This expression is valid for any coupling structure, such as antennas (single or multi-mode) and absorbers. For narrow band systems with bandwidth defined as BW $= f_2 - f_1$, where the integrand in (7.19) can be approximated constant around the central frequency f_0, one can rewrite (7.19) as

$$P_{abs}^{DS} \simeq k_B T_s BW \frac{\eta_{ap}(f_0)}{\eta_f(f_0)} \tag{7.20}$$

In the scientific literature, instead of the ratio $\eta_{ap}(f_0)/\eta_f(f_0)$, one typically finds the normalized throughput, $\mathcal{A}_{ref}\Omega_0/\lambda^2$, or the number of effective modes, m_{eff}, of the system [47], [50]. To clarify the discussion for the antenna community, one should consider that for single-mode antennas the aperture efficiency is proportional to the focusing efficiency itself; indeed, $\eta_{ap}^{ant} = \eta_{rad}\eta_f$, where η_{rad} is the radiation efficiency [139] (i.e., the ratio between the gain and the directivity in reflectors). Thus, the normalized throughput becomes

$$\frac{\mathcal{A}_{ref}\Omega_0}{\lambda_0^2} = \begin{cases} \dfrac{\eta_{ap}(f_0)}{\eta_f(f_0)}, & \text{for absorbers} \\ \eta_{rad}(f_0), & \text{for single-mode antennas.} \end{cases} \tag{7.21}$$

Therefore, for single-mode antennas: $\mathcal{A}_{ref}\Omega_A/\lambda_0^2 = \eta_{rad} \leq 1$ and the power received becomes $k_B T_s BW \eta_{rad}$, which is the standard expression in microwave radiometry [142]. Instead, for bare absorber, $\mathcal{A}_{ref}\Omega_A/\lambda_0^2$ can be a number much larger than unity. Note that for the case of *Lambert's* absorber without a reflector ($\eta_{ap} = 1$), the absorber's throughput becomes the well-known expression in radiometry [47]: $\mathcal{A}_{ref}\Omega_A = \lambda_0^2\eta_{ap}(f_0)/\eta_f(f_0) = \pi\mathcal{A}_{ref}$.

The term $\eta_{ap}(f_0)/\eta_f(f_0)$ is plotted in Fig. 7.9 for the case of an ideal absorber under a parabolic reflector with $f_\# = 2$. The normalized throughput $\mathcal{A}_{ref}\Omega_0/\lambda_0^2$, derived accordingly to [47] by using Airy pattern considerations, is also reported in Fig. 7.9. The agreement is very good since the calculations were done for an ideal absorber under a large $f_\#$ parabolic reflector. However, the analysis proposed in this paper can accurately quantify the normalized throughput for many other cases such as optics with small $f_\#$ (common in integrated lenses [11]), absorbers with a non-flat angular response [41], or even resonant absorbers [10, 21, 129]. As an example, Fig. 7.9 also shows the normalized throughput for an ideal absorber under a $f_\# = 0.6$ parabolic reflector. In such case, its value differs significantly from the one calculated with the Airy pattern formula [47], leading to a lower power received from a distributed incoherent source and, therefore, lower sensitivity.

7.6 Numerical Examples

In this section, the results calculated with the proposed methodology are compared with those obtained by using full-wave simulations. An absorber made of linear resistive strips above a $\lambda/4$ back reflector is

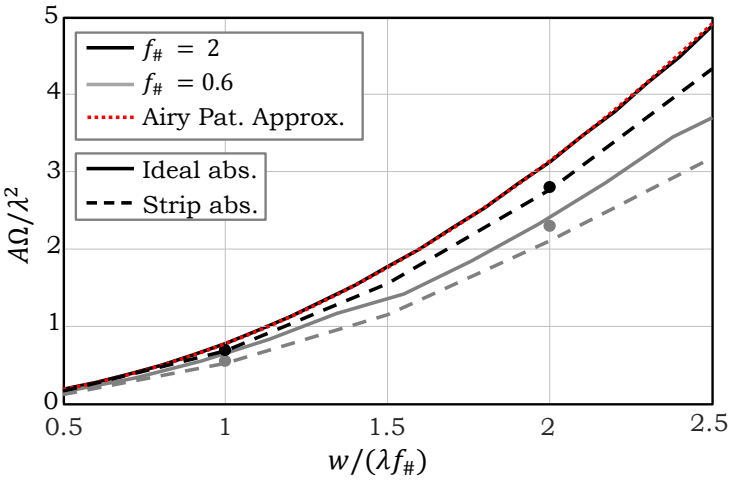

Figure 7.9: Normalized throughput calculated as η_{ap}/η_f versus the absorber size, w, for two optical systems with $f_\# = 0.6$ (gray) and $f_\# = 2$ (black). The solid lines corresponds to the geometry of the ideal absorbers, the dashed lines to an absorber based on resistive strips, and the filled circle marks to the relevant FW simulations. The dotted red line corresponds to the Airy pattern considerations in [47].

considered as a test case. For this case, a reference analytical circuit is available in [133]. The absorber is composed of resistive mesh strips with a surface resistance of $R_s = 10\ \Omega/\square$ and width of 2.7μm. The strips have a periodicity of $d_y = 102\mu$m, and back short distance of $h_{bs} = 150\mu$m. The total dimension of the absorber is $w \times w$ (Fig. 7.5). The operating frequency for this example is 500 GHz.

7.6.1 Large f-number Optics

As described in Section 7.4, the angular response for absorbers under a large $f_\#$ optical system, according to (7.14), is basically the convolution of the total field with the spatial domain of the absorber. In such a case, when the absorber can be considered ideal, the throughput can be evaluated using Airy pattern considerations as in [47]. The plane wave response of the considered absorber is shown in Fig. 7.3, showing similar angular response to the ideal absorber. The absorbed power has been evaluated by using the equivalent circuit proposed in [133], as well as the generic circuit for an arbitrary absorber shape described in Sec. 7.3.

In Fig. 7.10(a) and (b), the power absorbed by the linear strip mesh, placed under a parabolic reflector with $f_\# = 2$ and diameter $D = 100\lambda$, is shown versus the plane wave angle of incidence, for two different physical dimensions of the absorber. (The absorber is made of 7 and 14 resistive strips for the $w = 2\lambda$ and $w = 4\lambda$ cases, respectively.) The incident plane wave is assumed having amplitude $|E_0|$= 1V/m and polarization along x. The results are compared with those carried out by using full-wave simulations. Specifically, first the direct field focalized by the reflector on a square area at a z-quote above the absorber (Fig. 7.11) is evaluated by using the PO solver of GRASP. Then, the field is used as an external source in CST MS to compute the power dissipated into the resistive strips. Since the procedure has to be repeated for each angle of the plane wave impinging on the reflector, $\Delta\theta_i$, the computation of the angular response via the FW simulations is time-consuming, and for this reason the results are reported only for a limited number of incident angles. On the contrary, the FO spec-

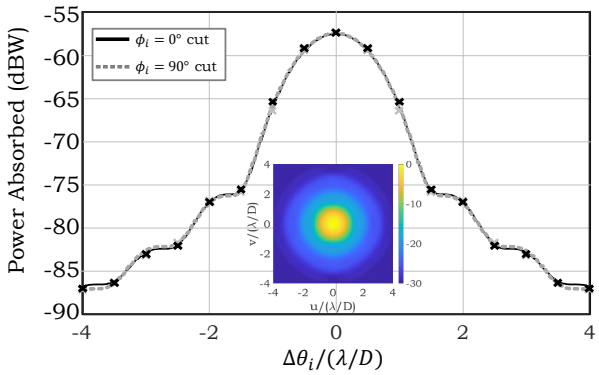

(a)

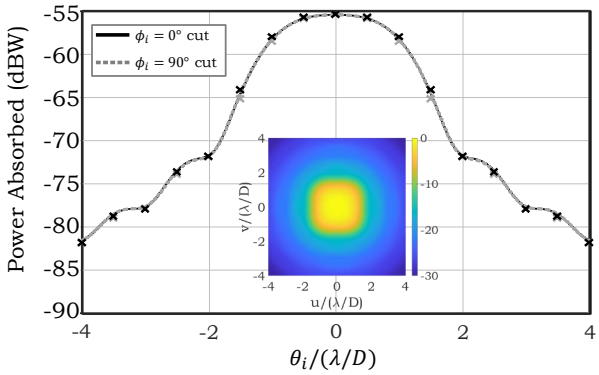

(b)

Figure 7.10: Power absorbed versus the plane wave incident angle (non-normalized angular response) of a linear strip absorber with side length w coupled to a reflector with $f_\# = 2$. (a) $w = \lambda f_\#$ and (b) $w = 2\lambda f_\#$. Solid lines: calculated by using (7.14). Cross marks: obtained via FW simulations. The inset illustrates the 2-D response in u-v coordinates.

tral method takes a few minutes for obtaining an accurate 2-D angular response of the imager. The agreement between both methods is excellent.

The aperture and the focusing efficiencies of a strip absorber under a $f_\# = 2$ parabolic reflector can be estimated by using both the FO and FW approaches. Results are summarized in Table 7.1, showing excellent agreement. Normalized throughputs can also be estimated for the cases given in Table 7.1 by using (7.21). The aperture efficiencies are slightly lower than those related to the ideal absorber (Fig. 7.8), due to the fact that the strip mesh structure presents a small mismatch with the incoming waves. In particular, the imaginary part of the strip absorbers presents an inductive behavior, that leads to only 93% absorption of the impinging power, for broadside plane wave illumination as shown in Fig. 7.3. The focusing efficiencies are instead comparable. Therefore, the normalized throughput is slightly lower than the one of the ideal absorber (Fig. 7.9).

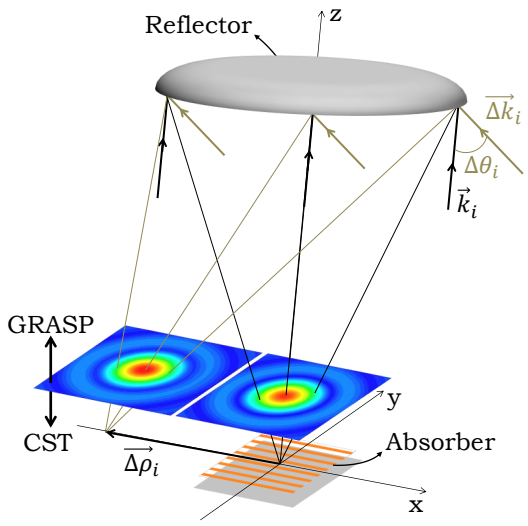

Figure 7.11: Schematic representation of the geometry under discussion and of the GRASP + CST full wave simulation procedure. The direct field is obtained by GRASP and then used as an external source in CST.

Table 7.1: Comparison of efficiencies for strip absorbers below a parabolic reflector with $f_\# = 2$

	Fourier Optics	Full Wave
$w = \lambda f_\#$	$\eta_{ap} = 48\%$ $\eta_f = 70\%$ $A\Omega/\lambda^2 = 0.7$	$\eta_{ap} = 49\%$ $\eta_f = 70\%$ $A\Omega/\lambda^2 = 0.7$
$w = 2\lambda f_\#$	$\eta_{ap} = 76\%$ $\eta_f = 27\%$ $A\Omega/\lambda^2 = 2.8$	$\eta_{ap} = 77\%$ $\eta_f = 27\%$ $A\Omega/\lambda^2 = 2.8$

7.6.2 Small f-number Optics

The lower the $f_\#$, the more difficult is to evaluate the performances of absorbers under optical systems. First, the absorber angular response cannot be approximated by a convolution with the broadside total field since the shape of the direct field changes significantly even for an incident angle of a couple of HPBWs due to the coma phase term (Fig. 2.7). Second, the absorber plane wave response can affect significantly the shape of the total spatial fields. Third, the absorber's overall physical dimension can be comparable to the wavelength, or even smaller, making the FO + Floquet-modes approach not applicable.

The calculated angular response of a strip absorber of $2\lambda f_\#$ (7 strips) in side length under a reflector with $f_\# = 0.6$ is shown in Fig. 7.12(b), and compared with FW simulations. The agreement is very good even if the absorber is only $1.2\lambda \times 1.2\lambda$. The FW absorbed power is slightly higher in the $\phi_i = 0°$ cut, which can be associated with edge effects due to the finiteness of the strips. Smaller absorber dimensions, such as the case shown in Fig. 7.12(a) (absorber with a $w = 0.6\lambda$ and only 3 strips), will

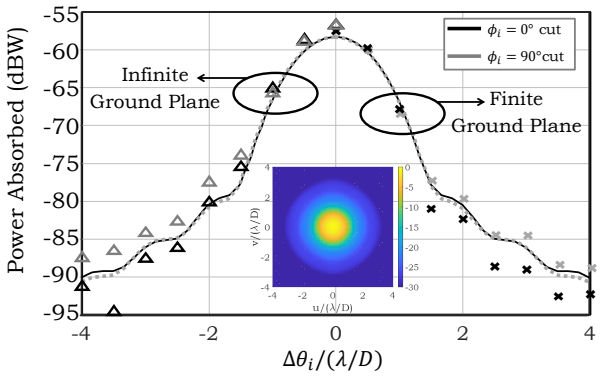

(a)

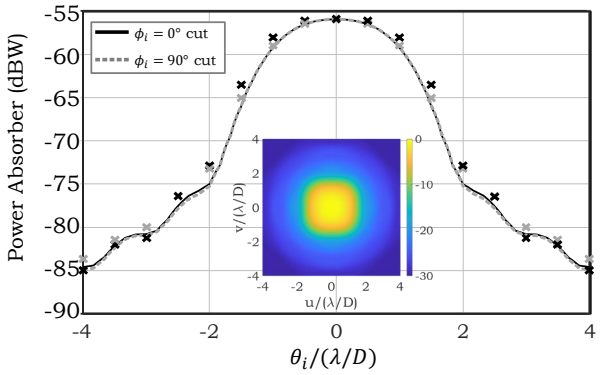

(b)

Figure 7.12: Power absorbed versus the plane wave incident angle (non-normalized angular response) of a linear strip absorber with side length w coupled to a reflector with $f_\# = 0.6$. (a) $w = \lambda f_\#$ and (b) $w = 2\lambda f_\#$. Solid lines: calculated by using (7.10). Cross marks: obtained via FW simulations. The inset illustrates the 2-D response in u-v coordinates.

lead to larger discrepancies between the FO and FW simulations. Indeed, in such case, the absorber effective area is larger than the physical one as shown in Fig. 7.4, and the edge effects are even more significant. Despite this, the agreement with FW simulations is still quite good as shown in Fig. 7.12(a) for both a finite and an infinite back short.

The values of the simulated aperture and focusing efficiencies are summarized in Table 7.2 for both absorber dimensions. The FW simulated focusing efficiencies are about 10% different in both cases due to the edge effects, whereas the aperture efficiency of the smallest case ($w = \lambda f_\#$) is 15% higher than predicted with the FO tool due to a larger effective area than the physical one. The values of the aperture efficiency for both cases are lower than the values given for large $f_\#$, due to the variation of the absorber response to the incident plane waves, as shown in Fig. 7.3; instead, the focusing efficiency is higher than the cases shown in Table 7.1, because of the coma distortion in the direct field.

Table 7.2: Comparison of efficiencies for strip absorbers below a parabolic reflector with $f_{\#} = 0.6$

	Fourier Optics	Full Wave
$w = \lambda f_{\#}$	$\eta_{ap} = 40\%$ $\eta_f = 74\%$ $A\Omega/\lambda^2 = 0.53$	$\eta_{ap} = 46\%$ $\eta_f = 82\%$ $A\Omega/\lambda^2 = 0.56$
$w = 2\lambda f_{\#}$	$\eta_{ap} = 68\%$ $\eta_f = 32\%$ $A\Omega/\lambda^2 = 2.1$	$\eta_{ap} = 67\%$ $\eta_f = 29\%$ $A\Omega/\lambda^2 = 2.3$

As it can be seen in Table 7.1 and 7.2, as the strip absorbers side length increases, the aperture efficiency of the system increases. However, larger side length also leads to lower focusing efficiency. These results are in line with the ones shown in Fig. 7.8, for ideal absorbers. As shown in this figure, the optimum side length value for ideal absorber, in terms of high aperture efficiency and good imager resolution (high focusing efficiency), is $w \simeq 1.25\lambda_0 f_{\#}$. In the case of an absorber with non-ideal response (e.g. strip absorbers) coupled to a QO system with small f-number (large comma phase distortions), the optimal side length could be a different value.

In Fig. 7.9, the estimated values for the normalized throughputs in case of the linear resistive mesh are also shown for the two considered reflectors, using both the FO approach and the FW simulations. The values obtained for all cases are lower than the ones estimated in [47]. It can be noted that for some cases the absorber receives up to 40% less power than the one estimated in [47], leading to a less sensitive instrument.

7.7 Conclusion

Passive imaging cameras at sub-millimetre wavelengths are being developed by using bare absorbing meshes without any antenna coupling (lens or horn) structures in the focal plane of a focusing system. The design of such arrays is typically done resorting to geometrical considerations or basic broadside plane wave incidence analysis. In this chapter a spectral electromagnetic model, that is based on linking a plane wave spectral representation of the direct field focused by the optical system with a Floquet-waves representation of the field in the absorbing mesh, is described. The results obtained by the present model have been compared, with excellent agreement, with those obtained by FW simulations. Thus, the proposed spectral method provides an accurate and efficient way to estimate the key optical properties of the imager inside the region of validity of the FO.

The most important design aspect that emerges from this chapter, for focusing systems in reception, is associated with the introduction of the intuitive focusing efficiency parameter. This parameter leads to two important conclusions. First, when comparing bare absorber FPAs and antenna feeders of equivalent dimensions, the latter leads to higher focusing efficiencies, and therefore better imaging resolution. Only very tightly sampled absorber based FPAs lead to a comparable trade-off in terms of received power and angular resolution, when compared to antenna based FPAs. Second, while for antennas it is well known that the power received from a distributed incoherent source is $P_{ant}^{DS} = \eta_{rad} k_b T_s BW$,

for absorber based FPAs, the corresponding received power is typically quantified introducing an effective number of modes: $P_{abs}^{DS} = m_{eff} \times k_b T_s BW$. Here, it is shown that the effective number of modes m_{eff} can be conveniently evaluated as the ratio between the aperture, η_{ap}, and the focusing efficiency, η_f.

Chapter 8

A Dual Band Focal Plane Array with Frequency Selective Absorbers

Passive imaging cameras at sub-millimetre wavelengths with large format focal plane arrays are being developed as the next generation of security screening systems. In this chapter, a dual-band focal plane array (FPA) for security imagers at sub-millimetre wave frequencies is presented. The detectors are based on bolometric superconducting kinetic inductance resonators, which allows the development of large FPAs at medium cryogenic temperatures. Two frequency selective absorber (FSA) sets coupled to superconductive resonator lines are designed to implement a dual color security imager. The performance of the dual band imager is evaluated using the spectral analysis approach that combines Fourier Optics with a Floquet-modes field representation, as presented in previous chapter. The geometry of the unit cells is based on a Jerusalem cross configuration and the designed FSAs show a stable angular response and a rejection 1 *to* 3 *of the undesired bandwidth. The detectors in the dual band FPA are distributed over a hexagonal grid to maximize their physical size and then improve their sensitivity. The effective pattern of the imager coupled to a black body point source over a wide frequency band (bandwidth ratio of* 6 : 1*) was demonstrated experimentally with excellent agreement to the one estimated by using the proposed spectral technique.*

8.1 Introduction

As discussed in Ch. 1, the next generation of THz imagers for stand-off detection of concealed weapons, [20, 120, 121, 122], will require wide Field-of-Views (FoVs), at quasi-video rate, higher than 10 Hz. The architecture of such imagers is typically composed of a Quasi-Optical system, a focal plane array (FPA), and a mechanical scanner. A FPA with a large number of elements would dramatically reduce the need for a fast-mechanical re-pointing of the optics, and, consequently, allows a much longer integration time for the detectors (comparable in this case to the frame rate), thus relaxing the required detector sensitivity.

Promising solutions for development of sub-millimetre wavelength FPAs in the order of several thousands of detectors are based on kinetic inductance detectors (KIDs) [12, 97, 143]. The KIDs are incoherent superconductor-based detectors and many of them can be coupled to a single low-frequency readout line, decreasing significantly the complexity of large FPA architectures. The coupling of the KIDs to the readout line is based on low-frequency superconductive resonators with high-quality factor. The radiation at sub-millimetre wavelengths can be absorbed either via antennas coupled to resistive transmission lines [12] or bare absorbers [144]. The power absorption corresponds to a shift of the resonant frequency and a decrease of the quality factor.

KIDs can operate in two different regions. The non-equilibrium mode relies on the finite lifetime of the quasi-particle excitations [12]. Here, we concentrate on the kinetic inductance bolometer (KIB) mode in which the superconductor is in a local thermal equilibrium with its surroundings, and the detection is based on the temperature dependence of the Kinetic Inductance, as originally proposed in [145].

The noise equivalent power (NEP) of KIDs operating in non-equilibrium mode is in the order of $10^{-20}\ W/Hz^{1/2}$ [12] for operation temperature below 1 K. This configuration was used for security imagers in [21]. The main drawback of this solution is the high cost of the required top-performance cryostat.

In the thermal region, KIBs measure the temperature change of a thermally isolated volume due to the THz radiation being absorbed. Similar to non-equilibrium mode, the variation in the inductance of the structure can be readout via superconductive resonators. However, in this region, the requirement for the operating temperature is relaxed to about 5 to 10K, allowing the use of low-cost cryogenic coolers. The NEP of these detectors is in the order of $10^{-15}\ W/Hz^{1/2}$ [41], much higher than the non-equilibrium mode, but sufficient for security applications. Therefore, KIBs provide the possibility of having large FPAs with medium-cooled temperature and a reduced cost for passive imaging [41].

Exploiting this technology, in this study, a FPA suited for future security applications is designed as shown in Fig. 8.1(a). The outer diameter of the FPA has been set to $\varnothing = 24$ cm, corresponding to the maximum useful window of the cryostat. The basic structure of the focal plane and the detectors is depicted in the micro-photographs of Fig. 8.1(b) and (c). The total number of the detectors is 8208, organized on six detector tiles with 80mm $\times$ 75mm active area consisting of 1368 detectors. The thermal isolation is obtained via through-wafer released membrane which is perforated to optimize the thermal coupling to the substrate, and to minimize the heat capacity. For readout, the thermometer is tuned into an individual RF readout frequency with an off-membrane tuning capacitor C_i and matched to a 50 Ω readout line with a coupling capacitor $C_{c,i}$, as schematically illustrated in Fig. 8.1(d). Here, i refers

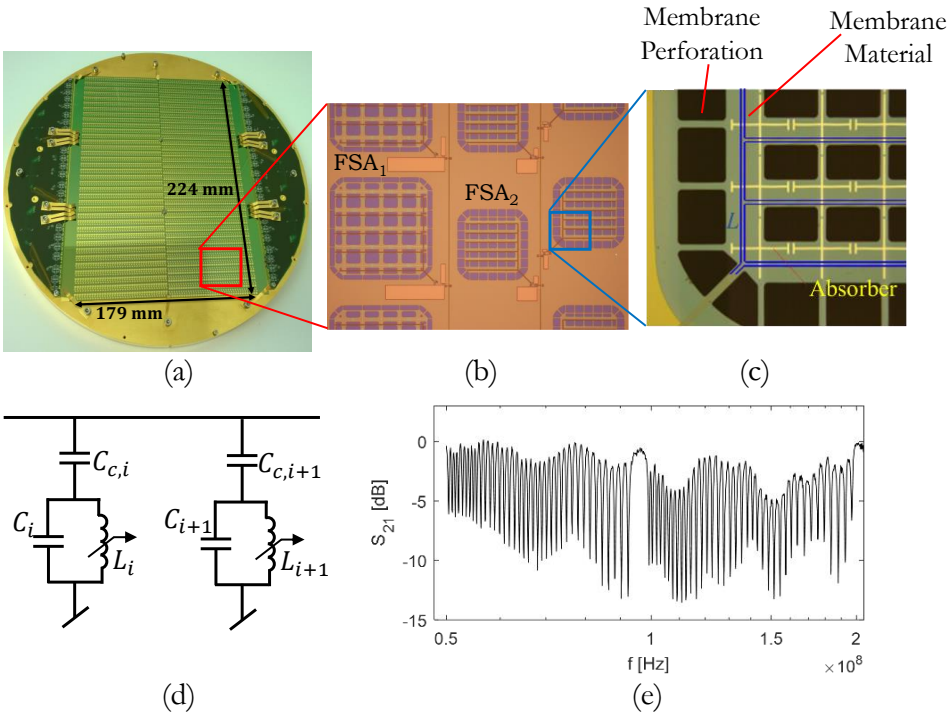

Figure 8.1: (a) Dual-band FPA with 8208 KIBs. (b) Micro-photograph illustrating the two FSA sets. (c) Zoom-up showing a piece of detector membrane and the structures on it. The kinetic inductance thermometer L is emphasized in blue for clarity. (d) Electrical equivalent circuit of a piece of multiplexed readout line. (e) Readout band transmission spectrum within a readout channel with each spike corresponding to an individual readout frequency of a detector.

to the detector index within a readout channel consisting of 114 detectors per channel in this case. The total number of readout channels is 72. The readout band transmission within one readout channel is plotted in Fig. 8.1(e). As it can be seen, the readout frequency band for this particular channel is from 50 to 200 MHz. Similar data were acquired from 15 readout channels indicating good detector yield (> 95%) in line with the data of [41]. Moreover, in [146], concealed object detection has been demonstrated with the imaging system which is described in this study, i.e., the same optical system together with the designed dual-band FPA.

Security applications demand high probability of detection, which can be achieved by using passive images taken at different frequency bands [147], i.e., multi-band images. To this end, we propose here to modify the absorber design in [143] to be frequency selective [148] around specific frequency bands. The FPA will then consist of frequency selective absorbers (FSAs) for the lower bandwidth centered at 250 GHz; interleaved with the ones for the higher bandwidth centered at 500 GHz, these detectors are referred to as FSA1 and FSA2 , respectively, in Fig. 8.1(b). The proposed architecture can be operated in combination with a linear scanner to generate fully sampled images in the two bands. Each FSA detector set has been designed to absorb in its corresponding frequency band of operation and reject the radiation from the other band with a factor of 1 to 3. The use of a single-frequency selective layer has been chosen as a compromise between the cost and the rejection factor. The quasi optical system of the imager is a dual-lens architecture described in [39], which allows full body imaging. The f-number

$f_{\#}$ (ratio between the focal distance and diameter of the optics) is set to 2. Obtaining a two-dimensional (2-D) image of the full human body is required from the application point of view. To achieve this requirement, a sparse 2-D absorber-based array is placed at the focal plane of the dual-lens system. By combining this configuration with a one-dimensional (1-D) mechanical scanner, the field of view (FoV) is fully imaged in two dimensions.

In order to analyse the performance of an imager based on a FPA made of bare absorbers, the spectral Fourier Optics (FO) technique described in Chapter 2 is used. This technique couples the spectrum of the optical system with Floquet-modes representation in the surrounding of the periodic absorber as in Sec. 7.3. This technique provides an accurate methodology to derive the point spread function (PSF) and efficiency of the imager to monochromatic point sources. The effective PSF of the imager coupled to a black-body point source over a wide frequency band (bandwidth ratio of $6:1$) was estimated theoretically and demonstrated experimentally. Finally, the performance of the imager coupled to a distributed incoherent source in terms of the sensitivity is evaluated.

This chapter is structured as follows. Section 8.2 describes the design of the FSAs for the two operational bandwidths. The architecture of the dual-band FPA is discussed in Section 8.3. In Section 8.4, the experimental validation of the performance of the imager in terms of the effective PSF is presented. Concluding remarks are reported in Section 8.5.

8.2 FSA-Based KIBs

In this section, the geometry of the proposed detectors is presented and analysed. The selected architecture and the design considerations used to optimize the frequency, angular, and polarization responses are discussed. Moreover, the optimization of the FSA including the KIB resonator lines along with its performance is reported.

8.2.1 Design Considerations

The geometry of the KIBs as introduced in [41] is shown in the inset of Fig. 8.2. The thermal confinement is achieved by placing the absorber and kinetic inductance thermometer on a 200nm thick SiN membrane. The on-membrane structure is composed of two layers: a resistive mesh grid, 100nm thick TiW layer, with a surface resistance of $R_s = 5\Omega/\square$, and a superconducting meander strip, 100nm thick, acting as the thermometer below the grid. The superconductor material is NbN with the nominal critical temperature of 11 K as estimated from the calibration measurements of films deposited with similar parameters. The surface impedance of the superconductive material, in the sub-millimetre wavelengths, is shown in Fig. 8.2 as estimated from the theory of Mattis and Bardeen [149]. The layers are separated by a thin SiO_2 layer with the thickness of 150nm and dielectric constant $\varepsilon_r \simeq 5$. The mesh grid absorbs the incoming radiation, and heats the elements on the membrane, which in the operating temperature range of 5-10 K are essentially in thermal equilibrium. The thermal conductivities from the membrane to the substrate of the membranes are estimated from the geometry and experimentally recorded material parameters in [41] to be 190 and 140nW/K for the FSA1 and FSA2 detectors, respectively. The temperature dependence of the superconducting kinetic inductance is then used to readout the temperature change.

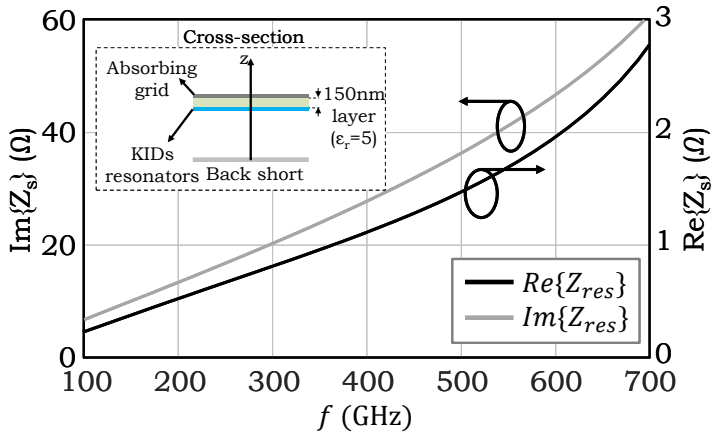

Figure 8.2: Surface impedance of the proposed superconductive resonator. Inset shows the cross section of the detectors where the resistive layer, the resonator lines, and thin dielectric membrane are indicated by the colors gray, blue, and green, respectively.

In this chapter, the goal is to design the detector's geometry as two different FSA layouts each with a limited bandwidth around 250 and 500 GHz, respectively, with a nearly flat angular response up to 30°. This requirement is due to the geometrical size of the FPA with respect to the dual-lens system. At the worst case, i.e., for detectors at the edge of the FPA, the rays arriving from the dual-lens system illuminate the detector with a maximum incident angle of 30°.

For broadside plane-wave incidence, a resistive square mesh, Fig. 8.3(a), can be modeled using an equivalent circuit model, Fig. 8.3(b), with a resistance and an inductance in parallel to a transmission line representing the fundamental Floquet-modes. The lumped elements values can be calculated analytically [133], and are reported in Table 8.1, where R, L, and C parameters represent the lumped resistance, inductance, and capacitance, respectively. In order to introduce a frequency selectivity to the resistive layer, the mesh grid can be loaded with a distributed capacitance using the geometry of Fig. 8.3(c), typically referred to as a Jerusalem Cross (JC) [150]. The corresponding equivalent circuit is shown in Fig. 8.3(d), and it presents an additional capacitance compared to the mesh grid, that allows a resonant behavior. The geometrical parameters of the designed sets of FSAs are reported in Table 8.2 (columns 2 and 4), where λ_1 and λ_2 are the wavelengths at 250 and 500 GHz, respectively, whereas the corresponding lumped components, derived using CST MWS [79] simulation, are listed in Table 8.1. As shown in Fig. 8.4(a) (solid lines), the FSAs introduce a frequency selectivity not present in the original mesh grid.

The absorption rate and out of band rejection of a freestanding resistive layer can be improved by using a back short. The use of a quarter wavelength back short for the FSA1 will introduce a significant rejection in the 500 GHz band. The FSA2 is instead designed with a much closer back short, to short circuit the lower part of the frequency band. The capacitive behavior in the FSA2 compensates the inductance introduced by the back short, allowing a reasonable impedance match to the free-space

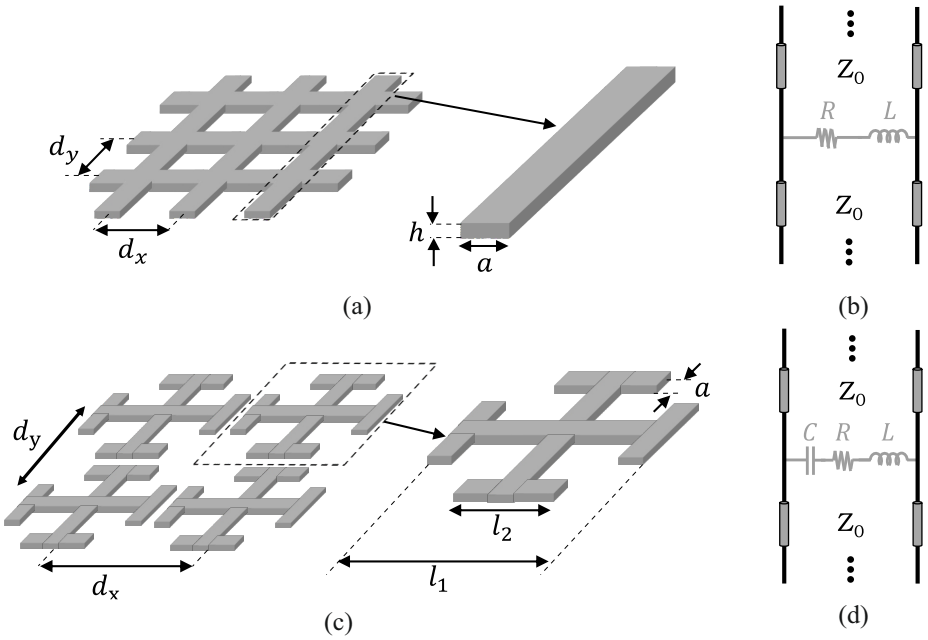

Figure 8.3: Geometry (a) and equivalent circuit representation (b) of a resistive squared mesh. Geometry (c) and equivalent circuit representation (d) of a freestanding FSA.

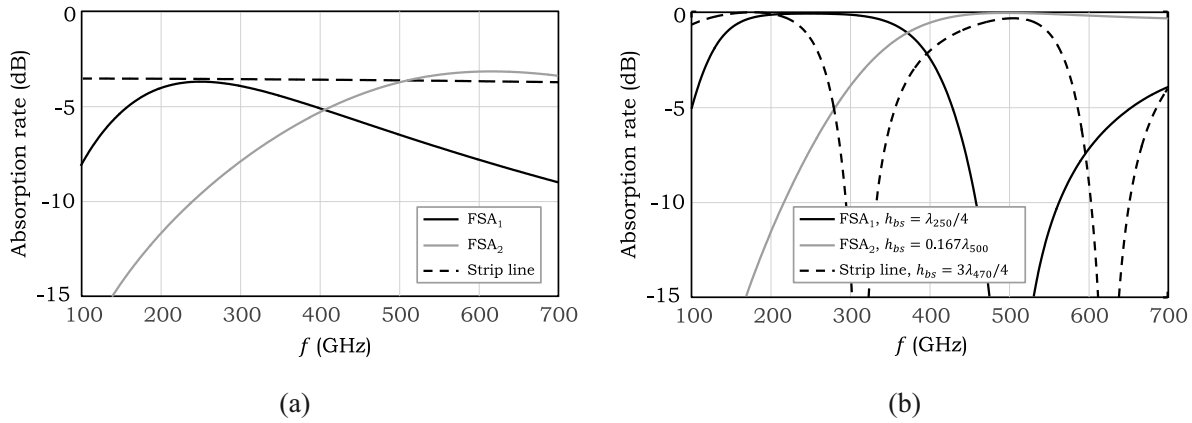

Figure 8.4: Absorption rate, simulated with CST MWS, of a continuous strip line compared to two free-standing FSAs under a broadside plane wave incident: (a) Without and (b) with the back short layer.

impedance. The back short distance h_{bs} for the two FSA sets are reported in Table 8.2, and the described frequency response is shown in Fig. 8.4(b). The frequency selectivity could be further enhanced if the detectors were fabricated using a multilayer periodic structure, similar to [137]. However, one should take into account that in this study, a reflect/absorb frequency selective structure is desired instead of a transmit/absorb one.

Table 8.1: Lumped elements of the circuit model

Parameter	Mesh Grid	JC FSA1	JC FSA2
R	417 Ω	420 Ω	270 Ω
L	1.015×10^{-10} H	2.45×10^{-10} H	1.07×10^{-10} H
C	-	16.5×10^{-16} F	6.25×10^{-16} F

Table 8.2: Design parameters of the FSAs

Parameter	Free Standing FSA1	FSA1 + Resonator	Free Standing FSA2	FSA2 + Resonator
a	$0.003\lambda_1$	$0.005\lambda_1$	$0.005\lambda_2$	$0.008\lambda_2$
l_1	$0.241\lambda_1$	$0.238\lambda_1$	$0.242\lambda_2$	$0.237\lambda_2$
l_2	$0.108\lambda_1$	$0.042\lambda_1$	$0.042\lambda_2$	$0.043\lambda_2$
l_3	-	$0.033\lambda_1$	-	$0.243\lambda_2$
h_{bs}	$0.250\lambda_1$	$0.250\lambda_1$	$0.167\lambda_2$	$0.167\lambda_2$
d	$0.250\lambda_1$	$0.250\lambda_1$	$0.250\lambda_2$	$0.250\lambda_2$
a_{res}	-	$0.003\lambda_1$	-	$0.007\lambda_2$
d_{res}	-	$0.071\lambda_1$	-	$0.063\lambda_2$
Δ_{res}	-	$0.004\lambda_1$	-	$0.008\lambda_2$

8.2.2 Proposed Unit Cell Implementation

The KIB detection mechanism requires additional superconductive thermometer lines underneath the FSA separated by a dielectric membrane as mentioned in Section 8.2.1. These superconductive lines can be modeled, as two thin horizontal strip lines with the sheet impedance as estimated from the theory of Mattis and Bardeen [149], as shown in Fig. 8.2. Due to the presence of the superconducting lines, the absorption rate of the FSAs, in terms of frequency and polarization response, is significantly altered. These effects, however, can be compensated for by modifying the geometry of the JC FSAs differently for vertical and horizontal polarizations. The proposed FSA unit cells combined with the resonators are shown in Fig. 8.5, and their geometrical parameters are reported in Table 8.2 (columns 3 and 5). In Fig. 8.6, the simulated absorption rates for both optimized FSA sets are shown. The frequency variation is comparable to the one of the free-standing design. Moreover, no significant variation was observed for incidence angles up to 30° for both polarizations.

Since the FSA and the resonator lines are separated by an electrically thin membrane, the structures in Fig. 8.5 are difficult to model using lumped elements because of the coupling between the layers via higher order Floquet-modes. Therefore, an equivalent circuit model based on an admittance matrix $\bar{Y}_{abs}(\vec{k}_\rho)$ representing the scattering of the FSA unit cells, as described in Sec. 7.3, will be used in the next sections to evaluate the coupling of the FSA KIBs to the optical system. Such matrix was evaluated using CST MWS simulations with periodic boundary conditions.

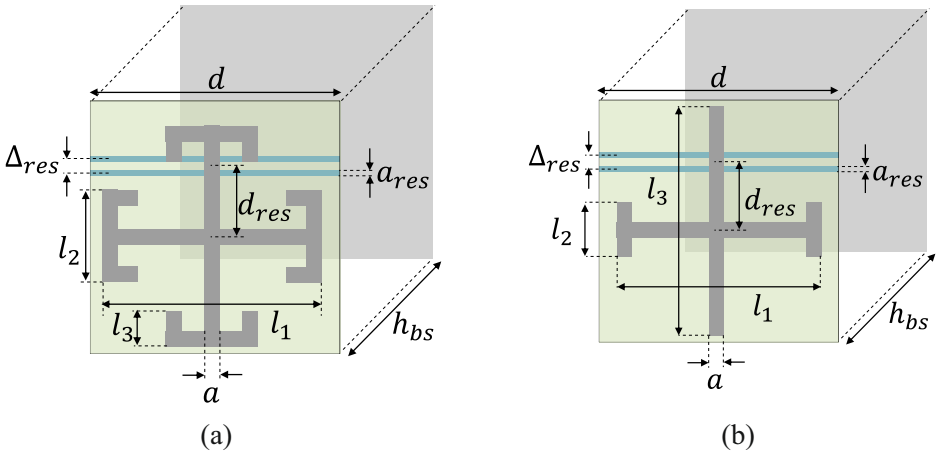

Figure 8.5: Unit cell of FSAs including the superconductive layer and their geometrical parameters. (a) FSA1 . (b) FSA2.

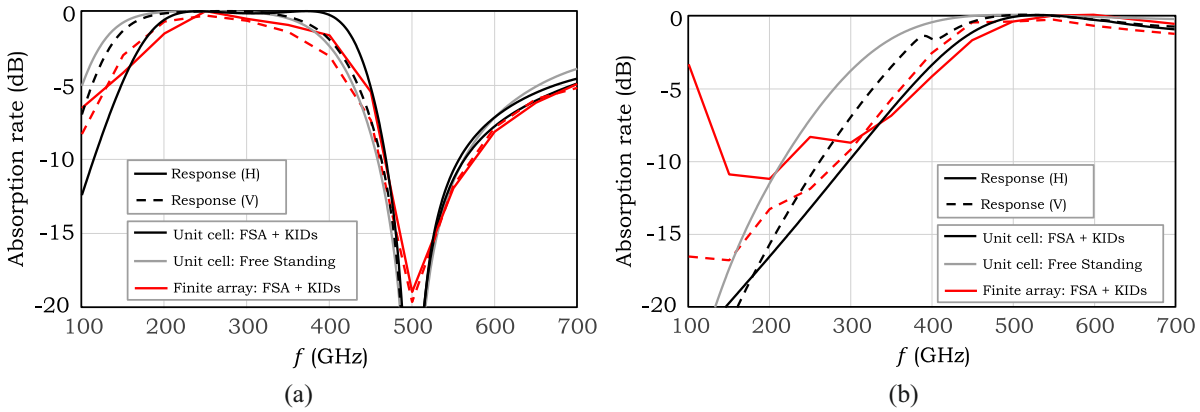

Figure 8.6: Absorption rate, simulated with CST MWS, of the optimized design including the resonator layer compared to the free-standing design: (a) FSA1 , (b) FSA2 . The response for the horizontal and vertical polarizations is referred to as H and V, respectively.

8.3 Dual-Band FPA

In this section, the design of the KIBs-based FPA for dual-band operation is presented. The distribution of the FSA-based KIBs over the focal plane is defined as a tradeoff between the expected imager sensitivity, the half power beam-width (HPBW), the mechanical requirements, and the fabrication constrains of the detector.

8.3.1 Focal Plane Configuration

The sensitivity of the imager can be estimated as its noise equivalent temperature difference (NETD), which determines the ability of the system in detecting variations in the temperature of the source. The expression of NETD for the absorbers in the focal plane can be expressed as [22]

$$NETD = \frac{1}{\sqrt{2\tau_i^p}} \frac{NEP}{\partial P_{DS}/\partial T} \tag{8.1}$$

where P_{DS} is the power received by the imager from a distributed incoherent source in two polarizations, NEP is the noise equivalent power of the detectors, and τ_i^p is the integration time per pixel. The NEP of bolometers, such as the KIBs considered in this study, follows the classical phonon noise expression as given in [143].

In a fully sampled FPA, the integration time is inversely proportional to the frame rate $\tau_i^p = 1/f_r$. Here, instead, the available detectors on the focal plane are divided between the two bands of interest and a linear scanner is needed to generate fully sampled images. Therefore, the integration time per pixel in (8.1), $\tau_i^p = \frac{1}{f_r N_s}$, is reduced by the scanning penalty ratio N_s , which in turn leads to a sensitivity degradation. This penalty can be compensated by increasing the power received by the detectors with a larger physical area and more bandwidth.

For non-fully sampled FPAs, the optimum configuration in terms of sensitivity typically leads to a distribution of the detectors over a hexagonal grid combined with a 2-D jiggling mechanism, [47, 49], since this allows for the largest physical dimensions of the detectors. However, a FPA based on bare absorbers suffers from a significant penalty in angular resolution for large dimensions as described in [151]. Moreover, a 2-D jiggling mechanism requires a scanner operating at much higher speed than the frame rate [49]. Instead, here, the FPA configuration has been designed to be compatible with a single-axis scanning mechanism. The proposed FPA is a sparse 2-D array of detectors placed in a hexagonal grid. This configuration is combined with a 1-D mechanical scanner to fully fill the field of view. The layout of a portion of the FPA is shown in Fig. 8.7(a). Moreover, the arrow shown in the figure indicates the direction of the scanning mechanism. A passive image requires a sampling of the focal plane field at $0.5\lambda_0 f_\#$ [47], when a square grid FPA is considered. Instead, in the current design, a 45° grid FPA is used, allowing the spacing between the FPA elements to be enlarged to $0.61\lambda_0 f_\#$ [49]. Since the number of sampling points is frequency dependent, the number of FSA2 detectors will be twice the number of FSA1 detectors. The location of the lower bandwidth detectors is shown in Fig. 8.7(b) with filled black circles. They are located in linear vertical arrays with a spacing of approximately 2 mm and the horizontal distance between them is 6.2 mm. The mechanical scanner will operate in the 45° plane and will acquire $N_{s,1} = 6$ image pixels [non-filled circles in Fig. 8.7(b)] per detector. The detectors at the higher band are instead distributed in interleaved tilted arrays as shown in Fig. 8.7(c). As a result, the scanning time penalty will be $N_{s,2} = 12$. This layout has been chosen for three reasons: 1) to maximize the physical area for the higher frequency pixels, 2) to use the same scanning mechanism for both frequencies, and 3) to optimize the silicon wafer use, considering the fabrication tolerances. The physical dimensions of the two detector sets are fixed to $w_1 = 0.625\lambda_1 f_\#$ and $w_2 = 0.75\lambda_2 f_\#$, respectively. These values lead to a comparable utilization of the optical aperture to the one of an antenna-based FPA [151].

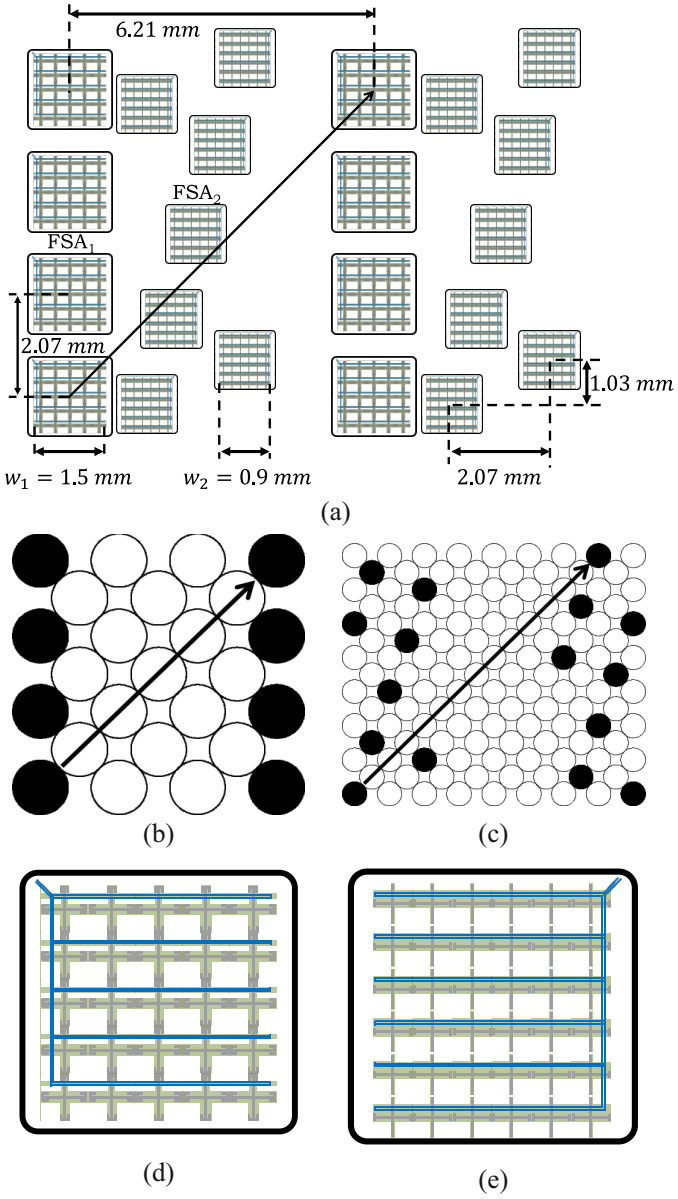

Figure 8.7: (a) Portion of the dual-band FPA. The arrow indicates the direction of the axis of the mechanical scanner. Schematic representation of the FPA configuration including the position of the actual detectors (black) and the scanned pixels (white) for (b) FSA1 . (c) FSA2. The arrow indicates the scanning direction. Detector layouts are shown (d) for FSA1 and (e) for FSA2.

8.3.2 Detector Layout

Once the FPA configuration is fixed and the resonator lines are designed, the layout of the detectors can be defined, FSA1 and FSA2 sets consist of arrays of 5×5, Fig. 8.7(d), and 6×6 elements, Fig. 8.7(e), respectively. The layout of the FPA and a micrographic photo of the two FSA sets are shown

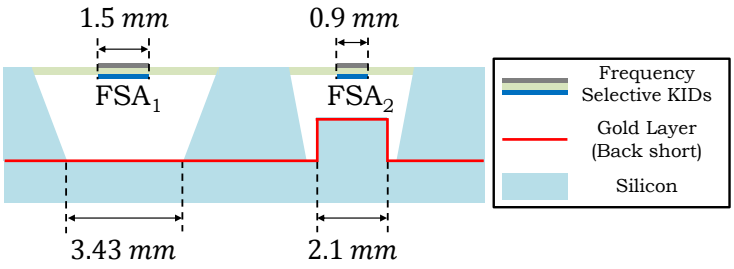

Figure 8.8: Cross-sectional view of the two sets of FSA KIBs.

in Fig. 8.1(a) and (b), respectively. Because of the fabrication process, the cross section of the detectors will be as schematically reported in Fig. 8.8. The response of the finite FSA arrays with the actual fabricated ground plane dimensions and with finite resonator lines was evaluated using CST MWS. The corresponding results are shown in Fig. 8.6, red curves. The finite and relatively small ground plane affects the rejection null of the higher band for FSA1 [see Fig. 8.6(a)]. Instead, the actual size of the resonator of FSA2 is responsible of the appearance of a resonant behavior at low frequencies [see Fig. 8.6(b)]. The reason is that the length of the resonators is approximately half wavelength at 190 GHz. As expected, since the resonators are placed horizontally, the resonance is only visible in the horizontal polarization. As discussed in Section 8.4, the effect of this unwanted behavior on the imager performance is negligible.

8.4 Measured Performance

In this section, the experimental performance of the imager in terms of PSF, effective PSF, and sensitivity is reported. The Quasi-Optical system of the imager consists of an inversely magnified dual-lens structure as shown in Fig. 8.9 and described in [39]. In order to limit the absorption of out-of-band radiation, two low-pass filter windows are placed in the optical path between the lenses and the FPA.The upper frequency limit of filters 1 and 2 (−3 dB frequency response) are 684 and 1000 GHz, respectively. Since the thickness of these filters is small in terms of the wavelength, the insertion losses of the two filter stages are negligible.

The imager performance is first estimated using the spectral analysis technique presented in Chapter 2. In the analysis, the implemented FSA KIBs (see Fig. 8.5) are modeled as an admittance matrix $\bar{Y}_{abs}(\vec{k}_\rho)$ computed using CST MWS [79], and linked to the spectrum of the optical system (estimated here via Physical Optics simulations). The differences with the procedure described in Chapter 2 and the current configuration are detailed in 8.4.1. The effective PSF of the imaging system is then compared to the measurement results. The sensitivity of the system is also evaluated theoretically at the end of this section using the response to a distributed incoherent source.

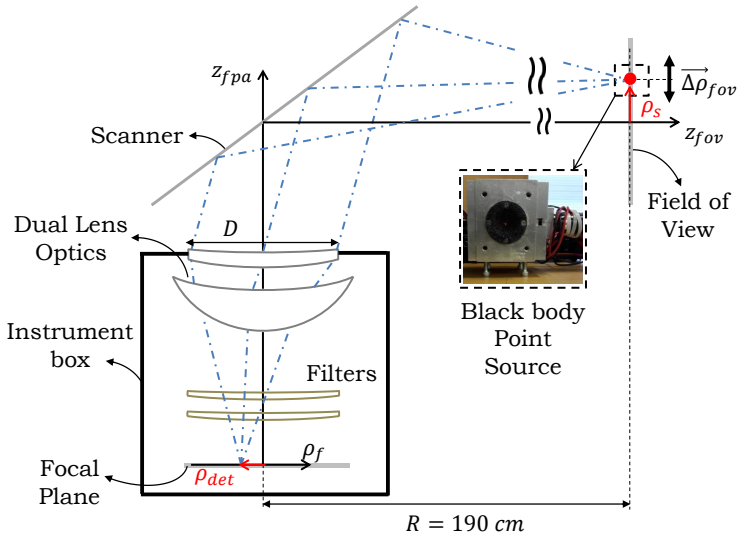

Figure 8.9: Schematic representation of the imaging system, including the dual lens optics and the low-pass filter stages. The point source is placed at $\vec{\rho}_s$ in the FoV which corresponds to a specific detector placed at $\vec{\rho}_{det}$ in the focal plane. Arbitrary positions in the FPA are described by the vector$\vec{\rho}_f$.

8.4.1 Evaluating the Power Received by the FSAs below the Near Field System

In Chapter 2, a generic methodology to evaluate the power received by a distributed absorber under a parabolic reflector was presented. Here, this methodology is applied to the combination of the proposed FSA KIBs and near-field imaging optics described in [39]. In order to use the spectral analysis tool presented in Chapter 2, for this geometry, the plane-wave spectrum of the dual-lens optics is evaluated using the commercial software GRASP [53]. The dual-lens optics, without including the filter stages, was simulated with a monochromatic point source placed at the position of $\vec{\rho}_s$, see Fig. 8.9, in the image plane. This location is chosen to be coincident with the maximum field at the location of the detector $\vec{\rho}_{det}$ for which the measurement is performed, i.e., $\vec{\rho}_s = \mathcal{M}\vec{\rho}_{det}$ with $\mathcal{M}$ being the optical magnification.

The field transmitted by the dual lens was then evaluated via GRASP simulations over an equivalent FO sphere centered at the detector position $\vec{\rho}_{det}$ (see Fig. 8.10). By substituting these fields as the Geometrical Optics fields, $\vec{E}^{GO}(\vec{k}_\rho, \vec{\rho}_s)$, $\vec{E}^d$ in (7.3), one can follow the same steps to obtain the spatial fields representing the response of the absorber to the optical system $\vec{e}^t(\vec{\rho}_f, \vec{\rho}_s)$ and $\vec{h}^t(\vec{\rho}_f, \vec{\rho}_s)$, where the position of the source is explicitly indicated by $\vec{\rho}_s$. Finally, the power absorbed by the FSA KIBs is evaluated as

$$P_{abs}(f, \vec{\rho}_s) = \frac{1}{2} Re\{ \int_{-w/2}^{w/2} \int [\vec{e}^t(\vec{\rho}_f, \vec{\rho}_s) \times \vec{h}^{t*}(\vec{\rho}_f, \vec{\rho}_s)] \cdot \hat{z} dS \} \tag{8.2}$$

where w is the side length of the FSA.

The effective area of the optical system can be evaluated directly from the power absorbed from the source location $P_{abs}(f, \vec{\rho}_s)$. The effective area relates to the amplitude of the active Poynting vector of the source $|\vec{S}_{in}(\vec{\rho}_s)|$ at the aperture of the optical system as

$$\mathcal{A}_{eff}(f) = \frac{P_{abs}(f, \vec{\rho}_s)}{|\vec{S}_{in}(\vec{\rho}_s)|}. \tag{8.3}$$

Note this definition applies when the amplitude of the point source over the aperture is uniform. We can define an aperture efficiency $\eta_{ap}(f)$ related to (8.3) by dividing by the physical area of the optical system $\mathcal{A}_{ph}$. In the measurement setup, there are two filter stages which are not simulated in GRASP. Therefore, the aperture efficiency is approximated by

$$\eta_{ap}(f) \simeq \eta^1_{filt}(f)\eta^2_{filt}(f)\frac{P_{abs}(f, \vec{\rho}_s)}{|\vec{S}_{in}(\vec{\rho}_s)|\mathcal{A}_{ph}} \tag{8.4}$$

where $\eta^1_{filt}(f)$ and $\eta^2_{filt}(f)$ are the frequency response of the two filter stages.

In order to derive the PSF of the detectors centered at the source location $\vec{\rho}_s$, we can use the following approximation (described also in Chapter 2), valid only for small displacements $\vec{\Delta\rho}_{fov}$ (see Fig. 8.9), as follows:

$$P_{abs}(f, \vec{\rho}_s + \vec{\Delta\rho}_{fov}) \simeq \frac{1}{2}Re\{\iint_{-w/2}^{w/2} [\vec{e}^t(\vec{\rho}_f - \vec{\Delta\rho}_f, \vec{\rho}_s) \times \vec{h}^{t*}(\vec{\rho}_f - \vec{\Delta\rho}_f, \vec{\rho}_s)] \cdot \hat{z}dS\} \tag{8.5}$$

where $\vec{e}^t(\vec{\rho}_f - \vec{\Delta\rho}_f, \vec{\rho}_s)$ and $\vec{h}^t(\vec{\rho}_f - \vec{\Delta\rho}_f, \vec{\rho}_s)$ are the spatial fields translated by $\vec{\Delta\rho}_i = -\vec{\Delta\rho}_{fov}/\mathcal{M}$ (see Fig. 8.10). The PSF can then be expressed as follows:

$$F(f, \Delta\Omega_{fov}) = \frac{P_{abs}(f, \vec{\rho}_s + \vec{\Delta\rho}_{fov})}{P_{abs}(f, \vec{\rho}_s)} \tag{8.6}$$

where $\Delta\Omega_{fov}$ corresponds to the angular position of the displaced source as shown in Fig. 8.10.

8.4.2 Monochromatic Point-Source Response

In this section, the response of the imager to a monochromatic point source is evaluated for two detectors (one per each frequency band) located at a distance of $\rho_{det} = 31$ mm from the center of the FPA. These locations corresponding to pixels in the FoV located 25.82 cm away from the center of the image plane (ρ_s in Fig. 8.9). This particular configuration is the same one used in the measurements (see Section 8.4.3).

As disscuesd in 8.4.1, by using the methodology described in Chapter 2, one can obtain the spatial fields representing the response of the absorbers to the optical system $[\vec{e}_t(\vec{\rho}_f, \vec{\rho}_s), \vec{h}_t(\vec{\rho}_f, \vec{\rho}_s)]$. By

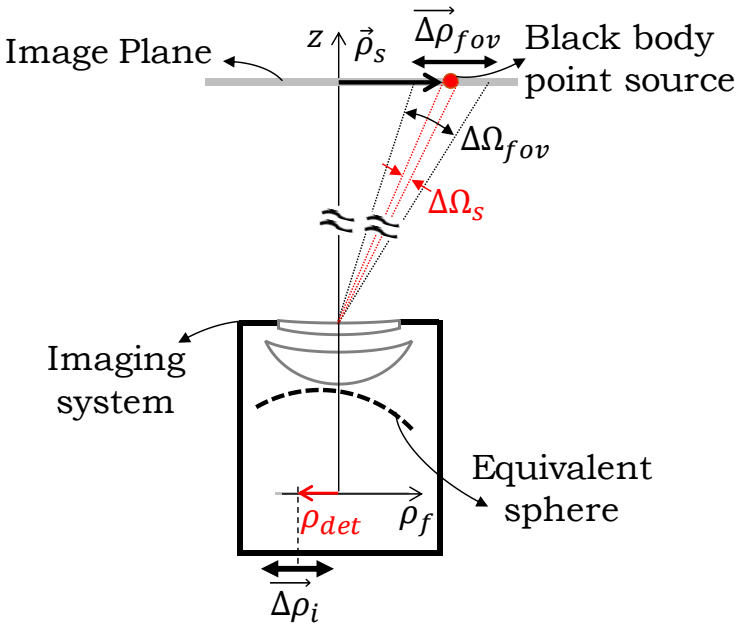

Figure 8.10: Simplified schematic of the imaging system illuminated by a black-body point source located at $\vec{\rho}_s + \vec{\Delta\rho}_{fov}$.

integrating these fields, it is possible to calculate the power received by the imager as a function of the source position as given in (8.2). By normalizing the power received at broadside by the Poynting vector incident on the optical aperture, we can derive the effective area of the imager, (8.3), and from that the aperture efficiency as (8.4). The aperture efficiencies for the two detectors are shown in Fig. 8.11. The maximum efficiency is approximately 20% in both bandwidths and the results for the two polarizations are comparable. This aperture efficiency includes the spill-over associated to the diffracted fields in the focal plane, the ohmic and reflection losses of the dual lens, the response of the two filter stages, and the frequency response of the FSAs. Moreover, a full-wave simulation, similar to the one described in Sec. 7.6, is performed to validate this efficiency. Specifically, GRASP simulation software [53] was used to obtain the direct field generated by the optical system above the detector plane. This direct field is then used as the source in CST MWS to obtain the power dissipated in the absorbers similar to Sec. 7.6. The efficiency obtained using the full-wave simulation is also reported in Fig. 8.11. As mentioned in Section 8.3.2, the resonant behavior at low-frequencies found in the finite simulations for the horizontal polarization in FSA2 does not significantly affect the aperture efficiency. The reason is that the absorbed power in the lower portion of the band is dominated by a very low spill-over efficiency.

The PSF of the imager represents the received power as a function of the position of the point source in the FoV $\vec{\rho}_s + \vec{\Delta\rho}_{fov}$ (see Fig. 8.9). The PSF is calculated as described in 8.4.1, (8.5) and (8.6), for both FSA sets over the operational frequency bands, 100 to 625 GHz. In Fig. 8.12, the 2-D PSF of both FSA sets is shown for several frequency points. It can be noticed that the received power outside the specific bandwidth of the two FSAs is low, confirming the predicted rejection. As described in Chapter 7, the PSF of an absorber-based imaging system widens rapidly as the absorber dimension enlarges. This effect can be seen by comparing the PSF of FSA2 at 500 GHz with the one at 625 GHz. Moreover, the maximum power received by FSA1 at 500 GHz is about 10 dBW lower than the one received at 250

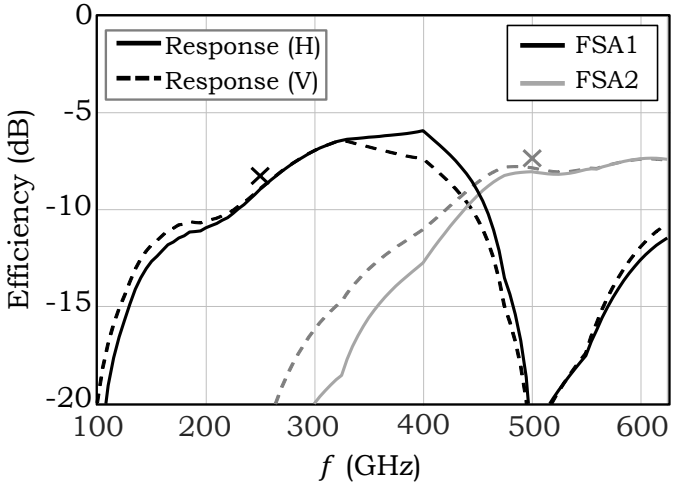

Figure 8.11: Aperture efficiency of the two FSA sets (FSA1 with side length 1.5 mm and FSA2with side length 0.9 mm). The cross marks represent the results obtained using the full-wave simulations for horizontal polarization.

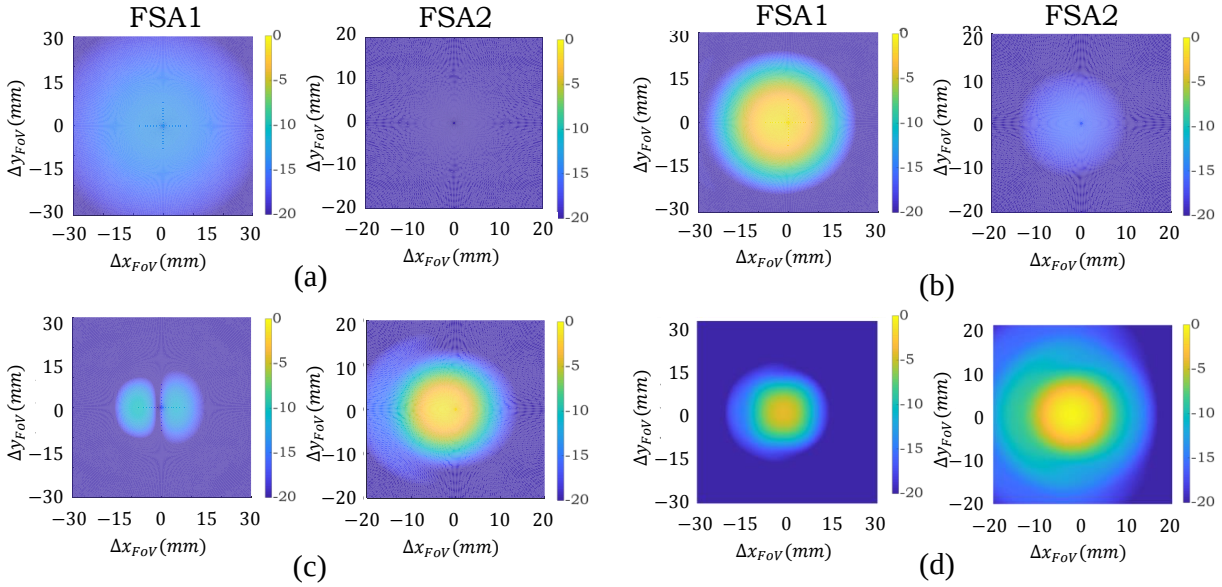

Figure 8.12: Two-dimensional PSF of the imager for FSAs 1 and 2 at left and right sides, respectively, normalized to the maximum value of the function for vertical polarization. At (a) 100 GHz, (b) 250 GHz, (c) 500 GHz, and (d) 625 GHz.

GHz. This result is an agreement with the aperture efficiencies shown in Fig. 8.11. The 1-D cut of the PSFs is shown in Fig. 8.13 at 250 and 500 GHz for FSA1 and FSA2 , respectively. Since the PSFs for both polarizations are similar, only the results for the vertical polarization are reported here. The PSF obtained using the full-wave simulations (GRASP+CST) is also reported in the figure showing a very good agreement.

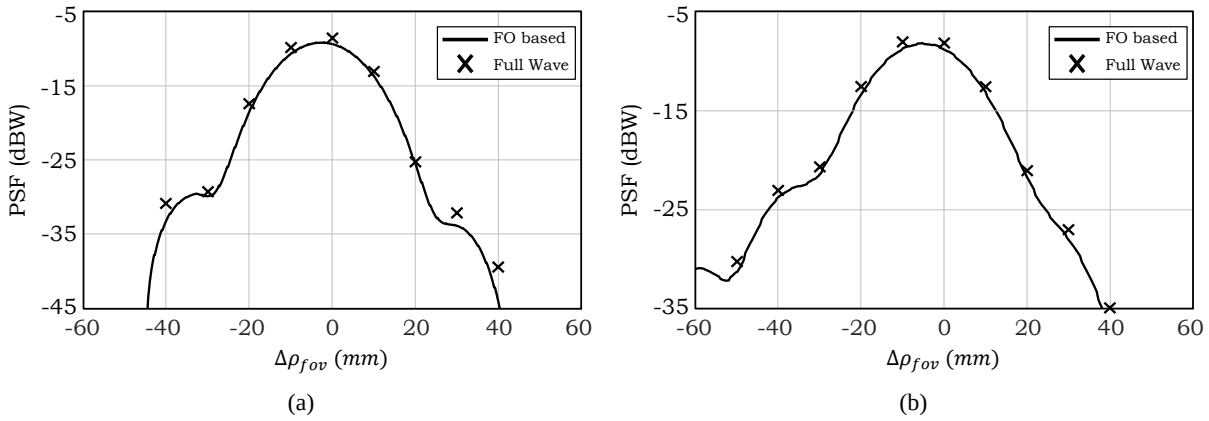

Figure 8.13: x-cut of the PSF of the imager for both FSAs at the central frequency of their operating band. (a) At 250 GHz, for FSA1 . (b) At 500 GHz, for FSA2 , for vertical polarization. The cross marks represent the results obtained using the full-wave simulations.

8.4.3 Incoherent Point-Source Response

In Section 8.4.2, the aperture efficiency and PSF are calculated as a function of the operation frequency points assuming monochromatic point sources. In the following, the response of the imager to an incoherent point source, radiating over the whole frequency band (BW = 100 to 625 GHz), is evaluated. The quality of an image is indeed dictated by the power received over the whole bandwidth. This power, in the Rayleigh Jean's limit, for a small source with an average temperature of T_s , can be expressed as [142]

$$P_{DS}^{VP/HP}(\Delta\Omega_{fov}) = \int_{BW}\int_{\Omega_s} \frac{k_B T_s}{\lambda^2} A_{eff}^{VP/HP}(f) F^{VP/HP}(f, \Delta\Omega_{fov}) d\Omega df \tag{8.7}$$

where BW represents the bandwidth of the system, the superscripts VP/HP represent the vertical and horizontal polarizations, respectively, A_{eff} is the effective area of the optical system, $F(f, \Delta\Omega_{fov})$ is the PSF of the optical system (or plane-wave response), $\Delta\Omega_{fov}$ corresponds to the angular position of the displaced source with respect to the central position of the source as shown in Fig. 8.10 (it can be related to the lateral displacement of the source by $\Delta\Omega_{fov} \simeq \Delta\rho_{fov}/R$), and Ω_s is the solid angle of the source.

For a point source placed at $\vec{\rho}_s + \vec{\Delta\rho}_{fov}$, the solid angle of the source reduces to $\Delta\Omega_s$ (see Fig. 8.10). Therefore, the angular range of the integral in (8.7) can be simplified to $\Delta\Omega_s$. By normalizing by the term $k_B T_s A_{phy} \Delta\Omega_s$, one can then derive an expression for an *effective* PSF, similar to what it is presented in [22] for single-mode antennas, as follows:

$$EF(\Delta\Omega_{fov}) = \int_{BW} \frac{\eta_{ap}(f)}{\lambda^2} F(f, \Delta\Omega_{fov}) df \tag{8.8}$$

This effective PSF was measured for two detectors (one per each band) at a distance from the center of the FPA, $|\vec{\rho}_{det}|$= 31 mm using the setup shown in Fig. 8.9. The black-body point source with the

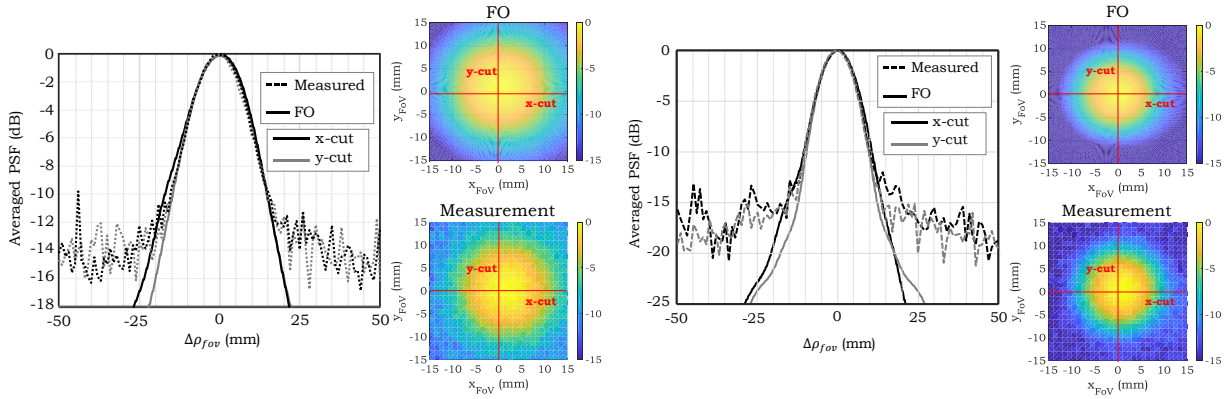

(a) (b)

Figure 8.14: Normalized effective PSF compared between the proposed method and the measurement for (a) FSA1 and (b) FSA2 sets, for vertical polarization. The inset indicates the 2-D patterns.

Table 8.3: Estimated imager performance.

	FSA1	FSA2
$\Delta\rho^{ave}_{HPBW}$	1.59 cm	1.11 cm
$\Delta\rho^{Dif}_{HPBW}$	@ 250GHz: 2 cm	@ 500GHz: 1 cm
NEP	$2.1 \times 10^{-14}\ W/Hz^{1/2}$	$1.7 \times 10^{-14}\ W/Hz^{1/2}$
NETD	98 mK	156 mK

aperture of 2 mm is equivalent to the one used in [12]. The measurement was performed by laterally displacing the black-body point source in the FoV. The results are shown in Fig. 8.14 for both FSA1 and FSA2 and compared to the theoretical computation based on the proposed spectral methodology. The theory and the experiments are in excellent agreement until −10 dBi. Below this value, the noise due to the measurement setup is dominant. The pattern shows good symmetry, and its HPBW is reported in Table 8.3 and compared to the diffraction limited HPBW. The latter can be calculated as the HPBW of an Airy pattern corresponding to the optical aperture ($\simeq$ 16 cm), at the central frequencies of FSA1 and FSA2. The HPBW of the designed imager is comparable to the diffraction limited case.

8.4.4 Distributed Incoherent Source Response

As discussed in Chapter 7, the power received by an absorber under an optical system from a distributed source can be expressed as a spectral integral of the effective number of modes as follows:

$$P^{VP/HP}_{DS} = k_B T_s \int_{BW} m^{VP/HP}_e(f) df \tag{8.9}$$

where $m^{VP/HP}_e(f) = \dfrac{\eta^{VP/HP}_{ap}(f)}{\eta^{VP/HP}_{f}(f)}$ is the effective number of modes. The focusing efficiency $\eta^{VP/HP}_f(f)$

Table 8.4: In and out of band estimated normalized Throughputs.

	FSA1	FSA2
Operation Band	100 GHz - 450 GHz	450 GHz - 625 GHz
Rejection Band	450 GHz - 625 GHz	100 GHz - 450 GHz
$(m_e)^{in}(VP/HP)$	16.8% / 15.7%	11.5% / 11.8%
$(m_e)^{out}(VP/HP)$	3.5% / 3.6%	2.5% / 3.6%

quantifies how much the imager solid angle enlarges with respect to the diffraction limited case (see Sec. 7.4).

For a dual-band system, one can represent the power received from the incoherent distributed source as a summation of the in-band and out-band contributions

$$P_{DS}^{VP/HP} = k_B T_s BW_{tot}[(m_e^{VP/HP})^{in} + (m_e^{VP/HP})^{out}] \tag{8.10}$$

where BW_{tot} is the total available bandwidth from 100 to 625 GHz and $(m_e)^{in}$ and $(m_e)^{out}$ are the *in-band* and *out-band* effective number of modes, respectively. These numbers of modes can be calculated for each FSA sets as

$$(m_e^{VP/HP})^{in} = \frac{1}{BW_{tot}} \int_{BW_{in}} \eta_{ap}^{VP/HP}(f)/\eta_f^{VP/HP}(f)df \tag{8.11}$$

$$(m_e^{VP/HP})^{out} = \frac{1}{BW_{tot}} \int_{BW_{out}} \eta_{ap}^{VP/HP}(f)/\eta_f^{VP/HP}(f)df \tag{8.12}$$

where BW_{in} and BW_{out} are the in-band and out-band operation bandwidths, respectively, of each detector set as defined in Table 8.4. The same table reports the averaged in-band and out-band effective number of modes for both FSA sets and both horizontal and vertical (H/V) polarizations. The rejection is slightly larger than 1 to 3 (as required) for both FSA sets. The rejection would improve if a multilayer FSA [150] was integrated in the KIBs.

By considering only the in-band contribution in (8.10) and using (8.1) and (8.9), the sensitivity, NETD, for the pixels associated to each of the bands (including the corresponding scanning penalties discussed in Section 8.3.1) has been estimated. The values of sensitivity are reported in Table 8.3, together with the estimated NEPs measured similarly to the one described in [143]. The reported NETDs are sufficient for security applications [147]. We note that the NETDs are a factor of 3 to 5 lower than those reported from calibrations using an extended black-body source in [41]. The difference stems predominantly from lower optical losses in the optimized materials, and higher average effective number of modes over the in band operation bandwidth. A practical demonstration of concealed object detection, demonstrating sufficient radiometric contrast in detection, is reported in [146].

8.5 Conclusion

In this chapter, a dual-band FPA for security imaging at sub-millimetre wave frequencies has been presented. The detectors are based on KIBs, which allow the development of large FPAs at medium-cooled temperature. Two FSA sets coupled to superconductive resonator lines were designed to implement a dual-color security imager. The geometry of the unit cells is based on a Jerusalem Cross configuration and the designed FSAs show a stable angular response and a rejection 1 to 3 of the undesired bandwidth.

The performance of the dual-band imager was evaluated using a FO technique coupled to a Floquet-modes analysis. The effective PSF of the imager coupled to a black-body point source over a wide frequency band (bandwidth ratio of $6:1$) was estimated and successfully validated experimentally. The NETD of the imaging system is estimated to be below 200 mK for both frequency bands, and the HPBW of the effective pattern is comparable to the one of a diffraction limited Quasi-Optical system.

Part IV

Conclusions and Future Outlooks

Chapter 9

Conclusions and Future Outlooks

This dissertation describes the research work carried out over a period of four years (from December 2015 to December 2019) at THz Sensing group, Delft University of Technology. The project was supported by ERC Starting Grant (ERC-2014-StG LAA-THz-CC), No. 639749.

This work is focused on developing spectral techniques for analysing Quasi-Optical (QO) components coupled to antenna or absorber based detectors operating at (sub)-millimetre wavelengths with wide field-of-views (FoVs). This work also includes the design procedure for a few practical antenna based systems with wide band performance as well as wide FoVs. Moreover, absorber based detectors were modeled using these developed tools leading to introduction of terminologies well understood by the antenna communities. These terminologies provide the possibility of comparing the performance of antenna and absorber based systems.

In this chapter, the conclusion and the most significant results of the research are summarized and, moreover, future outlooks for continuation of this research are discussed.

9.1 Development of Coherent Fourier Optics Methodology

Imaging systems at millimetre and sub-millimetre wavelengths are entering a new era with the development of large format arrays of detectors. Typically, such FPAs are coupled to a QO component. A Geometrical Optics (GO)- Fourier optics (FO) based technique for deriving the Plane Wave Spectrum (PWS) of QO components in reception was presented. In particular, this PWS is derived analytically for three QO component, parabolic reflector, elliptical lens, hyperbolic lens, illuminated by broadside or slightly skewed plane wave incident angles. Moreover, a numerical GO method is also described for the cases when the component is illuminated by plane waves with large incident angles. By introducing the off-focus FO approach, the proposed PWS representation can be used to analyze, and design systems composed of tens of thousands of pixels, while the original FO would provide accurate spectra for only a few tens of elements. Field matching technique is employed in this work to evaluate the coupling between antenna feeders and their QO systems. This technique is reviewed and a few simple test cases of antenna coupled QO components are analysed with excellent agreement with the full wave simulations.

Furthermore, the original Fourier Optics (FO) procedure has been extended to derive the spec-

trum of the incident field on a reference system centered on antennas located at a large distance from the focus. The procedure, named here "Coherent" FO (CFO), has been used to express the spectrum of the incident field in realistic cases which include large arrays of lenses within reflectors focal planes. In particular, the methodology can be linked to spectral techniques commonly used for arrays, such as Floquet-modes theory, for analysing absorbing mesh grids, and antenna in reception formalism to analyse the performance of antenna feeders in reception. By also employing the off-focus FO approach, the proposed Coherent FO representation can be used to analyse and design wide field-of-view QO systems based on Fly's eye lens array configuration. Moreover, the applicability region of standard Fourier Optics (FO) method is extended to the vertical direction with respect to the focal plane of a focusing QO component.

The work described in Part I of this thesis is published in journal papers number 3, 4 and 5 (see page 181).

9.2 Advanced Multi-Component Quasi-Optical Systems Based on Antenna Feeders

Methods for analysing the coupling between multiple QO components were discussed. In general, two QO component can be coupled geometrically or in the diffraction region. The former refers to scenarios where QO components are placed far away from focus points of one another; whereas the later describes scenarios where a QO component (secondary) is located close to caustic points (focus point) of a focusing (primary) QO component.

In the Geometrical Optics (GO) method, the EM radiation integral is approximated asymptotically for observation points far from the focus point. As the result, GO is accurate for representing geometrical coupling between QO components, and inaccurate for representing the diffractive couplings. In such cases, CFO can be employed to derive the PWS of the primary QO component, since in this method the EM radiation integral is asymptotically approximated assuming observation points close to the focus. As the result of this representation, the coupling to secondary components can be evaluated as the summation of their responses to each one of these plane waves.

A fly's eye lens array coupled to absorbers or antennas is a common FPA architecture for wide FoV imagers. Typically, such FPAs are coupled to a QO system involving reflectors. In such architecture, a full-wave electromagnetic analysis of the entire system is not feasible since it is numerically cumbersome and time-consuming. Here, CFO technique is used to assess the scanning performance of a large format lens based FPA configuration. The approach simplifies the design of the lens focal plane array since both the lens shape and feeder radiation properties can be derived directly from the PWS without the need of using an optimization algorithm. In this configuration, all the lens feeders are placed over a flat surface, enabling monolithic integration at high frequencies. The surface shape of the lenses is linked directly to the phase of the incident PWS, while the radiation of the lens feeders is matched to the amplitude of the PWS via a Gaussian model approximation. For simplicity, the main reflector aperture is modeled as a symmetric non-oversized parabola. The obtained performances, validated via a conventional PO analysis, show significantly lower scan loss than it would be obtained by placing

Gaussian horns in the optimal focal surface of such reflector. The synthesized lens FPA achieved a scan loss below 1 dB while scanning up to ±17.5° with directivity of 52dBi complying with the needs for future sub-millimetre security imagers. The technique is validated via a standard Physical Optics code with an excellent agreement.

The design of a wide band QO system for the ASTE telescope based on a hyper-hemispherical leaky lens antenna is described in this thesis. The lens antenna is optimized to maximize its coupling to a parabolic reflector. The design procedure is based on a field matching technique in reception. The Quasi-Optical system has an average illumination efficiency over 70% in the whole $3:1$ relative bandwidth. Including the feeder losses, an averaged aperture efficiency of 65% is obtained. The pattern in the sky of the system is also simulated in GRASP. The side lobe, and the cross-polarization level of this pattern, over the bandwidth, is below −16dB, and −18dB, respectively. The preliminary beam pattern measurement of this design, performed by SRON, is also reported with good agreement to the one predicted by the tool. By using a foam based AR coating, which shows stable performance in cooling cycle tests, DESHIMA 2.0 system will be fully tested in the coming months.

Finally, a QO architecture to achieve wide band wide scanning performance in a (sub)-millimetre imaging and sensing system is also proposed. In order to design the elements of this lens based FPA architecture, with multiple transmitting surfaces close to one another, a fast and accurate analysis tool based on the combination of FO and GO techniques was developed. The tool was discussed and validated against a time-consuming multi-surface PO code with excellent agreement. Moreover, as a proof of concept of the proposed QO system, an example scenario is provided and its performance over a $3:1$ relative bandwidth is evaluated. For the central element of the proposed QO system, the design achieved 1 dB of scan loss over the whole band while scanning up to ±7 beams at the center of the frequency band. Therefore, based on this preliminary study, without anticipating difficulties in the implementation of the actual Quasi-Optical system, potentially, about 5600 broad band beams with low scan loss can be generated using a 5 by 5 multi-lens focal plane array.

The work described in Part II of this thesis will be published in journal papers number 4, and 6 (see page 181).

9.3 Quasi-Optical Systems with Absorber Based Focal Plane Arrays

Currently, commercially feasible passive imaging cameras at sub-millimetre wavelengths are emerging using FPAs of bare absorbing meshes, without any antenna coupling (lens or horn) structures. The design of such arrays is typically done resorting to geometrical considerations or basic broadside plane wave incidence analysis. A spectral electromagnetic model for such configurations is proposed. The model is based on linking the developed PWS representation of the direct field with a Floquet-wave representation of the field in the surrounding of absorbing mesh. By using this representation basic figures of merit in absorber based imaging systems are derived: point source response, aperture efficiency, point spread function, focusing efficiency, and in-coherent distributed source response. The results obtained by the present model have been compared, with excellent agreement, with those ob-

tained by full wave simulations. Thus, the proposed spectral method provides an accurate and efficient way to estimate the key optical properties of the imager inside the region of validity of the FO.

The most important design aspect that emerges here, for focusing systems in reception, is associated with the introduction of the intuitive focusing efficiency parameter. This parameter leads to two important conclusions. First, when comparing bare absorber FPAs and antenna feeders of equivalent dimensions, the latter leads to higher focusing efficiencies, and therefore better imaging resolution. Only very tightly sampled absorber based FPAs lead to a comparable trade-off in terms of received power and angular resolution, when compared to antenna based FPAs. Second, while for antennas it is well known that the power received from a distributed incoherent source is $P_{ant}^{DS} = \eta_{rad} k_b T_s BW$, for absorber based FPAs, the corresponding received power is typically quantified introducing an effective number of modes: $P_{abs}^{DS} = m_{eff} \times k_b T_s BW$. Here, it is shown that the effective number of modes m_{eff} can be conveniently evaluated as the ratio between the aperture, η_{ap}, and the focusing efficiency, η_f.

Moreover, a dual-band FPA for security imaging at sub-millimetre wave frequencies has been presented in this thesis. The detectors are based on Kinetic Inductance Bolometers (KIBs), which allow the development of large FPAs at medium-cooled temperature. Two Frequency Selective Absorber (FSA) sets coupled to superconductive resonator lines were designed to implement a dual-color security imager. The geometry of the unit cells is based on a Jerusalem Cross configuration and the designed FSAs show a stable angular response and a rejection 1 to 3 of the undesired bandwidth.

The performance of the dual-band imager was evaluated using the described technique. The effective Point Spread Function (PSF) of the imager coupled to a black-body point source over a wide frequency band ($6:1$) was estimated by VTT and successfully validated experimentally. The NETD of the imaging system is estimated to be below 200 mK for both frequency bands, and the HPBW of the effective pattern is comparable to the one of a diffraction limited Quasi-Optical system.

The work described in Part III of this thesis is published in journal papers number 2, and 3 (see page 181).

9.4 Future Outlooks

The future outlooks for this thesis are summarized in two parts, future theoretical developments, and future design possibilities:

Future Theoretical Developments

- In this work, the reflector systems are modeled by equivalent on-axis parabolic reflectors. In order to analyse the performance of the proposed designs below realistic QO systems, Geometrical Optics (GO) will be employed to model the propagation through standard reflector systems such as Dragonian, confocal, and Cassegrain dual-reflector configurations.

- The developed GO based code for analysing the propagation of EM waves through dielectric materials should be revised to accurately represent the interaction between multiple transmitting

surfaces. In this thesis, the GO code does not compute the principal directions of the transmitting wavefronts after the first transmitting surface. By removing this limitation, the GO code can be employed to analyse the interaction of EM fields, with generic wavefronts, with arbitrary configured cascaded dielectric surfaces. As a result, further developments in this regard are planned.

- The lateral applicability region of Fourier Optics (FO) was extended over the focal plane by introducing off-focus FO spheres. This step allowed us to analyse large format FPAs. The FO method also has a limited applicability region in the vertical direction with respect to the focal plane as discussed in this thesis. This applicability region can be shifted vertically by displacing the center of FO sphere in the vertical directions for off-focus FO spheres. In future work, this shift will be employed to cover the surface of larger lenses at the edge of the proposed Fly's eye configuration to further extend its scanning capability.

- Based on the developed codes in this thesis, a Graphic User Interface (GUI) in MATLAB environment is already published. This GUI provides the possibility for users to design simple QO systems in reception without entering into the theoretical details. Advanced codes for analysing the coupling between multiple QO components as well as Physical Optics codes for multiple transmitting surfaces (analysis in transmission) will be packaged into similar interfaces.

Future Designs

- By employing the proposed method in Ch. 4, the development of a monolithically integrated wide scan lens based FPA is in progress. The feeders in this FPA are based on resonant leaky wave antennas [152]. The permittivity of the resonant cavity of this feeder can be tuned to change the directivity of its radiation pattern. The FPA will be placed below a dual-reflector system to demonstrate its applicability for future short-range security imagers.

- As an application scenario for CFO method (Ch. 4), a wide scan lens based FPA for short-range security imagers is proposed in this thesis. The CFO method can be easily applied to design of wide scan FPAs for other scenarios and applications such as satellite communications in Ka band.

- Wide band wide scanning QO systems are essential components for the future multi-color wide field-of-view imagers. A few examples of these systems are already proposed in the literature: pico-seconds pulsed radar for security imaging at stand-off distances [36], or concepts similar to the Multi Object Spectrometer with an Array of superconducting Integrated Circuits (MOSAIC) for future astronomical observations (conceptually similar to [153, 154, 155]). The developed techniques in this work can be employed for designing such systems based on advanced multi-lens FPA architectures.

- In this thesis the performance of FPAs based on bare absorbers is discussed and compared to antenna based FPAs. The resolution of absorber based imagers, i.e. their capability to distinguish point sources, is worse than antenna based FPAs with comparable element sizes. Moreover, since absorbers can receive more power from off-broadside directions with respect to antennas, the amount of undesired radiation reaching the detector can be significantly larger with respect to

antennas. In addition, for bolometer based detectors such as the Kinetic Inductance Bolometers of CONSORTIS passive system (Ch. 8), the detector noise decreases by reducing the absorbing area. Lens absorber based FPAs can potentially solve these problems and already have been proposed in [66]. The developed method in Ch. 7 can be extended for the design of such FPAs.

9.5 Impact of the Research

The work described in this dissertation has led to a number of journal and conference publications (see page 181). One MSc. thesis was co-supervised with topics related to Chapter 2 of this dissertation, and the co-supervision of a second Master student is on-going. Moreover, the research performed in the second Msc. thesis project in combination with the described work in Chapter 4 was nominated for the best paper award in antennas category in European Conference on Antennas and Propagation (EuCAP) 2020.

Appendix A

Derivation of the Standard Fourier Optics Representation of the Focal Field

In this Appendix, the standard Fourier Optics (FO) representation of the focal fields of a Quasi-Optical (QO) component is discussed as well as its limits of applicability. Firstly, Physical Optics (PO) representation of fields in a scattering problem is reviewed. Secondly, this technique is employed to obtain the focal field scattered by a QO component. Finally, following a few approximation steps, the standard FO representation of the focal field for this scattering scenario is derived.

A high frequency technique for analysing the scattering and transmission from surfaces is the PO approximation. PO based analysis is well known, and here, the method is briefly discussed, since standard Fourier Optics representation of the focal fields is derived as an approximation on the fields obtained by PO. PO is a well-established approach for calculating the electromagnetic field scattered by an electrically large object. This technique can be applied to arbitrary shaped structures when the PO current approximations are applicable. As a result, PO proves to be a reliable validation method that represent an accurate model for the interaction of electromagnetic fields with scattering surfaces.

One can calculate the electric field radiated from a surface, see Fig. A.1, using equivalent electric and magnetic surface currents, $\vec{j}$ and $\vec{m}$, and the spatial Green's function (GF) of the medium, $\bar{G}^{ej}$ and $\bar{G}^{em}$, as:

$$\vec{e}(\vec{r}) = \iint_{S'} \bar{G}^{ej}(\vec{r} - \vec{r}') \cdot \vec{j}(\vec{r}')dS' + \iint_{S'} \bar{G}^{em}(\vec{r} - \vec{r}') \cdot \vec{m}(\vec{r}')dS' \tag{A.1}$$

where $\vec{r}$ and $\vec{r}'$ indicate the positions of the observation and source, respectively; the domain of the integration in (A.1), S', is the surface of the scatterer.

The surface currents in (A.1) can be derived using the equivalence theorem. In a scattering scenario, one can assume that incident EM fields, $\vec{E}^i$ and $\vec{H}^i$, are impinging on the scattering surface and EM scattered fields, $\vec{E}^s$ and $\vec{H}^s$, are radiated from the surface. One can introduce equivalent electric and magnetic currents on this surface as:

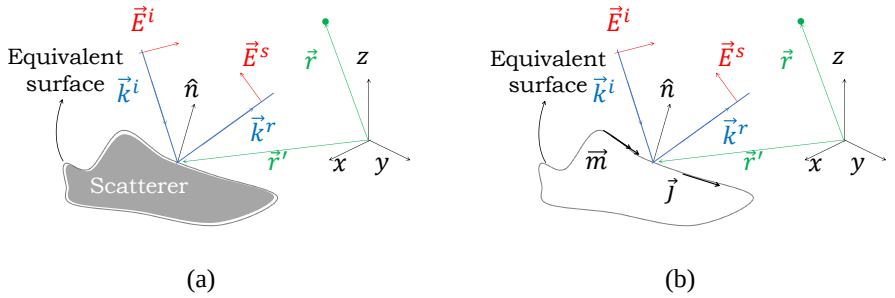

Figure A.1: A schematic representation of a reflection scattering problem. (a) The geometry. (b) The equivalent problem including the equivalent surface currents.

$$\vec{j}(\vec{r}') = \hat{n} \times [\vec{H}^i(\vec{r} = \vec{r}') + \vec{H}^s(\vec{r} = \vec{r}')] \tag{A.2a}$$

$$\vec{m}(\vec{r}') = -\hat{n} \times [\vec{E}^i(\vec{r} = \vec{r}') + \vec{E}^s(\vec{r} = \vec{r}')] \tag{A.2b}$$

where $\hat{n}$ is the normal vector of the equivalent surface pointing toward outside from the scatterer, Fig. A.1. One should note that the term $(\vec{r} = \vec{r}')$ emphasizes the fact that these fields are evaluated at the surface of the scatterer. As result of the equivalence theorem, the scatterer can be removed and these equivalent currents are radiating in a homogeneous uniform medium (see Fig. A.1(b)) using (A.1).

In PO approximation, the incident field at each point on the object is locally assumed to be a plane wave impinging on a flat infinite surface. Therefore, the scattered field, on the equivalent surface, can be approximated using reflection or transmission coefficients, and its direction of propagation is approximated using the Snell's law. Moreover, in the PO approach, the GF of a homogeneous uniform medium is approximated by only its radiative part (i.e. $\vec{\nabla} \simeq -jk\hat{k}$, where k is the wave number of the medium, and $\hat{k} = \dfrac{\vec{r} - \vec{r}'}{|\vec{r} - \vec{r}'|}$). As a result, (A.1) can be expressed as

$$\vec{e}(\vec{r}) = \iint_{S'} j\vec{k} \times \vec{m}(\vec{r}') \frac{e^{-jk|\vec{r}-\vec{r}'|}}{4\pi|\vec{r} - \vec{r}'|} dS' - j\omega\mu \iint_{S'} [\vec{j}(\vec{r}') - \{\hat{k} \cdot \vec{j}(\vec{r}')\}\hat{k}(\vec{r}')] \frac{e^{-jk|\vec{r}-\vec{r}'|}}{4\pi|\vec{r} - \vec{r}'|} dS' \tag{A.3}$$

where ω is the angular frequency, and μ is the permeability of the medium. Similarly, the scattered magnetic field can be calculated using its corresponding GFs, i.e. $\bar{G}^{hj}$ and $\bar{G}^{hm}$.

Let us now assume the scattering problem of a focusing QO component illuminated by an incident plane wave from $\hat{k}^i$ direction, as shown in Fig. A.2. An incident plane wave of amplitude E_0 can be expressed as

$$\vec{E}^i(\vec{r}) = E_0 \hat{p}^i e^{-jk\hat{k}^i \cdot \vec{r}} \tag{A.4a}$$

$$\vec{H}^i(\vec{r}) = \frac{1}{\zeta} \hat{k}^i \times \vec{E}^i(\vec{r}) \tag{A.4b}$$

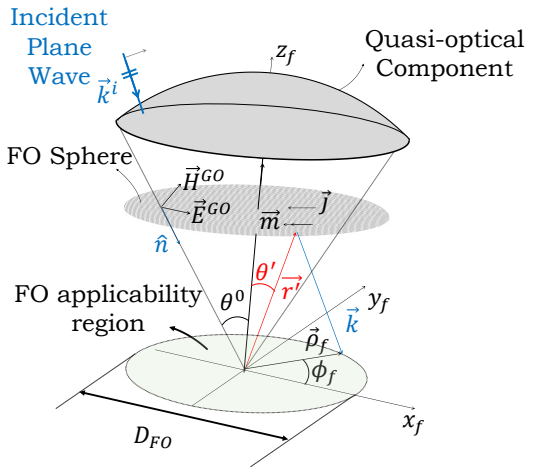

Figure A.2: Scattering problem of a focusing QO component illuminated by an incident plane wave from $\hat{k}^i$ direction.

where $\hat{p}^i$ represents the polarization of the incident plane wave, and ζ is the characteristic impedance of the medium.

One can apply the equivalence theorem over the QO surface or over any other arbitrary surface. In this case, let us apply the theorem on an equivalent sphere centered at the focus of the QO component, Fig. A.2. This decision leads to simpler expressions for the scattered field, and provides the possibility of representing the focal field as a Plane Wave Spectrum. To calculate the equivalent currents on this surface using (A.2), the scattered EM fields on this surface, $\vec{E}^{GO}$ and $\vec{H}^{GO}$, are needed. These fields can be calculated resorting to a Geometrical Optics (GO) method as discussed in Appendix B and summarized in Sec. 2.3.1, or using analytical expressions for canonical QO components illuminated by plane waves from broadside and slightly skewed incident directions, as described in Secs. 2.3.2 and 2.3.3. The analytical expressions for the GO field are defined over the angular sector subtended by the optical system (θ^0), as shown in Fig. A.2. Moreover, one can neglect the contribution of the incident field on the equivalent currents over this sphere. As a result these currents can be represented as

$$\vec{j}(\vec{r}') = -\hat{r}' \times \vec{H}^{GO}(\vec{r}') \tag{A.5a}$$

$$\vec{m}(\vec{r}') = \hat{r}' \times \vec{E}^{GO}(\vec{r}') \tag{A.5b}$$

One can calculate the field at the focal plane of QO component, $\vec{e}_f(\vec{\rho}_f)$ using (A.3) as:

$$\vec{e}_f(\vec{\rho}_f) = \iint_{S'} j\vec{k} \times \vec{m}(\vec{r}') \frac{e^{-jk|\vec{\rho}_f - \vec{r}'|}}{4\pi|\vec{\rho}_f - \vec{r}'|} dS' - j\omega\mu \iint_{S'} [\vec{j}(\vec{r}') - \{\hat{k} \cdot \vec{j}(\vec{r}')\}\hat{k}(\vec{r}')] \frac{e^{-jk|\vec{\rho}_f - \vec{r}'|}}{4\pi|\vec{\rho}_f - \vec{r}'|} dS' \tag{A.6}$$

By performing four approximations on (A.6), one can represent $\vec{e}(\vec{\rho}_f)$ as a summation of plane waves or a plane wave spectrum (PWS). In the following, these approximations are discussed.

Local Plane Wave Approximation

By representing the field scattered by the QO component on the equivalent sphere using the GO technique, this scattered field is approximated, locally, as a plane wave. Here we approximate the direction of the propagation of this local plane wave by $\hat{k}^s \simeq -\vec{r}'$, where $\hat{k}^s$ is the scattered field direction determined in GO representation of the field using Snell's Law. As a result, the magnetic field can be expressed in terms of the electric field as:

$$\vec{H}^{GO}(\vec{r}') = \frac{1}{\zeta}\hat{k}^s(\vec{r}') \times \vec{E}^{GO}(\vec{r}') \simeq -\frac{1}{\zeta}\hat{r}' \times \vec{E}^{GO}(\vec{r}') \tag{A.7}$$

By substituting (A.7) in (A.5a), one can also represent the electric surface current as a function of the electric field as:

$$\vec{j} = \frac{1}{\zeta}\hat{r}' \times [\hat{r}' \times \vec{E}^{GO}] \tag{A.8}$$

Approximation on the Amplitude of the Integrand

In order to simplify the integrand in (A.6), we expand the term $|\vec{\rho}_f - \vec{r}'| = R_{FO}\sqrt{1 + \frac{|\vec{\rho}_f|^2}{R_{FO}^2} - 2\frac{\vec{\rho}_f \cdot \hat{r}'}{R_{FO}}}$ into its Maclaurin series:

$$|\vec{\rho}_f - \vec{r}'| \simeq R_{FO}\Big[1 - \frac{\rho_f}{R_{FO}}\hat{\rho}_f \cdot \hat{r}' + \frac{\rho_f^2}{2R_{FO}^2}\{1 - (\hat{\rho}_f \cdot \hat{r}')^2\} + \frac{\rho_f^3}{2R_{FO}^3}(\hat{\rho}_f \cdot \hat{r}') + ...\Big] \tag{A.9}$$

where $\rho_f = |\vec{\rho}_f|$, and $R_{FO} = |\vec{r}'|$ is the radius of the equivalent sphere. One can approximate the amplitude component in the integrand of (A.6) by taking only the first term in this expansion, i.e.

$$\frac{1}{|\vec{\rho}_f - \vec{r}'|} \simeq \frac{1}{R_{FO}} \tag{A.10}$$

By introducing a relative error function, the applicability region of (A.10) is derived. This amplitude error function is expressed as:

$$\varepsilon_{amp} = \frac{\frac{1}{|\vec{\rho}_f - \vec{r}'|} - \frac{1}{R_{FO}}}{\frac{1}{|\vec{\rho}_f - \vec{r}'|}} \simeq \frac{\rho_f}{R_{FO}}\sin\theta' \tag{A.11}$$

where θ' is the elevation angle of the surface of the equivalent sphere, Fig. A.2. The worst case scenario, in terms of errors in this approximation, occurs when $\sin\theta'$ is maximum, i.e. $\sin\theta' = \sin\theta^0$, where θ^0 is the maximum rim angle of the QO component and can be related to its f-number, $f_\#$, as:

$$\sin\theta^0 = \frac{1}{2f_\#} \tag{A.12}$$

Assuming a $\varepsilon_{amp} = 20\%$ error margin, the applicability region for this amplitude approximation is:

$$\rho_{f,amp} \leq 0.4 f_\#^2 D \tag{A.13}$$

where D is the diameter of the QO component, and when taking the largest FO sphere radius, $f_\# = R_{FO}/D$.

Approximation on the Vectorial Components of the Integrand

In (A.6), $\vec{k} = k\hat{k} = k\dfrac{\vec{\rho}_f - \vec{r}'}{|\vec{\rho}_f - \vec{r}'|}$ represents the propagation vector from the source to the observation point, and k is the propagation constant. When $|\vec{r}'| \gg |\vec{\rho}_f|$, this vectorial component of the radiation integral can be approximated as:

$$\hat{k} \simeq \frac{\vec{\rho}_f}{R_{FO}} - \hat{r}' \simeq -\hat{r}' \tag{A.14}$$

Assuming again a 20% error margin, the validity region of this approximation is:

$$\rho_{f,v} \leq 0.2 f_\# D \tag{A.15}$$

In practice, the condition imposed by approximation on amplitude (A.13) is less restrictive that the one on the vectorial component (A.15).

By substituting (A.5b) and (A.8) in (A.6), and applying the vectorial and amplitude approximations, one can represent the focal field as:

$$\vec{e}_f(\vec{\rho}_f) = j2k \int_0^{2\pi} \int_0^{\theta^0} [\hat{r}' \times \{\vec{E}^{GO} \times \hat{r}'\}] \frac{e^{-jk|\vec{\rho}_f - \vec{r}'|}}{4\pi R_{FO}} R_{FO}^2 \sin\theta' d\theta' d\phi' \tag{A.16}$$

Approximation on the Phase of the Integrand

By neglecting the third or higher order terms (with respect to ρ_f) in the Maclaurin expansion of (A.9), the term, $|\vec{\rho}_f - \vec{r}'|$, in (A.16), can be approximated as:

$$|\vec{\rho}_f - \vec{r}'| = R_{FO} - \vec{\rho}_f \cdot \hat{r}' + \frac{\rho_f^2}{2R_{FO}} \tag{A.17}$$

The error function of this approximation can be represented as the neglected terms:

$$\varepsilon_\Phi \simeq k[\frac{\rho_f^2}{2R_{FO}}(\hat{\rho_f} \cdot \hat{r}')^2 - \frac{\rho_f^3}{2R_{FO}^2}(\hat{\rho_f} \cdot \hat{r}')] \tag{A.18}$$

The worst case scenario in (A.18) is when $\hat{\rho_f} \cdot \hat{r}' = -\sin\theta^0 = -\frac{1}{2f_\#}$. By choosing acceptable error margin of $\pi/8$, the applicability region of the phase approximation can be expressed as

$$\frac{4\rho_f^3 D}{R_{FO}^3} + \frac{2\rho_f^2 D^2}{R_{FO}^3} - \lambda \leq 0 \tag{A.19}$$

where λ is the wavelength in the medium. By solving the cubic inequality in (A.19), and taking the positive and real solution, the applicability region for the phase approximation can be expressed by the parameter $\rho_{f,\phi}$. For large f-number cases, the third order term in (A.19) can be neglected even from the phase error function, and $\rho_{f,\phi}$ can be expressed as

$$\rho_{f,\phi} \leq f_\# \sqrt{0.5 f_\# D\lambda} \tag{A.20}$$

By combining the derived restrictive conditions, the applicability region of the FO approximation can be expressed by a maximum diameter, in the focal plane and around the center of the equivalent sphere (see Fig. A.2):

$$D_{FO} = \min\{0.4Df_\#, 2\rho_{f,\phi}\} \tag{A.21}$$

For most practical cases, by combining the conditions (A.20) and (A.15), this applicability region can be represented in a closed form as:

$$D_{FO} = f_\# \min\{0.4D, \sqrt{2f_\# D\lambda}\} \tag{A.22}$$

These approximations lead to the Fourier Optics representation of the scattered field by a QO component:

$$\vec{e}_f(\vec{\rho}_f) = \frac{jkR_{FO}e^{-jkR_{FO}}e^{-jk\frac{|\rho_f|^2}{2R_{FO}}}}{2\pi} \int_0^{2\pi}\int_0^{\theta^0} [\hat{r}' \times \{\vec{E}^{GO} \times \hat{r}'\}] e^{-jk\vec{\rho}_f \cdot \hat{r}'} \sin\theta' d\theta' d\phi' \tag{A.23}$$

It is worth noting that this standard representation of FO and its corresponding applicability region ((A.22) or (A.21)) are valid for observation points on the focal plane, i.e. $\vec{\rho}_f$ and $z_f = 0$.

The focal field can also be represented in terms of cylindrical spectral variables, $k_\rho = k \sin\theta'$ and ϕ'. The differentials in the two coordinates are related as $dk_\rho = k_z d\theta'$, where $k_z = \sqrt{k^2 - k_\rho^2}$. The FO representation of the focal field in cylindrical coordinates is then expressed as

$$\vec{e}_f(\vec{\rho}_f) = \frac{jR_{FO}e^{-jkR_{FO}}e^{-jk\dfrac{|\rho_f|^2}{2R_{FO}}}}{2\pi}\int_0^{2\pi}\int_0^{k_{\rho 0}}\frac{1}{\sqrt{k^2-k_\rho^2}}[\hat{r}'\times\{\vec{E}^{GO}\times\hat{r}'\}]e^{jk_\rho\rho_f\cos(\phi_f-\phi')}k_\rho dk_\rho d\phi' \tag{A.24}$$

where $k_{\rho 0} = k\sin\theta'$, $\phi_f = \arctan(\dfrac{y_f}{x_f})$, and $\vec{\rho}_f = x_f\hat{x} + y_f\hat{y}$.

One can also change the cylindrical spectral variables in (A.25) to Cartesian spectral variables, $k_x = k_\rho\cos\phi'$ and $k_y = k_\rho\sin\phi'$. In this case the focal field can be expressed as:

$$\vec{e}_f(\vec{\rho}_f) = \frac{jR_{FO}e^{-jkR_{FO}}e^{-jk\dfrac{|\rho_f|^2}{2R_{FO}}}}{2\pi}\int_{-\infty}^{+\infty}\int_{-\infty}^{+\infty}\frac{1}{\sqrt{k^2-k_\rho^2}}[\hat{r}'\times\{\vec{E}^{GO}\times\hat{r}'\}]e^{jk_x x_f}e^{jk_y y_f}dk_x dk_y \tag{A.25}$$

Here, one should keep in mind that the domain of $\vec{E}^{GO}$ is limited. For analytical representation of the scattered GO field on the equivalent sphere, this limitation is the maximum subtended angle of the QO component. For cases where numerical GO is employed, this limitation comes from the ray tracing code. In this code, the QO component is illuminated by an incident plane wave from skew direction. The scattered rays are then propagated from the QO surface toward the focal plane, up to the position where each ray intersects with the equivalent sphere.

One can rearrange the focal field representation in (A.25) as an inverse Fourier transform of a spectral field plus a quadratic phase term, as:

$$\vec{e}_f(\vec{\rho}_f) = \frac{e^{-jk\dfrac{|\rho_f|^2}{2R_{FO}}}}{4\pi^2}\int_{-\infty}^{+\infty}\int_{-\infty}^{+\infty}\vec{E}^{FO}e^{jk_x x_f}e^{jk_y y_f}dk_x dk_y \tag{A.26}$$

where

$$\vec{E}^{FO}(k_x,k_y) = \frac{j2\pi R_{FO}e^{-jkR_{FO}}}{\sqrt{k^2-(k_x^2+k_y^2)}}\hat{r}'\times[\vec{E}^{GO}(k_x,k_y)\times\hat{r}'] \tag{A.27}$$

The integral in (A.26) is similar to an inverse Fourier transform, except for the quadratic phase term, $e^{-jk\rho_f^2/(2R_{FO})}$, in front. By neglecting this phase term, one can assume that $\vec{E}^{FO}(k_x, k_y)$ represents the Plane Wave Spectrum (PWS) of $\vec{e}_f(\vec{\rho}_f)$. In other words, the field at the focal plane is represented as a summation of plane waves coming from different directions (k_x and k_y) with varying amplitudes $\vec{E}^{FO}(k_x, k_y)$.

Appendix B

Geometrical Optics Propagation from Reflective and Refractive Surfaces

The EM fields reflected by curved multiple surfaces can be evaluated using a Geometrical Optics (GO) formalism as described in [71] and [72]. The propagation of GO fields through dielectric surfaces is instead, to our knowledge, not exhaustively treated in the literature, despite the fact that it is a key issue for analysing integrated lenses. This appendix reports the formulas necessary to describe the field propagation using GO approximation from both reflective and refractive surfaces. The procedure for the latter is explicitly derived here, and the final formulas for the reflective surfaces, following the same steps, are also provided.

Let us consider the scenario depicted in Fig. B.1 where a large dielectric object is illuminated by an incident wave $\vec{E}^i(\vec{Q}) = E_0 \hat{p}^i e^{-jk_i f(\vec{Q})}$ with polarization $\hat{p}^i$, k_i is the wave number in the incident medium, and $f(\vec{Q})$ is the incident phase function; the vector $\vec{Q}$ identifies an arbitrary point on a smooth interface of the two media from reference point $\vec{Q}_0$. This point can be expressed as a function of the surface curvature properties [72]. Namely by the principal unit directions of the surface, $\hat{U}_1$, and $\hat{U}_2$, and its principal radii of curvature, R_1, and R_2:

$$\vec{Q} = Q_1 \hat{U}_1 + Q_2 \hat{U}_2 - \hat{n}\left[\frac{1}{2R_1}Q_1^2 + \frac{1}{2R_2}Q_2^2\right] \tag{B.1}$$

where $Q_1 \hat{U}_1 + Q_2 \hat{U}_2$ are coordinates in the local tangent plane from reference point $\vec{Q}_0$. The phase function of an incident astigmatic wavefront at each position on the surface, $\vec{Q}$, can be approximated up to the quadratic order as [72]:

$$f(\vec{Q}) \simeq f(\vec{Q}_0) + \hat{k}^i(\vec{Q}) \cdot \vec{Q} + \frac{1}{2\rho_1^i(\vec{Q})}[\hat{X}_1^i(\vec{Q}) \cdot \vec{Q}]^2 + \frac{1}{2\rho_2^i(\vec{Q})}[\hat{X}_2^i(\vec{Q}) \cdot \vec{Q}]^2 \tag{B.2}$$

where $f(\vec{Q}_0)$ is the phase of the incident wave at the reference position, $\vec{Q}_0$; $\hat{X}_1^i$ and $\hat{X}_2^i$ are the principal directions of the incident wavefront and they are related to the propagation vector as: $\hat{k}^i = \hat{X}_1^i \times \hat{X}_2^i$,

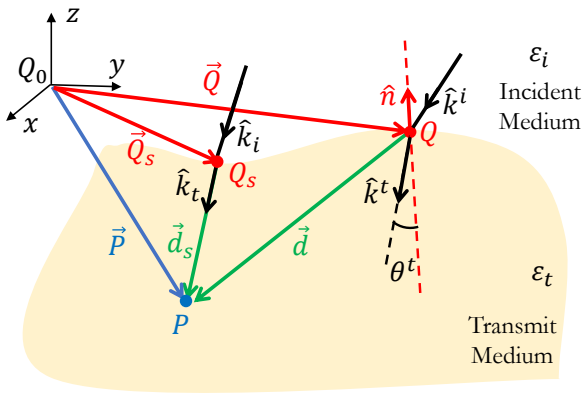

Figure B.1: A 2D sketch of an arbitrary refraction scenario.

and ρ_1^i and ρ_2^i are the principal radii of the incident wave front. In (B.2), the dependency of all of these five parameters to a position on the surface is explicitly shown by $(\vec{Q})$.

By applying the equivalence theorem, the electric field at an arbitrary observation point $\vec{P}$, from reference point $\vec{Q}_0$, inside the dielectric object enveloped by the surface S_Q, can be represented as follows:

$$\vec{E}^t(\vec{P}) = jk_t \iint_{S_Q} [\hat{d} \times \vec{m}^t(\vec{Q}) + \zeta_t \hat{d} \times \hat{d} \times \vec{j}^t(\vec{Q})] \frac{e^{-jk_t d}}{4\pi d} dS_Q \tag{B.3}$$

where k_t and ζ_t are the wavenumber and impedance in the transmitting medium, respectively; $\vec{d} = d\hat{d} = \vec{P} - \vec{Q}$ represents the distance from a point Q on the surface to the observation point P; $\vec{m}^t$ and $\vec{j}^t$ are the magnetic and electric equivalent currents, respectively. Under the GO/PO approximation, these currents are related to the transmitted fields at the interface S_Q as follows:

$$\vec{j}^t(\vec{Q}) = -\hat{n} \times \vec{H}^t(\vec{Q}), \tag{B.4a}$$

$$\vec{m}^t(\vec{Q}) = \hat{n} \times \vec{E}^t(\vec{Q}), \tag{B.4b}$$

where $\hat{n}$ is the unit vector orthogonal to the surface S_Q pointing toward the incident medium (see Fig. B.1). The transmitted fields can be approximated assuming a locally flat surface (PO approximation)

$$\vec{E}^t(\vec{Q}) = \bar{\tau} \cdot \vec{E}^i(\vec{Q}) \tag{B.5a}$$

$$\vec{H}^t(\vec{Q}) = \frac{1}{\zeta_t} \hat{k}^t \times \vec{E}^t(\vec{Q}) \tag{B.5b}$$

where $\bar{\tau} = \tau^{TE} \hat{p}^{t,TE} \hat{p}^{i,TE} + \tau^{TM} \hat{p}^{t,TM} \hat{p}^{i,TM}$ is the transmission dyad; τ^{TE} and τ^{TM} are the TE and TM transmission coefficients on the surface, respectively; $\hat{p}^{i,TE/TM}$, and $\hat{p}^{t,TE/TM}$ represent the polarization

unit vectors of the incident and transmitted rays, respectively; $\hat{k}^t$ is the propagation direction of the transmitted ray. This parameter can be calculated using Snell's law as follows:

$$\hat{k}^t = \frac{\sqrt{\varepsilon_i}}{\sqrt{\varepsilon_t}}\hat{k}^i - \left[\frac{\sqrt{\varepsilon_i}}{\sqrt{\varepsilon_t}}\{\hat{k}^t \cdot \hat{n}\} + \frac{1}{\sqrt{\varepsilon_t}}\sqrt{\varepsilon_t - \varepsilon_i[1 - \{\hat{k}^i \cdot \hat{n}\}^2]}\right] \tag{B.6}$$

where ε_t and ε_i are the relative permittivity of the transmitting and incident medium, respectively.

By using the above expressions, the integrand in (B.3) can be rewritten as:

$$\vec{E}^t(\vec{P}) = jk_t \iint_{S_Q} \left[- \{(\hat{d} \cdot \hat{n})\bar{1} - \hat{n}\hat{d}\} + \{(\bar{1} - \hat{d}\hat{d}) \cdot [\hat{k}^t\hat{n} - \bar{1}(\hat{n} \cdot \hat{k}^t)]\}\right] \cdot (\bar{\tau} \cdot \vec{E}^i(\vec{Q}))\frac{e^{-jk_t d}}{4\pi d} dS_Q \tag{B.7}$$

In oscillating integrals like the one in (B.7), one can identify both a rapidly and a slowly varying function [72]. Therefore, they can be rewritten as:

$$\vec{E}^t(\vec{P}) = \iint_{S_Q} \vec{F}(\vec{Q})e^{-jk_0\Phi(\vec{Q})} dS_Q \tag{B.8}$$

where $\vec{F}(\vec{Q})$ is a slowly varying function, whereas

$$\Phi(\vec{Q}) = \sqrt{\varepsilon_t}d(\vec{Q}) + \sqrt{\varepsilon_i}f(\vec{Q}) \tag{B.9}$$

is a real, independent of k_0, and non-singular function which contains the phase terms of the integrand, i.e. the phase of the scalar Green's function of the medium where the wave is scattered when applying the equivalence theorem, and the phase of the incident wave.

This kind of oscillating integrals are asymptotically dominated by stationary phase points (if present in the integration domain). Therefore, one can asymptotically approximate them as follows. For every observation point $\vec{P}$, there can exist a stationary phase point, $\vec{Q}_s$ that verifies the following condition ($\vec{Q}_s$ in shown Fig. B.1):

$$\hat{d}_s = \hat{k}^t \tag{B.10}$$

To asymptotically evaluate (B.8), we expand the phase term quadratically around the stationary phase point. By using the small argument approximation, for any point $\vec{Q}$ close to $\vec{Q}_s$, d is represented up to its quadratic term as:

$$d \simeq |\vec{d}_s| - \hat{k}^t \cdot \vec{Q_s Q} + \frac{1}{2|\vec{d}_s|}\left[|\vec{Q_s Q}|^2 - (\hat{k}^t \cdot \vec{Q_s Q})^2\right] \tag{B.11}$$

Using (B.2) and (B.11), and assuming that for each position $\vec{Q}$, the reference point, $\vec{Q}_0$, is at the stationary phase point, $\vec{Q}_s$, the phase function (B.9) can be approximated up to the quadratic order as:

$$\Phi(\vec{Q}) \simeq \sqrt{\varepsilon_t}\left[|\vec{d}_s| - \hat{k}^t \cdot \vec{Q} + \frac{1}{2|\vec{d}_s|}\{|\vec{Q}|^2 - [\hat{k}^t \cdot \vec{Q}]^2\}\right] + \sqrt{\varepsilon_i}\left[f(Q_s) + \hat{k}^i \cdot \vec{Q} + \frac{1}{2\rho_1^i}[\hat{X}_1^i \cdot \vec{Q}]^2 + \frac{1}{2\rho_2^i}[\hat{X}_2^i \cdot \vec{Q}]^2\right] \tag{B.12}$$

By substituting $\Phi(\vec{Q})$ in (B.8), the integral can be asymptotically evaluated [72], as

$$\vec{E}^t(\vec{P}) \simeq \frac{2\pi\eth\vec{F}(\vec{Q}_s)e^{-jk_0\phi(\vec{Q}_s)}}{jk_0\sqrt{|\det H_\Phi(\vec{Q}_s)|}} \tag{B.13}$$

where $\vec{F}(\vec{Q}_s)$ is expressed as

$$\vec{F}(\vec{Q}_s) = -jk_t\frac{\hat{k}^t \cdot \hat{n}}{2\pi d_s}\left[\bar{\tau} \cdot \vec{E}^i(\vec{Q}_S)\right]; \tag{B.14}$$

$|\det H_\Phi(\vec{Q}_s)|$ is the determinant of the Hessian matrix of the phase term [72]; $\eth = 1, -1$, or j for the eigenvalues of the matrix both positive, or both negative, or with opposite signs, respectively. The Hessian matrix can be expressed as:

$$H_\Phi = \begin{bmatrix} \frac{\partial^2\Phi}{\partial^2 Q_1} & \frac{\partial^2\Phi}{\partial Q_1 \partial Q_2} \\ \frac{\partial^2\Phi}{\partial Q_1 \partial Q_2} & \frac{\partial^2\Phi}{\partial^2 Q_2} \end{bmatrix} \tag{B.15}$$

By substituting (B.1) in (B.12) and after extensive algebraic simplifications, $|\det H_\Phi(\vec{Q}_s)|$ can be expressed as:

$$
\begin{aligned}
|\det H_\Phi| = \varepsilon_t(\cos\theta^t)^2\Bigg\{ & \frac{1}{|\vec{d}_s|^2} + \frac{1}{|\vec{d}_s|}\frac{1}{\varepsilon_t(\cos\theta^t)^2}\Bigg[\frac{1}{\rho_1^i}\frac{\varepsilon_i}{\varepsilon_t}\Big\{\varepsilon_t[1-(\hat{X}_1^i\cdot\hat{n})^2]- \\
& \varepsilon_i[(\hat{k}^i\cdot\hat{U}_2)(\hat{X}_1^i\cdot\hat{U}_1)+(\hat{k}^i\cdot\hat{U}_1)(\hat{X}_1^i\cdot\hat{U}_2)]^2\Big\} \\
& + \frac{1}{\rho_2^i}\frac{\varepsilon_i}{\varepsilon_t}\Big\{\varepsilon_t[1-(\hat{X}_2^i\cdot\hat{n})^2]-\varepsilon_i[(\hat{k}^i\cdot\hat{U}_2)(\hat{X}_2^i\cdot\hat{U}_1)+(\hat{k}^i\cdot\hat{U}_1)(\hat{X}_2^i\cdot\hat{U}_2)]^2\Big\} \\
& - \frac{1}{R_1\sqrt{\varepsilon_t}}\Big[\sqrt{\varepsilon_i}\{\hat{k}^i\cdot\hat{n}+\sqrt{\varepsilon_t}\cos\theta^t\}\Big]\Big[\varepsilon_t-\varepsilon_i\{\hat{k}^i\cdot\hat{U}_2\}^2\Big] \\
& - \frac{1}{R_2\sqrt{\varepsilon_t}}\Big[\sqrt{\varepsilon_i}\{\hat{k}^i\cdot\hat{n}+\sqrt{\varepsilon_t}\cos\theta^t\}\Big]\Big[\varepsilon_t-\varepsilon_i\{\hat{k}^i\cdot\hat{U}_1\}^2\Big]\Bigg] \\
& + \frac{1}{\varepsilon_t(\cos\theta^t)^2}\Bigg[\frac{\varepsilon_i}{\rho_1^i\rho_2^i}[\hat{k}^i\cdot\hat{n}]^2-\frac{\sqrt{\varepsilon_i}}{R_1\rho_1^i}\{\sqrt{\varepsilon_i}[\hat{k}^i\cdot\hat{n}]+\sqrt{\varepsilon_t}\cos\theta^t\}\{\hat{X}_1^i\cdot\hat{U}_2\}^2- \\
& \frac{\sqrt{\varepsilon_i}}{R_2\rho_1^i}\{\sqrt{\varepsilon_i}[\hat{k}^i\cdot\hat{n}]+\sqrt{\varepsilon_t}\cos\theta^t\}\{\hat{X}_1^i\cdot\hat{U}_1\}^2-\frac{\sqrt{\varepsilon_i}}{R_1\rho_2^i}\{\sqrt{\varepsilon_i}[\hat{k}^i\cdot\hat{n}]+\sqrt{\varepsilon_t}\cos\theta^t\}\{\hat{X}_2^i\cdot\hat{U}_2\}^2- \\
& \frac{\sqrt{\varepsilon_i}}{R_2\rho_2^i}\{\sqrt{\varepsilon_i}[\hat{k}^i\cdot\hat{n}]+\sqrt{\varepsilon_t}\cos\theta^t\}\{\hat{X}_2^i\cdot\hat{U}_1\}^2+\frac{1}{R_1R_2}\{\sqrt{\varepsilon_i}[\hat{k}^i\cdot\hat{n}]+\sqrt{\varepsilon_t}\cos\theta^t\}^2\Bigg]\Bigg\}
\end{aligned}
\tag{B.16}
$$

where θ^t is the angle of the transmitted ray with respect to the normal vector, $\hat{n}$, as shown in Fig. B.1, and $\cos\theta^t = \frac{1}{\sqrt{\varepsilon_t}}\sqrt{\varepsilon_t - \varepsilon_i[1-\{\hat{k}^i\cdot\hat{n}\}^2]}$.

The term $\eth/\sqrt{|\det H_\Phi(\vec{Q}_s)|}$ can be expressed compactly in the following form:

$$
\frac{\eth}{\sqrt{|\det H_\Phi(\vec{Q}_s)|}} = \frac{d_s}{\sqrt{\varepsilon_t}\cos\theta^t}\sqrt{\frac{\rho_1^t\rho_2^t}{[d_s+\rho_1^t][d_s+\rho_2^t]}}, \tag{B.17}
$$

where ρ_1^t and ρ_2^t are the principal radii of curvature of the transmitted wave front, and the branch of the square root is chosen accordingly to the same considerations discussed in [71], in relation to the caustics position along the ray path with respect to the refraction point. By comparing (B.17) and (B.16), an equation system for the radii of curvature of the refracted wave front can be derived as follows:

$$\frac{1}{\rho_1^t}+\frac{1}{\rho_2^t}=\frac{1}{\varepsilon_t[\cos\theta^t]^2}\left\{\frac{1}{\rho_1^i}\frac{\sqrt{\varepsilon_i}}{\sqrt{\varepsilon_t}}\left[\varepsilon_t\left\{1-[\hat{X}_1^i\cdot\hat{n}]^2\right\}-\varepsilon_i\left\{[\hat{k}^i\cdot\hat{U}_2][\hat{X}_1^i\cdot\hat{U}_1]+[\hat{X}_1^i\cdot\hat{U}_2][\hat{k}^i\cdot\hat{U}_1]\right\}^2\right]+\right.$$
$$\frac{1}{\rho_2^i}\frac{\sqrt{\varepsilon_i}}{\sqrt{\varepsilon_t}}\left[\varepsilon_t\left\{1-[\hat{X}_2^i\cdot\hat{n}]^2\right\}-\varepsilon_i\left\{[\hat{k}^i\cdot\hat{U}_2][\hat{X}_2^i\cdot\hat{U}_1]+[\hat{X}_2^i\cdot\hat{U}_2][\hat{k}^i\cdot\hat{U}_1]\right\}^2\right]-$$
$$\frac{1}{R_1}\frac{1}{\sqrt{\varepsilon_t}}\left[\left\{\sqrt{\varepsilon_i}[\hat{k}^i\cdot\hat{n}]+\sqrt{\varepsilon_t}\cos\theta^t\right\}\left\{\varepsilon_t-\varepsilon_i[\hat{k}^i\cdot\hat{U}_2]^2\right\}\right]-$$
$$\left.\frac{1}{R_2}\frac{1}{\sqrt{\varepsilon_t}}\left[\left\{\sqrt{\varepsilon_i}[\hat{k}^i\cdot\hat{n}]+\sqrt{\varepsilon_t}\cos\theta^t\right\}\left\{\varepsilon_t-\varepsilon_i[\hat{k}^i\cdot\hat{U}_1]^2\right\}\right]\right\} \tag{B.18}$$

$$\frac{1}{\rho_1^t\rho_2^t}=\frac{1}{\varepsilon_t[\cos\theta^t]^2}\left\{\frac{\varepsilon_i}{\rho_1^i\rho_2^i}\left[\hat{k}^i\cdot\hat{n}\right]^2-\frac{\sqrt{\varepsilon_i}}{R_1\rho_1^i}\left\{\sqrt{\varepsilon_i}[\hat{k}^i\cdot\hat{n}]+\sqrt{\varepsilon_t}\cos\theta^t\right\}\left\{\hat{X}_1^i\cdot\hat{U}_2\right\}^2-\right.$$
$$\frac{\sqrt{\varepsilon_i}}{R_2\rho_1^i}\left\{\sqrt{\varepsilon_i}[\hat{k}^i\cdot\hat{n}]+\sqrt{\varepsilon_t}\cos\theta^t\right\}\left\{\hat{X}_1^i\cdot\hat{U}_1\right\}^2-\frac{\sqrt{\varepsilon_i}}{R_1\rho_2^i}\left\{\sqrt{\varepsilon_i}[\hat{k}^i\cdot\hat{n}]+\sqrt{\varepsilon_t}\cos\theta^t\right\}\left\{\hat{X}_2^i\cdot\hat{U}_2\right\}^2-$$
$$\left.\frac{\sqrt{\varepsilon_i}}{R_2\rho_2^i}\left\{\sqrt{\varepsilon_i}[\hat{k}^i\cdot\hat{n}]+\sqrt{\varepsilon_t}\cos\theta^t\right\}\left\{\hat{X}_2^i\cdot\hat{U}_1\right\}^2+\frac{1}{R_1R_2}\left[\sqrt{\varepsilon_i}\left\{\hat{k}^i\cdot\hat{n}\right\}+\sqrt{\varepsilon_t}\cos\theta^t\right]^2\right\} \tag{B.19}$$

Equations (B.18) and (B.19) represent the radii of curvature for transmitted wavefronts in the case of incident astigmatic wavefronts. In the case of an incident plane wave, an important special case in this thesis, the radii of curvature of incident wave front are $\rho_1^i=\rho_2^i=\infty$. Therefore, in the case of plane wave incidence, (B.18) and (B.19) reduce to:

$$\frac{1}{\rho_1^t}+\frac{1}{\rho_2^t}=\frac{1}{\varepsilon_t[\cos\theta^t]^2}$$
$$\left\{-\frac{1}{R_1}\frac{1}{\sqrt{\varepsilon_t}}\left[\left\{\sqrt{\varepsilon_i}[\hat{k}^i\cdot\hat{n}]+\sqrt{\varepsilon_t}\cos\theta^t\right\}\left\{\varepsilon_t-[\hat{k}^i\cdot\hat{U}_2]^2\right\}\right]-\right.$$
$$\left.\frac{1}{R_2}\frac{1}{\sqrt{\varepsilon_t}}\left[\left\{\sqrt{\varepsilon_i}[\hat{k}^i\cdot\hat{n}]+\sqrt{\varepsilon_t}\cos\theta^t\right\}\left\{\varepsilon_t-\varepsilon_i[\hat{k}^i\cdot\hat{U}_1]^2\right\}\right]\right\} \tag{B.20}$$

$$\frac{1}{\rho_1^t\rho_2^t}=\frac{1}{\varepsilon_t[\cos\theta^t]^2}\left\{\frac{1}{R_1R_2}\left[\sqrt{\varepsilon_i}\left\{\hat{k}^i\cdot\hat{n}\right\}+\sqrt{\varepsilon_t}\cos\theta^t\right]^2\right\} \tag{B.21}$$

An expression similar to (B.17) can be derived for the case of reflective surfaces:

$$\frac{\delta}{\sqrt{|\det H_\Phi(\vec{Q}_s)|}}=\sqrt{\frac{\rho_1^r\rho_2^r}{[d_s+\rho_1^r][d_s+\rho_2^r]}}, \tag{B.22}$$

where ρ_1^r and ρ_2^r are the principal radii of curvature of the reflected wavefront. In this case, stationary phase point condition leads to $\hat{d}_s = \hat{k}^r$, where $\hat{k}^r$ is the direction of the reflected ray. Similarly, $|\det H_\Phi(\vec{Q}_s)|$ can be expressed for a reflected ray as:

$$
\begin{aligned}
|\det H_\Phi| = [\hat{k}^i \cdot \hat{n}]^2 \Bigg\{ & \frac{1}{|\vec{d}_s|^2} + \frac{1}{|\vec{d}_s|\rho_1^i} + \frac{1}{|\vec{d}_s|\rho_2^i} + \frac{1}{\rho_1^i \rho_2^i} + \frac{4}{R_1 R_2} - \frac{2}{\hat{k}^i \cdot \hat{n}} \Bigg[\\
& \frac{1}{R_1 |\vec{d}_s|} \left\{ [\hat{X}_1^i \cdot \hat{U}_2]^2 + [\hat{X}_2^i \cdot \hat{U}_2]^2 \right\} + \frac{1}{R_2 |\vec{d}_s|} \left\{ [\hat{X}_1^i \cdot \hat{U}_1]^2 + [\hat{X}_2^i \cdot \hat{U}_1]^2 \right\} + \\
& \frac{1}{R_1 \rho_1^i} \left\{ \hat{X}_1^i \cdot \hat{U}_2 \right\}^2 + \frac{1}{R_1 \rho_2^i} \left\{ \hat{X}_2^i \cdot \hat{U}_2 \right\}^2 + \frac{1}{R_2 \rho_1^i} \left\{ \hat{X}_1^i \cdot \hat{U}_1 \right\}^2 + + \frac{1}{R_2 \rho_2^i} \left\{ \hat{X}_2^i \cdot \hat{U}_1 \right\}^2 \Bigg] \Bigg\}
\end{aligned}
\tag{B.23}
$$

and the radii of curvature of the reflected wave front can be derived as follows:

$$
\frac{1}{\rho_1^r} + \frac{1}{\rho_2^r} = \left\{ \frac{1}{\rho_1^i} + \frac{1}{\rho_2^i} - \frac{2}{\hat{k}^i \cdot \hat{n}} \left[\frac{\left\{ \hat{X}_1^i \cdot \hat{U}_2 \right\}^2 + \left\{ \hat{X}_2^i \cdot \hat{U}_2 \right\}^2}{R_1} + \frac{\left\{ \hat{X}_1^i \cdot \hat{U}_1 \right\}^2 + \left\{ \hat{X}_2^i \cdot \hat{U}_1 \right\}^2}{R_2} \right] \right\} \tag{B.24}
$$

$$
\frac{1}{\rho_1^r \rho_2^r} = \frac{1}{\rho_1^i \rho_2^i} + \frac{4}{R_1 R_2} - \frac{2}{\hat{k}^i \cdot \hat{n}} \frac{1}{\rho_1^i} \left[\frac{\left\{ \hat{X}_1^i \cdot \hat{U}_2 \right\}^2}{R_1} + \frac{\left\{ \hat{X}_1^i \cdot \hat{U}_1 \right\}^2}{R_2} \right] - \frac{2}{\hat{k}^i \cdot \hat{n}} \frac{1}{\rho_2^i} \left[\frac{\left\{ \hat{X}_2^i \cdot \hat{U}_2 \right\}^2}{R_1} + \frac{\left\{ \hat{X}_2^i \cdot \hat{U}_1 \right\}^2}{R_2} \right] \tag{B.25}
$$

The same expressions can be found in [156].

Appendix C

Zernike Polynomials Expansion

One can represent an arbitrary function, $F(\rho, \phi)$, which is sufficiently smooth by Zernike Polynomials [92, 93] as

$$F(\rho, \phi) \simeq Z_N^M = \sum_{m=0}^{M} \sum_{n=m}^{N} [A_n^m O_n^M(\rho, \phi) + B_n^m E_n^M(\rho, \phi)] \tag{C.1}$$

where $0 \leq \rho \leq 1$ and $0 \leq \phi \leq 2\pi$; Z_N^M is a Zernike polynomial of order N and M; O_n^m and E_n^m are the odd and even Zernike Polynomials, respectively; A_n^m and B_n^m are the weight coefficient of these polynomials. These polynomials can be expressed as

$$O_n^m(\rho, \phi) = R_n^m(\rho) \sin(m\phi) \tag{C.2a}$$
$$E_n^m(\rho, \phi) = R_n^m(\rho) \cos(m\phi) \tag{C.2b}$$

where the radial function $R_n^m(\rho)$ is

$$R_n^m(\rho) = \begin{cases} \sum_{l=0}^{(n-m)/2} \dfrac{(-1)^l (n-l)!}{l! \left(\dfrac{n+m}{2} - l\right)! \left(\dfrac{n-m}{2} - l\right)!} & \text{if } n-m : even \\ 0 & \text{if } n-m : odd \end{cases} \tag{C.3}$$

These polynomials are orthogonal to one another. By using this property, we can project function $F(\rho, \phi)$ on each polynomial to find their weight coefficients:

$$A_n^m = \frac{\varepsilon_m [n+1]}{\pi} \int_0^1 G_o(\rho) R_n^m(\rho) d\rho \tag{C.4a}$$
$$B_n^m = \frac{\varepsilon_m [n+1]}{\pi} \int_0^1 G_e(\rho) R_n^m(\rho) d\rho \tag{C.4b}$$

where $\varepsilon_m = \begin{cases} 1 & \text{when } m = 0 \\ 2 & \text{when } m \neq 0 \end{cases}$ and

$$G_o(\rho) = \int_0^{2\pi} F(\rho, \phi) \sin(m\phi) d\phi \tag{C.5a}$$

$$G_e(\rho) = \int_0^{2\pi} F(\rho, \phi) \cos(m\phi) d\phi \tag{C.5b}$$

Bibliography

[1] L. B. Felsen, "Quasi-optical methods in microwave propagation and diffraction," *Appl. Opt.*, vol. 4, pp. 1217–1228, 1965.

[2] E. Karplus, "Communication with quasioptical waves," *Proc. IRE*, vol. 19, pp. 1715–1730, Oct. 1931.

[3] F. Sobel, F. L. Wentworth, and J. C. Wiltse, "Quasi-optical surface waveguide and other components for the 100 to 300 Gc region," *IEEE Trans. Microwave Theory Tech*, vol. MlT-9, pp. 512–518, 1961.

[4] A. F. Harvey, "Optical techniques at microwave frequencies," *Proceedings of the IEE - Part B: Radio and Electronic Engineering*, vol. 106, pp. 141–157, March 1959.

[5] R. Tremblay and A. Boivin, "Concepts and techniques of microwave optics," *Appl. Opt.*, vol. 5, pp. 249–278, 1966s.

[6] H. Hertz, "Ueber strahlen elektrischer kraft," *Ann. Phys. Chem*, vol. 36, pp. 769–783, 1889.

[7] G. Marconi, "Improvements in transmitting electrical impulses and signals, and in apparatus therefore," *British Patent Specification*, vol. 12, June 1896.

[8] "KOCHI ARTS and SCIENCE SPACE," Available: https://kartsci.org/science_computers/wireless-communications-radio/, Accessed: 2020-02-18.

[9] A. A. Kostenko, A. I. Nosich, and P. F. Goldsmith, "Historical background and development of soviet quasioptics at nearmm and submm wavelengths," p. 1715–1730, Oct. 2006.

[10] M. Calvo and et al., "The NIKA2 instrument, a dual-band kilopixel KID array for millimetric astronomy," *J. Low Temp. Phys*, vol. 184, pp. 816–823, 2016.

[11] G. J. Stacey and et. al, "SWCam: the short wavelength camera for the CCAT observatory," *Proc. SPIE*, vol. 9153, pp. 91530L, Aug. 2014.

[12] J. J. A. Baselmans and et al., "A kilo-pixel imaging system for future space based far-infrared observatories using microwave kinetic inductance detectors," *Astron. Astrphys.*, vol. 601, Sep. 2016.

[13] L. Ferrari and et al, "Antenna coupled MKID performance verification at 850 GHz for large format astrophysics arrays," *IEEE Trans. on Terahertz Sci. and Tech.*, vol. 8, pp. 127–139, Jan. 2018.

[14] B. A. Benson and et al., "SPT-3G: a next-generation cosmic microwave background polarization experiment on the South Pole telescope," *Millimeter, Submillimeter, and Far-Infrared Detectors and Instrumentation for Astronomy VII*, Jul. 2014.

[15] Y. Inoue and et al., "POLARBEAR-2: an instrument for CMB polarization measurements," *Millimeter, Submillimeter, and Far-Infrared Detectors and Instrumentation for Astronomy VIII*, vol. 9914, pp. 372–380, 2016.

[16] M. D. Niemack and et al., "ACTPol: a polarization-sensitive receiver for the Atacama Cosmology Telescope," *Millimeter, Submillimeter, and Far-Infrared Detectors and Instrumentation for Astronomy V*, Jul. 2010.

[17] T. Essinger-Hileman and et. al., "CLASS: the cosmology large angular scale surveyor," *Millimeter, Submillimeter, and Far-Infrared Detectors and Instrumentation for Astronomy VII*, vol. 9153, pp. 491 – 513, 2014.

[18] N. Galitzki and et al., "The next generation BLAST experiment," *Journal of Astronomical Instrumentation*, vol. 03, no. 02, Nov. 2014.

[19] H. Hui and et al., "BICEP array: a multi-frequency degree-scale CMB polarimeter," *Millimeter, Submillimeter, and Far-Infrared Detectors and Instrumentation for Astronomy IX*, Jul. 2018.

[20] K. B. Cooper, R. J. Dengler, N. Llombart, B. Thomas, G. Chattopadhyay, and P. H. Siegel, "THz imaging radar for standoff personnel screening," *IEEE THz Sci. and Technol.*, vol. 1, pp. 169–182, Sept. 2011.

[21] S. Rowe and et al., "A passive terahertz video camera based on lumped element kinetic inductance detectors," *Rev. Sci. Instrum.*, vol. 87, pp. 033105, Mar. 2016.

[22] S. van Berkel, O. Yurduseven, A. Freni, A. Neto, and N. Llombart, "THz imaging using uncooled wideband direct detection focal plane arrays," *IEEE Trans. THz Sci. Technol.*, vol. 7, pp. 481–492, Sept. 2017.

[23] F. García-Rial and et al., "Combining commercially available active and passive sensors into a millimeter-wave imager for concealed weapon detection," *IEEE Transactions on Microwave Theory and Techniques*, vol. 67, pp. 1167–1183, March 2019.

[24] D. A. Robertson and et al., "The CONSORTIS 16-channel 340-GHz security imaging radar," *Proc. SPIE: Passive and Active Millimeter-Wave Imaging XXI*, vol. 10634, 2018.

[25] R. Al Hadi and et al., "A 1 k-pixel video camera for 0.7–1.1 Terahertz imaging applications in 65-nm CMOS," *IEEE Journal of Solid-State Circuits*, vol. 47, pp. 2999–3012, Dec. 2012.

[26] E. Gandini, J. Svedin, T. Bryllert, and N. Llombart, "Optomechanical system design for dual-mode stand-off submillimeter wavelength imagers," *IEEE Trans. Terahertz Sci. Technol.*, vol. 7, pp. 393–403, July 2017.

[27] M. Agiwal, A. Roy, and N. Saxena, "Next generation 5G wireless networks: A comprehensive survey," *IEEE Communications Surveys & Tutorials*, vol. 18, pp. 1617–1655, 2016.

[28] T. S. Rappaport, J. N. Murdock, and F. Gutierrez, "State of the art in 60-GHz integrated circuits and systems for wireless communications," *Proceedings of the IEEE*, vol. 99, pp. 1390–1436, 2011.

[29] X. Wu, G. V. Eleftheriades, and T. E. van Deventer-Perkins, "Design and characterization of single- and multiple-beam mm-wave circularly polarized substrate lens antennas for wireless communications," *IEEE Transactions on Microwave Theory and Techniques*, vol. 49, pp. 431–441, March 2001.

[30] G. Godi, R. Sauleau, and D. Thouroude, "Performance of reduced size substrate lens antennas for millimeter-wave communications," *IEEE Trans. Antennas Propag.*, vol. 53, pp. 1278–1286, April 2005.

[31] J. Ala-Laurinaho and et al., "2-D beam-steerable integrated lens antenna system for 5G e-band access and backhaul," *IEEE Transactions on Microwave Theory and Techniques*, vol. 64, pp. 2244–2255, July 2016.

[32] A. Bisognin and et al., "Ball grid array module with integrated shaped lens for 5G backhaul/fronthaul communications in f-band," *IEEE Trans. Antennas Propag.*, vol. 65, pp. 6380–6394, Dec. 2017.

[33] T. Jaschke, B. Rohrdantz, H. K. Mitto, and A. F. Jacob, "Ultrawideband SIW-fed lens antenna," *IEEE Antennas and Wireless Propag. Letters*, vol. 16, pp. 2010–2013, 2017.

[34] A. Artemenko and et al., "Experimental characterization of e-band two-dimensional electronically beam-steerable integrated lens antennas," *IEEE Antennas and Wireless Propag. Letters*, vol. 12, pp. 1188–1191, 2013.

[35] M. Arias Campo and et al., "On the use of fly's eye lenses with leaky wave feeds for wideband communications," *IEEE Trans. Antennas Propag.*, vol. 8, pp. 2480–2493, April 2020.

[36] A. Fiorellini Bernardis, P. Sberna, A. Neto, and N. LLombart, "Signal to noise ratio for a picoseconds pulsed radar for imaging at stand-off distances," *EuCAP conference*, April 2019.

[37] A. Endo and et al., "First light demonstration of the integrated superconducting spectrometer," *Nature Astronomy*, 2019.

[38] A. Endo and et. al., "Wideband on-chip terahertz spectrometer based on a superconducting filterbank," *Journal of Astronomical Telescopes, Instruments, and Systems*, June 2019.

[39] E. Gandini, A. Tamminen, A. Luukanen, and N. Llombart, "Wide field of view inversely magnified dual-lens for near-field sub-millimeter wavelength imagers," *IEEE Trans. Antennas Propag.*, vol. 66, pp. 541–549, Feb. 2018.

[40] S. L. van Berkel and et al., "High resolution passive THz imaging array with polarization reusage in 22nm CMOS," *44th International Conference on Infrared, Millimeter, and Terahertz Waves (IRMMW-THz)*, pp. 1–2, Sep. 2019.

[41] A. Timofeev and et al., "Optical and electrical characterization of a large kinetic inductance bolometer focal plane array," *IEEE THz Sci. Technol.*, vol. 7, pp. 218–224, Mar. 2017.

[42] N. Oda and et al., "Microbolometer terahertz focal plane array and camera with improved sensitivity in the sub-terahertz region," *J. Infr., Millim., THz Waves*, vol. 36, pp. 947–960, Oct. 2015.

[43] F. Sakran, Y. Neve-Oz, A. Ron, M. Golosovsky, D. Davidov, and A. Frenkel, "Absorbing frequency-selective-surface for the mm-wave range," *IEEE Trans. Antennas Propag.*, vol. 56, pp. 2649–2655, Aug. 2008.

[44] P. L. Richards, "Bolometers for infrared and millimeter waves," *J. Appl. Phys.*, vol. 76, pp. 1–24, Mar. 1994.

[45] T. H. Büttgenbach, "An improved solution for integrated array optics in quasi-optical mm and submm receivers: The hybrid antenna," *IEEE Trans. Microw. Theory Techn.*, vol. 41, pp. 1750–1760, Oct. 1993.

[46] G. M. Rebeiz, L. P. B. Katehi, W. Y. Ali-Ahmad, G. V. Eleftheriades, and C. C. Ling, "Integrated horn antennas for millimeter-wave applications," *IEEE Antennas Propag. Mag.*, vol. 34, pp. 7–16, Feb. 1992.

[47] M. J. Griffin, J. J. Bock, , and W. K. Gear, "Relative performance of filled and feedhorn-coupled focal-plane architectures," *Appl. Opt.*, vol. 41, pp. 6543–6554, Nov. 2002.

[48] J. F. Johansson, "Millimeter-wave imaging theory and experiments," *Onsala Space Observatory, Kungsbacka, Sweden, Res. Rep. 151*, vol. 1, pp. 1, 1986.

[49] S. Rao, L. Shafai, and Eds. S. K. Sharma, *Handbook of Reflector Antennas and Feed Systems*, vol. 2, Artech House, Norwood, MA, USA, 2013.

[50] D. Rutledge and S. Schwarz, "Planar multimode detector arrays for infrared and millimeter-wave applications," *IEEE J. Quantum Electron*, vol. JQE-17, pp. 407–414, Mar. 1981.

[51] "OpticStudio, ZEMAX version 18.9," Available: https://www.zemax.com/products/opticstudio.

[52] "Leonardo da Vinci's notebook - Codex Arundel," Available: https://www.bl.uk/collection-items/leonardo-da-vinci-notebook, British Library.

[53] "TICRA Tools Version 19.0, ticra, copenhagen, denmark," Available: https://www.ticra.com/ticratools/.

[54] P. F. Goldsmith, *Quasioptical systems: Gaussian beam quasioptical propagation and applications*, Wiley, Hoboken, NJ, USA, 1997.

[55] P. S. Kildal, "Gaussian beam model for aperture-controlled and flareangle-controlled corrugated horn antennas," *IEE Proceedings H-Microwaves, Antennas and Propagation*, vol. 135, pp. 237–240, Aug. 1988.

[56] P. F. Goldsmith, "Quasi-optical techniques," *Proceedings of the IEEE*, vol. 80, pp. 1729–1747, Nov. 1992.

[57] L. B. Felsen and Nathan Marcuvitz, *Radiation and Scattering of Waves*, New York: Wiley, 1994.

[58] Robert E. Collin, *Field Theory of Guided Waves*, Wiley-IEEE Press, 1991.

[59] F. Mesa, C. Di Nallo, and D. R. Jackson, "The theory of surface-wave and space-wave leaky-mode excitation on microstrip lines," *IEEE Transactions of Microwave Theory and Technology*, vol. 47, pp. 207–215, 1999.

[60] F. Mesa and D. R. Jackson, "Investigation of integration paths in the spectral domain analysis of leaky modes on printed circuit lines," *IEEE Transactions of Microwave Theory and Technology*, vol. 50, pp. 2267–2275, 2002.

[61] A. Neto and S. Maci, "Green's function for an infinite slot printed between two homogeneous dielectrics. I. Magnetic current," *IEEE Transactions on Antennas and Propagation*, vol. 51, pp. 1572–1581, 2003.

[62] D. Cavallo, A. Neto, and G. Gerini, "Green's function based equivalent circuits for connected arrays in transmission and in reception," *IEEE Transactions on Antennas and Propagation*, vol. 59, pp. 1535–1545, May 2011.

[63] W. H. Syed, D. Cavallo, H. Thippur Shivamurthy, and A. Neto, "Wideband, wide-scan planar array of connected slots loaded with artificial dielectric superstrates," *IEEE Transactions on Antennas and Propagation*, vol. 64, pp. 543–553, Feb. 2016.

[64] V. H. Rumsey, "On the design and performance of feeds for correcting spherical aberration," *IEEE Trans. Antennas Propag.*, vol. 18, pp. 343–351, May 1970.

[65] O. Yurduseven, A. Freni, N. Llombart, and A. Neto, "On the use of Thevenin Circuits in distributed transmission lines and its consequences for antennas in reception," *EuCAP Conference*, 2016.

[66] N. Llombart, B. Blázquez, A. Freni, and A. Neto, "Fourier optics for the analysis of distributed absorbers under THz focusing systems," *IEEE Trans. THz Sci. Technol.*, vol. 5, pp. 573–583, Jul. 2015.

[67] A. Nagamune and P. H. Pathak, "An efficient plane wave spectral analysis to predict the focal region fields of parabolic reflector antennas for small and wide angle scanning," *IEEE Trans. on Antenna and Propag.*, vol. 38, pp. 1746–1756, Nov. 1990.

[68] E. Wolf, "Electromagnetic diffraction in optical systems—I. An integral representation of the image field," *Proc. Roy. Soc. A, Math. Phys. Sci.*, vol. 253, pp. 349–357, 1959.

[69] W. Rusch, A. Prata, Jr., Y. Rahmat-Samii, and R. A. Shore, "Derivation and application of the equivalent paraboloid for classical offset Cassegrain and Gregorian antennas," *IEEE Trans. Antennas Propag.*, vol. 38, pp. 1141–1149, Aug. 1990.

[70] O. Yurduseven and et. al., "A dual-polarized leaky lens antenna for wideband focal plane arrays," *IEEE Trans. Antennas Propag.*, vol. 64, pp. 3330–3337, 2016.

[71] P. H. Pathak, "High frequency techniques for antenna analysis," *Proceedings of the IEEE*, vol. 80, pp. 44–65, 1992.

[72] M. Albani, G. Carluccio, and P. H. Pathak, "Uniform ray description for the PO scattering by vertices in curved surface with curvilinear edges and relatively general boundary conditions," *IEEE Trans. on Antenna and Propag.*, vol. 59, pp. 1587–1596, May 2011.

[73] S. O. Dabironezare and et al., "Coherent fourier optics model for the synthesis of large format lens based focal plane arrays," *IEEE Trans. on Antenna and Propag.*, under review.

[74] S. Von Hoerner, "Strong coma lobes from small gravitational deformations," *Proc. IEEE*, vol. AP-28, pp. 652–657, Sept. 1980.

[75] Y. Lo, "On the beam deviation factor of a parabolic reflector," *IRE Transactions on Antennas and Propagation*, vol. 8, no. 3, pp. 347–349, May 1960.

[76] C. Dragone, "A first-order treatment of aberrations in Cassegrainian and Gregorian antennas," *IEEE Trans. Antennas Propag.*, vol. AP-30, pp. 331–339, May 1982.

[77] J. Ruze, "Lateral-feed displacement in a paraboloid," *IEEE Trans. Antennas Propag.*, vol. AP-13, pp. 660–665, Sept. 1965.

[78] R. C. Hansen, *Microwave Scanning Antennas*, vol. 1, Academic, New York, NY, US, 1964.

[79] "CST Microwave Studio Version 2018.00," Available: http://www.cst.com.

[80] D. Pasqualini and S. Maci, "High-frequency analysis of integrated dielectric lens antennas," *IEEE Trans. on Antenna and Propag.*, vol. 52, pp. 840–847, March 2004.

[81] A. W. Rudge and N. A. Adatia, "Offset-parabolic-reflector antennas: A review," *Proc. IEEE*, vol. 66, pp. 1592–1618, Dec. 1978.

[82] S. O. Dabironezare and et al., "A dual-band focal plane array of kinetic inductance bolometers based on frequency-selective absorbers," *IEEE Trans. on Terahertz Sci. and Tech.*, vol. 8, pp. 746–756, Nov. 2018.

[83] V. Galindo-Israel, W. Veruttipong, R. D. Norrod, and W. A. Imbriale, "Scanning properties of large dual-shaped offset and symmetric reflector antennas," *IEEE Trans. Antennas and Propag.*, vol. 40, pp. 422–432, Apr. 1992.

[84] A. Garcia-Pino, N. Llombart, B. Gonzalez-Valdes, and O. Rubinos-Lopez, "A bifocal ellipsoidal Gregorian reflector system for THz imaging applications," *IEEE Trans. Antennas Propag.*, vol. 60, pp. 4119–4129, Sep. 2012.

[85] W. P. Craig, C. M. Rappaport, and J. S. Mason, "A high aperture efficiency, wide-angle scanning offset reflector antenna," *IEEE Trans. Antennas and Propag.*, vol. 41, pp. 1481–1490, Nov. 1993.

[86] V. Krichevsky and D. Difonzo, "Optimum beam scanning in offset single and dual reflector antennas," *IEEE Trans. Antennas and Propag.*, vol. 33, pp. 179–188, Feb. 1985.

[87] A. W. Rudge and M. J. Withers, "New technique for beam steering with fixed parabolic reflectors," *Proc. Ins. Elec. Eng.*, vol. 118, pp. 857–863, July 1971.

[88] V. Galindo-Israel, Shung-Wu Lee, and R. Mittra, "Synthesis of a laterally displaced cluster feed for a reflector antenna with application to multiple beams and contoured patterns," *APS*, p. 432–435, 1977.

[89] C. Hung and G. Chadwick, "Corrected off axis beams for parabloic reflectors," *APS*, p. 278–281, 1979.

[90] S. Chang and A. Prata, "The design of classical offset dragonian reflector antennas with circular apertures," *IEEE Trans. Antennas Propag.*, vol. 52, pp. 12–19, 2004.

[91] S. B. Sorensen and K. Pontoppidan, "Lens analysis methods for quasioptical systems," *EuCAP Conference*, p. 1–5, 2007.

[92] F. Zernike, "Beugungstheorie des schneidenverfahrens und seiner verbesserten form, der phasenkontrastmethode," *Physica I*, 1934.

[93] A. Prata and W. V. T. Rusch, "A quadrature formula for evaluating Zernike polynomial expansion coefficients (antenna analysis)," *Digest on Antennas and Propagation Society International Symposium*, 1989.

[94] R. M. Goldstein, H. A. Zebken, and C. L. Werner, "Satellite radar interferometry: Two-dimensional phase unwrapping," *Radio Sci.*, vol. 23, pp. 713–720, 1988.

[95] "Veldlaser, s-Heerenberg, the Netherlands," Available: http://www.veldlaser.nl/.

[96] J. Redford and et. al., "The design and characterization of a 300 channel, optimized full-band millimeter filterbank for science with SuperSpec," *Proc. SPIE*, vol. 10708, pp. 1–8, July 2018.

[97] P. K. Day, H. G. LeDuc, B. A. Mazin, A. Vayonakis, and J. Zmuidzinas, "A broadband superconducting detector suitable for use in large arrays," *Nature*, vol. 425, pp. 817–821, Oct. 2003.

[98] J. Shi and et. al., "Quadruple-ridged flared horn operating from 8 to 50 GHz," *IEEE Trans. Antennas Propag.*, vol. 65, pp. 817–821, 2017.

[99] J. Yang and M. Pantaleev, "Truly conical eleven antenna: A new geometry for applications at high frequencies," *APS–Ursi*, 2016.

[100] A. Gonzalez and et. al., "Recent work on (sub-)mm-wave ultra wideband corrugated horns for radio astronomy," *EuCAP conference*, Mar. 2017.

[101] O. Yurduseven and et. al., "Wideband dielectric lens antenna with stable radiation patterns fed by coherent array of connected leaky slots," *IEEE Trans. Antennas Propag.*, vol. 62, pp. 1895–1902, 2014.

[102] A. Pascual Laguna and et. al., "Focused superconducting connected array for wideband sub-mm spectrometers," *EuCAP conference*, April 2018.

[103] K. Kouwenhove and et. al., "Optimized design for on chip Fabry-Pérot resonators," *18th International Workshop on Low Temperature Detectors*, July 2019.

[104] D. P. Neikirk K. D. B. Rutledge and D. P. Kasilingam, *Integrated circuit antennas in Infrared and Millimeter-Waves*, vol. 10, NewYork: Academic Press, 1983.

[105] A. Neto, "UWB, non dispersive radiation from the planarly fed leaky lens antenna Part I: Theory and design," *IEEE Trans. Antennas Propag.*, vol. 58, pp. 2238–2247, 2010.

[106] A. Neto and et. al, "UWB, non dispersive radiation from the planarly fed leaky lens antenna Part II: Demonstrators and measurements," *IEEE Trans. Antennas Propag.*, vol. 58, pp. 2248–2258, 2010.

[107] S. Bosma, "Quasi-optical system for the DESHIMA spectrometer," *Master Thesis, Delft University of Technology*, 2017.

[108] Darin Rosen and et. al., "Epoxy-based broadband antireflection coating for millimeter-wave optics," *Appl. Opt.*, vol. 52, pp. 8102–8105, 2013.

[109] "Kayaku advanced materials," Available: https://kayakuam.com/products/perminex-wafer-bonding-adhesives/, accessed on 03.03.2020.

[110] A. Nadolski and et al., "Broadband anti-reflective coatings for cosmic microwave background experiments," *Millimeter, Submillimeter, and Far-Infrared Detectors and Instrumentation for Astronomy IX*, Jul. 2018.

[111] "CAD model by Robert Huiting," SRON, *private communications*.

[112] D.G. Paveliev and et. al, "Experimental study of frequency multipliers based on a GaAs/AlAs semiconductor superlattices in the terahertz frequency range," *Semiconductors*, vol. 46, pp. 121–125, 2012.

[113] L. Pasquiniet and et. al, "Installation and commissioning of FLAMES, the VLT Multifibre Facility," *The Messenger*, vol. 110, pp. 1–9, Dec. 2002.

[114] O. LeFevre and et. al, "VIRMOS: visible and infrared multiobject spectrographs for the VLT," *Optical Astronomical Instrumentation*, vol. 3355, pp. 8 – 19, 1998.

[115] F. Eisenhauer and et. al, "SINFONI: integral field spectroscopy at 50-milli-arcsecond resolution with the ESO VLT," *Instrument Design and Performance for Optical/Infrared Ground-based Telescopes*, vol. 4841, pp. 1548 – 1561, 2003.

[116] R. Sharples and et. al, "Performance of the K-band multi-object spectrograph (KMOS) on the ESO VLT," *Ground-based and Airborne Instrumentation for Astronomy V*, vol. 9147, pp. 322 – 330, 2014.

[117] M. Alonso-delPino, C. Jung-Kubiak, T. Reck, N. Llombart, and G. Chattopadhyay, "Beam scanning of silicon lens antennas using integrated piezomotors at submillimeter wavelengths," *IEEE Trans. on Terahertz Sci. and Tech.*, vol. 9, pp. 47–54, Jan. 2019.

[118] C. A. Fernandes, J. R. Costa, and M. van der Vorst, "Design of a shaped double-shell lens feed for a quasi-optical reflector system," *IEEE Antennas and Propagation Society International Symposium*, p. 5331–5334, 2007.

[119] B. Schoenlinner and et. al, "Wide-scan spherical-lens antennas for automotive radars," *IEEE Trans. Microw. Theory Techn.*, vol. 50, pp. 2166–2175, Nov. 2002.

[120] R. Appleby and H. Wallace, "Standoff detection of weapons and contraband in the 100 GHz to 1 THz region," *IEEE Trans. on Antennas and Propag.*, vol. 55, pp. 2944–2956, Nov. 2007.

[121] E. Grossman, C. Dietlein, J. Ala-Laurinaho, M. Leivo, L. Gronberg, M. Gronholm, P. Lappalainen, A. Rautiainen, A. Tamminen, and A. Luukanen, "Passive terahertz camera for standoff security screening," *Appl. Opt.*, vol. 49, pp. E106–E120, Jul. 2010.

[122] E. Heinz, T. May, D. Born, G. Zieger, K. Peiselt, V. Zakosarenko, T. Krause, A. Krüger, M. Schulz, F. Bauer, , and H.-G. Meyer, "Progress in passive submillimeter-wave video imaging," *Proc. SPIE*, vol. 9078, pp. 907808, June 2014.

[123] C. N. Thomas and S. Withington, "Optical modeling techniques for multimode horn-coupled power detectors for submillimeter and farinfrared astronomy," *J. Opt. Soc. Amer. A.*, vol. 30, pp. 1703–1713, Aug. 2013.

[124] D. McCarthy and et. al, "Optical characterisation and analysis of multimode pixels for use in future far infrared telescopes," *Proc. SPIE*, vol. 9914, pp. 991413, Jul. 2016.

[125] B. Veidt and P. Dewdney, "Bandwidth limits of beamforming networks for low-noise focal-plane arrays," *IEEE Trans. Antennas Propag.*, vol. 53, pp. 450–454„ jan. 2005.

[126] J. Diao and K. F. Warnick, "On the bandwidth gap between the array-feed and cluster-feed regimes for broadband multifeed systems," *IEEE Trans. Antennas Propag.*, vol. 64, pp. 2207–2216, Jun. 2016.

[127] X. Gao and Z. Du, "Modelling of a paraboloid antenna for receiving and its equivalent circuit," *IET Microw., Antennas Propag.*, vol. 8, pp. 931–936, Sept. 2014.

[128] G. Rieke, *Detection of Light: From the Ultraviolet to the Submillimeter*, Cambridge Univ. Press, Cambridge, U.K., 2 edition, 2003.

[129] S. O. Dabironezare, E. Gandini, J. Hassel, A. Neto, and N. Llombart, "Design of a dual-band FSS based bolometer for security imagers at THz frequencies," *Proc. Eur. Conf. Antennas Propag. (EuCAP)*, Apr. 2016.

[130] R. L. Fante and M. T. McCormack, "Reflection properties of the Salisbury screen," *IEEE Trans. Antennas Propag.*, vol. AP-36, pp. 1443–1454, Oct. 1988.

[131] F. Gross and E. J. Kuster, "An optimized polarization sensitive Salisbury screen," *IEEE Trans. Antennas Propag.*, vol. AP-35, pp. 1492–1495, Dec. 1987.

[132] F. Costa, A. Monorchio, and G. Manara, "Analysis and design of ultra thin electromagnetic absorbers comprising resistively loaded high impedance surfaces," *IEEE Trans. Antennas Propag.*, vol. 58, pp. 1551–1558, May 2010.

[133] B. Blázquez, N. Llombart, D. Cavallo, A. Freni, and A. Neto, "A rigorous equivalent network for linearly polarized THz absorbers," *IEEE Trans. Antennas Propag.*, vol. 62, pp. 5077–5088, Oct. 2014.

[134] D. Cavallo, W. H. Syed, and A. Neto, "Closed-form analysis of artificial dielectric layers—Part I: Properties of a single layer under plane-wave incidence," *IEEE Trans. Antennas Propag.*, vol. 62, pp. 6256–6264, Dec. 2014.

[135] S. Maci, M. Caiazzo, A. Cucini, , and M. Casaletti, "A pole-zero matching method for EBG surfaces composed of a dipole FSS printed on a grounded dielectric slab," *IEEE Trans. Antennas Propag.*, vol. 53, pp. 70–81, Jan. 2005.

[136] A. Kazemzadeh and A. Karlsson, "Multilayered wideband absorbers for oblique angle of incidence," *IEEE Trans. Antennas Propag.*, vol. 58, pp. 3637–3646, Nov. 2010.

[137] G. I. Kiani, K. L. Ford, K. P. Esselle, A. R.Weily, and C. J. Panagamuwa, "Oblique incidence performance of a novel frequency selective surface absorber," *IEEE Trans. Antennas Propag.*, vol. 55, pp. 2931–2934, Oct. 2007.

[138] W. Tang, G. Goussetis, H. Legay, and N. J. G. Fonseca, "Efficient synthesis of low-profile angularly-stable and polarization-independent frequency-selective absorbers with a reflection band," *IEEE Trans. Antennas Propag.*, vol. 63, pp. 621–629, Feb. 2015.

[139] J. D. Kraus, *Antennas for all Applications*, McGraw-Hill, New York, NY, USA, 2 edition, 1997.

[140] R. E. Collin, *Antennas and Radiowave Propagation*, McGraw-Hill, New York, NY, USA, 1985.

[141] W. L. Stutzman and G. A. Thiele, *Antenna Theory and Design*, Wiley, Hoboken, NJ, USA, 1981.

[142] D. Long and F. T. Ulaby, *Microwave Radar and Radiometric Remote Sensing*, Artech House, Norwood, MA, USA, 2015,.

[143] A.V. Timofeev and et al., "Submillimeter-wave kinetic inductance bolometers on free-standing nanomembranes," *Superconductor Sci. Technol.*, vol. 27, pp. 1–7, Dec. 2013.

[144] S. Doyle, P. Mauskopf, J. Naylon, A. Porch, and C. Duncombe, "Lumped element kinetic inductance detectors," *J. Low Temp. Phys.*, vol. 151, pp. 530–536, Jan. 2008.

[145] D. G McDonald, "Novel superconducting thermometer for bolometric applications," *Applied Physics Letters*, vol. 50, no. 12, pp. 775–777, 1987.

[146] J. Hassel and et al., "Dual-band submillimeter-wave kinetic inductance bolometers and an imaging system for contraband object detection," *Proc. SPIE*, vol. 10634, pp. 10634F1–10634F6, May 2018.

[147] A. Luukanen, T. Kiuru, M. M. Leivo, A. Rautiainen, , and J. Varis, "Passive three-colour submillimetre-wave video camera," *Proc. SPIE*, vol. 8715, pp. 1–5, May 2013.

[148] F. Costa, A. Kazemzadeh, S. Genovesi, and A. Monorchio, "Electromagnetic absorbers based on frequency selective surfaces," *Forum Electromag. Res. Methods Appl. Technol.*, Jan. 2013.

[149] D. C. Mattis and J. Bardeen, "Theory of the anomalous skin effect in normal and superconducting metals," *Phys. Rev.*, vol. 111, pp. 412– 417, Jul. 1958.

[150] B. Munk, *Frequency Selective Surfaces Theory and Design*, Wiley-Interscience, New York, NY, USA, 2000.

[151] N. Llombart, S. O. Dabironezare, G. Carluccio, A. Freni, and A. Neto, "Reception power pattern of distributed absorbers in focal plane arrays: A Fourier Optics analysis," *IEEE Trans. Antennas Propag.*, vol. 66, pp. 5990–6002, Aug. 2018.

[152] N. Llombart, G. Chattopadhyay, A. Skalare, and I. Mehdi, "Novel terahertz antenna based on a silicon lens fed by a leaky wave enhanced waveguide," *IEEE Transactions on Antennas and Propagation*, vol. 59, no. 6, pp. 2160–2168, June 2011.

[153] S. C. Chapman, A. Tikhomirov, C. M. Bradford, and S. Hailey-Dunsheath, "A quasioptical steering system for the CCAT/XSPEC submillimeter multi-object spectrometer," *Millimeter, Submillimeter, and Far-Infrared Detectors and Instrumentation for Astronomy VII*, vol. 9153, pp. 645–653, 2014.

[154] P. F. Goldsmith and M. Seiffert, "A flexible quasioptical input system for a submillimeter multi-object spectrometer," *Publications of the Astronomical Society of the Pacific*, vol. 121, Jul. 2009.

[155] J. Hunacek and et al., "Detector modules and spectrometers for the TIME-Pilot [cii] intensity mapping experiment," *Millimeter, Submillimeter, and Far-Infrared Detectors and Instrumentation for Astronomy VIII*, vol. 9914, pp. 132–141, 2016.

[156] R. G. Kouyoumjian and P. H. Pathak, "A uniform geometrical theory of diffraction for an edge in a perfectly conducting surface," *Proc. IEEE*, vol. 62, pp. 1448–1461, Nov. 1974.

Summary

Fourier Optics Field Representations for the Design of Wide Field-of-View Imagers at Submillimetre Wavelengths

In recent years, advanced Quasi-Optical (QO) systems operating at (sub)-mm wavelengths are standard solutions for the state-of-the-art sensing and imaging applications. Improving the Field of View (FoV) and/or the operation bandwidth of these QO system are the key improvement steps in many applications. Due to the assumptions taken in developing the Gaussian beam propagation model, for analysing or designing QO systems with wide field-of-views (wide angle optics) coupled to complex (wide band) feeders, modeling the radiation phenomena using Gaussian beam is not appropriate. Here, a Geometrical Optics (GO) combined with Fourier Optics (FO) based technique for deriving the Plane Wave Spectrum (PWS) of QO components in reception is presented. The applicability region of the original FO procedure has been extended, and both magnitude and phase of the field at the focal plane of a QO component is now derived using the method. This procedure is named here "Coherent" FO (CFO), and has been used to express the spectrum of the incident field in realistic cases which include large format arrays of lenses within the focal planes of reflector systems. This representation can be linked to spectral techniques commonly used for arrays, such as Floquet-modes theory, for analysing absorbing mesh grids, and antenna in reception formalism to analyse the performance of antenna feeds in reception.

In this work, two types of coupling between QO components are described: Diffractive and Geometrical. The GO is employed to represent the geometrical coupling between QO components, while CFO technique is used to represent the diffractive coupling between a secondary QO component at the focal plane of a primary one. In particular, the latter technique is used to design large format lens based FPAs (Fly's eye configurations) under an equivalent parabolic reflector with optimal scanning performances. The synthesized lens FPA achieved scan losses much lower than the ones predicted by standard formulas for horn based FPAs. It is worth noting that the derived PWS can be directly used to define the lens and feeder properties without any iterative numerical optimization algorithms to achieve a solution with low scan loss. Here, scan loss of less than 1dB has been achieved while scanning up to $\pm 17.5°$ for an example relevant to the state-of-the-art wide-angle imaging systems. The proposed technique has been validated via a standard Physical Optics based analysis in transmission with excellent agreement.

Also, a wide band QO system for the ASTE telescope based on a hyper-hemispherical leaky lens antenna is presented. The lens antenna is optimized to maximize its coupling to a parabolic reflector. The designed QO system has an average illumination efficiency over 70% in the whole $3:1$ bandwidth

ratio. Including the feeder losses, an averaged aperture efficiency of 65% is obtained. The pattern in the sky of the system is also simulated in GRASP. The side lobe, and the cross-polarization level of this pattern, over the bandwidth, is below −16dB, and −18dB, respectively. The preliminary beam pattern measurement of this wide band QO system is included here.

A QO architecture to achieve wide band wide FoV performance in a (sub)-millimetre imaging and sensing system is also proposed. In order to design the elements of this lens based FPA architecture, with multiple transmitting surfaces close to one another, a fast and accurate analysis tool was developed. The tool is discussed and validated against a time-consuming multi-surface PO code with excellent agreement. Moreover, as a proof of concept of the proposed QO system, an example scenario is described and its performance over a $3:1$ bandwidth ratio is evaluated. For the central element of the proposed QO system, the design achieved 1 dB of scan loss over the whole band while scanning up to ± 7 beams at the center of the frequency band.

Currently, passive imaging cameras at sub-millimetre wavelengths based on focal plane arrays of bare absorbers are commercially attractive solutions. The design of such arrays is typically done resorting to geometrical considerations or basic broadside plane wave incidence analysis. In this work, instead, a spectral electromagnetic model is employed. In this model, the derived PWS of a QO system (the direct field focused by the QO system) is linked to a Floquet-waves representation of the field in the presence of a generic absorbing mesh. The results obtained by the model have been compared, with excellent agreement, with those obtained by full wave simulations. Thus, the proposed spectral method provides an accurate and efficient way to estimate the key optical properties of the imager inside the region of validity of the FO method. Moreover, a dual-band FPA for security imaging at sub-millimetre wave frequencies has been presented. The detectors are based on Kinetic Inductance Bolometers, which allow the development of large FPAs at medium-cooled temperature. The performance of the dual-band imager was evaluated using the described spectral technique. The effective Point Spread Function of the imager coupled to a black-body point source over a wide frequency band ($6:1$) was estimated and successfully validated experimentally. The Half Power Beam Width of the effective pattern is comparable to the one of a diffraction limited QO systems.

Samenvatting

Fourier Optics Veldrepresentaties voor het Ontwerp van Wide Field of View Beeldcamera's bij Sub-millimeter Golflengten

In de afgelopen jaren zijn geavanceerde Quasi-Optische (QO) systemen die op (sub)-mm-golflengtes werken standaardoplossingen voor de meest geavanceerde detectie- en beeldvormingstoepassingen. Het verbeteren van het gezichtsveld (FoV) en/of de operationele bandbreedte van deze QO-systemen zijn de belangrijkste verbeteringsstappen in vele toepassingen. Vanwege de aannames die zijn gedaan bij de ontwikkeling van het Gaussian beam propagation model, voor het analyseren of ontwerpen van QO-systemen met een breed gezichtsveld (groothoekoptiek) gekoppeld aan complexe (breedbandige) feeders, is het modelleren van de stralingsverschijnselen met behulp van de Gaussian beam niet geschikt. Hier wordt een Geometrische Optiek (GO) gecombineerd met Fourier Optiek (FO) gebaseerde techniek voor het afleiden van het Plane Wave Spectrum (PWS) van QO-componenten in de ontvangst gepresenteerd. Het toepasbaarheidsgebied van de oorspronkelijke FO procedure is uitgebreid, en zowel de grootte als de fase van het veld op het brandpuntsvlak van een QO component wordt nu afgeleid met behulp van de methode. Deze procedure wordt hier "Coherente" FO (CFO) genoemd, en is gebruikt om het spectrum van het invallende veld uit te drukken in realistische gevallen die grootformaat arrays van lenzen binnen de brandpuntsvlak van reflectorsystemen omvatten. Deze representatie kan worden gekoppeld aan spectrale technieken die vaak worden gebruikt voor arrays, zoals de Floquet-modus theorie, voor het analyseren van absorberende gaasroosters, en antenne in de ontvangst formalisme om de prestaties van de antenne feeds in de ontvangst te analyseren.

In dit werk worden twee soorten koppelingen tussen QO-componenten beschreven: Diffractief en Geometrisch. De GO wordt gebruikt om de geometrische koppeling tussen QO-componenten weer te geven, terwijl de CFO-techniek wordt gebruikt om de diffractieve koppeling tussen een secundaire QO-component in het brandvlak van een primaire component weer te geven. De laatste techniek wordt met name gebruikt om grootformaat FPA's (Fly's eye configuraties) op basis van lenzen te ontwerpen onder een equivalente parabolische reflector met optimale scanprestaties. De gesynthetiseerde FPA met lens bereikt scanverliezen die veel lager zijn dan die welke worden voorspeld door standaardformules voor FPA's op basis van hoorns. Het is het vermelden waard dat de afgeleide PWS direct kan worden gebruikt om de eigenschappen van de lens en de voeding te definiëren zonder iteratieve numerieke optimaliseringsalgoritmen om een oplossing met een laag scanverlies te bereiken. Hier is een scanverlies van minder dan 1dB bereikt tijdens het scannen tot ±17, 5° voor een voorbeeld dat relevant is voor de state-of-the-art groothoek-beeldvormingssystemen. De voorgestelde techniek is gevalideerd via een standaard Fysieke Optiek gebaseerde analyse in transmissie met een uitstekende overeenkomst.

Ook wordt een breedband-QO-systeem voor de ASTE-telescoop gepresenteerd op basis van een hyper-hemisferische lekke lensantenne. De lensantenne is geoptimaliseerd om de koppeling met een parabolische reflector te maximaliseren. Het ontworpen QO-systeem heeft een gemiddelde verlichtingsefficiëntie van meer dan 70% van de totale relatieve bandbreedte van 3 : 1. Inclusief de voedingsverliezen, wordt een gemiddelde diafragma-efficiëntie van 65% verkregen. Het patroon in de lucht van het systeem wordt ook gesimuleerd in GRASP. De zijlob, en het cross-polarisatie niveau van dit patroon, over de bandbreedte, is respectievelijk onder −16dB, en −18dB. De voorlopige straalpatroonmeting van dit breedbandige QO-systeem is hier opgenomen.

Er wordt ook een QO-architectuur voorgesteld om een breedbandige FoV en brede band-prestatie te bereiken in een (sub)-millimeterbeeld- en detectiesysteem. Om de elementen van deze op lenzen gebaseerde FPA-architectuur te ontwerpen, met meerdere zendvlakken dicht bij elkaar, werd een snel en nauwkeurig analyse-tool ontwikkeld. De tool wordt besproken en gevalideerd aan de hand van een tijdrovende multi-oppervlak PO-code met een uitstekende overeenkomst. Bovendien wordt als bewijs van het concept van het voorgestelde QO-systeem een voorbeeldscenario beschreven en worden de prestaties over een relatieve bandbreedte van 3 : 1 geëvalueerd. Voor het centrale element van het voorgestelde QO-systeem werd in het ontwerp 1 dB aan scanverlies over de hele band bereikt, terwijl in het midden van de frequentieband tot ±7-bundels werden gescand.

Op dit moment zijn passieve beeldcamera's op submillimetergolflengten op basis van focal plane arrays van kale absorbers commercieel aantrekkelijke oplossingen. Het ontwerp van dergelijke arrays wordt meestal gedaan op basis van geometrische overwegingen of basisbreedbandgolf-incidentieanalyse. In plaats daarvan wordt een spectraal elektromagnetisch model gebruikt. In dit model wordt de afgeleide PWS van een QO-systeem (het directe veld gefocust door het QO-systeem) gekoppeld aan een Floquet-golfweergave van het veld in de aanwezigheid van een generiek absorberend gaas. De resultaten van het model zijn, met een uitstekende overeenkomst, vergeleken met de resultaten van volledige golfsimulaties. De voorgestelde spectrale methode biedt dus een nauwkeurige en efficiënte manier om de belangrijkste optische eigenschappen van de imager binnen het geldigheidsgebied van de FO-methode in te schatten. Bovendien is een dual-band FPA voor veiligheidsbeeldvorming bij sub-millimetergolffrequenties gepresenteerd. De detectoren zijn gebaseerd op kinetische inductantiebolometers, die de ontwikkeling van grote FPA's bij een gemiddelde gekoelde temperatuur mogelijk maken. De prestaties van de dual-band imager werd geëvalueerd met behulp van de beschreven spectrale techniek. De effectieve Point Spread Function van de imager gekoppeld aan een black-body puntbron over een brede frequentieband (6 : 1) werd geschat en met succes experimenteel gevalideerd. De halve vermogensbundelbreedte van het effectieve patroon is vergelijkbaar met die van een QO-systeem met beperkte diffractie.

List of Publications

Journal Papers

J1. S. Sung, S. O. Dabironezare, N. Llombart, S. Selvin, N. Bajwa, S. Chantra, B. Nowroozi, J. Garritano, J, Goell, A. Li, S. X. Deng, E. Brown, W. S. Grundfest and Z. D. Taylor, "Optical System Design for Noncontact, Normal Incidence, THz Imaging of in Vivo Human Cornea," *IEEE Transaction on Terahertz Science and Technology* , vol. 8, no. 1, pp. 1-12, Jan. 2018.

J2. S. O. Dabironezare, J. Hassel, E. Gandini, L. Gronberg and N. Llombart, "A Dual Band Focal Plane Array with Frequency Selective Absorbers Based on Kinetic Inductance Detectors," *IEEE Transaction on Terahertz Science and Technology* , vol. 8, no. 6, pp. 746-756, Nov. 2018.

J3. N. Llombart, S. O. Dabironezare, G. Carluccio, A. Freni and A. Neto, "Reception Power Pattern of Distributed Absorbers in Focal Plane Arrays: a Fourier Optics Analysis," *IEEE Transactions on Antennas and Propagation*, vol. 66, no. 11, pp. 5990-6002, Nov. 2018.

J4. S. O. Dabironezare, G. Carluccio, A. Freni, A. Neto and N. Llombart, "Coherent Fourier Optics Model for the Synthesis of Large Format Lens Based Focal Plane Arrays," *IEEE Transactions on Antennas and Propagation*, under review.

J5. H. Zhang, S. O. Dabironezare, G. Carluccio, A. Neto and N. Llombart, "A Fourier Optics Tool to Derive The Plane Wave Spectrum of Quasi Optical Systems," *IEEE Antenna and Propagation Magazine*, submitted.

J6. S. O. Dabironezare, K. Karatsu, S. Yates, V. Murugesan, D. J. Thoen, J. Baselmans and N. Llombart, "Wide-band Quasi-Optical System for the ASTE Telescope with 3 : 1 Bandwidth Ratio at Sub-mm Wavelengths," *IEEE Transaction on Terahertz Science and Technology*, in preparation.

Conference Papers

C1. S. O. Dabironezare, E. Gandini, J. Hassel, A. Neto and N. Llombart, "Design of a Dual-Band FSS Based Bolometer for Security Imagers at THz Frequencies," *The 10th European Conference on Antennas and Propagation (EuCAP 2016)* , Davos, Switzerland, April 2016.

C2. S. O. Dabironezare, J. Hassel, L. Grönberg, E. Gandini, N. Llombart and A. Neto, "Optimization of Frequency Selective Absorbers for Sub-mm Security Imagers," *41st International Conference on Infrared, Millimeter and Terahertz Waves (IRMMW-THz 2016)*, Copenhagen, Denmark, September 2016.

C3. S. O. Dabironezare, G. Carluccio and N. Llombart, "Fourier Optics Analysis for Quasi-Optical Imagers with Large Focal Plane Arrays," *IEEE Antennas and Propagation International Symposium (APS 2017)*, San Diego, USA, July 2017.

C4. S. O. Dabironezare, A. Neto and N. Llombart, "Analysis of Absorbers under Quasi-Optical Systems: Distributed Incoherent Sources," *IEEE Antennas and Propagation International Symposium (APS 2017)*, San Diego, USA, July 2017.

C5. S. O. Dabironezare, G. Carluccio, A. Neto and N. Llombart, "Geometrical Optics – Fourier Optics Tool for the Analysis of Quasi-Optical Imagers with Large Focal Plane Arrays ," *International Conference on Electromagnetics in Advanced Applications (ICEAA 2017)*, Verona, Italy, September 2017.

C6. S. O. Dabironezare, J. Hassel, E. Gandini, L. Grönberg, H. Sipola, V. Vesterinen, N. Llombart and A. Neto, "Analysis of Absorber Based Imaging Systems with Distributed Incoherent Sources," *42nd International Conference on Infrared, Millimeter and Terahertz Waves (IRMMW-THz 2017)*, Cancun, Mexico, September 2017.

C7. J. Hassel, S. O. Dabironezare, and et. al, "Dual-band Submillimeter-wave Kinetic Inductance Bolometers and an Imaging System for Contraband Object Detection," *SPIE Defense + Security*, Orlando, Florida, United States, March 2018.

C8. S. O. Dabironezare, J. Hassel, E. Gandini, L. Grönberg, H. Sipola, V. Vesterinen and N. Llombart, "Broadband Experimental Validation of the Near Field Focusing Pattern of Frequency Selective Absorber Based Kinetic Inductance Detectors," *The 12th European Conference on Antennas and Propagation (EuCAP 2018)*, London, UK, April 2018.

C9. S. O. Dabironezare, G. Carluccio, A. Neto and N. Llombart, "Coherent Fourier Optics Analysis of Large Format Lens Based Focal Plane Arrays," *The 12th European Conference on Antennas and Propagation (EuCAP 2018)*, London, UK, April 2018.

C10. S. O. Dabironezare, G. Carluccio, A. Freni, A. Neto and N. Llombart, "Fourier Optics Based Analysis of Focal Plane Array of Distributed Absorbers," *The 12th European Conference on Antennas and Propagation (EuCAP 2018)*, London, UK, April 2018.

C11. S. O. Dabironezare, J. Hassel, E. Gandini, L. Grönberg, H. Sipola, V. Vesterinen and N. Llombart, "Dual Band Kinetic Inductance Bolometers for Submillimeter-wave Imaging: Experimental And Theoretical Optical Response," *43rd International Conference on Infrared, Millimeter and Terahertz Waves (IRMMW-THz 2018)* , Nagoya, Japan, September 2018.

C12. H. Zhang, S. O. Dabironezare, G. Carluccio, A. Neto and N. Llombart, "A GO/FO Tool for Analyzing Quasi-Optical Systems in Reception," *The 13th European Conference on Antennas and Propagation (EuCAP 2019)*, Krakow, Poland, April 2019.

C13. S. O. Dabironezare, G. Carluccio, A. Pascual Laguna, S. Hähnle, J. Baselmans and N. Llombart, "A Quasi-Optical System with 1 to 3 Relative Bandwidth for the ASTE Telescope," *The 13th European Conference on Antennas and Propagation (EuCAP 2019)*, Krakow, Poland, April 2019.

C14. Z. Zhang, K. Karatsu, S. O. Dabironezare, D. Thoen, B. Brandl and J. Baselmans, "Designing a Gas Cell Experiment for the Calibration of DESHIMA," *18th International Workshop on Low Temperature Detectors (LTD-18)*, Milan, Italy, July 2019.

C15. S. O. Dabironezare, G. Carluccio, A. Neto and N. Llombart, "Analyzing Lens Based Focal Plane Arrays using Coherent Fourier Optics," *IEEE Antennas and Propagation International Symposium (APS 2019)* , Atlanta, Georgia, USA, July 2019.

C16. H. Zhang, S. O. Dabironezare, G. Carluccio, A. Neto and N. Llombart, "A GO/FO Tool for Analyzing Quasi-Optical Systems in Reception," *44th International Conference on Infrared, Millimeter and Terahertz Waves (IRMMW-THz 2019)* , Paris, France, September 2019.

C17. S. O. Dabironezare, G. Carluccio, A. Pascual Laguna, S. Hähnle, J. Baselmans and N. Llombart, "Quasi-Optical System for the ASTE Telescope with 1:3 Bandwidth at Sub-mm Wave," *44th International Conference on Infrared, Millimeter and Terahertz Waves (IRMMW-THz 2019)* , Paris, France, September 2019.

C18. S. O. Dabironezare, M. Zhang, G. Carluccio, A. Freni, A. Neto and N. Llombart, "Design of a Wide-Scan Lens Based Focal Plane Array for Sub-millimeter Imaging Systems Using Coherent Fourier Optics," *14th European Conference on Antennas and Propagation (EuCAP 2020)* , Copenhagen, Denmark, March 2020, **nominated for the best paper award in antennas category**.

C19. S. O. Dabironezare, K. Karatsu, S. Yates, V. Murugesan, D. J. Thoen, J. Baselmans and N. Llombart, "Experimental Validation of the Beam Pattern of a Wide Band Quasi-Optical System for DESHIMA Spectrometer," *14th European Conference on Antennas and Propagation (EuCAP 2020)* , Copenhagen, Denmark, March 2020.

C20. S. O. Dabironezare, G. Carluccio, A. Neto and N. Llombart, "Analysis of Wide Band Wide-Scanning Quasi-Optical Systems Based on Fourier Optics," *14th European Conference on Antennas and Propagation (EuCAP 2020)* , Copenhagen, Denmark, March 2020.

C21. K. Karatsu, A.P. Laguna, S. O. Dabironezare, A. Endo, D.J. Thoen, V. Murugesan and J. Baselmans, "Development of Absolute Frequency Calibration System for Superconducting Integrated Spectrometer," *SPIE Astronomical Telescopes + Instrumentation* , Yokohama, Japan, June 2020.

C22. A. Pascual Laguna, K. Karatsu, J. Bueno, S. O. Dabironezare , D. J. Thoen, V. Murugesan, A. Endo and J. Baselmans, "Filter-Bank for Broadband Sub-Mm Wave Superconducting On-Chip Spectrometers," *SPIE Astronomical Telescopes + Instrumentation* , Yokohama, Japan, June 2020.

C23. A. Endo and et. al, "DESHIMA On ASTE: On-Sky Performance and Upgrade to Ultrawideband," *SPIE Astronomical Telescopes + Instrumentation* , Yokohama, Japan, June 2020.

C24. S. O. Dabironezare, K. Karatsu, S. Yates, A. Pascual Laguna V. Murugesan, D. J. Thoen and A. Endo, "Broadband Quasi-Optical System for DESHIMA Spectrometer," *SPIE Astronomical Telescopes + Instrumentation* , Yokohama, Japan, June 2020.

C25. S. O. Dabironezare, M. Zhang, G. Carluccio, A. Freni, A. Neto and N. Llombart, "Design of a Wide-Scan Lens based Focal Plane Array using Coherent Fourier Optics," *IEEE Antennas and Propagation International Symposium (APS 2020)*, Montreal, Quebec, Canada, July 2020.

C26. S. O. Dabironezare, G. Carluccio, A. Neto and N. Llombart, "Fourier Optics Analysis of Wide Band Wide Scan Quasi-Optical Systems," *IEEE Antennas and Propagation International Symposium (APS 2020)* , Montreal, Quebec, Canada, July 2020.

Thesis Co-Supervised

T1. H. Zhang, "A Graphic User Interface (GUI) for Analysis of Quasi-Optical Systems Based on Fourier Optics and Geometrical Optics Analysis Techniques," M.Sc. thesis, Delft University of Technology, Delft, The Netherlands, Oct. 2018.

T2. M. Zhang, "Designing Realistic Feeders based on Tunable Leaky Waveguide Antennas for a Large Format Lens based Focal Plane Array with Wide Scanning Capabilities," M.Sc. thesis, Delft University of Technology, Delft, The Netherlands, on-going.

Nominations

N1. Nomination for the *Best Paper Award in Antennas Category* at 14th European Conference on Antennas and Propagation (EuCAP 2020), Copenhagen, Denmark, March 2020, with the paper **C18.** listed in the conference publications.

Propositions Accompanying the Doctoral Thesis

1. Gaussian beam model can represent the EM fields propagation through multiple Quasi-Optical (QO) components. However, the Paraxial wave approximation used for deriving this model is appropriate only for scenarios with narrow field-of-views. In this thesis, a Fourier Optics based analysis is proposed as a technique for analysing QO systems with wide field-of-views. (This proposition pertains to this dissertation Ch. 1)

2. The Plane Wave Spectrum (PWS) of a large format lens based focal plane array under focusing system can be derived using Coherent Fourier Optics. This PWS is then used to obtain an optimal geometry in terms of low scan loss performance without employing iterative numerical optimization techniques. (This proposition pertains to this dissertation Ch. 3 and 4)

3. For both bare absorbers and antenna-based detectors under Quasi-Optical systems, conveniently, the effective number of modes can be evaluated as the ratio between the aperture and the focusing efficiencies. (This proposition pertains to this dissertation Ch. 7)

4. It is always better to push a newly developed method to its limits of applicability. Then when we propose it to the readers, they can better understand the capabilities as well as the limitations of this particular solution.

   Paraphrased private conversation with Prof. Nuria Llombart, Delft University of Technology

5. Statistically speaking, summing the luck of the population and integrating it over time leads to a zero value, i.e.:

$$L_{uck}^{tot} = \sum_{Population} \int_0^{t_{max}} L_{uck}(t, p) dt \simeq 0$$

   Personally, I find this law, and in general statistics, terrifying. However, this can be a soothing thought.

6. The recipe for tackling a problem is one-part understanding it, one-part coding your solution, at least a pinch of frustration now and then, and finally two-part debugging. The satisfaction

afterwards is the drive, but it lasts for a moment. Savour it, because it's time to prepare the next batch.

7. There are two types of people in the world: the ones who can extract relevant information from incomplete data sets.

8. In the game of life, you are dealt a hand at the beginning. Sure, you can play the cards you got. Unfortunately, some have to. Some do so by choice and might blame the dealer afterwards. At every given chance, it is best to spend your round drawing more cards from the deck.

9. The human species, throughout its rapid development over the past thousands of years, tends to model its perceived world. This behaviour leads to simplified problems and eventually solutions in reasonable time frames. However, a pitfall of this evolutionary skill is replacing the real world with an equivalent model in one's mind. One should always keep track of the assumptions made in modelling of a complex problem; otherwise, the measurements will not match the theory.

These propositions are considered opposable and defendable, and as such have been approved by the promotors Prof. dr. N. Llombart and Prof. dr. A. Neto

About the Author

Shahab Oddin Dabironezare was born on September 2, 1991 in Mashhad, Iran. He received his B.Sc. degree (cum laude) in Electrical Engineering-Communications from the Ferdowsi University of Mashhad, Mashhad, Iran, in 2013, and the M.Sc. degree in Electrical Engineering at Delft University of Technology, Delft, the Netherlands, in 2015. His Master thesis was part of the FP7 EU project CONSORTIS for developing airport security imagers at sub-millimetre wavelengths. He is currently working toward his Ph.D. degree at the THz Sensing Group in the Microelectronics department of the Electrical Engineering, Mathematics and Computer Science (EEMCS) faculty at Delft University of Technology, Delft, the Netherlands.

His Ph.D. topic is on the development of spectral techniques based on Fourier Optics for analysing and designing wide field-of-view Quasi-Optical systems. The developed techniques were then used for designing several THz imaging systems for security and astronomical applications, based on absorber and lens antenna focal plane arrays. This research has been carried out under the supervision of Prof. Nuria Llombart and Prof. Andrea Neto as promotors, and Dr. Giorgio Carluccio as daily supervisor. This project has been financed by the European Research Council (ERC) starting grant. The research has resulted in six journal publications and twenty-six proceedings in international conferences.

His research interests include, wide band antenna designs for millimetre and sub-millimetre wave applications, wide field-of-view imaging systems, Quasi-Optical systems, absorber based passive cameras, and analytical/numerical techniques in electromagnetic scattering problems.

During his Ph.D., he has co-supervised two M.Sc. students (Delft University of Technology, THz sensing group).

Acknowledgements

This work could not have been realized without the supervision, support, and guidance of many people. I am very lucky to have worked in an amazing research group as well as receiving tremendous amount of support from my partner, my family, and friends. You all not only made this ride possible but made it enjoyable. First of all, I would like to thank my promotors Prof. Nuria Llombart and Prof. Andrea Neto. The supervision I have received from you is at an exceptional level.

Nuria, your knowledge, determination, and work ethics are legendary. I feel so lucky and thankful for the chance you gave me to work with you as one of your students in your ERC project. And I look forward to achieve more goals with your help in the coming future. Your control over the vast number of projects, which are under your supervision, is one of your many qualities that I will always look up to. To put my experience on working with you in simple terms, your mere presence accelerates a discussion forward in an inconceivable speed.

Andrea, the range of your knowledge and experience in the field are honestly overwhelming. I always appreciated your fresh point of view on the projects at hand, and enjoyed the broad scale discussions on important life topics. I learned a lot from you, and not just about photons in Electromagnetics.

This thesis would have been a mess, if even existed, without the daily supervision of dr. Giorgio Carluccio. Giorgio, obviously, your supervision and knowledge on the work is invaluable. On top of that, your attention to details, how much you enjoy what you do, perseverance, and to sum up, your entire character traits makes up for an unique teacher. I couldn't be more lucky than to work with you over these years.

Prof. Freni, thank you for opening up time in your busy schedule when you visited our group in the summers. Discussions with you shaped this work into a presentable format.

To rest of the THz sensing group, thank you for being my work family. As I said before, you made this journey memorable and enjoyable. Daniel(l)e, coming to your office, or your occasional visits to ours was always something to look forward to. I enjoyed our gym and running sessions. Although I was terrible in the latter. Jochem, in my mind you are always a bright spotlight of knowledge. Every discussion with you felt like a rapid overdose of information which I enjoyed very much and hope for some more in the future. Juan, your visits to our room, and your exotic sense of humor are always cherished. Also thank you for being a semi-worthy opponent of mine in the "Who got the best T-Shirt" contest.

I would like to thank the other colleagues and friends of our group which created an environment mixed with exciting academic discussions, filled with things to learn, and also none-academic conversations, dr. Akira Endo, dr. Kenichi Karatsu, David Thoen, dr. Pieter de Visser, dr. Erio Gandini, dr. Ioan Lager, dr. Stephen Yates, Robert Huiting, dr. Darwin Blanco, and dr. Maria Alonso-delPino.

Special thanks to our amazing secretary team, particularly Everdine. Every year I look forward to decorate the Christmas tree with you. This is a tradition that I would miss a lot in coming years. Thanks for being an amazing human being and a superb secretary that makes our lives so much easier and smoother.

I have been in this group now for about 5 years. Many students have come, gone or will be gone soon. Thank you all for making me feel welcome here. Bea, Waqas, Ozan, Allesandro, in my mind you will always remain as the cool PhD guys.

My office mates over the years, we had so much crazy fun times together. Nuri, I hope that you are enjoying life.

Sebastian, thanks for all the fun discussion and activities we have done together. It have always been a joyful process to plan something with you. Sorry for being late for movies, but we both know that probably it will happen again. Also thanks for introducing me to D&D, and DMing our sessions.

Paolo, your presence was brief in our office, but very memorable. I am glad that you were transferred down stairs. On a serious note though, we miss you. Little Andrea, you only have been in our office for like a month. That went by quick, I hope you enjoy the next steps in your life and career.

Alejandro, we had so many crazy late nights in the office together. Somehow, we together developed a fun and strange roommate culture that always baffles the new comers and visitors. It has been a blast to have you sitting next to me. Thanks for tolerating me and being the immediate receiving end of my prank and for giving some back to me. The work related discussions we have are of equal quality.

Cristina, you were a bit late to the party as an office mate. But since you arrived to start your PhD here, you transferred our environment into something new. We had lots of nice coffee discussions over the years. And you organized many outside-work adventures for the rest of us. Thank you and you are truly missed here. Also the silence in the whole floor is a bit unnerving. Which brings me to Harshita, you also left recently which is equally responsible for the current terrifying silence in our entire floor. I wish you both the best for what is yet to come.

Sven, these past 5 years have been packed with your presence in my life. The experience is vast and hard to pin point some highlights. Just to give a tip of this iceberg, one day, you just entered our office and taught us how to make essential tools in case we went to prison. We shared lots of laughs, pranks, drinks and adventures. We shared many hotel rooms for conferences too. But, lets forget the super tiny ones. We hiked in abandoned paths which we clearly shouldn't have, and you made sure that I don't jump off cliffs while trying to avoid spider webs. As I said, its a difficult task to list your presence fully here. I hope we can coordinate some more of these memories in years to come.

Marta, our interactions were limited because of your complex work-study schedule. But the quality here beats the quantity. It was very nice that you could join us for after conference activities in Paris. Lets hope for more of that stuff and less conference stand duty!

Huasheng Zhang and Muhan Zhang, you are the first two master students that I was lucky to work with. Both of you changed my pre-PhD mind set that supervision is an impossible daunting task. This is because you both are very bright and also have been very patient with me. Thank you. I enjoyed every second of working with you.

To the fourth and beyond generations of our students in the group, from my point of view at least, Ralph, Cyrus, Diego, Sander(s)-Kevin, Arturo, Sjoerd, Bruno, Riccardo, Nina, Stefan, Delia, Steven, Esmee, Federica, Antonios, Enrico, and ZhengZheng you are (some were) ideal people to have in a research group: motivated, very bright, and fun people to interact with. It is always a nice bonus

(beside the coffee boost) to walk to our coffee room and share a talk with you.

To my friends over this almost 7 year experience in the Netherlands, you made this major transition smoother. My old roommates Tim and Theimo, I hope that you are having fun while studying.

Farzad, you need to practice your gaming skills a bit more. Get gudder man. Glad that you are relatively close by.

Rossi(t)za and Shailja, our coffee star walks to the library during our Master thesis were something that I remember well every time I walk in the same route. Our gatherings were, and still are, the recharge I need in my tough days. We should organize a pizza + movie on top of TU Delft library again.

My more ancient friends, Mahmoud, Mostafa and Morteza, you are scattered all over the globe, but I am glad that we are maintaining our friendship despite the physical distance. Sorry that I missed some of our gatherings in the past. Specially to Mahmoud, I put some *special* packages of corn flex in the cupboard for your next visit.

Bahram, Amir, Hani, and Ceena, our StarCraft LAN parties were magnificent in the old times. I am glad that some of you relocated to Europe and hopefully we will see each other more than just through monitor screens. Specially to Hani, it is not possible to print a gif, but you know what I mean.

My dear cousins, Ali and Farhad, our long Skype calls, Worm, and AoE II sessions boost my days. Hope to see you soon in Iran. Lets try a Hobbit-LoTR marathon this time.

My dear little sister, Shahrzad, I am so proud of you. Sorry to miss so many major moments in your life. But I look proudly from a distance at how much you have grown over the years. And I cherish all the memories we had together. And we will have a lot more. Probably hundreds of good cafes and restaurants opened up since I visited, lets try them all together. Looking forward to some new music suggestions from you, and also new books you and mom have been reading. No one could ever ask for a better sister. Send my regards to Marshall, pet him and give him some treats from me.

My companion in life, Mehrangiz, you have been an incredible pillar of support for me over these years. You are the reason why I consider myself an extremely lucky person. Life became a joyful adventure with you by my side. You hold me up in my hard days and I hope to do the same for you during yours. And then together we will rule the galaxies ... well I have been carried away ... Love you.

To my amazing parents,

پدر و مادر عزیزم،

فداکاری‌های شما من را به این نقطه از زندگی رسانده‌است. ممنونم برای تمام شب‌هایی که به غرغرهای من گوش دادید، برای تمامی حمایت‌هایتان در سالهای اخیر و همه‌ی سال‌های زندگیم. دوری از شما و شهرزاد و سفر به یک کشور دیگر بدون پشتوانه‌تان کار محالی بود. ممنون که این تصمیم سخت زندگی را برایم آسان‌تر کردید.

پدر عزیزم، تو همیشه من را به انجام بهتر کارهایم ترغیب کردی. اول دبستان من از املا فراری بودم و تو با من نشستی و در یک روز یک دفتر صد برگ را باهم پر کردیم. امتحان املا فقط یک مثال ساده از میزان انرژی و توجه توست. چقدر در مورد آینده‌ی من استرس و نگرانی داشتی و داری. از این به بعد کمتر نگران باش. من آرام آرام از تو یادگرفتم که برای رسیدن به نتیجه، اول باید خوب تلاش کرده باشم و اگر حس رضایت از تلاشم را دارم، همه‌چیز خوب است.

مادر عزیزم، چه صبح‌های زیادی ما با هم از سرخس برای کلاس‌های من به مشهد سفر ۲/۵ ساعته کردیم. چقدر به من آرامش دادی در زمانهای پر استرس. و چقدر خوب به من یاد دادی که اشکالی ندارد وقتی چیزی به وقف مراد نیست احساس غم داشته باشم، اما مهم است که در این حال ساکن نمانم و دوباره حرکت کنم. من از تو یادگرفتم که در کنار جدیت برای رسیدن به هدفهایم از زندگی لذت ببرم.

هردوی شما با هم به من یاد دادید چطور زندگی کنم. امیداوم بتوانم باعث افتخارتان باشم، همینطور که شما افتخار من هستین.